

Cavity quantum electrooptics

by

Rishabh Sahu

April, 2023

*A thesis submitted to the
Graduate School
of the
Institute of Science and Technology Austria
in partial fulfillment of the requirements
for the degree of
Doctor of Philosophy*

Committee in charge:

Jan Maas, Chair
Johannes M. Fink
Onur Hosten
Peter Rabl



Institute of
Science and
Technology
Austria

The thesis of Rishabh Sahu, titled *Cavity quantum electrooptics*, is approved by:

Supervisor: Johannes M. Fink, ISTA, Klosterneuburg, Austria

Signature: _____

Committee Member: Onur Hosten, ISTA, Klosterneuburg, Austria

Signature: _____

Committee Member: Peter Rabl, Technische Universität München, TUM School of Natural Sciences, Garching, Germany

Signature: _____

Defense Chair: Jan Maas, ISTA, Klosterneuburg, Austria

Signature: _____

Signed page is on file

© by Rishabh Sahu, April, 2023

CC BY-NC-SA 4.0 The copyright of this thesis rests with the author. Unless otherwise indicated, its contents are licensed under a [Creative Commons Attribution-NonCommercial-ShareAlike 4.0 International License](#). Under this license, you may copy and redistribute the material in any medium or format. You may also create and distribute modified versions of the work. This is on the condition that: you credit the author, do not use it for commercial purposes and share any derivative works under the same license.

ISTA Thesis, ISSN: 2663-337X

ISBN: 978-3-99078-030-5

I hereby declare that this thesis is my own work and that it does not contain other people's work without this being so stated; this thesis does not contain my previous work without this being stated, and the bibliography contains all the literature that I used in writing the dissertation.

I declare that this is a true copy of my thesis, including any final revisions, as approved by my thesis committee, and that this thesis has not been submitted for a higher degree to any other university or institution.

I certify that any republication of materials presented in this thesis has been approved by the relevant publishers and co-authors.

Signature: _____

Rishabh Sahu
April, 2023

Signed page is on file

Abstract

About a 100 years ago, we discovered that our universe is inherently noisy, that is, measuring any physical quantity with a precision beyond a certain point is not possible because of an omnipresent inherent noise. We call this - the quantum noise. Certain physical processes allow this quantum noise to get correlated in conjugate physical variables. These quantum correlations can be used to go beyond the potential of our inherently noisy universe and obtain a quantum advantage over the classical applications.

Quantum noise being inherent also means that, at the fundamental level, the physical quantities are not well defined and therefore, objects can stay in multiple states at the same time. For example, the position of a particle not being well defined means that the particle is in multiple positions at the same time. About 4 decades ago, we started exploring the possibility of using objects which can be in multiple states at the same time to increase the dimensionality in computation. Thus, the field of quantum computing was born. We discovered that using quantum entanglement, a property closely related to quantum correlations, can be used to speed up computation of certain problems, such as factorisation of large numbers, faster than any known classical algorithm. Thus began the pursuit to make quantum computers a reality.

Till date, we have explored quantum control over many physical systems including photons, spins, atoms, ions and even simple circuits made up of superconducting material. However, there persists one ubiquitous theme. The more readily a system interacts with an external field or matter, the more easily we can control it. But this also means that such a system can easily interact with a noisy environment and quickly lose its coherence. Consequently, such systems like electron spins need to be protected from the environment to ensure the longevity of their coherence. Other systems like nuclear spins are naturally protected as they do not interact easily with the environment. But, due to the same reason, it is harder to interact with such systems.

After decades of experimentation with various systems, we are convinced that no one type of quantum system would be the best for all the quantum applications. We would need hybrid systems which are all interconnected - much like the current internet where all sorts of devices can all talk to each other - but now for quantum devices. A quantum internet.

Optical photons are the best contenders to carry information for the quantum internet. They can carry quantum information cheaply and without much loss - the same reasons which has made them the backbone of our current internet. Following this direction, many systems, like trapped ions, have already demonstrated successful quantum links over a large distances using optical photons. However, some of the most promising contenders for quantum computing which are based on microwave frequencies have been left behind. This is because high energy optical photons can adversely affect fragile low-energy microwave systems.

In this thesis, we present substantial progress on this missing quantum link between microwave and optics using electrooptical nonlinearities in lithium niobate. The nonlinearities are enhanced

by using resonant cavities for all the involved modes leading to observation of strong direct coupling between optical and microwave frequencies. With this strong coupling we are not only able to achieve almost 100% internal conversion efficiency with low added noise, thus presenting a quantum-enabled transducer, but also we are able to observe novel effects such as cooling of a microwave mode using optics. The strong coupling regime also leads to direct observation of dynamical backaction effect between microwave and optical frequencies which are studied in detail here. Finally, we also report first observation of microwave-optics entanglement in form of two-mode squeezed vacuum squeezed 0.7 dB below vacuum level. With this new bridge between microwave and optics, the microwave-based quantum technologies can finally be a part of a quantum network which is based on optical photons - putting us one step closer to a future with quantum internet.

Acknowledgements

"Wait, let me push back the prism a bit!", I asked Matthias as he prepared to warm up our dilution refrigerator after about a year of it staying cold. Our experiment had been broken for a few months now. It was probably that diamond prism, flimsily attached to a metal rod using only glue, which finally gave up after months of being pushed back and forth. The only way we could do any experiment was by pushing the prism hard against the optical resonator sandwiching it tightly between the resonator and the metal rod. We were desperate to salvage any result that we could get no matter the state of the device. After all, the experiment had worked after multiple years of effort put in by my postdocs - Alfredo and William. After a few months of experimenting with a broken prism setup, we had finally decided to give up on our desperate endeavours, warm up the refrigerator and fix the problem properly.

Miraculously, when I pulled the prism back, it behaved normally beating any normal expectation from a system we thought was really broken. Pushing the prism back wasn't even needed, we just decided to do it on a whim! Nevertheless, after discovering this, we immediately pivoted back to our original plan and continued the measurements leading to not just one but multiple successful experiments with the same device.

In a similar turn of events, we came close to warming up again after we had tried enough measurements to prove entanglement between microwave-optics entanglement. The measurements showed entanglement but not clearly enough. Before deciding to warm-up, we again decided to take one more leap of faith and try a measurement in a completely new parameter domain. A measurement which would run for 6 days straight, longer than any measurement we had done until now. As it turns out, this was best measurement we had ever made clearly showing the sought entanglement without a doubt [SQH⁺23].

As a scientist, I must find it hard to say - even though I jokingly do - that luck was a big part of this journey. Maybe it was, but more importantly it was all the effort put in by the whole team, our electrooptics team. It was Alfredo's and Liu's solid understanding, William's magic hands, Georg's help and Johannes who kept over a watch making sure things were never pushed in the wrong direction. It was all this team effort combined which made the impossible seem possible; make an experiment, no matter how intricate and complicated it got, work against all odds with little problems. Therefore, I must thank my whole electrooptics team, It is because of them I was able to complete my PhD, full of experiments which got more and more difficult, with barely any hurdles along the way. Even writing papers with complicated theory was a breeze with an impeccable theory support from our collaborators in TU Wien - Yuri and Peter.

With experiments so big and complicated, many things would break asking for maintenance. Sometimes a solid idea which would make a hard task trivial would need only a small cable you don't have or a tiny connector you didn't know you ran out of. This would usually be the time for me to run to machine shop or electrical shop at ISTA. Whether it was a small

mechanical re-work or helping me find that one small cable I was missing, the friendly people at ISTA workshops always came through. I would like to thank them to helping me speed up any little idea I wanted to try. I would especially like to thank Todor who always helped us make our engineering drawings a reality with his expertise.

And it is not just small re-works one needs, sometimes there are certain equipment, electronic components or just advise that you may need when trying to debug experiments or solve problems in general. It is nice to have other labs working close ready to rescue you when you are in a pinch. I would like to thank Giorgos Katsaros and Onur Hosten for helping our team with whatever equipment we ever needed. I would especially like to thank Sebastian and Fritz not just for helping with borrowing different things but also for valuable discussions whenever it came to solving problems especially with our optical alignments.

I would also like to thank all the other services at ISTA. From handling a myriad deliveries to filling the liquid nitrogen tanks on time, it was all these services which always worked promptly and made sure everything went as smoothly and on time as possible. I would especially like to thank Sandra who was always there for any administrative help. She would help with every little annoying detail because we were too busy to figure things out ourselves.

And last but most definitely not the least, it is the friends made along the way which make the journey worthwhile. Especially for me, someone who came to a new country to start a new journey and had to start the whole social life from scratch, friends became really important. But I am glad I started this journey. At times, I feel like the whole thing was worth it just because of the friends I made along the way. I would like to thank all the people who not only made my journey at ISTA fun but also helped me grow as a person. There are way too many names to take here but I would like to thank all my lab members - Matilda, Andrea, Elena, Martin, Thomas and Farid. Thanks for all the help and making all the group events fun! Apart from that, I would also like to thank the closest people to me: Natália, Catalin and Misha. Thanks for always being there for me.

This work was supported by the European Research Council under grant agreement no. 758053 (ERC StG QUNNECT) and the European Union's Horizon 2020 research, innovation program under grant agreement no. 899354 (FETopen SuperQuLAN) and the Austrian Science Fund (FWF) through BeyondC (F7105).

About the Author

Rishabh Sahu completed a BS in Physics at Institute of Science and Technology, Kanpur (IITK) where he worked on Orbital Angular Momentum (OAM) of light. He also completed a MS in Physics at the same place where he worked on Finite Difference Time Domain (FDTD) simulations of Maxwell's equations. He joined IST Austria in September 2018. His main research include quantum optics, quantum physics and quantum communication. In April 2019, he affiliated with Johannes Fink's group where he started worked on microwave-optics transduction and entanglement.

List of Collaborators and Publications

1. **Rishabh Sahu**^{*}, Liu Qiu^{*}, William Hease, Georg Arnold, Yuri Minoguchi, Peter Rabl, and Johannes M. Fink. January 2023. [Entangling microwaves with optical light](#). [arXiv:2301.03315](#) (*Accepted in Science, publication in progress*)
2. Liu Qiu^{*}, **Rishabh Sahu**^{*}, William Hease, Georg Arnold, and Johannes M. Fink. October 2022. [Coherent optical control of a superconducting microwave cavity via electro-optical dynamical back-action](#). [arXiv:2210.12443](#) (*Accepted in Nature communications, publication in progress*)
3. **Rishabh Sahu**, William Hease, Alfredo Rueda, Georg Arnold, Liu Qiu, and Johannes M. Fink. March 2022. [Quantum-enabled operation of a microwave-optical interface](#). **Nature communications**, 13(1), 1-7.
4. William Hease, Alfredo Rueda, **Rishabh Sahu**, Mathhias Wulf, Georg Arnold, Harald G.L. Schwefel, and Johannes M. Fink. November 2020. [Bidirectional Electro-Optic Wavelength Conversion in the Quantum Ground State](#). **PRX Quantum**, 1(2):020315.

Table of Contents

Abstract	vii
Acknowledgements	ix
About the Author	xi
List of Collaborators and Publications	xii
Table of Contents	xiii
List of Figures	xv
List of Tables	xxiii
List of Algorithms	xxiii
1 Introduction	1
2 Cavity electrooptics	9
2.1 Electromagnetic waves in dielectrics	9
2.2 Wave mixing of electromagnetic fields in nonlinear media	11
2.3 Quantum treatment of electric field interaction in non-linear media	12
2.4 Cavity quantum electro-optics	12
2.5 Conclusion	18
3 Cavity electro-optics with whispering gallery modes	19
3.1 Introduction	19
3.2 Optical whispering gallery mode (WGM) resonators	20
3.3 Microwave whispering gallery modes	31
3.4 Nonlinear vacuum coupling constant	38
3.5 Suppressing the optical sidebands with WGM resonators	39
4 Experimental setup	43
4.1 Introduction	43
4.2 Low temperature experimental setup	43
4.3 Maintaining optical coupling during cooldown	44
4.4 Optical quality factor drop during the cooldown	48
4.5 Room temperature measurement setup	49
4.6 Conclusions	50

5 Transduction with a CW optical pump	53
5.1 Introduction	53
5.2 Theory	53
5.3 Experimental setup	54
5.4 Setup characterization	55
5.5 4-port calibration	58
5.6 Transduction measurements	59
5.7 Added noise	60
5.8 Conclusions	63
6 Low cooperativity pulsed transduction	65
6.1 Introduction	65
6.2 Experimental setup	65
6.3 Setup characterization	66
6.4 Low cooperativity conversion	68
6.5 Conclusions	69
7 High cooperativity pulsed transduction	71
7.1 Introduction	71
7.2 The five mode model	71
7.3 Experimental setup	75
7.4 System characterization	77
7.5 High cooperativity pulsed conversion	78
7.6 Thermal and quantum noise	82
7.7 Kerr effect	87
7.8 Conclusions	88
8 Electrooptic dynamical backaction	91
8.1 Introduction	91
8.2 Theory	92
8.3 Experimental setup	98
8.4 Mode characterization	98
8.5 Measurement	99
8.6 Results	100
8.7 Conclusions	108
9 Entanglement between microwave and optics	109
9.1 Introduction	109
9.2 Theory	110
9.3 Experimental setup	118
9.4 Measurement	120
9.5 System characterization	122
9.6 Data treatment	123
9.7 Results	131
9.8 Conclusions	138
10 Outlook	139
10.1 Introduction	139
10.2 New transducer design	140

10.3 Possible experiments with current imperfect transducer	141
10.4 Final conclusions	145
Bibliography	147
A Single photon electric field for a travelling wave	163
B Microwave transmission line calibration	165
C Experimental setups	169
C.1 Continuous wave optical pump setup	169
C.2 Low cooperativity CW optical pump setup	170
C.3 High cooperativity pulsed optical pump setup	170
C.4 Pulsed optical pump setup for two-mode squeezing	172
D Optical pump PID lock	175

List of Figures

1.1 Total added noise as a function of thermal added noise N_{in} and transduction coefficient η. The red dashed line shows the boundary below which a transducer is quantum-enabled which is suitable for heralded transduction schemes. The red solid line shows the boundary for quantum-limited transduction where deterministic transduction schemes start to work with finite fidelities. Various markers on the plot mark the state of art transducer experiments which have clearly reported their added noise and efficiency values, typically referred to device input/output ports at millikelvin temperatures.	6
2.1 A generic cavity electro-optic setup. \hat{a}_p , \hat{a}_s and \hat{a}_t are the annihilation operators corresponding to the optical pump and the Stokes and anti-Stokes sideband respectively. \hat{a}_o and \hat{a}_e represent the optical and microwave mode respectively. $\kappa_{i,\text{ex}}$ represent the extrinsic coupling rate of optical and microwave cavities.	13
2.2 Optical Stokes sideband suppression via off-resonant optical pumping.	15
3.1 Toroidal coordinate system (ρ, θ, ϕ) to solve modes in a WGM resonator with height h , radius R and radius of curvature at the rim P	20
3.2 Optical mode numerical simulations. a[b] shows the simulation of the eigen mode with $(\rho, \theta, \phi) = (1, 0, 20755)$ [$(\rho, \theta, \phi) = (2, 2, 20755)$] for an optical resonator disk of height 100 μm , radius 2.4 mm and radius of curvature 250 μm	21
3.3 Disk cutting process. Picture credits: Dante Loi and Paul Falthansl.	24
3.4 Lithium niobate cut disk on a custom-made aluminum post. Picture credits: Dante Loi and Paul Falthansl.	24
3.5 The second step of auto-centering process sanding the LN disk around the rotational axis of lathe. Picture credits: Dante Loi and Paul Falthansl.	25

3.6	Change in intrinsic optical mode quality factor after each polishing step along with the resonator rim's surface as inspected under a microscope. Figure credits: Dante Loi and Paul Falthansl.	26
3.7	Optical WGM resonator lapping process.	26
3.8	Evanescnt coupling of light to a WGM resonator via a prism.	27
3.9	Measured reflected optical power as a function of frequency. The different colors represent the different amount of extrinsic coupling rate adjusted via the prism piezo voltage. The prism piezo voltages plotted here are 0 V, 14 V, 23 V, and 29 V. The separation in x -direction is for illustration purpose and does not represent the actual mode frequency shift.	30
3.10	a Fitted total optical linewidth κ_o as a function of the prism piezo voltage. The dark like is an exponential fit to the data as shown in eqn. 3.17. b Calculated contrast of the optical modes as a function of the prism piezo voltage. The dark line is calculated from the κ_o fit.	31
3.11	Final microwave cavity design.	32
3.12	Microwave cavity FEM simulation. a , 2D distribution of single photon E_z field for $m = 1$ microwave mode at the plane which passes through the center of optical WGM resonator. b , Radial distribution of E_z from the shown 2D data in a passing through the max of azimuthal distribution. Dashed line represents the radius where optical mode is present. c , Azimuthal distribution of E_z from the 2D data in a along the radius represented by dashed line in b . Red line is a cosine function plotted on top. (Figure adapted from Ref. [HRS ⁺ 20].)	34
3.13	Room temperature characterization of microwave cavity.	36
3.14	Millikelvin temperature characterization of microwave cavity.	37
3.15	Direct measurement of vacuum coupling constant g_0 . Splitting observed in the optical mode on application of coherent microwave power. Figure adapted from Ref. [HRS ⁺ 20].	39
3.16	Characterization of an avoided crossing observed in an optical TE mode.	41
3.17	Partial hybridisation observed in an optical TE mode.	42
4.1	Final device assembly.	44
4.2	Coldown helper program GUI.	48
4.3	Optical dual parallel Mach-Zehnder interferometer used as single sideband modulator.	50
5.1	Reflected optical mode spectra for transduction results with a CW optical pump.	55
5.2	Microwave cavity properties in the presence of laser light. a Normalized reflected microwave spectra for the highest (lowest) applied pump power in red (blue). b (c) Change in microwave frequency resonance ω_e (intrinsic losses $\kappa_{e,in}$) as a function of applied optical pump power P_p on resonance. d Mixing chamber temperature T_f as a function of P_p with a power law fit $T_f \propto P_p^{0.48}$ (black line) of the intermediate power region. Figure adapted from Ref. [HRS ⁺ 20].	57
5.3	Four port calibration. Figure adapted from Ref. [HRS ⁺ 20].	58
5.4	a (b) Microwave to optics (optics to microwave) transduction measurement in the frequency domain measured using the SAs. Figure adapted from Ref. [HRS ⁺ 20].	59
5.5	a Calibrated total (internal) conversion efficiency in blue (orange) as a function of optical pump power P_p . b Bandwidth of conversion measured by sweeping the optical signal frequency and measuring the converted microwave signal. Figure adapted from Ref. [HRS ⁺ 20].	60

5.6	Measured output microwave noise spectra for $P_p = 0.23 \mu\text{W}$, $P_p = 14.82 \mu\text{W}$ and $P_p = 1.48 \text{mW}$ shown left to right. Figure adapted from Ref. [HRS ⁺ 20].	61
5.7	Frequency domain microwave noise characterization Microwave noise characteristics as a function of the optical pump power P_p . The black arrow marks the superconducting phase transition. The dashed gray lines indicate fitted power laws, specifically $\bar{n}_{wg} \propto P_p^{0.55}$ over the full range of powers, $\bar{n}_b \propto P_p^{1.14}$ up to $P_p \approx 2 \mu\text{W}$ (see inset), and $\bar{n}_b \propto P_p^{0.45}$ at higher powers. The error bars represent the 2σ fit error to Eqn. 5.6. Figure adapted from Ref. [HRS ⁺ 20].	62
5.8	Time domain microwave noise characterization Microwave output noise measured at resonance with a 500 kHz resolution bandwidth where the optical pump tone with $P_p = 1.48 \text{mW}$ is turned on at $t = 0$ for 1 minute. The inset shows the fastest heating rate of $1.1 \text{ photons s}^{-1}$. Figure adapted from Ref. [HRS ⁺ 20].	62
6.1	Time domain system characterization for low cooperativity measurements. a (b) , Normalized pulse reflection of a square pulse from the optical (microwave) cavity on and off resonance. The red curve is a theoretical fit obtained using time domain input-output theory. Figure adapted from Ref. [SHR ⁺ 22].	66
6.2	Bidirectional conversion measurements for low cooperativity a (b) , Optics-to-microwave (microwave-to-optics) conversion for a continuous wave optical pump of $P_p = 134 \mu\text{W}$. The measured input signal pulses are shown with dashed yellow lines and the converted signals with blue dots (red line is theory). Phase coherence and stability of the signal phase is shown in the insets. Rhombuses represent the phase imprinted on the input signal and the blue points represent phase values extracted from subsequently measured converted pulses. Figure adapted from Ref. [SHR ⁺ 22].	68
7.1	The 5 participating modes and their interactions. Figure adapted from Ref. [SHR ⁺ 22].	72
7.2	Pulsed mode characterization a (b) Pulsed characterization of optical (microwave) signal mode. Figure adapted from Ref. [SHR ⁺ 22].	77
7.3	Characterization for Stokes mode avoided crossing for the high cooperativity pulsed measurements. Figure adapted from Ref. [SHR ⁺ 22].	77
7.4	Theory of pulsed conversion a (b) Theoretical microwave to optics conversion with a pulsed optical pump and continuous signal (a pulsed optical signal and continuous pump). The solid (dashed) lines represent the case with $S^2 = 0.22$ ($S^2 = 0.0$). Figure adapted from Ref. [SHR ⁺ 22].	79
7.5	High cooperativity bidirectional conversion. Top (bottom) row panels show results for microwave-to-optics (optics-to-microwave) conversion. a (c) , Converted signal pulses (bright dots are calibrated measurements and lines are theory) for a 300 ns long optical pump pulse measured with a 500 Hz repetition rate for a CW signal (solid lines) and a pulsed signal (dashed lines). b (d) , Measured IQ quadrature modulation of the converted signal pulse (red lines) and the applied IQ quadrature modulation to the input signal (gray dashed lines) for $C = 0.49$. Figure adapted from Ref. [SHR ⁺ 22].	81
7.6	High cooperativity bidirectional conversion with 100 ns long optical pump pulse. a (b) Microwave to optics (optics to microwave) converted pulses (bright dots are calibrated measurements and lines are theory) for a 100 ns long optical pump pulse and a CW signal measured with a 500 Hz repetition rate. Figure adapted from Ref. [SHR ⁺ 22].	82

7.7	Transduction efficiency summary. a (b) Summary of measured steady state for microwave to optics (optics to microwave) conversion. Figure adapted from Ref. [SHR ⁺²²].	82
7.8	Microwave output noise as a function of average optical pump power. Output microwave noise dynamics measured on long time scales as a function of pulse repetition rate for optical pump pulses corresponding to $C \sim 0.38$. The region between vertical dashed lines marks the time interval during which the optical pump pulses are turned on. Figure adapted from Ref. [SHR ⁺²²].	83
7.9	Equivalence of added thermal microwave noise CW optical power and optical pulses with same average optical power. Figure adapted from Ref. [SHR ⁺²²].	84
7.10	Output noise time dynamics and summary. a , $N_{e,\text{out}}$ for a 300 ns long optical pump pulse ($C = 0.38$) for different repetition rates f_{rep} (P_{avg}) measured with a 10 MHz bandwidth centered at the microwave resonance. The blue shaded region shows the times span when the optical pump is on. The gray arrows mark the noise change as predicted from theory. b , $N_{o,\text{out}}$ for the same optical pump pulses and various f_{rep} (P_{avg}) measured with a 10 MHz bandwidth centered at the optical signal frequency. The noise pulses are separated in time for better visibility. c , Compilation of all measured N_{out} for different time-averaged optical pump powers P_{avg} . Red and blue points represent measured $N_{e,\text{out}}$ with 10 MHz and 100 kHz bandwidths respectively. Green points represent $N_{o,\text{out}}$ measured with 10 MHz bandwidth. The solid lines represent power law fits. The green dashed line shows the predicted $N_{o,\text{out}}$ using the measured $N_{e,\text{out}}$. All the points are taken with $C = 0.38$ ($\eta_{\text{tot}} = 11.4\%$) except for the first three blue points which correspond to $C = 0.20$ ($\eta_{\text{tot}} = 8.0\%$), 0.24 ($\eta_{\text{tot}} = 9.1\%$), and 0.3 ($\eta_{\text{tot}} = 10.3\%$) respectively. (Figure adapted from Ref. [SHR ⁺²²]).	85
7.11	a (b) Density plot of the calculated $N_{e,\text{out}}$ ($N_{o,\text{out}}$) with 10 MHz bandwidth as a function of C and \bar{n}_e for $S^2 = 0.22$. The top 4 (first 3) measurements of $N_{e,\text{out}}$ ($N_{o,\text{out}}$) for the same S taken from Fig. 7.10a (b) are shown as circles with experimental values represented by the inside color. Figure adapted from Ref. [SHR ⁺²²].	86
7.12	Inferred quantum cooperativity for the measured output noise values shown in Fig. 7.10(c). Figure adapted from Ref. [SHR ⁺²²].	86
7.13	a (b) Inferred optics-to-microwave $N_{eo,\text{in}}$ (microwave-to-optics $N_{oe,\text{in}}$) equivalent added input noise as a function of C and \bar{n}_e for $S^2 = 0.22$. Crosses mark the lowest 5 blue measurement points in Fig. 7.10(c). Figure adapted from Ref. [SHR ⁺²²].	87
7.14	Observation of amplification due to Kerr effect. a (b) Time domain conversion in the microwave to optics (optics to microwave) direction for 100 ns optical pump pulses of different power and C . The points joined by light colored lines are measured experimentally. The thin bright lines are theoretical only taking into account the $\chi^{(2)}$ effect. After $C \approx 1$, we observe a delayed parametric amplification event. The measured transmission reaches as high as 11.4 in case of microwave to optics conversion and 13.1 in case of microwave to optics conversion (not visible). Figure adapted from Ref. [SHR ⁺²²].	88
8.1	Theoretical coherent optical response in the symmetric case at different C. The left panel corresponds to the optical probing around the Stokes mode, while the right panel corresponds to optical probing around the anti-Stokes mode. (Parameters: $\kappa_o/2\pi = 30\text{MHz}$, $\eta_o = 0.3$, $\kappa_e/2\pi = 10\text{MHz}$) Figure adapted from Ref. [QSH ⁺²²].	94

8.2 Theoretical coherent multimode electro-optical dynamical back-action in normal and reversed dissipation regime. The two left panels correspond to the normal dissipation regime with $\kappa_o \gg \kappa_e$. (Parameters: $\kappa_o/2\pi = 30\text{MHz}$, $\eta_o = 0.3$, $\kappa_e/2\pi = 10\text{MHz}$, $\eta_e = 0.3$, and $C = 0.5$) The red and blue solid curves correspond to the Stokes and anti-Stokes case with $C = 0.5$, while the dashed curves correspond to the original reflection coefficient with $C = 0$. The two right panels correspond to the reversed dissipation regime with $\kappa_o \ll \kappa_e$. (Parameters: $\kappa_o/2\pi = 1\text{MHz}$, $\eta_o = 0.3$, $\kappa_e/2\pi = 10\text{MHz}$, $\eta_e = 0.3$, and $C = 0.5$). Figure adapted from Ref. [QSH ⁺ 22].	96
8.3 Optical modes. The optical TE mode family for dynamical backaction measurements. The separation between the more contrasted lobe between each mode is stated in table 8.1. We pump the mode 2 for symmetric scattering case, mode 3 for anti-Stokes mode suppression and mode 5 for Stokes mode suppression. Figure adapted from Ref. [QSH ⁺ 22].	98
8.4 Dynamics of reflected probe tone. Temporal on-resonant response $R(\omega)$ [cf. Eq. 8.20] between pulse on and off (pump peak power $\sim 500\text{mW}$). Left panel shows the symmetric case ($\omega_p = \omega_2$), with on-resonant microwave response (turquoise blue curve) in the upper panel and optical Stokes (orange curve) and anti-Stokes (turquoise blue curve) responses in the lower panel. Right panel shows the two asymmetric cases, i.e. the on-resonant microwave and optical Stokes responses (red curves) in the Stokes case ($\omega_p = \omega_3$), and the resonant microwave and optical anti-Stoke responses (blue curves) in the anti-Stokes case ($\omega_p = \omega_5$). Figure adapted from Ref. [QSH ⁺ 22].	101
8.5 Stationary backaction in microwave mode. Microwave response measurements with the same pump power as in Fig. 8.4. The upper panel shows the stationary $R_e(\omega)$, with fitting curves as solid lines. The lower panel shows the reconstructed microwave reflection $ S_{ee}(\omega) ^2$ with the pump on (solid curve) and off (dashed curve) from the fitted parameters. Figure adapted from Ref. [QSH ⁺ 22].	102
8.6 Microwave mode parameter change due to backaction. Fitted microwave frequency shift and linewidth change versus cooperativity C . Dashed lines are theoretical curves. Error bars represent the 95% confidence interval of the fit. Figure adapted from Ref. [QSH ⁺ 22].	102
8.7 Stationary backaction in optical modes. Measurements with same pump power as in Fig. 8.4, with the two left panels for Stokes mode probing and the two right panels for anti-Stokes mode probing. The upper panel shows $R_o(\omega)$ with fitting curves (solid lines). The lower panel shows reconstructed optical reflection $ S_{oo}(\omega) ^2$ with pulse on (solid curve) and off (dashed curve) in logarithmic scale, which demonstrates EOIA in the Stokes case and EOIT in the anti-Stokes case. Figure adapted from Ref. [QSH ⁺ 22].	103
8.8 Optical reflection change due to backaction. The upper panel shows $ S_{oo}(\omega_s) ^2$ for the two Stokes mode probing cases, while the lower panel shows $ S_{oo}(\omega_{as}) ^2$ for the two anti-Stokes mode probing cases. The corresponding theoretical curves are shown as dashed lines. Error bars indicate two standard deviations. Figure adapted from Ref. [QSH ⁺ 22].	104

8.9	Transient backaction in microwave mode. Instantaneous coherent microwave responses during the pump pulse obtained for the same pump power as in Fig. 8.4. In each pump configuration, we perform a joint fit of $R_o(\omega)$ over the time of the pulse with the full dynamical back-action model, and extract the time dependent $C(t)$ (upper panel). Similarly, we perform a joint fit of $R_e(\omega)$ to obtain the frequency and linewidth changes (dots) over time, with corresponding theoretical curves (dashed lines) using the above fitted parameters from the optical coherent response. Error bars represent the 95% confidence interval of the fit. Figure adapted from Ref. [QSH ⁺ 22].	105
8.10	Excess delayed backaction in microwave. Instantaneous coherent microwave response in the symmetric case ($J_{s/as} = 0$) with different pulse lengths. a (b) show The on-resonant $\omega_e = FSR$ (off-resonant $\omega_e \neq FSR$) cases. The corresponding pulse end and the bounce of the delayed back-action are indicated with turquoise blue and purple dots, where the time difference is t_{ex} . The mean lifetime τ_{ex} is fitted from exponential decay of $R_e(\omega_e)$ after the bounce, shown as orange and blue curves in the left and right panels. Figure adapted from Ref. [QSH ⁺ 22].	106
8.11	Extracted bounce time t_{ex} after the pulse is off and the mean decay time τ_{ex} as a function of pulse length. The blue and red curves correspond to the on-resonant and off-resonant cases. Figure adapted from Ref. [QSH ⁺ 22].	107
8.12	Fitted microwave frequency and linewidth change after the optical pulse. Different color corresponds to different C . Figure adapted from Ref. [QSH ⁺ 22].	107
9.1	Schematic pulse sequence of a single measurement for two-mode squeezing measurements. Figure adapted from Ref. [SQH ⁺ 23].	121
9.2	Normalized reflection intensity $ S_{oo} ^2$ spectra of optical modes \hat{a}_o , \hat{a}_p and \hat{a}_t in red, green and blue respectively. a (b) shows the optical mode spectra of the first (second) set of modes with the anti-Stokes and Stokes scattering ratio $S = -10.3$ dB (-3.1 dB). The dashed line marks the effective FSR between the pump mode \hat{a}_p and the optical mode \hat{a}_o . Figure adapted from Ref. [SQH ⁺ 23].	122
9.3	Example single shot time-domain measurement. a (b) show the measured microwave (optical) output signal downconverted at 40 MHz. The shaded part in each case shows the region of the SPDC signal (the first optical pump pulse). For a single pulse, the SNR of a SPDC signal is too small to be seen. However, during the second optical pump pulse, a coherent response is seen in both signal outputs where the phase can be measured with high SNR for each single shot. Figure adapted from Ref. [SQH ⁺ 23].	124
9.4	Averaged time-domain measurement. a (b) Measured output power in the \hat{a}_e (\hat{a}_o) mode in units of photons per second in a 1 Hz bandwidth and averaged over a million experiments. The SPDC signals are shown in the insets with the dashed gray lines indicating the calibrated detection noise floor $N_{j,add} + 0.5$. Figure adapted from Ref. [SQH ⁺ 23].	124
9.5	Accuracy of phase correction scheme. The histogram shows the difference in the measured phase between the first and second optical pump pulse. Figure adapted from Ref. [SQH ⁺ 23].	125
9.6	Post-pulse selection. The measured coherent optical power during the second optical pump pulse depends on the optical heterodyne gain and the received optical signal power. a shows the normalized histogram of this measured optical power over all the collected pulses. The same histogram after pulse post selection is shown in b . Figure adapted from Ref. [SQH ⁺ 23].	126

9.7	Raw frequency domain measurements. a shows the measured output spectra for time region before (during, after) the first optical pulse shown in cyan (purple, orange) as well as the cold cavity baseline in grey. Similarly, b shows the output spectra for the optical output before (during, after) the first optical pulse in cyan (green, orange). Figure adapted from Ref. [SQH ⁺ 23].	127
9.8	Microwave waveguide noise as a function of the average optical pump power. The error bars represent 2σ error. The solid line is a power law fit. We find the power law is actually quite close to a linear function. Figure adapted from Ref. [SQH ⁺ 23].	127
9.9	Output noise in frequency-domain. a Microwave output power spectral density vs. $\Delta\omega_e = \omega - \omega_e$ centered on resonance right during the three different time-snippets from Fig. 9.1. Yellow and green dashed lines are fits to a Lorentzian function, which yields the microwave bath occupancies before and after the entangling pulse. Error bars represent the 2σ statistical standard error and the shaded regions represent the 95% confidence interval of the fit. b Optical output power spectral density vs. $\Delta\omega_o = \omega_o - \omega$ during and after the first optical pump pulse. The in-pulse noise spectra are fit jointly with theory. Figure adapted from Ref. [SQH ⁺ 23].	128
9.10	Joint quadratures as a function of LO phase. a. Joint quadratures at resonance $X_+(\Delta\omega = 0)$ and $P_+(\Delta\omega = 0)$ are plotted as a function of the local oscillator phase ϕ . b. Δ_{EPR} as a function of ϕ . The shaded region in both plots represents the 2σ statistical error. Figure adapted from Ref. [SQH ⁺ 23].	129
9.11	Correcting the time delay between microwave and optical pulses. The plots show the local oscillator phase ϕ_{\min} which minimizes $\Delta_{\text{EPR}}(\Delta\omega, \phi)$ as a function of detuning frequency $\Delta\omega$. a (b) shows the case when the time difference of arrival between the microwave and optics signals was 25 ns (≈ 0 ns). The solid lines are the linear fit to the experimental data. Figure adapted from Ref. [SQH ⁺ 23].	130
9.12	Quadrature histogram raw data. Normalized difference of the two-variable quadrature histograms obtained during and before the optical pump pulse based on the data shown in Figs. 9.9 and 9.15. Figure adapted from Ref. [SQH ⁺ 23].	130
9.13	Measured covariance matrix V_{ij} in its standard form plotted for $\Delta\omega_j = 0$ from the data in Fig. 9.9. Figure adapted from Ref. [SQH ⁺ 23].	132
9.14	Wigner function marginals at resonance Wigner function marginals of different output quadrature pairs in comparison to vacuum for $\Delta\omega_j = 0$ from the data in Fig. 9.14. The contours in blue (grey) represent the $1/e$ fall-off from the maximum for the measured state (vacuum). Figure adapted from Ref. [SQH ⁺ 23].	132
9.15	Squeezing with 250 ns optical pump pulse Data from Fig. 9.14. Top panel, the measured average microwave output noise $\bar{V}_{11} = (V_{11} + V_{22})/2$ (purple), the average optical output noise $\bar{V}_{33} = (V_{33} + V_{44})/2$ (green) and the average correlations $\bar{V}_{13} = (V_{11} - V_{24})/2$ (yellow) as a function of the measurement detunings. The solid lines represent the joint theory fit and the dashed lines are individual Lorentzian fits to serve as a guide to eye. The middle (bottom) panel shows two-mode squeezing Δ_{EPR}^- in red (anti-squeezing Δ_{EPR}^+ in blue) calculated from the top panels. The darker color error bars represent the 2σ statistical error and the outer (faint) 2σ error bars also include the systematic error in calibrating the added noise of the measurement setup. Figure adapted from Ref. [SQH ⁺ 23].	134
9.16	Squeezing with 600 ns optical pump pulse Refer to figure caption of Fig. 9.15.	135

9.17 Power dependence of CM elements. The top panel shows the microwave mode thermal bath occupancy $\bar{n}_{e,\text{int}}$ for before-pulse, after-pulse and in-pulse regimes as a function of the peak optical pump power at the device and the corresponding cooperativity. The bottom two panels show the <i>on-resonance</i> squeezing Δ_{EPR}^- and anti-squeezing Δ_{EPR}^+ calculated from the middle panel along with theory (solid lines). The darker color error bars represent the 2σ statistical error and the outer (faint) error bars also include systematic errors. Figure adapted from Ref. [SQH ⁺ 23].	136
9.18 Squeezing with 600 ns optical pump pulse Refer to figure caption of Fig. 9.15. Figure adapted from Ref. [SQH ⁺ 23].	137
10.1 Proposed new design of transducer. The new design was proposed by Rueda <i>et al.</i> [RHF ¹⁹]. The main difference from the design in this thesis is that now the optical resonator is clamped at the center and an evaporated film of superconducting material extends up to the optical mode forming the capacitor rings. Optical fields are represented in green and those for microwave in blue. Figure adapted from Ref. [RHF ¹⁹].	140
10.2 All-optical qubit readout. A continuous probe tone at optical resonance is sent the optical resonator. The optical resonator couples to the microwave cavity at ω_e with the parametrically enhanced coupling constant g_{eo} . The microwave cavity is connected to the qubit cavity (at ω_q) with a transmission line with transmission constant η . Depending on the state of the qubit, $\omega_e = \omega_q$ or $ \omega_e - \omega_q \gtrsim \kappa_q$, the linewidth of qubit cavity. The change in the reflected optical signal which indicates the state of the qubit depends on g_{eo} and η .	143
B.1 Characterization of the added noise in the microwave detection chain. Measured output noise from a 50Ω calibration load as a function of its temperature T_f . The measured noise is plotted in units of photons as $N_{\text{det}}^{50\Omega} = P_{50\Omega}/(\hbar\omega_e GB)$. The dashed line at the bottom represents the fitted vacuum noise level in addition to the added noise. The red line and shaded region represents the fit and the 95% confidence interval around it. (Figure adapted from Ref. [SQH ⁺ 23].)	166
B.2 Microwave added noise and gain spectra. a (b) The measured added noise in units of photons as $N_{\text{det}}^{50\Omega} = P_{50\Omega}/(\hbar\omega_e GB)$ (gain) as a function of microwave frequency. The shaded area represents the 2σ error in fit from eqn. B.3. (Figure adapted from Ref. [SQH ⁺ 23].)	167
C.1 Continuous wave optical pump experimental setup. (Figure taken from Ref. [HRS ⁺ 20].)	170
C.2 Low cooperativity CW optical pump experimental setup. (Figure taken from Ref. [SHR ⁺ 22].)	171
C.3 High cooperativity pulsed optical pump experimental setup. (Figure taken from Ref. [SHR ⁺ 22].)	172
C.4 Pulsed optical pump experimental setup for two-mode squeezing. (Figure taken from Ref. [SQH ⁺ 23].)	173
D.1 The PID circuit used in optical pump lock. a 3D rendering of the designed PID circuit. b Final completed circuit. Various measurement ports and used knobs and stitches are labelled.	175

D.2 Circuit schematic for the PID lock used for optical pump lock. The PID controls the current to a Peltier element which changes the temperature of an optical cavity, in turn changing its frequency.	177
--	-----

List of Tables

3.1 Microwave frequency ω_e change and corresponding drop in electric field E_z at the location of the optical mode and corresponding vacuum coupling constant g_0 as a function of gap between the capacitor rings and the optical resonator for room temperature (RT) and low millikelvin temperature (LT). The change in temperature is simulated via change in dielectric constant of lithium niobate.	34
5.1 Mode characterization for CW pump transduction.	57
6.1 System parameters for low cooperativity measurements.	67
7.1 System parameters for high cooperativity pulsed measurements.	78
8.1 Calibrated frequency separation of the adjacent optical modes, shown as the distance between the main dip of each optical modes.	98
8.2 Fit parameters for the split modes. κ_o and κ_m correspond to the total loss rate of the TE and corresponding TM mode. δ_o and δ_m correspond to the cavity detuning of TE and corresponding TM mode to the main dip of the split mode, which is centered to zero in Fig. 8.3.	99
8.3 Measurement details for different mode and probing configurations. The pump mode and probe mode indexes are given for each probing configurations. Microwave frequency is adjusted accordingly to match the pump and probing mode separation.	99
B.1 The added noise and gain in microwave detection chain (1σ errors shown)	167

List of Algorithms

5.1 Dynamic step size digital laser lock.	56
---	----

CHAPTER

1

Introduction

It was about 100 years ago when Einstein, Podolsky and Rosen (EPR) started a debate about the fundamental nature of reality [EPR35]. They argued against a new interpretation of reality given by quantum physics saying that, under certain circumstances, the postulates of quantum physics violate the local realism of the universe. Einstein was especially against quantum physics because quantum physics not only dealt with an inherent randomness in the universe but also it seemed to postulate non-local realism or information travelling faster than the speed of light - something which was impossible according to his theory of relativity. Just two months after EPR published their argument, Niels Bohr shot it down essentially saying that non-locally correlated information is random until causally connected [Boh35]. In other words, only random information is instantaneously transferred while any useful signal is still limited to speed to light as theory of relativity predicts. Erwin Schrödinger also weighed in on the topic and gave the phenomenon its name - "quantum entanglement" and called it "the characteristic trait of quantum physics" [Sch35].

Optical photons, with their ability to preserve quantum mechanical properties even at room temperature, pioneered the fundamental experiments verifying the existence of quantum entanglement about 50 years ago [FC72]. This was followed by demonstration of quantum entanglement between various other entities [HHHH09] such as electrons, spins, atoms, ions, mechanical vibrations and even living objects [LTN⁺22].

Today, we know quantum entanglement as a resource which separates quantum applications from their classical counterparts giving them distinct advantages in computation, communication and meteorology [HHHH09]. In the field of quantum communication, it has given birth to a whole new field of quantum cryptography dealing with securely distributing information that is guaranteed to be free of eavesdropping by the fundamental laws of universe [KLH⁺15, XMZ⁺20]. On top of that quantum dense coding has shown higher channel capacities on channels that can share entanglement [GLLG19]. Experimentally, optical photons have already been used to distribute entanglement over tens of kilometer [YML⁺20]. This can be further scaled with the help of quantum repeaters [CdF⁺05, RNH⁺12, RKRR14, RWM⁺18, BRM⁺20, PHB⁺21, KGK⁺23, AEE⁺22]. On the meteorology front, quantum entanglement can be used to go beyond the classical precision limit or yield better statistical precision with fewer measurements [GLM11, DRC17].

Nevertheless, one of the most important applications of entanglement is in computation [GI19]. We have witnessed significant growth in classical computation power by making the transistor -

the smallest logical element - smaller and smaller. But now these transistor sizes have reached the atomic limits and it gets more and more difficult to keep the computation purely classical at these scales. The solution is to use a quantum computer which uses quantum entanglement to gain a computational advantage in solving many problems over classical computers.

Over the last two decades, many systems have been used to demonstrate quantum control and stability for quantum computation - photons [ZWD²⁰], trapped ions [MCD²¹], electron spins [PTD¹²], nuclear spins [PTD¹³], quantum dots [BHJ²²] and other dopants in solids such as nitrogen-vacancy centers [PG08], atomic ensembles [BL20], topological qubits [NSS⁰⁸] and superconducting circuits [AAB¹⁹]. Each platform has its own pros and cons. Photons have excellent coherence times since they don't interact with the environment but, due to the same reason, it is a challenge to make efficient two-qubit gates for photons since they also don't easily interact with each other [SP19]. Trapped ions have shown great coherence times and one-and two-qubit gate fidelities but slow gate times and scalability issues remain a challenge [BCMS19]. Nuclear spins also boast very long coherence time (on the order of hours) owing to their isolation from noisy environment but the same property makes it really hard to efficiently control them [ZHA¹⁵]. This makes weakly interacting nuclear spins an ideal candidate for quantum information storage or quantum memories.

Microwave based platforms for quantum computation, such as superconducting circuits [HWFZ20] and electrostatically defined quantum dots [XPv²¹], provide a sweet spot high level of control (gate times $\sim 100\text{ ns}$) and good coherence times (going up to $\sim 1\text{ ms}$). A distinct advantage of microwave-based qubits is that these can simply be etched on a silicon chip much like today's classical microprocessors [ZKW²²]. As a result, the best systems for superconducting qubits boast ~ 50 qubits [AAB¹⁹] and same for quantum dot based system is up to 16 qubits [BHJ²²]. A quantum computer based on superconducting circuits even achieved quantum supremacy (it made calculations impossible to complete on a classical computer) in 2019 and showed tangible improvement in logical errors using more physical qubits [AAA²³]. However, since they are based on microwave frequencies, they can only operate at millikelvin temperatures where the microwave frequency modes are in their ground state and superconductors are near loss-less.

The progress of quantum technologies in the last decades has unambiguously shown that no single quantum platform is the universal solution. We need to combine the best features of all the available platforms together. In the future, a network of remote hybrid quantum nodes, capable of storage and processing quantum information, seamlessly communicating with each other via distributed entanglement based on optical photons and bolstered by quantum repeaters, would be needed for general-purpose quantum computing and communication [KBK¹⁵].

A distributed quantum network of quantum information processing nodes which can all share entanglement would be an amazing resource [Kim08]. Distributed quantum computing would allow not only for scalability of quantum computation but also cross-verification of classically intractable quantum processor results [CCC20, KMC22]. Apart from distributed quantum computing [ACC²²], quantum communication [PPH²²] and quantum cryptography related uses, a quantum network would also be useful for distributed quantum sensing [GBB²⁰, ZZ21, CVM²³]. It is now a well known result that a distributed network of entangled quantum sensors can have significantly more sensitivity when measuring an aggregate property of all the separate measurements [ZZ21, LZL²¹]. Using this result, proposals have been made for a globally synchronised clock network [KKB¹⁴, MZF¹⁸], spatially separated telescopes sharing entanglement which can measure a distant events with better accuracy [GJC12, DBJK²¹, KBDGL19], and quantum phase imaging [PKD18, ZZL²¹]. Another application is blind

quantum computing, where by classically interacting with two quantum processors which share entanglement and solving a part of problem on each processor, one can securely conduct remote quantum computation without any processor knowing the final result of quantum computation [HZM⁺17].

Motivated with this future of hybrid quantum networks, efforts have been made to connect various localized quantum platforms with flying optical photons. Various qubit platforms have shown remote entanglement between remote quantum nodes including trapped ions [KGK⁺23], atomic ensembles [CdF⁺05], optically-addressed quantum dots [DSG⁺16], rare-earth ions [UCB⁺12] and qubits based on imperfections in NV centers [BHP⁺13]. Notably, trapped ions were shown to be entangled over a distance 230 m [KGK⁺23] and 3-node entanglement distribution was demonstrated with NV center qubits via optical photons [PHB⁺21]. Nevertheless, qubit platforms based on microwave technology - superconducting qubits and electrically addressed quantum dots have yet not been connected via room temperature channels owing to their incapability of directly coupling to optical frequency photons.

The lack of this vital connection did not go unnoticed and proposals to achieve such links started surfacing about 10 years ago. One of the common theme for these proposals was to use mechanics or phonons to link microwave and optics together [SP11, RL11, BVAC13] owing to rapid development of optomechanics [GHV⁺09, SAR⁺09, PW09, AKM14] and experimental demonstrations of coupling between microwave photons and phonons [THRL08, RNM⁺10]. Other proposals included electrooptic interfaces [Tsa10, Tsa11] atomic interfaces such as clouds of ultracold atoms [HKR⁺12], coupling superconducting qubits to spins in NV centers via magnetic coupling [MWT⁺10], via rare-earth ion doped crystals [OLB⁺14] and magneto-optic modulation [WCL14].

One of the first experimental demonstrations used mechanical motion to couple microwave and optics together. They were almost immediately divided into two categories - low frequency capacitively-coupled mechanics with a membrane [APP⁺14, BSS⁺14] and high frequency piezoelectrically-coupled mechanics [BVAC13]. The former use a mechanical motion of a membrane, part of which is capacitively coupled to a microwave resonator and another part to mirror of an optical Fabry-Perót cavity. Using such system, a significant result from the group at NIST came already in 2014 boasting bidirectional coherent conversion efficiency of $\sim 10\%$ between classical microwave and optics signals using a thin film silicon nitride membrane. Although, the conversion efficiency was quite high, the noise performance of the transducer was not up to the mark owing to the low frequency (1.8 MHz) mechanical oscillator used which was far from its ground state even at millikelvin temperatures. Additionally, it also limited the conversion bandwidth of the transducer. For these systems, the main source of noise - thermal noise in the mechanical mediatory mode - is shared with both the microwave and optical modes. Since the source of the noise is the same, the output noise on the microwave and optics side is correlated. Using this fact, one can measure the noise from one of the reflected output signals and use a feedforward protocol to effectively cancel the noise from the other output. 4 years later, the group used this technique to bring down the added noise level to 38 quanta while simultaneously achieving a higher conversion efficiency of 47% [HBU⁺18]. This was further improved to just 3.2 added noise photons for the same conversion efficiency [BKU⁺22]. Recently, the group has demonstrated readout of a superconducting qubit in the optics domain using their transducer [DUM⁺22]. It was the first demonstration yet which shows that the qubit suffers from minimal backaction due to thermal noise added by the transducer. Opto-mechanical transducers, meanwhile, were also demonstrated fully-integrated on a chip by Arnold *et al.* in 2020 [AWB⁺20]. The demonstrated total bidirectional conversion efficiency

1. INTRODUCTION

was 1% with the output noise on the order of 100s of quanta.

On chip designs are a lot more prevalent on the piezo-optomechanics side [VSPC16, HFZ⁺20, JSD⁺20, HPC⁺22, WDB⁺22]. In these devices, a phononic-photonic cavity is used where mechanical and optical modes are co-localized for high opto-mechanical coupling. The mechanical modes are also coupled to microwave electric field via piezoelectric effect. The mechanical mode in these devices are also of higher frequency - usually on the order of gigahertz. As a result, these modes are easier to cool to the ground state. In 2019, Forsch *et al.* showed first successful microwave-optics transduction with a mechanical mode in its ground state using a pulsed optical pump although with a limited conversion efficiency of 5.5×10^{-12} [FSW⁺20]. One main factor limiting these transducers is the microwave coupling efficiency which is limited by impedance mismatch between the microwave transmission line and high impedance piezo-electric device. A solution to this is to go around this problem by fabricating a qubit along side of the transducer on the chip and use a hybridised microwave-mechanics mode to avoid coupling an itinerant microwave signal directly to the transducer via a waveguide. This was demonstrated by Mirhosseini *et al.* in 2020 where by using a transmon qubit directly coupled to the transducer, they were able to measure Rabi-oscillations of the qubit in the optical domain - an astounding feat for the time [MSKP20]. The total conversion efficiency improved significantly from other similar systems and total detection efficiency from qubit to the photon detector was reported as $\sim 10^{-6}$. However, the main drawback of this system is that the scattered optical pump pulse generates a lot of quasi-particles which breaks the superconductivity and destroys the state of the qubit. This problem is not observed for previously-stated opto-mechanical transducers [DUM⁺22].

Apart from mechanical systems, microwave-optics transduction has also been demonstrated with cold atom systems such as Rydberg atoms using 4-wave and 6-wave mixing processes [HVG⁺18, VGH⁺19, PMFS19] with efficiencies usually hovering around $\sim 1\%$. There is one notable exception where Kumar *et al.* showed an internal (external) conversion efficiency of 58%(2.5%) and thermal added noise referred to input¹ of only 0.6 quanta. Here also, the total conversion efficiency suffered from poor microwave coupling efficiency of ~ 0.06 (optical coupling efficiency is good 0.58) [KSS⁺23]. Transduction has also been shown with ferro-magnonic mode called the Kittle mode [HOT⁺16, ZZH⁺20] and with rare-earth ion magneto-optical devices [BRX⁺20] albeit with very low conversion efficiencies $\sim 10^{-10}$.

All the transduction approaches that we discussed till now use an intermediary mode that can simultaneously couple to microwave and optics modes. However, there is a direct means of achieving microwave to optics coupling.

Electro-optics effect or its linear version - the Pockels effect - was discovered in late 19th century by Friedrich Carl Alwin Pockels who discovered that applying electric field to certain crystals would change their refractive index. A varying electric field in time - say of a microwave frequency - would apply the same modulation to the optical light. This turned out to be a boon for our current communication technology. Our current high bandwidth communication is based on microwave frequencies which are the fastest data rates that can be processed by classical microprocessors. However, microwave frequencies travel in metal waveguides with high transmission losses. Encoding the same information on high-bandwidth optics through electro-optic modulation changed the whole scheme since light travelled in optical fibers with extremely low loss $\sim 0.4 \text{ dB/km}$. Moreover since optical fibers are cheap and small, electro-optic modulators became ubiquitous in our standard communication technology.

¹described later in the introduction

There was still one problem with electro-optic modulators. They are quite inefficient owing to really small nonlinearities in only a few special crystals. The microwave power needed to modulate with any significant modulation depth even in the best available electrooptic crystals, like lithium niobate, needs microwave powers ~ 1 W. About 30 years ago, people realized that whispering gallery mode (WGM) resonators, which confine the fields in a concave space, offered high quality factors which can effectively enhance the nonlinearity in the crystal by increasing the interaction time with the nonlinear material, making them an attractive pursuit for many application which relied on high optical nonlinearities [SMM⁺16, LCC17]. Proposals and experiments with optical WGM resonators combined with 2D microwave resonators began in early 2000s [CHL01, ISMM03, MSI⁺07] to resonantly enhance the electrooptic coupling. Using cavities to enhance the effective nonlinearity increased the electrooptic modulation efficiency but at the cost of giving up modulation bandwidth since high quality cavities needed would have smaller bandwidths.

Around 2010, Mankei Tsang proposed a quantum electrooptic device which would be triply resonant - optical pump and optical and microwave signals are all resonant modes[Tsa10, Tsa11]. With the right parameters, such a device would be able to do direct quantum transduction between microwave and optical photons. Two main approaches sprouted from following the proposed endeavour. On-chip approaches based on a 2D microwave cavity coupled to a thin film optical WGM cavity [JPB⁺16, SZR⁺17, FZC⁺18, WMA⁺20, HSZ⁺20, MWP⁺20, FXL⁺21, XSF⁺21] and another with a 3D microwave cavity which contained the optical WGM resonator (made from a z -cut lithium niobate wafer) inside realized by Rueda *et al.* [RSC⁺16, HRS⁺20, SHR⁺22].

The 2D microwave cavity approach uses a thin film aluminium nitride (AlN) optical WGM resonator. The main advantage of this approach is that the super thin film of AlN allows a stronger overlap between the microwave and optical fields allowing vacuum coupling rates of ~ 300 Hz. The higher vacuum coupling rate allows for higher cooperativities with less optical pump power. Fan *et al.* demonstrated a conversion efficiency of 2% with a transducer working at 2 K [FZC⁺18]. However, there are major drawbacks to using thin-film and 2D cavities with small mode volumes. Since a superconducting microwave cavity is in close proximity to high energy optics, there is a good possibility to break Cooper pairs and produce quasi-particles which would inevitably shift the microwave mode resonance and increase internal loss rates [WMA⁺20, FXL⁺21]. Moreover, for smaller mode volumes, undesirable optical nonlinear effects such as photorefractive effect and thermo-optic effect can also shift the optical resonance making it impossible to pump more than a certain amount of power in the optical cavity [JLL⁺17, JPM⁺19].

In this thesis, we work with a WGM 3D microwave resonator which houses a bulk 5 mm radius and ~ 100 μ m thick WGM optical resonator made out of lithium niobate [HRS⁺20, SHR⁺22]. Our machined cm-sized aluminium microwave cavity does not suffer heavily from quasi-particle poisoning. The reason is that the produced quasi-particles on the surface get diluted in the bulk limiting their density increase which keeps the mode from deforming. Nevertheless, we discuss the small effects from quasi-particles in chapter 8. Similarly, the bulk lithium niobate supports a large optical mode volume which prevents nonlinearities like photorefractive and thermo-optic effect from kicking in even for large amount of pumped optical power. Consequently, we are able to inject ~ 100 mW of optical power without any undesirable effects making our system the first to demonstrate high electrooptic cooperativities ~ 1 .

With high electrooptic cooperativity, we are able to do a lot of challenging experiments such as high efficiency bi-directional microwave-optics quantum transduction, observe direct

1. INTRODUCTION

dynamical backaction between microwave and optics (similar to what people observed in optomechanics [AKM14]) and even entanglement between microwave and optics. These experiments form the crux of this thesis.

Transduction of quantum signals require good transduction efficiency as well as extremely low added noise [ZSST20]. Efficiency is easy to understand, however we need to be careful how we describe the noise performance of the transducer. A good noise merit to capture noise properties of the transducer is to define added noise referred to the input N_{in} ,

$$N_{ij,\text{in}} = N_{i,\text{out}}/\eta_{ij} \quad (1.1)$$

where $i, j \in \{e, o\}$ represent the microwave or optics port, $N_{i,\text{out}}$ is the output noise at one port and η_{ij} is the conversion efficiency in $j \rightarrow i$ direction. An intuitive way to understand N_{in} is to imagine it as the number of thermal noise photons measured at the output of the transducer for every single transduced photon from the same port. This means when $N_{\text{in}} = 1$, there is an equal probability to detect a noise photon and a transduced signal photon. When $N_{\text{in}} < 1$, we call it quantum-enabled transducer regime, where certain heralded quantum communication protocols which utilize heralded nonlinear detection method can be used to transduce quantum information [KRH⁺21].

A quantum-limited transducer, that can deterministically transduce quantum states, needs $N_{\text{in}} < 0.5$ for a conversion efficiency close to 1 [Cav82, ARC⁺15]. In this case, we need to also consider the effect of quantum noise $N_q = 1/2|1 - 1/\eta|$ which includes the loss in efficiency as an extra penalty. The total effective noise referred to the input is then $N_{\text{in,tot}} = N_{\text{in}} + N_q$. Fig. 1.1 shows the overview of the state of the art in quantum transduction by plotting the total added noise $N_{\text{in,tot}}$ as a function of N_{in} and η and marking various reported results as markers of different shapes.

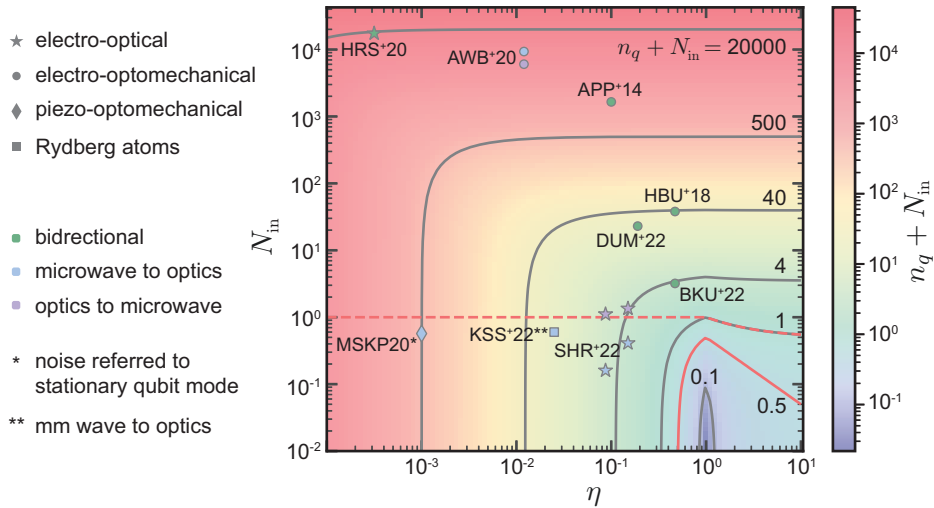


Figure 1.1: **Total added noise as a function of thermal added noise N_{in} and transduction coefficient η .** The red dashed line shows the boundary below which a transducer is quantum-enabled which is suitable for heralded transduction schemes. The red solid line shows the boundary for quantum-limited transduction where deterministic transduction schemes start to work with finite fidelities. Various markers on the plot mark the state of art transducer experiments which have clearly reported their added noise and efficiency values, typically referred to device input/output ports at millikelvin temperatures.

There are a number of results which are in the quantum-enabled regime including the one's presented in this thesis [SHR⁺22]. However, the limit of quantum-limited conversion is still

far from reach. The total conversion efficiencies need to be improved significantly which are currently limited by coupling efficiencies of the transducer cavities to the microwave and optical waveguides. Thus, cavities with much better quality factors need to be engineered such that they can be overcoupled to the waveguides. However, quantum-limited transduction is not the only way towards deterministic quantum transduction.

Quantum dense coding has already showed that a combination of classical communication and quantum entanglement can improve the channel capacity of a communication channel [GLLG19]. We can use a similar technique here to establish qubit state transfer via an optical channel. If entanglement can be shared between two qubits, the quantum channel capacity, assisted by classical communication, is never zero irrespective of the quality of entanglement shared [WCFZ21, AMFR22]. This is in contrast to a quantum channel powered only by transduction used twice - first microwave to optics and then optics to microwave - which can drop to zero under a certain required set of parameters [WCFZ21]. Compared to using transduction, the channel capacity for entanglement is also always higher for the same parameters of a transducer (since it is assisted by classical channel) [RHB19, ZWZ⁺20]. Consequently, using teleportation protocols is more desired than using direct transduction.

However, to produce microwave-optics entanglement, extremely low thermal mode occupancies are needed since a small amount of thermal noise is enough to overpower any quantum correlations and kill any produced entanglement. This is a huge challenge to overcome since microwave mode is at a low frequency (\sim GHz) and tend to easily get hot. Producing entanglement requires a lot of optical pump power which would inevitably heat the nearby microwave cavity and also produce quasi-particles, which will contribute in adding to this thermal noise. We discuss these challenges and ways to overcome them in more details in chapter 9 where we demonstrate production of microwave-optics entanglement using our device.

CHAPTER 2

Cavity electrooptics

2.1 Electromagnetic waves in dielectrics

As the name suggests, an electromagnetic (EM) wave is comprised of oscillating electric and magnetic fields which are usually treated as modes of a harmonic oscillator with a specific frequency in classical electrodynamics. These electric and magnetic fields of an EM wave can interact with the charges and magnetic fields of the materials they are passing through. The materials in turn reacts on application of such external fields. Application of an external electric field would cause formation of positive and negative regions polarizing the material. For an ideal linear medium, the polarization \vec{P} is proportional to the applied external field \vec{E} ,

$$P_i = \epsilon_0 \chi_{ij}^{(1)} E^j \quad (2.1)$$

where ϵ_0 is the permittivity of vacuum and $\chi_{ij}^{(1)}$ is the first-order electric susceptibility. $\chi_{ij}^{(1)}$ is a second rank tensor which is due to the fact that the induced polarization need not be parallel to the applied electric field.

For linear media, the polarization can only oscillate with the same frequency as the applied external field. As a result, an EM wave interacting with a linear material can at most only pick up a phase change as it is passing through the material. However, the first order proportionality breaks down for most materials when high amplitude electric fields are applied. This is because with high amplitude electric fields, the motion of charges in the materials cannot be described as a simple harmonic oscillator anymore.

With high amplitude electric field, the polarization response is nonlinear and is expressed in a power series as,

$$P_i = \epsilon_0 \chi_{ij}^{(1)} E^j + \epsilon_0 \chi_{ijk}^{(2)} E^j E^k + \epsilon_0 \chi_{ijkl}^{(3)} E^j E^k E^l + \dots \quad (2.2)$$

where, $\chi_{ijk}^{(2)}$ is the second order electric susceptibility tensor of rank three and $\chi_{ijkl}^{(3)}$ is the third order electric susceptibility tensor of rank four and so on. In principle the higher order susceptibility tensors are always present but they are exponentially weaker as their order increases. Thus, their effect is visible only with high magnitude electric fields.

Another thing to note is that if the dielectric material is centrosymmetric, then the even-orders of the susceptibility are zero. The reason is that, for a centrosymmetric crystal, if the applied electric field changes sign ($\vec{E} \rightarrow -\vec{E}$), the polarization must also change sign ($\vec{P} \rightarrow -\vec{P}$).

However, for the even terms, the sign change cancels out, leaving the only possibility for them to be zero.

The higher order nonlinearities allow for more exotic phenomena than a simple phase shift to an EM wave. One of the most useful applications of higher order nonlinearity is to mix different frequency EM waves to produce sum and difference frequency generation. This is discussed analytically in section 2.2.

Electro-optic effect This is a nonlinear effect where an external electric field induces a refractive index change in the material [Boy08]. The change in refractive index is described in terms of the impermeability tensor $\eta_{ij} = 1/\epsilon_{ij}$, where ϵ_{ij} is the relative permeability,

$$\Delta\eta_{ij} = r_{ijk}E^k + R_{ijkl}E^kE^l \quad (2.3)$$

where r_{ijk} and R_{ijkl} are the linear (rank three) and the quadratic (rank four) electro-optic tensors respectively. These tensors are responsible for Pockels and Kerr effect respectively. In case of the Pockels effect, the change in refractive index is linearly proportional to the applied electric field E while in the Kerr effect, the refractive index is proportional to the square of the applied electric field. Note that Pockels effect is applicable only for a slowly varying applied electric field (compared to frequency of light). Nevertheless, the frequency of the applied electric field can be on the order of multiple gigahertz.

The Pockels effect corresponds to the second order nonlinearity and is related to the $\chi_{ijk}^{(2)}$ tensor as (see Appendix A of Ref. [RS18]),

$$\chi_{ijk}^{(2)} = -\frac{n^4}{2}r_{ijk} \quad (2.4)$$

where, n is the refractive index. As explained earlier, since Pockels effect is a second-order (even) nonlinearity, it is absent in centrosymmetric crystals.

Moreover, since the permeability tensor ϵ_{ij} is real and symmetric, its inverse η_{ij} must also be real and symmetric. This means that the linear electrooptic tensor r_{ijk} must also be symmetric in the first two indices. Historically, people have studied electro-optic materials way before nonlinear optics came along. As a result, the electro-optic tensor formalism was established with the first two indices contracted as $r_{ijk} \rightarrow r_{hk}$ with,

$$h = \begin{cases} 1 & \text{for } ij = 11, \\ 2 & \text{for } ij = 22, \\ 3 & \text{for } ij = 33, \\ 4 & \text{for } ij = 23 \text{ or } 32, \\ 5 & \text{for } ij = 13 \text{ or } 31, \\ 6 & \text{for } ij = 12 \text{ or } 21 \end{cases} \quad (2.5)$$

In this thesis, we work only with lithium niobate crystals - a triclinic 3m structure with the linear electro-optic tensor [Mat78]

$$r_{hk} = \begin{bmatrix} 0 & -r_{22} & r_{13} \\ 0 & r_{22} & r_{13} \\ 0 & 0 & r_{33} \\ 0 & r_{51} & 0 \\ r_{51} & 0 & 0 \\ -r_{22} & 0 & 0 \end{bmatrix}, \quad (2.6)$$

with $r_{13} = 8.6$, $r_{22} = 3.4$, $r_{33} = 30.8$ and $r_{51} = 28 \text{ pm/V}^1$.

2.2 Wave mixing of electromagnetic fields in nonlinear media

In this section, we work with the simplest case of a monochromatic EM wave given by,

$$\mathbf{E}(\mathbf{r}, t) = [E_1(t)u(r)e^{-i\omega t} + E_1^*(t)u^*(r)e^{i\omega t}] \mathbf{e} \quad (2.7)$$

where, $E_1(t)$ is the slowly-varying electric field amplitude, $u(r) = e^{i\mathbf{k}\cdot\mathbf{r}}$ with \mathbf{k} being the wave vector of magnitude $|k| = \omega/c'$ and $c' = (\mu\epsilon)^{-1/2}$ is the wave velocity in the medium, and \mathbf{e} is a unit vector in the direction of the electric field.

Here, we consider the easiest case of three-wave mixing through a second-order non-linearity. The second order polarization changes in the presence of external electric fields as

$$P^{(2)} = \epsilon_0 \chi_{ijk}^{(2)} E^j E^k. \quad (2.8)$$

Consider two monochromatic fields E_1 and E_2 oscillating with frequencies ω_1 and ω_2 ($\omega_1 \gg \omega_2$) respectively. Substituting this in the above equation, we see that the second order polarization can oscillate with new frequencies,

$$\begin{aligned} P^{(2)} = & \epsilon_0 \chi_{ijk}^{(2)} E_1^j E_2^k e^{-i(\omega_1+\omega_2)t} + \epsilon_0 \chi_{ijk}^{(2)} E_1^{j*} E_2^{k*} e^{i(\omega_1+\omega_2)t} \\ & + \epsilon_0 \chi_{ijk}^{(2)} E_1^{j*} E_2^k e^{i(\omega_1-\omega_2)t} + \epsilon_0 \chi_{ijk}^{(2)} E_1^j E_2^{k*} e^{-i(\omega_1-\omega_2)t}. \end{aligned} \quad (2.9)$$

The first two terms in the above expansion describe the sum frequency generation (SFG) and the last two terms difference frequency generation (DFG). The newly scattered frequency EM wave due to the polarization term $P^{(2)}$ oscillates with frequency ω_3 , which is $\omega_3 = \omega_1 + \omega_2$ or $\omega_3 = \omega_1 - \omega_2$ for SFG and DFG respectively. In principle, both these processes can occur in the same system, however, for that, the participating EM waves need to satisfy some additional constraints known as phase matching. These will be discussed later in section 2.4.

The energy stored in the polarization is calculated as

$$\begin{aligned} dU^{(2)} &= \int dt \langle \mathbf{E}_3 \cdot \dot{\mathbf{P}} \rangle \\ &= 2\epsilon_0 \chi_{ijk}^{(2)} [E_3^i E_2^{j*} E_1^{k*} + E_3^i E_2^{j*} E_1^k] + \text{c.c.} \end{aligned} \quad (2.10)$$

Here, the terms, which do not satisfy either of SFG or DFG relation, have an oscillating term in time domain and therefore, have a vanishing integral. The factor 2 in the Eqn. 2.10 is characteristic to second-order non-linearity and comes from the permutation relations of $\chi^{(2)}$ [RS18, ABDP62].

The stored energy in a volume V is, then, described as

$$\int \langle dU^{(2)} \rangle = 2 \int dV \epsilon_0 \chi_{ijk}^{(2)} [E_3^i E_2^{j*} E_1^{k*} + E_3^i E_2^{j*} E_1^k] + \text{c.c.} \quad (2.11)$$

The right hand side of the above equation is basically the spatial mode overlap of the involved electric fields. The exact form of E or the distribution of electric fields governs the field overlap and gives us the so-called 'phase matching' conditions. When these phase matching conditions are met, the spatial overlap is the maximum and the $\chi^{(2)}$ non-linearity is observed (via generation of new frequencies) to its full extent.

¹Values for a congruent lithium niobate crystals.

2.3 Quantum treatment of electric field interaction in non-linear media

Although there are many classical applications of non-linear effects, this work focuses on quantum applications. Hence, the quantum treatment of the interaction between the electric fields in dielectric media is needed. For this purpose, we define the electric field operator [MW95]

$$\hat{\mathbf{E}}_j(\mathbf{r}, t) = i\sqrt{\frac{\hbar\omega}{2\epsilon V_{\text{eff}}}}(\psi_j(\mathbf{r})\hat{a}_j e^{-i\omega_j t} - \psi_j^\dagger(\mathbf{r})\hat{a}_j^\dagger e^{i\omega_j t}), \quad (2.12)$$

where, ψ_j is the spatial mode distribution over the effective volume V_{eff} and \hat{a}_j and \hat{a}_j^\dagger are the annihilation and creation operators respectively.

The interaction Hamiltonian \hat{H}_{int} is obtained from Eqn. 2.11 after substituting the electric field operator from above

$$\hat{H}_{\text{int}} = 2\epsilon_0\chi^{(2)}\sqrt{\frac{\hbar^3\omega_1\omega_2\omega_3}{8\epsilon_1\epsilon_2\epsilon_3V_1V_2V_3}}\int dV(\psi_3\psi_2^\dagger\psi_1^\dagger\hat{a}_3\hat{a}_2^\dagger\hat{a}_1 + \psi_3\psi_2^\dagger\psi_1\hat{a}_3\hat{a}_2^\dagger\hat{a}_1) + c.c. \quad (2.13)$$

The two terms in the interaction Hamiltonian represent the two possible processes - the first term represents the difference frequency generation $\omega_1 = \omega_2 - \omega_3$ and the second term represents generation of sum frequency $\omega_2 = \omega_1 + \omega_3$.

The interaction Hamiltonian can be reorganized as $\hat{H}_{\text{int}} = \hbar g_0(\hat{a}_3\hat{a}_2^\dagger\hat{a}_1^\dagger + \hat{a}_3\hat{a}_2^\dagger\hat{a}_1) + c.c.$, where the integral over the volume has been absorbed into a coupling constant g_0 ,

$$g_0 = 2\epsilon_0\chi^{(2)}\sqrt{\frac{\hbar\omega_1\omega_2\omega_3}{8\epsilon_1\epsilon_2\epsilon_3V_1V_2V_3}}\int dV(\psi_3\psi_2^\dagger\psi_1^\dagger). \quad (2.14)$$

This coupling constant g depends only on the geometry, which in turn defines the electric field distribution, for a given material or the value of $\chi^{(2)}$. This means a better coupling constant can be engineered by engineering a bigger overlap between the electric fields and reducing their effective volume. This is achieved via cavities, which support the said fields and ensure maximal overlap between them. The coupling constant g_0 is usually referred to as the vacuum coupling rate. It describes the rate of nonlinear electrooptic coupling for a single photon.

2.4 Cavity quantum electro-optics

In this work, we use the electrooptic nonlinearity where an optical field is modulated by an external applied electric field. Consequently, the effective refractive index of dielectric (affecting the optical EM fields) can be modulated by up to several gigahertz. This modulation produces two optical sidebands through difference and sum frequency generation. Classically, a simple electro-optic modulator can be made by putting a electro-optic material, such as Lithium Niobate, between a parallel plate capacitor connected to a voltage oscillating with, for example, microwave frequency. Such devices have found application in various domains such as high-speed communication via optics, laser printing and digital data recording. However, these devices are not fit for quantum applications such as quantum transduction between microwave and optical photons, essentially due to the low efficiency of modulation, which stems from ineffective coupling between the electric and optical fields. In other words, the coupling constant g from Eqn. 2.14 is really small resulting in $V_\pi \sim 6\text{ V}$. Compared to the single

photon voltages in a typical superconducting qubit which is $\sim \mu\text{V}$, there is multiple orders of magnitude difference making commercially available electrooptic modulators unsuitable for efficiently converting single photons from qubits.

The high coupling constant required for quantum applications can be obtained by maximizing the electric field overlap and reducing the effective mode volume (see Eqn. 2.14). Both of these conditions can be met by smartly designing cavities for both microwave and optical fields which simultaneously maximize the overlap between the fields and prolong the time which the fields spend interacting. This idea of cavity quantum electro-optics was first theorized by Mankei Tsang in 2010 [Tsa10] (although a similar system for classical applications was already demonstrated by Ilchenko *et al.* [ISMM03]). Mankei suggests simultaneously placing an electro-optic dielectric in an optical cavity as well as in the capacitor of a microwave resonator as shown in Fig. 2.1.

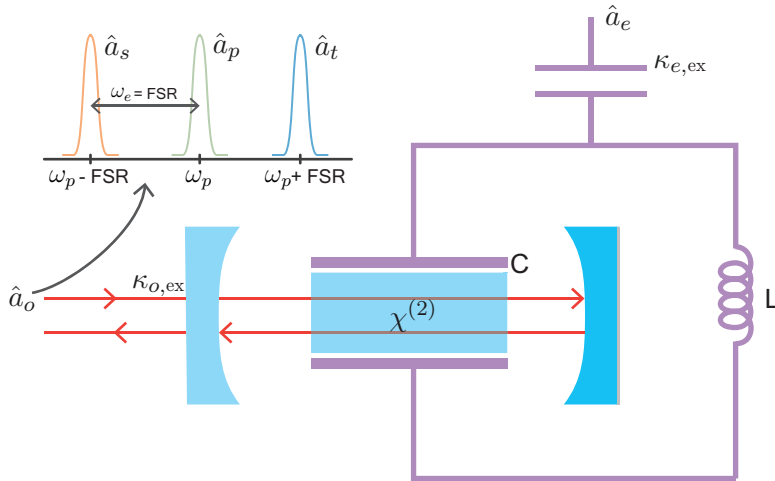


Figure 2.1: **A generic cavity electro-optic setup.** \hat{a}_p , \hat{a}_s and \hat{a}_t are the annihilation operators corresponding to the optical pump and the Stokes and anti-Stokes sideband respectively. \hat{a}_o and \hat{a}_e represent the optical and microwave mode respectively. $\kappa_{i,\text{ex}}$ represent the extrinsic coupling rate of optical and microwave cavities.

In the shown setup, the optical cavity (with one partially reflecting mirror) supports optical modes with different frequencies separated by the free spectral range (FSR). If we carefully choose the capacitance C and inductance L of the microwave resonator, we can match the optical FSR with the resonance frequency of the microwave resonator. In this case, this ensures energy conservation when photons are converted between optical sideband modes and the microwave mode. Thus, for this case, matching the microwave mode frequency with the optical FSR is enough to satisfy the phase-matching condition allowing the microwave and optical fields to interact with each other.

The Hamiltonian of the full system is, then, described as,

$$\hat{H} = \hat{H}_0 + \hat{H}_{\text{int}}, \text{ with} \quad (2.15)$$

$$\hat{H}_0 = \hbar w_p \hat{a}_p^\dagger \hat{a}_p + \hbar w_s \hat{a}_s^\dagger \hat{a}_s + \hbar w_t \hat{a}_t^\dagger \hat{a}_t + \hbar w_e \hat{a}_e^\dagger \hat{a}_e, \quad (2.16)$$

$$\hat{H}_{\text{int}} = \hbar g_0 (\hat{a}_p \hat{a}_s^\dagger \hat{a}_e^\dagger + \hat{a}_p \hat{a}_t^\dagger \hat{a}_e) + c.c. \quad (2.17)$$

where the full Hamiltonian is divided into a constant \hat{H}_0 and the part with the mode interaction

\hat{H}_{int} , \hat{a}_p , \hat{a}_s and \hat{a}_t describe the center optical pump mode², the lower sideband Stokes mode and the upper sideband anti-Stokes mode annihilation operators respectively. \hat{a}_e describes the low frequency electrical part, the microwave mode annihilation operator. They oscillate with their respective frequencies but since we impose the phase-matching conditions, $\omega_s = \omega_p - \omega_e$ and $\omega_t = \omega_p + \omega_e$. Also, note that in our system $\omega_p, \omega_t, \omega_s \sim 193 \text{ THz}$ and $\omega_e \sim 9 \text{ GHz}$.

The interaction Hamiltonian in Eqn. 2.17 has two terms. The first term $\hat{a}_p \hat{a}_s^\dagger \hat{a}_e^\dagger$ represents the downconversion of the the optical pump mode \hat{a}_p to the optical Stokes mode and the microwave mode. The second term $\hat{a}_p \hat{a}_t^\dagger \hat{a}_e$ is a sum frequency generation term where the optical pump and the microwave mode combine to produce the optical anti-Stokes mode. The conjugate $\hat{a}_p^\dagger \hat{a}_t \hat{a}_e^\dagger$ of the second term captures the downconversion of anti-Stokes optical mode to produce the optical pump mode along with the microwave mode. The modes interact via the vacuum coupling constant g_0 which has already been described in Eqn. 2.14.

The vacuum coupling rate g_0 is enhanced by the optical pump mode. If we drive the \hat{a}_p mode with a coherent tone, assuming a non-depleting pump, the interaction Hamiltonian in the Eqn. 2.17 is approximated as [HRS⁺20]

$$\hat{H}_{\text{int}} = \underbrace{\hbar g_0 \sqrt{n_p} (\hat{a}_s^\dagger \hat{a}_e^\dagger + \hat{a}_s \hat{a}_e)}_{\text{downconversion}} + \underbrace{\hbar g_0 \sqrt{n_p} (\hat{a}_t^\dagger \hat{a}_e + \hat{a}_t \hat{a}_e^\dagger)}_{\text{beam-splitter}}, \quad (2.18)$$

where, the optical pump mode has been approximated to be non-depleting coherent mode with field amplitude $\alpha_p = \sqrt{n_p}$. n_p is the number of the optical pump photons in the optical resonator. As a result, the coupling between the signal modes (the optical sidebands and the microwave modes) is effectively enhanced by the presence of the optical pump photons. This results in parametrically enhanced coupling constant $g = g_0 \sqrt{n_p}$. Intuitively, in presence of more pump photons, a signal photon has higher probability of finding a pump photon and interacting with it resulting in better coupling rates.

The first part of the Hamiltonian in Eqn. 2.18, effectively the two-mode squeezing term, can be used to amplify a microwave or optical (at the Stokes mode frequency) signal via the process of stimulated down-conversion or it can be used to produce a two-mode squeezed state between microwave and optical frequency via spontaneous downconversion. The second part is a beam-splitter like interaction between the optical anti-Stokes mode \hat{a}_t and the microwave mode \hat{a}_e . Similar to a beam-splitter where a photon number different ports beam-splitter is conserved, in this beam-splitter like interaction a photon from one mode is destroyed when a photon in other mode is produced to conserve the photon number. As a result, this term can be used to transduce photons from one mode to another (microwave-optics conversion) fundamentally without adding any additional noise.

In an optical system with symmetric FSR around the \hat{a}_p mode, the microwave mode will interact with both the optical Stokes and the anti-Stokes mode simultaneously. However, for most applications, we want to suppress one effect while working with the other one because they impair each-other's effect. For example, while trying to generate two-mode squeezing between microwave and optics, the beam-splitter interaction would up-convert the downconverted microwave signal to the optical anti-Stokes mode increasing the loss on the microwave side. Similarly, when trying to transduce signals between microwave and optics, the two-mode squeezing term would amplify the vacuum noise and add it to the converted signals reducing the fidelity of the transduction.

²It is called pump mode because later we will treat the center mode as a classical coherent mode with infinite photons.

A simple way of suppressing one process of the two interaction processes is to detune the coherent optical pump from the optical pump mode \hat{a}_p as shown in Fig. 2.2. The microwave mode is, then, matched to the frequency difference between the required optical sideband (given by the needed interaction process) and the detuned optical pump. This ensures resonant scattering in case of the required interaction process and off-resonant scattering in case of the other process. This suppresses the participation of the unnecessary optical mode. However, the price is payed by higher pump power requirements to achieve the same intra-cavity photon numbers due to off-resonant pumping.

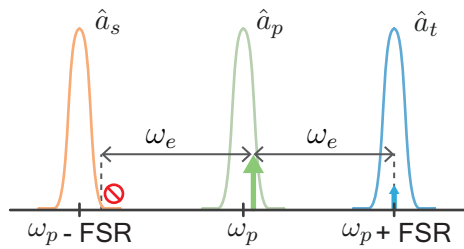


Figure 2.2: Optical Stokes sideband suppression via off-resonant optical pumping.

2.4.1 Steady state solutions for an open system

The beam-splitter interaction By suppressing one of the optical sidebands and, thus, one of the two processes in the Hamiltonian - beam splitter interaction or amplification, we can consider an effective Hamiltonian between only two signal modes - one optical sideband mode and the microwave mode. Let us consider the case when only the optical Stokes sideband is suppressed by pumping the optical pump off-resonance as shown in Fig. 2.2. The effective interaction Hamiltonian, then, is simply,

$$\hat{H}_{\text{int}} = \hbar g_0 \sqrt{n_p} (\hat{a}_t^\dagger \hat{a}_e + \hat{a}_t \hat{a}_e^\dagger) \quad (2.19)$$

This Hamiltonian effectively represents a beam-splitter interaction between modes \hat{a}_t and \hat{a}_e . Using Heisenberg's equation of motion, we can write the time dependence of these modes as

$$\dot{\hat{a}}_t = -i\omega_t \hat{a}_t - ig_0 \sqrt{n_p} \hat{a}_e, \quad (2.20a)$$

$$\dot{\hat{a}}_e = -i\omega_e \hat{a}_e - ig_0 \sqrt{n_p} \hat{a}_t. \quad (2.20b)$$

These equations describe the energy oscillation between the two coupled modes.

For an open system, the Hamiltonian needs to be modified slightly to accommodate coupling between the modes and their environment, *i.e.* a microwave coaxial cable and an optical fiber. The total coupling rate κ_i ($i \in \{o, e\}$) is the sum of two parts - the internal loss rate $\kappa_{i,\text{in}}$ and the external loss rate $\kappa_{i,\text{ex}}$. The internal loss rate $\kappa_{i,\text{in}}$ accounts for the losses to the environment through various loss channels such as material absorption. $\kappa_{i,\text{ex}}$, on the other hand, signifies the coupling rate to an external waveguide through which photons can be coupled into and out of the mode (see Chapter 5 in Ref. [MS99]).

Substituting $\hat{x}(t) = \hat{X}(t)e^{i\omega t}$ ($\hat{x} \in \{\hat{a}_t, \hat{a}_e\}$ and $\hat{X} \in \{\hat{A}_t, \hat{A}_e\}$), where \hat{X} is the slowly varying part, we can go into the rotating frame of each respective mode. The full set of quantum

Langevin equations [SZ97, GZ00] can, then, be written as,

$$\dot{\hat{A}}_t = -\frac{\kappa_o}{2}\hat{A}_t - i\Delta_t\hat{A}_t - ig_0\sqrt{n_p}\hat{A}_e + \sqrt{\kappa_{o,\text{ex}}}\delta\hat{a}_{t,\text{ex}} + \sqrt{\kappa_{o,\text{in}}}\delta\hat{a}_{t,\text{in}} \quad (2.21\text{a})$$

$$\dot{\hat{A}}_e = -\frac{\kappa_e}{2}\hat{A}_e - i\Delta_e\hat{A}_e - ig_0\sqrt{n_p}\hat{A}_t + \sqrt{\kappa_{e,\text{ex}}}\delta\hat{a}_{e,\text{ex}} + \sqrt{\kappa_{e,\text{in}}}\delta\hat{a}_{e,\text{in}} \quad (2.21\text{b})$$

where, $\Delta_i = \omega - \omega_i$ are the detuning around the respective mode resonances and $\delta\hat{a}_{i,\text{in}}$ and $\delta\hat{a}_{i,\text{ex}}$ are Langevin noise operators. These noise operators satisfy the following equations,

$$\langle\delta\hat{a}_{j,k}(t)\delta\hat{a}_{j,k}(t')^\dagger\rangle = (\bar{n}_k + 1)\delta(t - t'), \quad (2.22\text{a})$$

$$\langle\delta\hat{a}_{j,k}(t)^\dagger\delta\hat{a}_{j,k}(t')\rangle = \bar{n}_k\delta(t - t'), \quad (2.22\text{b})$$

where $k \in (\text{in}, \text{ex})$ and n_{in} and n_{ex} are the bath and waveguide noise occupancy respectively.

These equation can be solved in time domain as well as in frequency domain assuming a steady state solution. Here, we will discuss the steady state frequency domain solutions. Numerical time domain solutions will be discussed later in chapter 7.

Before proceeding to solve for the steady state solution, it helps to write these set of equations in a vector form,

$$\dot{\mathbf{v}}(t) = \mathbf{M}\mathbf{v}(t) + \mathbf{K}\mathbf{A}(t), \quad (2.23)$$

where $\mathbf{v}(t)$ is $[\hat{A}_t, \hat{A}_t^\dagger, \hat{A}_e, \hat{A}_e^\dagger]$,

$$\mathbf{M} = \begin{bmatrix} -i\Delta_o - \frac{\kappa_o}{2} & 0 & -ig & 0 \\ 0 & i\Delta_o - \frac{\kappa_o}{2} & 0 & ig^* \\ -ig^* & 0 & -i\Delta_e - \frac{\kappa_e}{2} & 0 \\ 0 & ig & 0 & i\Delta_e - \frac{\kappa_e}{2} \end{bmatrix}, \quad (2.24)$$

$$\mathbf{K} = \begin{bmatrix} \sqrt{\kappa_{o,\text{in}}} & 0 & \sqrt{\kappa_{o,\text{ex}}} & 0 & 0 & 0 & 0 \\ 0 & \sqrt{\kappa_{o,\text{in}}} & 0 & \sqrt{\kappa_{o,\text{ex}}} & 0 & 0 & 0 \\ 0 & 0 & 0 & 0 & \sqrt{\kappa_{e,\text{in}}} & 0 & \sqrt{\kappa_{e,\text{ex}}} \\ 0 & 0 & 0 & 0 & 0 & \sqrt{\kappa_{e,\text{in}}} & 0 \end{bmatrix}, \quad (2.25)$$

and $\mathbf{A}(t) = [\delta\hat{a}_{t,\text{in}}, \delta\hat{a}_{t,\text{in}}^\dagger, \delta\hat{a}_{t,\text{ex}}, \delta\hat{a}_{t,\text{ex}}^\dagger, \delta\hat{a}_{e,\text{in}}, \delta\hat{a}_{e,\text{in}}^\dagger, \delta\hat{a}_{e,\text{ex}}, \delta\hat{a}_{e,\text{ex}}^\dagger]$.

Equation 2.23 is solved in the Fourier domain, yielding

$$\mathbf{v}(\omega) = \mathbf{S}(\omega)\mathbf{A}'(\omega), \quad (2.26)$$

where $\mathbf{S} = [-\mathbf{M} - i\omega\mathbb{1}]^{-1}$ and $\mathbf{A}'(\omega) = \mathbf{K}\mathbf{A}(\omega)$. The output field can be obtained via the input-output theorem [GC85, Tsa11],

$$\hat{A}_{j,\text{out}}(\omega) = -\hat{A}_{j,\text{in}} + \sqrt{\kappa_{j,\text{ex}}}\hat{A}_j, \quad (2.27)$$

with $j=t,e$.

The set of $\hat{A}_{j,\text{out}}$ form the transfer matrix between the modes. The different elements of the matrix describe the distribution of field amplitudes in different modes with $\hat{A}_{j,\text{in}}$ as the input field amplitude.

By multiplying the two relevant matrix elements (conjugates of each other), we derive the power scattered in optical mode in presence of microwave and vice-versa. This gives us the

total conversion efficiency between the modes - total conversion efficiency stands for waveguide to waveguide efficiency. It is calculated as

$$\eta_{\text{tot}} = \eta_e \eta_o \frac{4C}{(1 + C)^2}, \quad (2.28)$$

where, $\eta_j = \kappa_{j,\text{ex}}/\kappa_j$ is the mode coupling efficiency and $C = 4g^2/(\kappa_o \kappa_e)$ is the cooperativity, which is described next.

Cooperativity It is the figure of merit in our system which can be intuitively understood as the enhanced coupling rate normalized with the geometric mean of the total loss rates in the system. More intuitively, it compares the rate of conversion/coupling between the two signal modes - optical and microwave - with the loss rates in the system.

The total conversion efficiency increases with cooperativity until it reaches its maximum value at $C = 1$. Increasing cooperativity beyond that reduces the total conversion efficiency because in the strong coupling regime of $C > 1$, the coupling rate exceeds the loss rate and, thus, the converted signal from one mode to the other can now convert back to the original mode before it is lost to the environment or coupled out from the waveguide. In other words, when the enhanced coupling rate g exceeds the loss rates in the system, the energy between the modes can oscillate between the two modes.

For the purpose of transduction, we don't want the energy to oscillate and thus want to always work with cooperativity close to 1 but never exceeding it. For $C = 1$, the total conversion efficiency η_{tot} is limited by the product of the coupling efficiencies g to the two modes. This corresponds to the power lost when trying to couple in and out of the cavity. This loss can be managed by increasing the coupling efficiency η_i , *i.e.* by ensuring that the external coupling rate is much higher than the internal losses of the cavity. However, increasing the external coupling rate comes at the cost of increased total loss, which means for the same amount of vacuum coupling rate g_0 , more optical pump power is needed to achieve the same cooperativity. High optical pump powers have a multitude of issues as will be discussed in the next chapters.

The amplification interaction The Hamiltonian for the amplification interaction between the optical Stokes mode \hat{a}_s and the microwave mode \hat{a}_e can be solved in the same way as described above. Effectively only the sign of the interaction between the two coupled modes changes. Since this is an amplification interaction, the interaction of the signal mode (s/e) with the pump mode amplifies both itself and produces a copy in the other signal mode (e/s). This can be interpreted as quasi-conversion and we can again define a total 'conversion' efficiency between the modes which is only slightly different

$$\eta_{\text{tot}} = \eta_e \eta_o \frac{4C}{(1 - C)^2} \quad (2.29)$$

The 'conversion' efficiency now approaches infinity as cooperativity approaches 1. Technically, it is wrong to use the word conversion for this interaction since this is a stimulated downconversion of the optical pump photon due to interaction with a signal photon. Thus, in this case, the photon number in any signal mode is not depleted, both are amplified by the optical pump.

At the limit of $C = 1$, the downconverted signal photons can once again stimulate the optical pump photon to downconvert before they are lost to the environment. This means that coupling signal power from outside is no more necessary and the amplification is self-sustainable. Since,

the rate of generation of downconverted signal photons exceed the loss rates, the amplified signal grows exponentially. This is called the region of parametric instability. In this regime, a seed signal is lased with the help of optical pump in the limit $C \geq 1$. In practice, however, the signal cannot grow exponentially. Lasing depletes the optical pump significantly and the signal is amplified exponentially until the optical pump is depleted below $C < 1$. At this stage, an equilibrium is reached which depends on the input optical pump power among other parameters.

2.5 Conclusion

In this chapter, we have discussed a toy-experiment with cavity electrooptics. We explored the different interactions of microwaves with the Stokes and anti-Stokes optical sideband modes of the optical cavity and discussed briefly the steady state solutions of single sideband resolved interactions - beam-splitter interaction and amplification interaction. In the next chapter, we will discuss the full electrooptic system we used to do experiments in more detail including the involved physics which has a few more elements than the toy model discussed in this chapter.

CHAPTER 3

Cavity electro-optics with whispering gallery modes

3.1 Introduction

In the last chapter, we saw that the use of resonances boosts the electro-optic coupling as photons live longer in the resonator and, thus, interact with the non-linear medium for longer. However, apart from making a higher quality resonator, squeezing the modes to a smaller volume (resulting in higher energy density) and making sure the interacting field modes overlap as much as possible also increases the interaction efficiency. It is the geometry of the resonators which determines the mode energy density and mode overlap and hence, the interaction efficiency.

In this chapter, we describe our device where we do cavity electro-optics using whispering gallery resonators. A whispering gallery mode (WGM) is a mode-confined by concave walls where it propagates while getting continuously reflected. In optics, a WGM resonator can be made using a disk with polished circumference of a high refractive-index material. The light then is confined within the disk due to total internal reflection. In our device, we keep such an optical WGM resonator in a 3D microwave resonator which also supports a microwave WGM. The microwave mode electric field are confined between two concave metallic rings. The optical WGM resonator is placed between these two rings. This not only helps bring down the resonant frequency of the microwave cavity to several GHz (by increasing the capacitance between the rings) but also ensures maximal mode overlap between the optical and microwave fields.

The optical WGM resonator is made out of lithium niobate which is routinely used in the telecommunication industry for phase modulation of optical light due to its high $\chi^{(2)}$ non-linearity. More specifically, we use the highest r_{33} electro-optic coefficient of *z*-cut lithium niobate to couple microwave and optical light most efficiently.

In the following sections, the optical and microwave WGM resonators are discussed in detail including their supported modes, fabrication and coupling to external waveguides. The non-linear vacuum coupling constant is, then, calculated for our system. Finally, suppressing the interaction of the microwave mode with either the optical Stokes or anti-Stokes sideband via the optical mode hybridisation is discussed.

Acknowledgement and contributions Optical resonator fabrication process presented in this chapter was initially developed by William Hease and Alfredo Rueda and further continued by Dante Loi and Paul Falthansl. Various images which showcase the fabrication process are taken by Dante Loi and Paul Falthansl and are acknowledged accordingly.

3.2 Optical whispering gallery mode (WGM) resonators

The optical WGM resonators are essentially an ellipsoidal dielectric with a refractive index higher than the surrounding media such that the light is trapped inside the high refractive index dielectric through total internal reflection [LCC17]. In our case, the resonators are made out of lithium niobate which is a birefringent crystal with two refractive indices - an extraordinary refractive index $n_e = 2.13$ and an ordinary refractive index $n_o = 2.21$ at 1550 nm. As a result, the WGM resonators made of out of lithium niobate support modes with different polarization, transverse electric (TE) and transverse magnetic (TM) with slightly different free spectral ranges (FSRs).

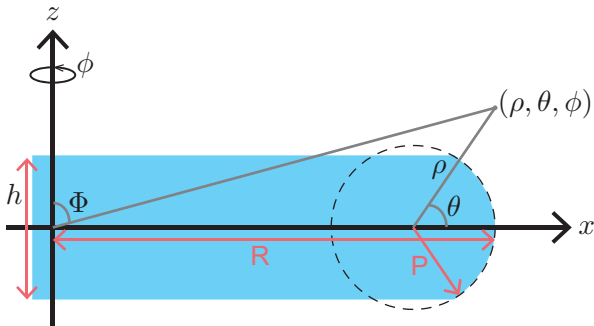


Figure 3.1: Toroidal coordinate system (ρ, θ, ϕ) to solve modes in a WGM resonator with height h , radius R and radius of curvature at the rim P .

3.2.1 Modes in a cylindrical resonator

For a uniaxial cylindrical crystal of radius R , height h and radius of curvature at the rim P , the supported WGMs can be calculated analytically using the Helmholtz equation. The solution of the WGM electric field given in toroidal coordinates (ρ, θ, ϕ) and shown in Fig. 3.1 [BSS⁺13, FSSL16] is

$$\mathbf{E}_{q,p,m}^{\nu}(\mathbf{r}) \approx \begin{cases} E_0 \exp(-\frac{\theta^2}{2\theta_m^2}) H_p(\frac{\theta}{\theta_m}) \mathcal{A} [f_{m,q}^{\nu}(\rho)] e^{im\phi} & \text{if } \rho < P \\ A_{\nu} \exp(-\frac{\theta^2}{2\theta_m^2}) H_p(\frac{\theta}{\theta_m}) \exp(-\kappa_{\nu}(\rho - P)) e^{im\phi} & \text{if } \rho > P, \end{cases} \quad (3.1)$$

where, ν represents the two orthogonal polarizations - TE (parallel to symmetry axis) and TM (perpendicular to symmetry axis), $\kappa_{\nu} = k_0 \sqrt{n_{\nu}^2 - 1}$, $q = \{1, 2, \dots\}$ is the radial mode number representing the number of maxima in electric field intensity along the radial direction ρ , $p = \{0, 1, 2, \dots\}$ is the polar mode number and $m = \{0, 1, 2, \dots\}$ is the azimuthal mode number representing the number of maxima in the electric field intensity along the azimuthal direction ϕ . H_p and \mathcal{A} are the Hermite polynomials of degree p and Airy functions respectively. E_0 is a normalization constant. A_{ν} describes the evanescent field amplitude which is different

for two polarizations,

$$A_\nu = \begin{cases} E_0 \mathcal{A} [f_{m,q}^{\text{TE}}(P)] & \text{if TE} \\ E_0 (2n_o^4 - n_o^2)^{-1/2} \mathcal{A} [f_{m,q}^{\text{TM}}(P)] & \text{if TM.} \end{cases} \quad (3.2)$$

The abbreviations used in previous two equations are exanded as,

$$f_{m,q}^\nu(\rho) = (P + \Delta_\nu - \rho)/u_m - \alpha_q, \quad (3.3)$$

$$\theta_m = (\tilde{R}_\nu/P)^{3/4} \frac{1}{\sqrt{m}}, \quad (3.4)$$

$$u_m = 2^{-1/3} m^{-2/3} \tilde{R}_\nu, \quad (3.5)$$

$$\Delta_\nu = \begin{cases} \frac{1}{k\sqrt{n_e^2-1}} & \text{if TE} \\ \frac{1}{n_o^2 k \sqrt{n_o^2-1}} & \text{if TM,} \end{cases} \quad (3.6)$$

where, the effective radius $\tilde{R} = R + \Delta_\nu$ and α_q is the q -th root of the Airy function.

The mode amplitudes can also be solved using finite element method (FEM) simulations in COMSOL. Fig. 3.2 shows a 2D axisymmetric simulation for an ellipsoidal WGM resonator (geometry shown in Fig. 3.1) with $h = 100 \mu\text{m}$, $R = 2.4 \text{ mm}$ and $P = 250 \mu\text{m}$. The fundamental mode with $(\rho, \theta, \phi) = (1, 0, 20755)$ and a higher order mode with $(\rho, \theta, \phi) = (2, 2, 20755)$ are shown. The difference in mode distribution between the theory and the numerical simulation typically has a deviation of less than 3% (see Chapter 3 in Ref. [RS18] and also Ref. [BSS⁺13]).

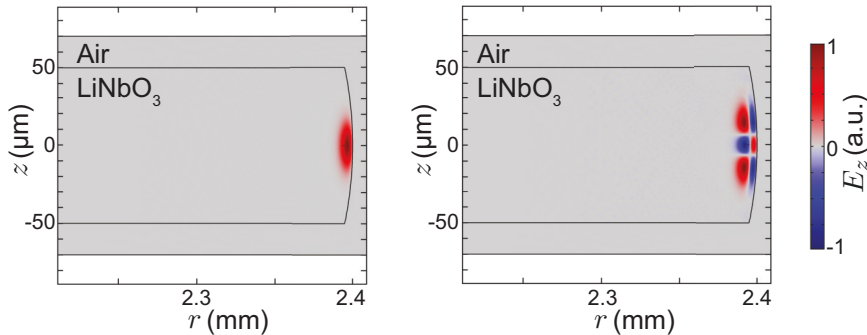


Figure 3.2: **Optical mode numerical simulations.** a[b] shows the simulation of the eigen mode with $(\rho, \theta, \phi) = (1, 0, 20755)$ [$(\rho, \theta, \phi) = (2, 2, 20755)$] for an optical resonator disk of height $100 \mu\text{m}$, radius 2.4 mm and radius of curvature $250 \mu\text{m}$.

3.2.2 Losses in optical WGM resonator

In theory, the quality factor of these modes is limited only by radiation and material losses. Radiation loss occurs due to finite total internal reflection from curved surfaces. There is an analytical expression for the quality factor limited by radiation loss for light trapped in a sphere [Ora02],

$$Q_{\text{radiation}} \approx \frac{2\pi R}{\lambda_0 \sqrt{n^2 - 1}} \eta \exp \left(\frac{4\pi R}{\lambda_0} \cosh^{-1}(n) - \sqrt{n - 1/n} \right) \quad (3.7)$$

where, η is 1 (n^{-2}) for TE (TM) modes where n is the refractive index of the material. A sphere is a good approximation for the whispering gallery modes trapped inside a resonator shown in Fig. 3.2.

Similarly, the material loss due to absorption (due to impurities in the crystal) in the bulk material also limits the internal quality factor. It is usually described as a spatial exponent decay of the intensity in the bulk, α_{material} , the loss coefficient. Under the assumption of small α_{material} , the quality factor limit due to material losses can be defined as,

$$Q_{\text{material}} \approx \frac{2\pi n}{\lambda_0 \alpha_{\text{material}}} \quad (3.8)$$

In the limit of large radius R , however, the main source of loss is practically the scattering due to an imperfect surface. Since the losses are added, the total quality factor is related to the individual loss channels as,

$$Q_{\text{tot}}^{-1} = Q_{\text{radiation}}^{-1} + Q_{\text{material}}^{-1} + Q_{\text{surface}}^{-1} \quad (3.9)$$

Usually, $Q_{\text{surface}}^{-1} \gg Q_{\text{radiation}}^{-1}, Q_{\text{material}}^{-1}$. As a result, the final quality factor of the device comes down to the fabrication process and how good the concave surface of the WGM resonator is polished. The fabrication process is discussed in detail in the next section.

3.2.3 Material choice for optical WGM resonator

This work remains focused mostly on lithium niobate due to its high electro-optic coefficient. There are 3 main types of lithium niobate (LN) crystals that we have experimented with - congruent LN without magnesium doping and stoichiometric LN with and without magnesium doping. The difference between the two kinds of LN crystals is in the way these crystals are grown [KMC⁹⁶]. Crystals grown from by simply melting a congruent mixture of 1 : 1 lithium to niobium results in crystals with lithium to niobium ratio of 0.945. This lower amount of lithium allows for more number of defects in the crystal such as lithium vacancies. Stoichiometric crystals have a higher ratio of lithium to niobium of 0.979 which means smaller amount of probable defects. On a side note, small amount of magnesium doping in lithium niobate crystals has shown higher resistance of crystals to large optical powers [MBPT20].

In our experiments, WGM resonators made from the stoichiometric LN without the magnesium doping has resulted in the highest observed quality factors (up to 8×10^8). Quality factors of crystals made with congruent LN without Mg doping and stoichiometric LN with Mg doping have always resulted in slightly lower quality factors (up to 2×10^8). However, the maximum achievable quality factor is not the only consideration when it comes to choosing the material. Different types of LN crystals also have different physical properties, some of which can make the crystal better in fabrication purposes. Notably, we have found that working with stoichiometric non-doped LN crystals is observed to be more difficult due to their more brittle nature possibly due to a more perfect crystalline structure.

Additionally, there are other material options apart from LiNbO_3 such as barium titanate (BaTiO_3) and lithium tantalate (LiTaO_3), which also feature high electro-optic non-linearities. Lithium tantalate (LiTaO_3) has a specific advantage: it features only a negligible amount of birefringence compared to lithium niobate ($n_o = 2.1138$ and $n_e = 2.1162$) [MHS¹¹]. A smaller birefringence can be advantageous to get higher quality factor optical modes (especially TE modes). We believe that the birefringence in lithium niobate limits the quality factors of

supported TE modes because slightly different refractive indices in two directions result in a different round trip times for the two components of TE mode making it less resonant in the resonator after a few round trips. Another advantage of using lithium tantalate (LT) optical resonators was that the microwave resonators with LT optical resonators had a higher quality factor - possibly due to lower piezoelectric losses (discussed in section 3.3.4). However, the fact that LT has a smaller refractive index of 2.11 than LN means that a WGM resonator of the same radius will have a larger free spectral range (FSR). This would change the complete design and fabrication process of the full transducer - a microwave cavity which can account for a higher FSR with the new optical resonator made with lithium tantalate has to be designed. A lower dielectric material (lithium tantalate compared to lithium niobate) reduces the supported microwave frequency by ~ 2 GHz for the same cavity geometry. Increasing the microwave resonance frequency by changing the resonator geometry back to the supported optical FSR has proven to be rather challenging. As a result, we have not yet pursued fully-assembled devices featuring lithium tantalate yet.

Other materials such as barium titanate have also not been looked into due to time constraints even though they may turn out to be viable alternatives.

3.2.4 Fabrication of optical WGM resonator

In practice, to achieve the highest possible optical quality factor, it is imperative that rim surface of the optical WGM resonator has the least possible surface roughness. As a result, fabrication of optical resonators with a good rim surface is a crucial step in the fabrication of the whole transducer. Over the years, the technique and materials used in the fabrication of these resonators has been perfected by various group members. William Hease and Alfredo Rueda started developing the initial fabrication techniques which were further worked by William, Dante Loi and Paul Falthansl. A summary of these developed techniques is given here.

Cutting disk The optical resonators are made from a $2\text{ cm} \times 2\text{ cm}$ z -cut LN crystal slab which is $500\text{ }\mu\text{m}$ thick. The crystal is glued using wax to a microscope slide to help protect the edges of LN wafer during the drilling process. The glued LN crystal and slide are, then, glued to an aluminum plate with a wax glue to stabilize the crystal while cutting a disk out of it. The aluminum plate is mounted on a precision XY stage. The stage is equipped with a spring which pushes the crystal against a high precision lathe equipped with a hollow stainless steel rod of 5.3 mm inner diameter. The spring equipped stage applies a constant force of 0.05 – 0.1N during the whole disk cutting process. The hollow steel rod is lubricated with WD-40 and a layer of slurry with $9\text{ }\mu\text{m}$ diamond particles is applied between the cutting rod and the LN wafer. The lathe, then, rotates the cutting rod at 80 Hz to drill the LN wafer. The process can take anywhere from 5 mins to 40 mins. To determine whether the drilling is complete, we measure the XY position of the stage with calipers and wait until the drill has travelled the required distance. The cut disk with glued LN wafer and glass slide can be removed by heating the wax glue. The LN wafer is, finally, separated from the glass slide by heating the assembly which melts the glue.

The cut disk has a diameter of $\sim 5.8\text{ mm}$. This gives us enough room to shape and polish the disk to its final desired diameter $\sim 5.0\text{ mm}$.

Auto-centering process After the disk is cut, it is mounted on a custom-made aluminum post with wax glue shown in Fig. 3.4. The stainless steel post is, then, mounted on a lathe for

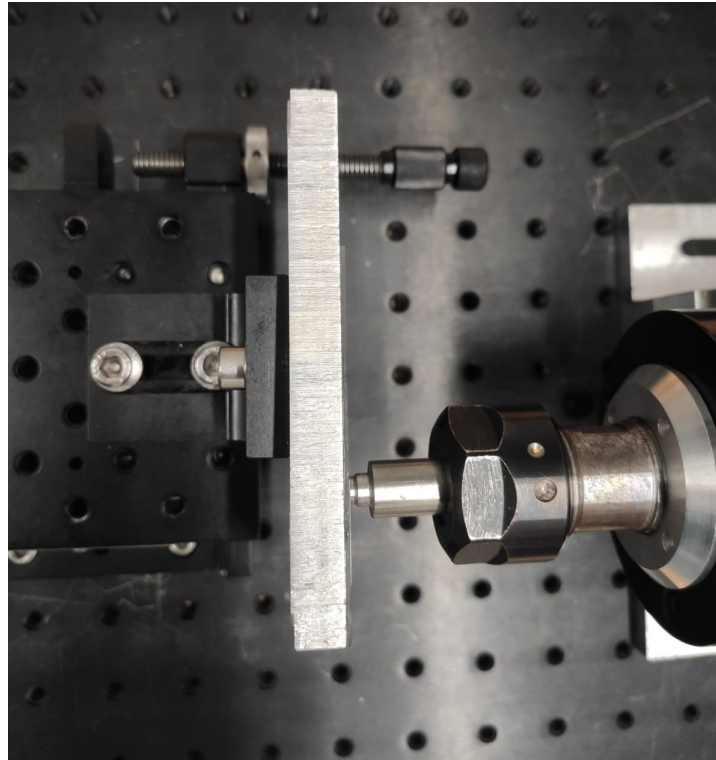


Figure 3.3: Disk cutting process. Picture credits: Dante Loi and Paul Falthansl.

further processing of the disk into a WGM resonator.



Figure 3.4: Lithium niobate cut disk on a custom-made aluminum post. Picture credits: Dante Loi and Paul Falthansl.

In our experience, we have found that polishing to a high degree, which yields higher quality factor resonators, is possible only when the disk does not wobble as it rotates on the lathe. This would naturally happen if the center of the disk is not aligned with the center of rotation of the spindle. Manually aligning the disk on the stainless steel post before mounting the whole thing on a spindle is difficult as it is almost impossible to predict a slightly random axis of rotation of the spindle. Consequently, we have developed a technique for auto-centering the disk on the spindle. For that purpose, when the disk is mounted on the spindle, the wax glue

that holds the disk on the post is left hot and slightly melted. In this state, the disk can still move on the post. The spindle is then rotated at a small RPM and the disk is gently pushed on the rim while the disk wobble is monitored through a microscope. This process is complete when any significant disk wobble cannot be observed through the microscope.

The auto-centering process further continues to make the centering even more perfect. After the glue has cooled and the disk is firmly mounted on the spindle, the disk is rotated at a higher RPM of 100 Hz. A piece of P1000 roughness sandpaper stuck on an aluminum plate which is setup on a XYZ stage is slowly brought in contact with the rotating disk (see Fig. 3.5). This process removes any extra material which would otherwise cause wobble, essentially, shaping the disk to be circular around the rotational axis of the spindle. Note that once the disk is shaped around the rotational axis of the spindle, the post of the disk cannot be removed and re-inserted into the spindle anymore. Doing so would void the guarantee that the disk is still perfectly centered causing the wobble to come back. After this process, the diameter of the sanded down disk reduces to 5.2 mm.



Figure 3.5: The second step of auto-centering process sanding the LN disk around the rotational axis of lathe. Picture credits: Dante Loi and Paul Falthansl.

Shaping The next step in the resonator fabrication is shaping a convex rim from a flat rim from the previous centering process. This shaping is done using a smoother P2000 sand paper. During the shaping process, great care is needed to keep the rim aligned to the center, *i.e.*, keep the rim profile as symmetric as possible. Experimentally, we have found the best radius of curvature for the rim to be between 0.8 mm and 1.0 mm in order to get the highest possible mode quality factors.

Polishing After shaping the resonator, its surface needs to be polished. The polishing is done in several steps. First, the disk is polished using a slurry with increasingly fine diamond grain size - 9 μm , 3 μm and 1 μm , each time for 3 min. Between the steps the disk is cleaned thoroughly. We make sure that there is no residue left from the previous polishing step to prevent contamination. The final step of polishing is done using a chemical-mechanical polishing (CMP) mix. This polishing is done using a 50-50 mix of CMP slurry and WD-40

lubricant. This solution is poured between a quarter arch of a rubber o-ring and the LN disk while the disk rotates at about 6000 RPM. The polishing process is done for 5 minutes at a time and the disk surface is inspected after each round. This last polishing step can be repeated up to 3 times. Thereafter, the quality factor of the disk saturates to around a billion, given a high quality LN wafer was used. An inspection under the microscope reveals the disk surface to be near flawless.

The disk surface after each round of polishing along with the measured optical mode quality factor is shown in Fig. 3.6.

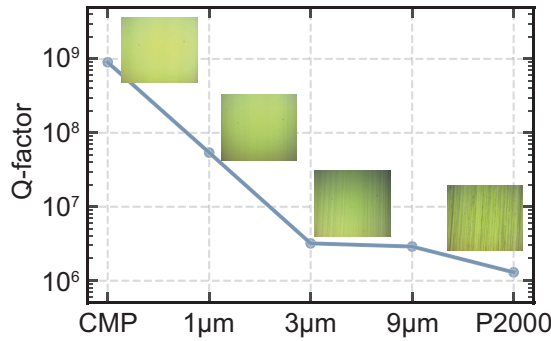


Figure 3.6: Change in intrinsic optical mode quality factor after each polishing step along with the resonator rim's surface as inspected under a microscope. Figure credits: Dante Loi and Paul Falthansl.

Lapping The final step in optical resonator fabrication is reducing the thickness from 500 μm to the desired $\sim 150 \mu\text{m}$ while maintaining a symmetric rim profile. We will see in section 3.3 that a thinner optical resonator allows for a stronger coupling between microwave and optical modes. We polish the top and bottom of the disk with a lapping machine. This lapping stage is done after the shaping and polishing because it is easier to achieve the desired large rim radius and polish the disk without altering this curvature when the disk is still thick. The lapping is done in two stages - using a 9 μm particle size diamond slurry paste to remove material and using the CMP mix for final polishing. The disk is lapped by an equal amount on both sides to keep the center of radius of curvature aligned to the center of the disk. The summary of the lapping process is shown in Fig. 3.7.

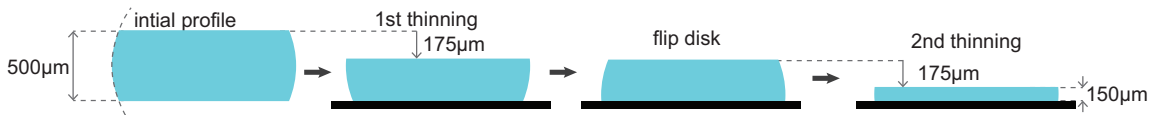


Figure 3.7: Optical WGM resonator lapping process.

To lap the disk, we glue the disk on the metal plate using the wax. In this step, it is very important that enough wax is used such that some of the wax covers the polished rim of the resonator to protect it during the lapping process. One also needs to especially take care of any bubbles that may form in the wax when the disk is mounted. Consequently, the wax is heated well above its melting point to ensure its liquid state. Moreover, multiple attempts of mounting the disk and inspection are needed to ensure that no bubbles are present in the wax around the disk. When the disk is properly mounted, the process of lapping the disk can be continued.

3.2.5 Coupling via frustrated total internal reflection

Coupling of optical power to the WGM resonator is done via a diamond prism. Light is focused via a GRIN (gradient index) lens on one of the flat surfaces on the prism which is facing towards the optical WGM resonator as shown in Fig. 3.8. The angle of the incident light is adjusted such that the angle of incidence of light on the flat surface Φ is greater than the critical angle resulting in total internal reflection from the prism surface. However, beyond the surface of total internal reflection, there exists an evanescent field which can overlap with the evanescent field of the optical resonator if the prism is brought close enough to the WGM resonator.

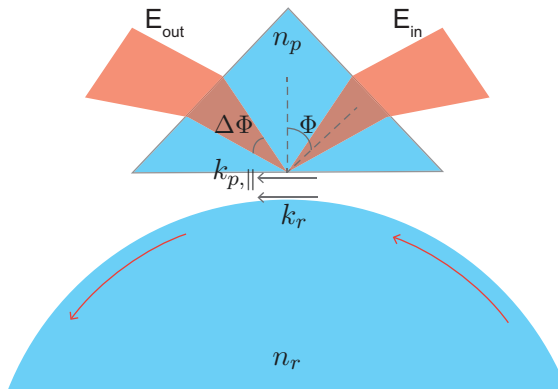


Figure 3.8: Evanescent coupling of light to a WGM resonator via a prism.

Using Snell's law, we can derive the angle required to couple the light into the optical resonator. Since the frequency of light is the same, the wave vector in the optical resonator k_r and the prism k_p follow,

$$\frac{k_r}{n_r} = \frac{k_p}{n_p} \quad (3.10)$$

where, n_p (n_r) is the refractive index of the prism (resonator). The magnitude of k_p in the direction of k_r is $k_{p,\parallel} = k_p \sin(\Phi)$. For efficient coupling, $k_{p,\parallel} = k_r$, hence, the most efficient coupling angle is achieved at $\Phi = \arcsin(n_r/n_p)$. This is only possible when the condition $n_p > n_r$ must be satisfied.

However, a closer inspection of this criteria reveals that the coupling condition is much more relaxed. Since the optical resonator has a curved surface, the wave-vectors of the evanescent fields wrap around it. This means the wave-vectors of the evanescent field parallel to prism surface form a distribution of different magnitudes around the center value k_r . As a result, it is possible to couple power into the optical resonator even with a prism with $n_p < n_r$ for a certain range of incident angles Φ . The range increases when $n_p > n_r$ as there are many more possibilities where some component of wave vectors can overlap.

It is worth noting that for lithium niobate the TE and TM modes correspond to different refractive indices. As a result, there is a separate range of Φ for which coupling is efficient to TE or TM modes. In our case, we also have a range of Φ angles for which coupling is observed to both TE and TM modes simultaneously.

The more relaxed coupling condition has been derived in Ref. [SFV⁺17],

$$(n_r - n_p)k \leq \sqrt{\frac{\kappa}{R}} \quad (3.11)$$

where $k = 2\pi/\lambda$ is the free space wave-vector, $\kappa = k\sqrt{n_r^2 - n_h^2}$ with n_h being the refractive index of medium between the prism and the resonator and R is the major radius from Fig. 3.1.

Estimating the mode mismatch factor Λ Coming with the right incident angle ensures a finite amount of coupling to the optical resonator. However, to achieve efficient coupling, one must also investigate the mode overlap between the incident mode shape and the mode shape accepted by the optical resonator. In practice, we input a Gaussian mode shape to the prism surface using a single mode fiber. However, as seen in the previous subsection, the mode shape of the WGM resonator is never perfectly symmetric. This means it is difficult to get full mode overlap with a Gaussian input beam. The mismatch in the mode shapes is described as the mode overlap between the Gaussian mode and the optical WGM as Λ .

A lot of work has been done to understand and minimize this mode mismatch factor. In Ref. [SFV⁺17], the far-field distribution of the emitted WGM is calculated in terms of the Fourier components. In chapter 3 section 4 of Ref. [RS18], this is expanded in terms of divergence angles in two directions. In Ref. [SFF⁺14], the emitted mode shape is directly measured. They show that modes with $p = 0$ have an ellipsoidal (nearly Gaussian) profile while modes with $p = 2$ have a flat-top profile and modes with $p > 4$ start to get more than one lobe. This means that at least for modes with $p = 0$, the divergence angles in two directions would suffice to describe the far-field distribution of emitted WGMs, since it is just an ellipsoidal shape.

In Ref. [RS18], this ratio is calculated as,

$$\frac{\Delta\Phi}{\Delta\Theta} = \cos(\Phi_c)\sqrt{\frac{R}{P}}\sqrt{1 + \frac{n_r}{\sqrt{n_r^2 - 1}}\left(\frac{P}{R}\right)^{1/2}} \quad (3.12)$$

where $\Delta\Phi$ and $\Delta\Theta$ are the divergence angles in two directions. If this ratio is 1, then the far-field pattern is nearly Gaussian. Approximating to first order, the ratio is 1 when,

$$P = R[1 - (n_r/n_p)^2]. \quad (3.13)$$

In Ref. [SSMY09], they use this design to achieve a 99.96% coupling efficiency.

However, if the parameters of the optical resonator cannot be fine tuned, the coupling efficiency could also be significantly increased by using a suitable elliptical lens along with a spherical lens between the single mode fiber and the prism.

3.2.6 Optical mode characterization in the frequency domain

In our experiments, we used an optical WGM resonator with major radius $R = 2.5$ mm, the rim radius $P \approx 0.7$ mm and a height which was lapped down to $h = 150$ μ m. The optical modes are characterized via the reflection spectrum from the single coupling port (prism). The laser frequency is swept continuously and the reflected power is measured by a photodetector. The reflected optical power around a mode resonance is given as [HRS⁺20],

$$|S_{oo}(\Delta\omega)|^2 = 1 - \frac{4\kappa_{ex,o}\Lambda^2(\kappa_o - \Lambda^2\kappa_{ex,o})}{\kappa_o^2 + 4(\Delta\omega)^2} \quad (3.14)$$

where $\Delta\omega = 0$ defines the mode resonance, κ_o is the total optical linewidth of the optical mode, $\kappa_{ex,o}$ is the coupling loss of the mode and Λ is the factor accounting for the spatial

mode mismatch between the optical WGM and the Gaussian mode from the single mode fiber. The coupling ratio or coupling efficiency η_o is defined as $\eta_o = \kappa_{\text{ex},o}/\kappa_o$, where the total linewidth κ_o is the sum of intrinsic $\kappa_{\text{in},o}$ and extrinsic $\kappa_{\text{ex},o}$ optical linewidths. The mode is critically-coupled when $\eta_o = 0.5$, under-coupled for $\eta_o < 0.5$ and over-coupled for $\eta_o > 0.5$.

The optical mode is characterized completely by three parameters - the total linewidth κ_o , the coupling efficiency η_o and the mode mismatch factor Λ . From just the reflection spectrum, only κ_o can be properly defined. For a given mode contrast, the coupling efficiency η_o has two possible values, even for perfect mode matching $\Lambda = 1$, corresponding to an under-coupled or an over-coupled mode. Since the coupling efficiency only affect the mode contrast, we can simply try to solve for η_o at mode resonance as,

$$1 - (|S_{oo}(0)|^2)_{\Lambda=1} = \frac{4}{\kappa_o} \eta_o (1 - \eta_o) \quad (3.15)$$

The quadratic equation points to two solutions of η_o - one being > 0.5 and the other being < 0.5 .

Putting the mode mismatch factor in the mix,

$$1 - |S_{oo}(0)|^2 = \frac{4}{\kappa_o} \Lambda^2 \eta_o (1 - \Lambda^2 \eta_o), \quad (3.16)$$

we can simply consider $\Lambda^2 \eta$ as the new effective coupling efficiency. In other words, by fitting just the reflection spectrum we can find only two possible values of $\Lambda^2 \eta$ with there being infinitely many pairs of (Λ, η) which will fit the reflection spectrum.

To discriminate between an over-coupled and an under-coupled mode (the two roots of Eqn. 3.15), one can observe the phase of reflected light. This technique is used to characterize the microwave mode where the coupling efficiency cannot be tuned in-situ. In case of optical modes however, we can tune the coupling efficiency by changing the distance between the coupling prism and the optical WGM resonator. The external coupling rate $\kappa_{\text{ex},o}$ depends strongly on the distance between the prism and the WGM resonator d ,

$$\kappa_{\text{ex},o} = \kappa_{\text{ex},o}^{\max} \exp(-k_0 d) \quad (3.17)$$

where, $\kappa_{\text{ex},o}^{\max} = \kappa_{\text{ex},o}(d = 0)$ is the maximum possible external coupling and $k_0 = \omega_0 \sqrt{n_{\text{LN}}^2 - 1}/c$ with ω_0 being the optical mode resonance frequency and n_{LN} the corresponding refractive index of lithium niobate.

We sweep the external coupling rate $\kappa_{\text{ex},o}$ by sweeping the distance between the prism and the optical resonator. The prism is glued to a rod which is mounted on a piezo. By controlling the voltage of on the piezo, we can sweep the $\kappa_{\text{ex},o}$. Here we make a few assumptions - Λ and $\kappa_{\text{in},o}$ don't change with the prism motion and the distance travelled by the piezo is linearly proportional to the applied voltage. We sweep the prism piezo voltage and record the optical reflected power as a function of frequency. Fig. 3.9 shows reflected optical spectra for various $\kappa_{\text{ex},o}$ values.

When the prism is retracted enough, the modes are undercoupled and $\kappa_{\text{ex},o} < \kappa_{\text{in},o}$. As the prism is brought closer, $\kappa_{\text{ex},o}$ increases and the modes gets more and over coupled. The contrast of the modes increases as shown in Fig. 3.9. However, we also see the baseline comes down. The baseline lowers as the prism is brought closer to the disk because the disk perturbs the reflection coating of the prism increasing the scattering losses. Moreover, the baseline

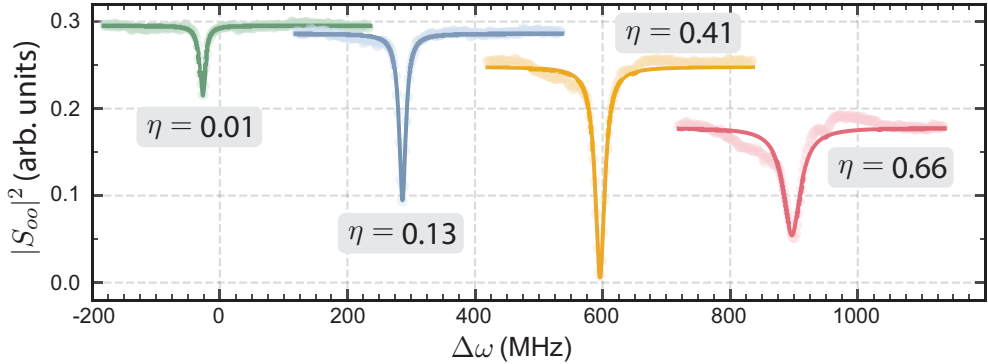


Figure 3.9: **Measured reflected optical power as a function of frequency.** The different colors represent the different amount of extrinsic coupling rate adjusted via the prism piezo voltage. The prism piezo voltages plotted here are 0 V, 14 V, 23 V, and 29 V. The separation in x -direction is for illustration purpose and does not represent the actual mode frequency shift.

gets distorted as a lot of modes, which were previously too undercoupled to be seen and, thus, hidden in the baseline, start to get coupled and effectively bring down the whole baseline.

When the total linewidth of the modes gets doubled, this is the point when modes are critically coupled $\kappa_{\text{ex},o} = \kappa_{\text{in},o}$. Because of the presence of the mode mismatch factor Λ_o , the modes might not have full contrast at critical coupling. The mode contrast is defined as normalized mode depth, $(|S_{oo,\text{off}}|^2 - |S_{oo,\text{on}}|^2)/|S_{oo,\text{off}}|^2$, where $|S_{oo,\text{on}}|^2$ and $|S_{oo,\text{off}}|^2$ are on- and off-resonance reflection intensity. Another way to look at it is, even though coupling efficiency $\eta_o = 0.5$, the 'effective' coupling efficiency $\Lambda^2\eta_0 < 0.5$ still. The contrast keeps increasing when the prism is pushed further increasing the $\kappa_{\text{ex},o}$ until it hits the maximum and decreases when the effective coupling $\Lambda^2\eta_0 > 0.5$. The red mode in Fig. 3.9 shows the situation of an overcoupled mode with lower contrast.

By fitting a Lorentzian function to all the measured optical spectra, we can extract the total linewidth of the modes. This is shown in Fig. 3.10a along with the exponential fit as instructed in Eqn. 3.17. We find the intrinsic linewidth of the optical modes $\kappa_{\text{in},o} = 10.5$ MHz. The linewidth doubles at the prism voltage of 25 V marking the point of critical coupling.

We plot the contrast of the mode calculated from the Lorentzian fits in Fig. 3.10b. Ideally, the contrast as a function of η_o is given as $4\Lambda^2\eta_o(1 - \Lambda^2\eta_o)$ under the assumption that Λ remains constant as we sweep $\kappa_{\text{ex},o}$. For $\Lambda < 1$, we would get the max contrast of 1.0 only when the mode is overcoupled, however, as one can see in Fig. 3.10, the contrast already reaches a value of 1 at $\eta < 0.5$ (marked by dashed lines). This points to the fact that maybe Λ does not remain constant as we sweep $\kappa_{\text{ex},o}$.

Irrespective whether Λ remains constant, at critical coupling, we can use the contrast to calculate the mode mismatch factor $\Lambda = 0.87$. This way, by sweeping the distance between prism and resonator and recording the reflection spectra, we can fully characterize the optical mode and determine all the required parameters $\eta_o, \kappa_o, \Lambda$.

In chapter 7, we will also characterize modes in the time domain and discuss the advantages and drawbacks of characterizing modes in time domain.

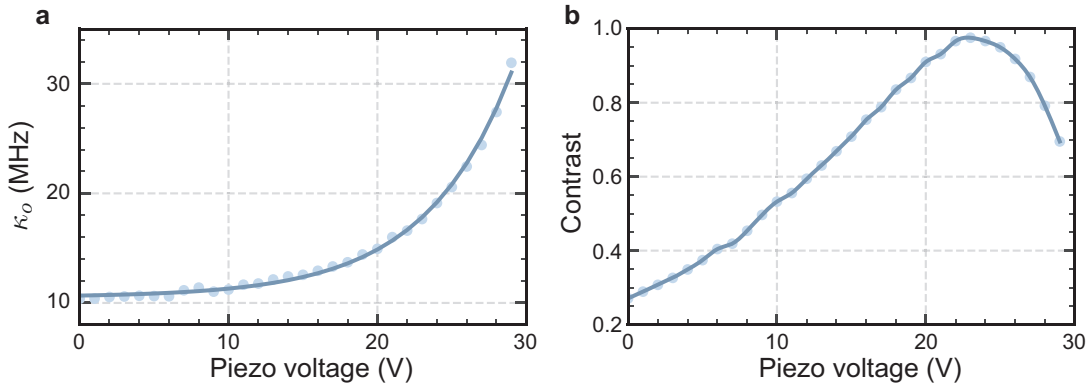


Figure 3.10: **a** Fitted total optical linewidth κ_o as a function of the prism piezo voltage. The dark line is an exponential fit to the data as shown in eqn. 3.17. **b** Calculated contrast of the optical modes as a function of the prism piezo voltage. The dark line is calculated from the κ_o fit.

3.3 Microwave whispering gallery modes

It is not just the optical cavities which can confine optical fields through repeated reflections, microwave cavities can also do the same. Using metals like aluminium, copper and gold, electric fields can be almost perfectly confined. The high electron density in these metals sets their plasma frequency, the frequency beyond which no propagation is allowed, on the order of THz. This allows microwave frequencies (GHz) to reflect perfectly with skin depths less than a micron.

However, microwave frequencies have large wavelengths \sim cm and it hard to calculate an analytical solution (like in the case of optics) for WGMs that are also of the similar size as the microwave wavelengths. Consequently, one has to rely on numerical simulations such as finite-element method (FEM) to determine allowed the mode shape and frequency in a resonators. Nevertheless, FEM simulations are an easy and accurate way to determine the modes in a WGM resonator.

3.3.1 3D whispering gallery mode resonator design

Before starting the fabrication of the resonator, we finalize the design using the FEM eigenfrequency simulations in COMSOL. The basic structure of the microwave cavity (shown in Fig. 3.11) is a hollow cylinder with only a few interruptions - two small openings to allow coupling of optical light from the optical WGM resonator to optical waveguides, a notch that contains the prism which helps couple in the optical light and an opening for a metallic pin to couple in and out microwave power from a coaxial cable (microwave waveguide). The hollow microwave cavity features two capacitor rings which hold the lithium niobate optical resonator in between (marked in blue in Fig. 3.11). This not only ensures that the microwave fields overlap perfectly with the optical fields for best coupling but also the dielectric between the capacitor rings increase the effective capacitance of the microwave cavity and helps drop the resonant frequency of microwave mode to around the optical FSR. The rings are cut at diametrically opposite points along a plane which also contains the optical prism. The cut fixes the angular position of electric field intensity minima and aligns the $m = 1$ microwave mode (with two intensity minima) at these cut parts. The microwave coupling pin is, then, placed at a 90° angle of the cut where a intensity maxima will be expected. A hole is drilled

for the same purpose seen on the left side of the blue capacitor rings in the top cavity part matching to a 50Ω coaxial waveguide.

The resonance frequency of the cavity can be adjusted by adjusting the volume of the center part of the cavity which slightly changes the capacitance of the cavity. For a given optical resonator with defined radius (which fixes the FSR) and thickness, we can design a microwave cavity with exact dimensions so as to match the frequency of the $m = 1$ microwave mode close to optical FSR.

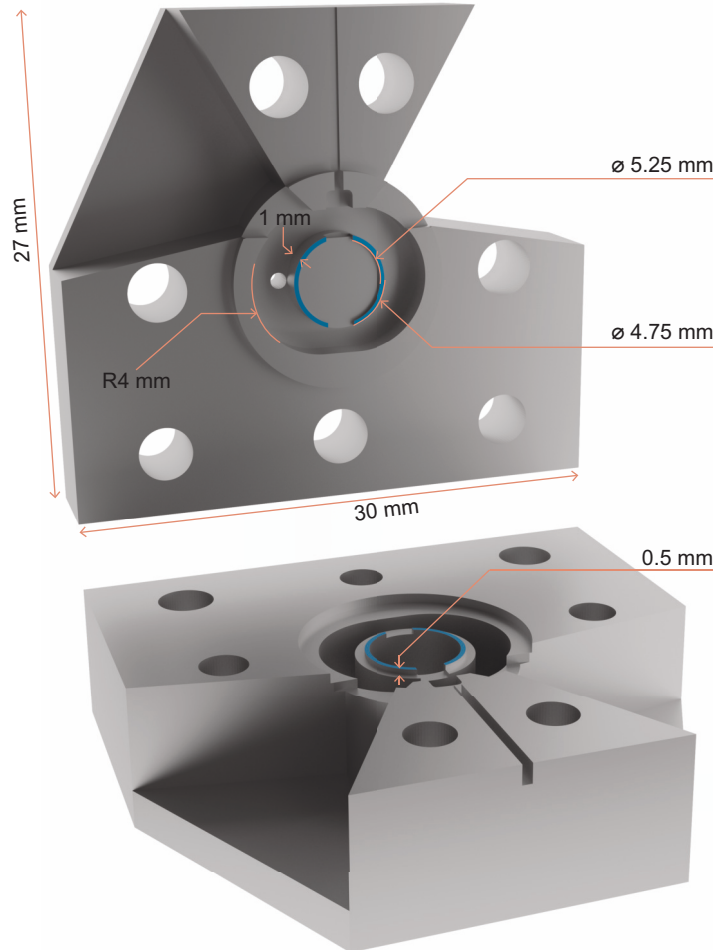


Figure 3.11: Final microwave cavity design.

In practice, the microwave resonance frequency can be quite different from the one in the design process. The reason is an uncertain amount of air-gap between the capacitor rings of the microwave cavity and the optical WGM resonator. Even a few μm change in the air-gap can change the resonant frequency of the microwave cavity by 100s of MHz (see Table 3.1). Despite the best attempt at controlling this gap, we cannot design the microwave cavity with a resonance frequency accuracy of below 100 MHz. Moreover, during the cooldown of device to cryogenic temperatures, the gaps can change unexpectedly shifting the resonance frequency of the microwave mode. This is on top of the frequency shift which happens as the dielectric constant of lithium niobate changes as it is cooled down to cryogenic temperatures but this resonance shift is more predictable.

To combat the unexpected resonance shift of microwave frequency and allow it to be tuned exactly equal to the optical FSR, a tuner is placed in the microwave cavity. The tuner is

simply a piece of metallic rod which can be moved in-situ even when the device is in cryogenic conditions. It is in the hollow cavity below the optical WGM resonator where it can be moved up and down via a nanopositioner. Moving the tuner up and down changes the volume of the microwave cavity, thus, changing its resonance frequency. During an experiment, the tuner can be exactly placed with nanometer accuracy allowing the microwave resonance to be tuned with a precision of $<1\text{ MHz}$.

During the design process, we change the geometry of the cavity to simultaneously allow for as high tuning range as possible while still keeping the center frequency of the microwave cavity at the optical FSR. This reduces the chances of having any mismatches in frequencies after the device has been cooled down to cryogenic temperatures.

In its retracted position, the tuner is far away from the optical resonator increasing the cavity volume and reducing the resonant microwave frequency. The shift in resonance frequency as the tuner is retracted drops off exponentially with the distance of the tuner and the optical resonator. On the other hand, the microwave frequency is very sensitive to the distance between the tuner and the optical resonator when the tuner is close to the optical resonator. In practice, when tuning blindly (without being able to see the tuner position in realtime), we cannot risk pushing the tuner too close to the fragile optical resonator possibly breaking the optical resonator. To prevent this, we calibrate the tuner range at room temperature when we can still observe the distance between the tuner and the optical resonator. As a result, we accept the range in which the tuner can be tuned to be from $100\text{ }\mu\text{m}$ to $4\text{ mm} - 100\text{ }\mu\text{m}$ being a cautionary distance and 4 mm being the distance after which the tuner ceases to have any effect.

The final design of the microwave cavity is shown in Fig. 3.11 with the exact dimensions which maximizes the range of microwave frequency tuning while keeping the center frequency of that range to be around the optical FSR of 8.8 GHz . FEM simulations with the final microwave cavity design are used to simulate the available range of microwave frequencies with the tuner as a function of the gap between the capacitor rings and the optical resonator. The simulated values are shown in table 3.1. The range of tuning actually remains constant as a function of the gap, however, the whole range shifts up as the gap increases.

3.3.2 Finite element method (FEM) simulations

As described above, we used FEM simulations to design the microwave cavity. Specifically, in the simulation we search for eigen frequencies of a given geometry with given boundary conditions - in this case, all boundary conditions used are 'perfect conductor', since the microwave cavity is made of superconductor.

Allowed eigen frequencies for a cavity geometry can be searched both for room temperature case and the low mK temperature case. The only difference between these cases is the permittivity tensor for anisotropic lithium niobate for the temperatures at around 9 GHz frequency. The permittivity tensor used for lithium niobate at room temperature is $\{42.5, 42.5, 26.0\}$, and at low temperature it is $\{42.5, 42.5, 22.77\}$ [MD85].

The simulation output is a number of frequencies which are allowed in the geometry along with the mode distribution. Searching for the mode $m = 1$ (which looks like as shown in Fig. 3.12a), we obtain the corresponding frequency. The simulations can also be used to understand the $m = 1$ mode in more detail. Fig. 3.12b shows the radial profile of the single photon electric field E_z in the center of the dielectric in z -direction with the azimuthal direction containing

Gap (μm)		Tuner retracted (4 mm)			Tuner inserted (100 μm)		
RT	$\omega_e/2\pi(\text{GHz})$	$E_z(\text{mV/m})$	$g_0/2\pi(\text{Hz})$	$\omega_e/2\pi(\text{GHz})$	$E_z(\text{mV/m})$	$g_0/2\pi(\text{Hz})$	
0.0	7.02	12.0	40.8	9.01	13.7	46.6	
0.5	7.63	11.4	38.8	9.79	13.1	44.6	
1.0	8.18	11.0	37.4	10.5	12.6	42.9	
1.5	8.66	10.5	35.7	11.1	12.0	40.8	
2.0	9.08	10.1	34.4	11.6	11.4	38.8	
LT	$\omega_e/2\pi(\text{GHz})$	$E_z(\text{mV/m})$	$g_0/2\pi(\text{Hz})$	$\omega_e/2\pi(\text{GHz})$	$E_z(\text{mV/m})$	$g_0/2\pi(\text{Hz})$	
0.0	7.39	12.8	43.5	9.48	14.6	49.7	
0.5	7.95	12.3	41.8	10.2	14.1	48.0	
1.0	8.47	11.9	40.5	10.8	13.6	46.2	
1.5	8.92	11.3	38.4	11.3	13.0	44.2	
2.0	9.33	11.0	37.4	11.8	12.3	41.8	

Table 3.1: Microwave frequency ω_e change and corresponding drop in electric field E_z at the location of the optical mode and corresponding vacuum coupling constant g_0 as a function of gap between the capacitor rings and the optical resonator for room temperature (RT) and low millikelvin temperature (LT). The change is temperature is simulated via change in dielectric constant of lithium niobate.

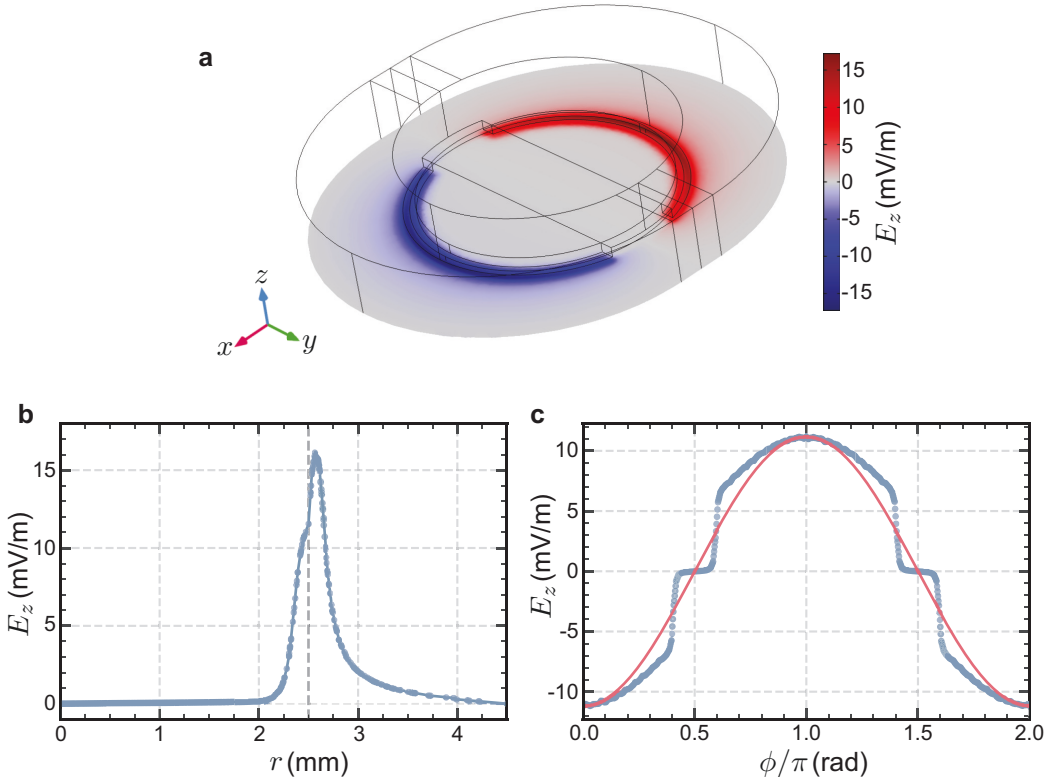


Figure 3.12: **Microwave cavity FEM simulation.** **a**, 2D distribution of single photon E_z field for $m = 1$ microwave mode at the plane which passes through the center of optical WGM resonator. **b**, Radial distribution of E_z from the shown 2D data in **a** passing through the max of azimuthal distribution. Dashed line represents the radius where optical mode is present. **c**, Azimuthal distribution of E_z from the 2D data in **a** along the radius represented by dashed line in **b**. Red line is a cosine function plotted on top. (Figure adapted from Ref. [HRS⁺20].)

the highest field amplitude. The dashed line marks the spot where the optical modes would be present (according to the diameter of the optical resonator). At this point (marked by dashed line), we can also plot the E_z profile in azimuthal direction along the circumference which is shown in Fig. 3.12c. The profile looks very similar to a cosine function which is plotted on top in red. We will approximate the E_z distribution to prefect cosine shape in the next section to estimate the g_0 vacuum coupling constant.

The electric field in z -direction, which contributes towards coupling with optics, is probed at the spot where the optical mode exists (dashed line in Fig. 3.12). This probed value from the simulations is also recorded in the Table 3.1 as E_z . The value is used to finally calculate the non-linear vacuum coupling constant g_0 as discussed in section 3.4. Value of g_0 sharply drops as the air gaps between the capacitor rings and the optical resonator increase.

3.3.3 Fabrication of microwave 3D cavity

Material The first thing to consider before fabricating the cavity is to decide the material. The two metals we have tried are aluminum and copper. In the past, we tried to make the cavities with copper since copper provided not just excellent electrical conductivity but also thermal conductivity at cryogenic temperatures [MLR⁺²¹]. Good thermal conductivity helps thermalize the device to mixing chamber allowing it to cool down faster when heated by any stray optical light. However, when enclosing a fragile lithium niobate resonator between metallic copper rings, we found them easily breaking making the assembling process of the device challenging.

As a result, we moved to using relatively softer pure aluminum metal. Pure aluminum becomes superconducting below 1.2 K but is a bad thermal conductor at cryogenic temperatures. This means that a microwave cavity made out of pure aluminum would not be able to quickly dissipate the heat generated by the optical light inside. However, pure aluminum, being soft, can even bend slightly around the LN crystal allowing the optical resonator to form a micro dent in the aluminum capacitor rings making final assembly of device less challenging. We also used a dummy LN disk (unpolished) to assemble the device as a first step. This made sure that this micro dent has been created with low risk and the real optical resonator would have even smaller chance of breaking.

Machining Since pure aluminum is soft, machining it is slightly challenging. The cavity is fabricated at the machine shop facility in our institute. Great care needs to be put in the dimensions such that the final cavity has the resonance frequency as designed. Most important is the distance between the capacitor rings in the closed cavity. If this distance is too small, it can crush the LN disk during the assembly process. If it is too large, large air-gaps would drastically change the resonance frequency of the microwave cavity from the original design.

Consequently, the first step after receiving the cavity from the machine shop is to measure the distance between capacitor rings for a closed cavity. This is done by measuring the distance between the capacitor ring top surfaces and the top surface of the cavity pads which sit on each other when the cavity is closed for both parts of the cavity. We made this measurement with a digital microscope and measured several points over the pads to get an average distance between rings and pads. This helped us identify if the pads or the rings were too uneven or crooked at an early stage and whether the distance between the rings was as designed. Any discrepancies found were adjusted in subsequent machining steps.

After this the cavity was ready to house a LN disk and for room temperature microwave resonance measurements.

3.3.4 Characterization of the microwave mode

The microwave mode is coupled via a single coaxial 50Ω port, via a metallic pin which reaches inside the cavity exciting the mode. We characterize the mode using the scattering parameter $S_{ee}(\omega)$ which is measured using a vector network analyzer (VNA) as a function of frequency. The complex $S_{ee}(\omega)$ contains the loss information in amplitude as well as the relative phase difference. This information is enough to characterize the microwave cavity completely.

Room temperature characterization After assembling the finished cavity, we characterize it at room temperature. The room temperature characterization is shown in Fig. 3.13. The reflected power $|S_{ee}|^2$ is fit with a Lorentzian function revealing the fit mode frequency as 8.796 GHz with a total linewidth of $\kappa_e/2\pi = 32$ MHz.

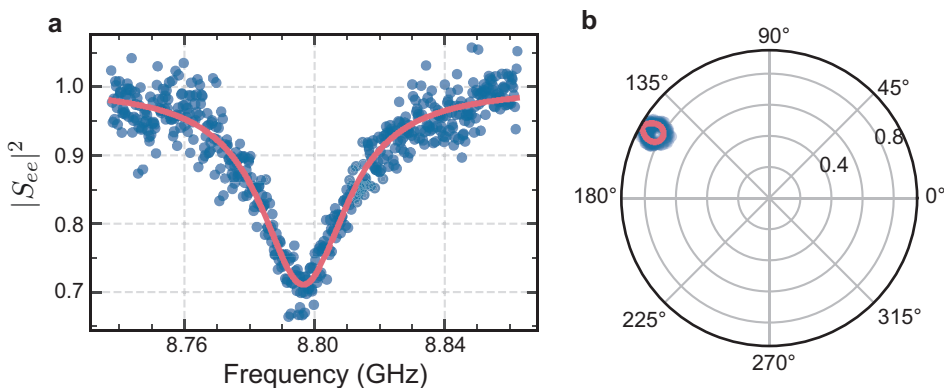


Figure 3.13: Room temperature characterization of microwave cavity.

The full model including phase dependence the phase of reflected signal and the phase due to frequency detuning is given as,

$$S_{ee}(\omega) = \exp(-i\theta\omega - i\theta_0) \left[1 - \frac{2\kappa_e}{\kappa + 2i(\omega - \omega_0)} \right] \quad (3.18)$$

where, ω_0 is the resonance frequency and $\kappa(\kappa_e)$ is the total (external) linewidth. The first exponent accounts for any extra phase that might be picked up due to delay in the measurement line. With this full model, we can fit the individual quadratures and, thus, fit the phase. Such a phase fit plot is shown in Fig. 3.13b as a polar plot. The polar plot clearly shows that the mode is very under-coupled as the knot made by the phase plot over the mode does not even approach the origin. For an overcoupled mode, the knot will include the origin within it. The coupling efficiency η_e was fit to be 0.078 - making the internal loss rate $\kappa_{e,in}/2\pi = 29.5$ MHz and the external coupling rate $\kappa_{e,out}/2\pi = 2.5$ MHz.

We expect the mode to be undercoupled at room temperature since aluminum has a larger electrical losses at room temperature drastically increasing the internal losses. When the sample is cooled down to millikelvin temperatures, the aluminum would become superconducting reducing the internal losses and overcoupling the cavity up to around critical coupling.

We also measured the range of tunability of microwave cavity at room temperature and found it to be from 8.40 GHz to 9.22 GHz. Although, the upper limit of this range can be uncertain

since we cannot exactly push the tuner very close to the optical resonator (due to risk of breaking the resonator), the lower limit is a reliable measurement. The lower limit of the tunability range is used to determine the air gaps we have in the device between the capacitor rings and the optical resonator. From Table 3.1, we predict a small air gap of about $1\text{ }\mu\text{m}$ which is enough to account for this observed frequency mismatch.

Low temperature characterization A sample characterization of the microwave cavity at millikelvin temperature is shown in Fig. 3.14. The fit parameters are - resonance at 8.799 GHz with total linewidth of 11 MHz and coupling efficiency $\eta_e = 0.42$. At low temperature, the internal losses have decreased to $\kappa_{e,\text{in}}/2\pi = 6.4$ MHz but simultaneously the external coupling rate increased to $\kappa_{e,\text{in}}/2\pi = 4.6$ MHz possibly due to metal contraction which changed the length of the coupling pin inside the microwave cavity.

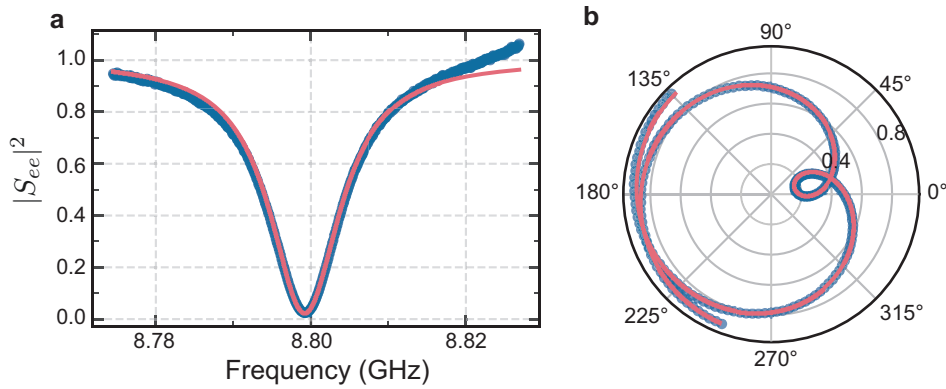


Figure 3.14: Millikelvin temperature characterization of microwave cavity.

The tuning range of the microwave cavity increased from 8.40 GHz to 9.22 GHz at room temperature to 8.7 GHz to 9.19 GHz. Again, the higher end of the tuning range is rather arbitrary as explained above. However, the increase in the lower end of the tuning frequency range is exactly as expected from Table 3.1.

Piezoelectric losses at low temperature The microwave mode, although close to critically coupled at low temperature, still wasn't overcoupled. The internal losses of the microwave cavity changes with the use of the dielectric (which or if any) between the capacitor rings. This has been experimentally studied in detail in appendix C of Ref. [RS18]. Without any dielectric, high quality factors ($\sim 1 \times 10^5$) can be obtained but when using lithium niobate in the microwave cavity, the quality factors drop to $\sim 1 \times 10^3$ even at millikelvin temperatures. We believe that the reason behind this is not only the dielectric loss [ZWG⁺23] but also an extra loss tangent for the microwave mode due to piezoelectric properties of lithium niobate [JZ02]. We speculate that the electric field between the capacitor rings of the microwave cavity excites phonons in the optical disk resonator. Since the disk is clamped at the edges, the inelastic oscillations due to clamping losses can create an extra loss tangent which increases the total internal losses for the microwave cavity. These losses are studied in detail in Ref. [HSZ⁺20]. It is shown that microwave internal losses drop periodically corresponding to the acoustic resonances of lithium niobate crystal. To overcome these losses, we propose a new center-clamped design which is discussed in detail in chapter 10.

3.4 Nonlinear vacuum coupling constant

In this section, we will calculate the nonlinear vacuum coupling constant for the WGM resonator electro-optic device described in this chapter. Without any loss of generality, the coupling constant is derived for only the process of up-conversion from the microwave mode to the optical anti-Stokes mode. It is the same for the down-conversion process.

Starting from Eqn. 2.14, we can plug-in a few simplifications relevant to our system. For ease of calculation, firstly, we can assume the two optical frequencies are approximately equal ($\omega_1 \approx \omega_2 = \omega_o$) and similarly $\epsilon_1 \approx \epsilon = \epsilon_o$ and $V_1 \approx V_2 = V_o$. Also, we replace subscript 3 with e , rendering,

$$g_0 = 2\epsilon_0\chi^{(2)} \frac{\omega_o}{\epsilon_o V_o} \sqrt{\frac{\hbar\omega_e}{8\epsilon_e V_e}} \int dV (\psi_e \psi_2^\dagger \psi_1). \quad (3.19)$$

The optical whispering gallery mode follows a profile as, $\psi_1(r, \theta, \phi) = \Psi_1(r, \theta)e^{-im\phi}$ and the anti-Stokes optical signal mode follows $\psi_2(r, \theta, \phi) = \Psi_2(r, \theta)e^{-i(m+1)\phi}$. The $m = 1$ microwave mode similarly follows, $\psi_e(r, \theta, \phi) = \Psi_e(r, \theta)e^{-i\phi}$. Since, the optical modes are tightly confined, we can assume that the microwave mode amplitude remains constant over the whole optical mode in radial and axial direction and is equal to $\Psi_{e,0}$. ψ_e can then be taken out of the integral, leaving the integral as $\int dV \Psi_2^\dagger \Psi_1 = V_o$, the total optical mode volume. Finally, we can replace $\chi^{(2)} = -(n^4 r)/2$, where n is the refractive index and r is the electro-optic coefficient (see appendix A of Ref. [RS18]),

$$g_0 = n^2 r \omega_o \sqrt{\frac{\hbar\omega_e}{8\epsilon_e V_e}} \Psi_{e,0} \quad (3.20)$$

The single photon electric field of a travelling wave can be written as (see appendix A),

$$E_\Omega(x, t) = \sqrt{\frac{\hbar\Omega}{2\epsilon V}} \Psi \left[e^{-i(k_x x - \Omega t)} + e^{i(k_x x - \Omega t)} \right] = E_\Omega^+ + E_\Omega^- \quad (3.21)$$

In the above, we assumed the microwave mode is also travelling. We can replace the single photon electric field in the formula for g_0 as,

$$g_0 = \frac{1}{2} n^2 r \omega_o |E_\Omega^+| \quad (3.22)$$

where, E_Ω is the single photon electric field of the microwave mode. Note that, only one part of the electric field contributes towards up-conversion.

However, in our microwave WGM resonator, the microwave mode is not travelling, rather it is a stationary wave. A stationary wave comprises of two travelling waves travelling in opposite directions – in case of WGM a clockwise and a counter-clockwise wave. Then, the stationary wave electric field can be expanded as,

$$E_{st} = E_c^+ + E_c^- + E_{cc}^+ + E_{cc}^-, \quad (3.23)$$

out of which, only one of the components contributes towards the up-conversion process (say E_c^+). From the COMSOL simulations, we probe the single photon electric field at the maxima

E_{st} for a stationary wave. Since only a quarter of this electric field contributes towards the up-conversion process, the nonlinear coupling constant is finally given as,

$$g = \frac{1}{8} n^2 r \omega_0 |E_{st}| \quad (3.24)$$

where, E_{st} is the single photon electric field amplitude of a standing wave as obtained from COMSOL.

3.4.1 Room temperature characterization of g_0

In this subsection, we describe the technique of using optical mode splitting due to applied microwave power to determine the nonlinear coupling constant between the optics and the microwave. Intuitively, this splitting occurs because applying a DC electric field changes the refractive index of the crystal and moves the optical mode [RSC¹⁶]. When an electric field, which is changing fast, for example at 9 GHz, is applied, the mode responds and moves at the same frequency. As a result, on average, we will detect a mode split pattern which looks like in Fig. 3.15.

This process of splitting of optical mode due to intra-cavity microwave pump photons is studied analytically and experimentally in Ref. [RSK¹⁹]. The magnitude of this splitting is derived to be $S/(2\pi) = 4\sqrt{n_e} g_0$, where n_e is the number of intracavity photons in the microwave cavity.

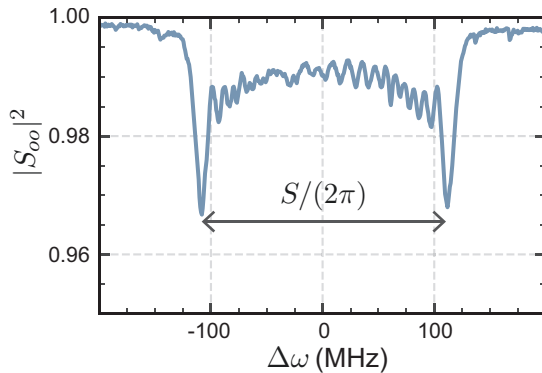


Figure 3.15: Direct measurement of vacuum coupling constant g_0 . Splitting observed in the optical mode on application of coherent microwave power. Figure adapted from Ref. [HRS²⁰].

The measurement shown in Fig. 3.15 corresponds to 9.3 dBm of microwave power applied on resonance. After accounting for the attenuation, this corresponds to about 2.3×10^{12} photons in the cavity. The splitting we measured was $S/(2\pi) = 220$ MHz resulting in a measured value of $g_0^{\text{rt}}/(2\pi) = 36.1$ Hz at room temperature. We expect a gap of slightly more than 1 μm from section 3.3.4. For this gap, we can expect a $g_0/(2\pi)$ value of ∼35 Hz from Table 3.1 depending on the frequency of microwave cavity. This measurement was made at 8.8 GHz (= optical FSR), as a result, the measured value $g_0^{\text{rt}}/(2\pi) = 36.1$ Hz is close to expected value from simulations.

3.5 Suppressing the optical sidebands with WGM resonators

In the last chapter, we saw that the microwave mode can interact with both the Stokes and the anti-Stokes optical sidebands. Interaction with different sidebands is responsible for a

different process - either beam-splitter like interaction or amplification like interaction. We also discussed that usually, in practice, we only want to have one kind of interaction in our system. Consequently, we try to suppress the interaction with one optical sideband by pumping on the optical pump with an effective detuning and later adjusting the microwave frequency to the effective FSR of the sideband we want to work with.

However, this way of suppressing the optical sideband is not very efficient. Pumping off-resonance means that a lot of pump photons just get reflected without entering the optical cavity. The number of photons inside the resonator scale as a function of detuning ($\Delta\omega$) from resonance as

$$n_p(\Delta\omega) = \frac{P}{\hbar\omega_0} \frac{4\kappa_{\text{ex}}}{\kappa^2 + 4\Delta\omega^2} \quad (3.25)$$

where, P is the applied pump power and ω_0 is the frequency of the applied pump. This means that to get the same number of photons in the resonator (or achieve the same cooperativity), one needs more optical pump power by a factor of $1 + 4\Delta\omega^2/\kappa^2$. Higher required pump power means more reflected power, which in turn, means more stray high-energy photons in the dilution refrigerator which can heat it up or worse, break Cooper pairs in the superconducting microwave cavity producing free quasi-particles. We will discuss the adverse impact of these quasi-particles in future chapters. As a result, a technique to suppress the optical sidebands without pumping off-resonance is enticing.

Luckily, another way to suppress the optical sideband is possible in case of WGM resonators made out of lithium niobate. Lithium niobate, being an anisotropic crystal, has two different refractive indices and supports two kind of mode families with slightly different FSRs. The two mode families (TE and TM), although being of orthogonal polarization, are nevertheless coupled to each other. This is because the optical resonator has a curved rim which means both TE and TM modes have small components in the direction of each other's polarization - allowing for a small amount of mode overlap and hence, coupling.

Since the two mode families are coupled, whenever the modes from these families are degenerate, an anti-crossing between the modes is seen [RSC⁺16]. By changing the electric field across the lithium niobate crystal, the refractive index and, thus, the FSR of the optical modes can be tuned. As a result, the splitting in an anti-crossing can be controlled using an external constant electric field.

Mathematically, we can write the interaction Hamiltonian for the coupling as,

$$H_{\text{int}} = \hbar J \hat{a}_s \hat{a}_{sm} + \text{c.c.}, \quad (3.26)$$

where, J is the coupling rate and \hat{a}_{sm} is the annihilation operator for the TM mode degenerate with the Stokes optical mode \hat{a}_s .

Then, ignoring the quantum noise, the set of quantum Langevin equations are written as,

$$\dot{\hat{a}}_s = -\frac{\kappa_o}{2} \hat{a}_s - i\Delta \hat{a}_s - iJ \hat{a}_{sm} + i\sqrt{\kappa_{o,\text{ex}}} F_s, \quad (3.27a)$$

$$\dot{\hat{a}}_{sm} = -\frac{\kappa_{sm}}{2} \hat{a}_{sm} - i\Delta_{sm} \hat{a}_{sm} - iJ \hat{a}_s, \quad (3.27b)$$

where, $F_s = \sqrt{P_s/(\hbar\omega_s)}$ is a coherent drive term, Δ is the detuning of the coherent drive from the \hat{a}_s mode resonance, Δ_{sm} is the detuning of the \hat{a}_{sm} mode from the TE mode (\hat{a}_s) resonance and κ_{sm} is the total loss rate of the \hat{a}_{sm} mode.

These equations can be solved in the frequency domain assuming steady state as,

$$a_s(\Delta) = \frac{i\sqrt{\kappa_{o,\text{ex}}} F_s}{(i\Delta + \kappa_o/2) + \frac{J^2}{i\Delta_{sm} + \kappa_{sm}/2}}, \quad (3.28)$$

Finally, the output field of the TE mode is calculated as, $a_{s,\text{out}} = \sqrt{\kappa_{o,\text{ex}}} - F$. We use this formalism to characterize the avoided crossing in the frequency domain.

A experimental sample characterization of such an avoided crossing is shown in Fig. 3.16. The measurement of the anti-crossing was done by sweeping the laser (coherent drive) frequency across the avoided crossing. The obtained data is fit using Eqn. 3.28. For this fit, we assume that the mode characterization of TE mode is already done using the techniques discussed in section 3.2.6. This leaves only fit parameters which are related to the TM mode. The fit parameters obtained from Fig 3.16 are $J/2\pi = 51.5$ MHz, $\kappa_{sm}/2\pi = 8.1$ MHz and $\Delta_{sm}/2\pi = 2.5$ MHz.

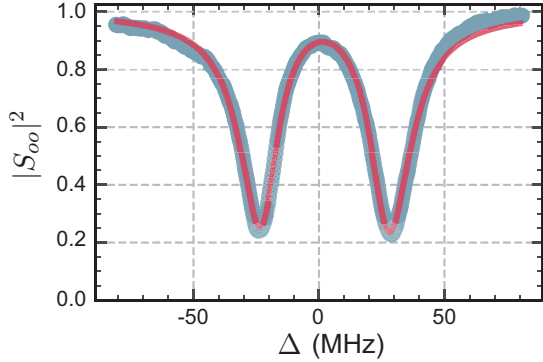


Figure 3.16: Characterization of an avoided crossing observed in an optical TE mode.

It is worth understanding intuitively the function of each fit parameter in the fit. For an undercoupled TE mode, the linewidth of the TM mode κ_{sm} changes the contrast of the avoided crossing. The smaller the κ_{sm} , the more contrast in the avoided crossing. The coupling rate J determines the size or the distance between the two peaks of the avoided crossing. Finally, the detuning Δ_{sm} determines the symmetry between two peaks as changing this detuning sweeps the TM mode over the TE mode.

The hybridisation of one optical sideband reduces the scattering rate of microwave photons to that optical sideband. The reduced scattering rate suppresses the corresponding process—either beam splitter interaction or amplification interaction, from the Hamiltonian. We express the magnitude of degree of suppression with the ratio of scattering rates to the two optical sidebands. This is discussed in more details in chapter 7.

Experimenting with mode hybridisation In our devices, we do not have the means to apply a direct voltage across the lithium niobate crystal. As a result, we cannot control the mode hybridisation at will. Rather we depend on searching for an avoided crossing that occurs naturally at a random spot. The process is as following,

- Find a high quality critically coupled optical mode in the whole FSR. In one FSR, there are a plethora of modes, most of which are either too broad or undercoupled.
- The chosen mode will repeat at each FSR. Scan multiple FSRs with the laser.
- Since there are also many TM modes in a given FSR, there is a chance of finding an avoided crossing with the mode of interest.
- Once such a hybridised mode is found. Make sure that the same mode in the neighbouring opposite FSR is not split (hybridised). This is to ensure that the wanted scattering rate

to the relevant optical sideband doesn't get suppressed and the pump mode is critically coupled¹ to maximize the cooperativity for a given amount of optical pump power.

With this method, we can sometimes find modes with a perfect hybridisation as desired and as shown in Fig. 3.16. However, often we find modes with imperfect hybridisation when the TM mode is not exactly degenerate with the TM mode resulting in mode hybridisation with asymmetric avoided crossing (shown in Fig. 3.17). In the following, we discuss how we can also use the imperfect mode hybridisation to suppress the desired optical sideband.

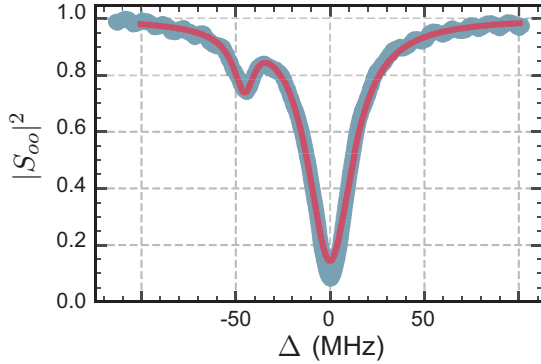


Figure 3.17: Partial hybridisation observed in an optical TE mode.

Working with asymmetric FSR Many times we find a TE mode coupled to a TM mode, but is not completely degenerate with the TM mode. This results in either an extremely asymmetric avoided crossing or if the modes are even further detuned then we don't see any avoided crossing at all, rather just the shift of the TE mode from the usual FSR. In such cases, the coupling to the non-degenerate TM mode simply shift the TE mode. This results in an asymmetric FSR with respect to a weakly hybridised mode. If we choose this mode as the optical pump, the effective FSR between the pump and the two optical sidebands will be different. Thus, we can use such an arrangement to obtain the same effective system of suppression as discussed in chapter 8 (pumping off-resonance) but without the cons of actually having to pump off-resonance. We can also use a weakly hybridised mode such the one shown in Fig. 3.17 as the optical pump. Although this is an avoided crossing with a small very asymmetric splitting, we can simply pump at the point of highest contrast. Since the splitting is weak, the maximum contrast is only slightly reduced from an unhybridised mode. Thus, the pump power required to achieve the same cooperativity is only slightly more.

Finding such asymmetric FSRs can be challenging. Modes with small satellites can be hard to spot and modes with even weaker hybridisation are even more difficult to spot. However, as we will discuss in the next chapter, we use two different optical paths for the optical signal and the pump. This makes it easy to quickly get a rough idea of any asymmetric FSRs in the neighbouring modes. If with rough measurements an asymmetric FSR is suspected, finer measurements can be made to check the degree of asymmetry.

¹The number of photons inside the resonator are maximum at critical coupling for a given amount of input power.

CHAPTER 4

Experimental setup

4.1 Introduction

In this chapter, we discuss the practical details of working with a WGM resonator based electro-optic device. When cooling down the assembled device to millikelvin temperatures, the optical couplings can change due to metal contraction. Therefore, the final assembly of the device needs a set of piezos to control input-output optical coupling and a microwave cavity frequency which need to be tunable in-situ. During the cooldown, we use the piezos to maintain the mode couplings in place. Here, we discuss the algorithm that we use to achieve the same. Finally, we discuss the structure of experimental setup built around the device to carry out the final measurements with the device. The full experimental setup changes slightly with different experiments each time so the detailed experimental setups are discussed in the appendix C for each experiment presented in the thesis.

4.2 Low temperature experimental setup

Fig. 4.1 shows the electro-optic device in the top center with all the necessary equipment surrounding it. The light from single mode fibers is coupled through gradient index lenses (GRIN lens) which focus the light on the prism surface which is inside the aluminum microwave cavity. The two GRIN lenses are mounted on an XYZ piezo-stack each. The more powerful Z-piezo carries two other piezos which can move horizontally. The piezos we use are from Attocube - ANPx101 for horizontal directions and ANPz101 for the vertical direction. All the piezos are configured to work at millikelvin temperature and were bought with LT (low temperature) option. The setup allows us to align the GRIN lenses with a nanometer accuracy.

The GRIN lenses and the single mode fibers are glued with a NOA61 glue which is cured using ultraviolet light. Using a glue which is fluid before curing and which gets cured using the application of light allows us to glue the optical components without disturbing the coupling.

The prism is mounted on a ANPx101 piezo shown in the middle of the picture. An aluminum rod, to which the prism is glued to, is attached to the prism piezo. Adjustment of this piezo with direct voltage is essential since it controls the external coupling rate $\kappa_{\text{ex},o}$ by adjusting the distance between the prism to the optical resonator. Fig. 3.10 shows how sensitive $\kappa_{\text{ex},o}$ is to applied voltage to the piezo.

4. EXPERIMENTAL SETUP

Another ANPz101 piezo carries the microwave frequency tuner rod which is mounted under the device and cannot be seen in the picture.

Finally, the microwave is coupled via copper waveguide with an SMA connector pin attached to the top of the device.

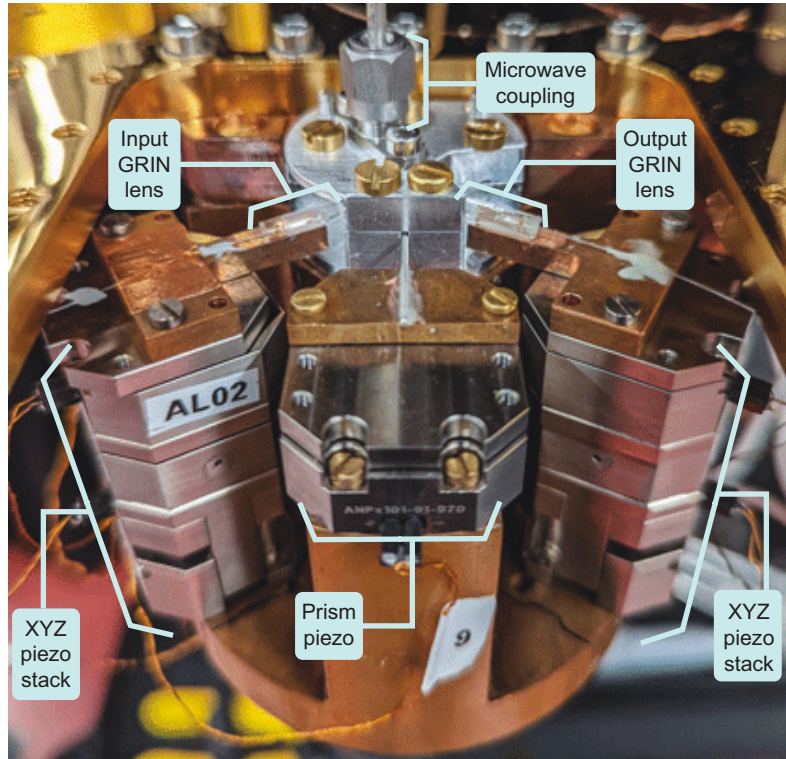


Figure 4.1: Final device assembly.

As can be seen in the picture, all the piezos and the electro-optic device are mounted on a custom designed copper block that minimizes the coupling angle changes as the device is cooled down. We couple the optics while the device is mounted on the copper block. Finally when input and output coupling to GRIN lenses reaches a satisfactory level (in the past, we have been able to achieve $> 50\%$ transmission with $> 65\%$ contrast for critically coupled optical modes), the optical components are glued, the whole copper block is mounted on the mixing chamber plate of a He^3/He^4 dilution refrigerator. Part of the mixing chamber plate can be seen in the picture on the top left and right. The copper block facilitates the thermalization of all the equipment to the mixing chamber plate's millikelvin temperature upon cooldown.

Since the whole assembly is made out of metal and is cooled down from room temperature $\sim 300\text{ K}$ to $\sim 0\text{ K}$, a lot of thermal contraction can be expected. Due to the complex geometry of the device, it is hard to predict the distance and the direction in which optical couplers will move as a result of this temperature change. As a result, we need to constantly move the optical couplers via the XYZ piezo stack to maintain optical coupling through out the cooldown process.

4.3 Maintaining optical coupling during cooldown

In the previous section, we discussed how the optical coupling can change as a result of temperature change during cooldown and metal assembly. The optical coupling has to be

maintained by moving the input-output coupler positions in-situ via the XYZ piezo stack. This can be done manually. However, the cooldown from room temperature to 4 K can take about 30 hours and constantly adjusting the coupling for 30 hours is a rather daunting task.

The process of keeping the modes coupled can be partially automatized requiring much less input from an experimenter. To write an automatic program which can maintain the optical coupling, we need to understand the changes during the cooldown. In order of magnitude of the rate of change (fastest to slowest), the following things change during the cooldown:

- **Coupling efficiency of modes** The optical mode coupling efficiency is extremely sensitive to the distance between the prism and the optical resonator. This coupling changes the fastest during the cooldown. One can expect to change the prism voltage few times per minute during the steepest temperature gradients during the cooldown. While cooling down, the prism tries to get closer and closer to the optical resonator, so it is essential that we keep moving the prism back lest it rams into the optical resonator possibly breaking the whole setup.
- **Polarization of light** The next fastest thing to adjust is the polarization of light. In our setup, we use several meters of optical fiber inside the dilution refrigerator for future expansion. As this fiber goes through a large temperature gradient, the polarization of light passing through it changes quite drastically. As a result, polarization of light has to be adjusted at least once an hour. Since, the polarization degree of freedom is one-dimensional, it is easy to adjust and maximize the coupling using polarization before doing something more complicated.
- **Input-output coupling** The coupling of the optical resonator to the input and output coupling fibers changes the slowest. This coupling has to be changed systematically and in pairs as we discuss next.

Algorithm to maintain coupling We now describe the procedure to maintain the optical coupling during the cooldown. We start with the optical mode in the best possible achievable coupling. Several modes are monitored at the same time by sweeping the laser frequency wide enough to cover at least one FSR. The idea is, on the oscilloscope, one should see high quality optical modes with enough separation between them such that the mean of the full waveform approximately represents the reflected baseline. With this prepared setup, the following detailed algorithm has been implemented to maintain optical coupling:

1. Calculate the mean, max, min and variance of the waveform which displays the reflected optical mode spectra. Here, we assume that the mean is approximately the reflected baseline. The difference between the max and the min is an indication of the contrast. The variance reflects the two states of the baseline - when the modes are under-coupled or critically-coupled, the reflected baseline is rather flat and when the prism gets too close to the optical resonator, the modes get overcoupled and many more modes get coupled (leaving the baseline not flat anymore) increasing the variance of the waveform (We touched upon this topic in section 3.2.6.).
2. When the optical modes are coupled as desired, we must store the value of the mean, max, min and variance as the ideal desired one. Also, some thresholds are set for the mean, max–min and variance values such that when the measured values of these parameters go below the threshold, some action is triggered.

4. EXPERIMENTAL SETUP

3. If the prism gets too close, the modes get overcoupled. This will mostly increase the variance but it may also decrease the contrast (max-min). Moving the prism back with the DC voltage¹ will solve this. If the applied DC voltage is already at zero, one back step with step voltage is needed but it will end up under-coupling the modes most probably. Follow next step to solve this issue.
4. When the prism is too far from the resonator and the modes are undercoupled, the variance will be low as desired but the contrast will also be low which is not wanted. In this case, the prism needs to moved forward to rectify the issue and get all the parameters within the threshold targets. Consequently, we can increase the DC voltage applied to the prism piezo. If the applied DC voltage is too high (say 35 V), then a forward step with step voltage is needed to fix the situation. Follow step 3 to fix the overcoupling issue if it arises after step forward.
5. The above two steps work only if one of the two - contrast or variance are out of their thresholds. If the variance is high while the contrast is low, it means that the prism is too close and retracting it back is not going to increase the contrast. In this case, either the polarization has drifted or the coupling to the GRIN lenses has drifted.
6. We choose to first adjust the simple one-dimensional parameter - polarization. If adjusting the polarization via the polarization paddles gets the contrast back to normal, then the problem is easily solved, otherwise we move to the next step.
7. Finally, the only thing that can be wrong is input-output coupling to GRIN lenses. In theory, this is a 12 dimensional space with 3 spatial directions and 3 angles each for input and output couplers. In our current design, we do not optimize the angles of GRIN lenses. This leaves us with 6 dimensions corresponding to spatial directions to tweak. In practice, one of these directions is movement along the grin lens which changes the size of focus spot on the prism surface. The focus size changes rather slowly with length travelled by grin lens in this direction, so the affect it has on the coupling efficiency is minimal. During the cooldown, the couplers don't drift enough to change the focal spot drastically, we can simply ignore this direction for both input and output during cooldown.
8. Ignoring these two dimensions (corresponding to both input and output couplers) reduces the coupling problem to four dimensions. The rest of the four dimensions are coupled to each other due to the geometry of the problem. For example, if the z-direction of input coupler is moved in up-direction, the transmission will go down since the reflected spot will also move up with respect to the output coupler. Hence, the output coupler needs to be moved up as well. Similarly, the x-direction of input and output are inversely coupled. If input-x is moved in one direction, the output-x needs to be moved in opposite direction to maintain the transmission. Moving input and output couplers in tandem is a usual optical coupling technique and known as 'beam walking' in the community. By moving both input and output couplers pair-wise, we are essentially moving the focused spot on the prism surface and trying to find the spot on the surface where the mode coupling with the optical resonator is the best.

¹Piezo position can be finely adjusted by applying a DC voltage but with a limited range which is limited by range of DC voltage (typically 0 V - 50 V). Better range is achieved by sending a sawtooth-like voltage to piezo which causes a slip-stick motion to coarsely move the piezo farther. Here, we refer to this mode of motion of piezo as stepping.

9. In our case, however, there is one extra coupling between the Z and X direction. Since the piezo stacks are not perfectly vertical, moving in vertical direction slightly changes in horizontal direction as well. For this reason, we adjust the vertical direction first and then adjust the horizontal direction.
10. Finally, the order in which the coupling is adjusted is Z-in up, then Z-out up to maintain transmission. Then, check if it improved the contrast. If it did, keep moving them up until it stops helping and go back to last best coupling point. If moving up never made the contrast better, then move them down together and check the contrast and find the best coupling point in vertical direction.
11. Repeat the same exercise in horizontal direction, except move the two piezos in opposite direction to maintain contrast. If moving in one direction does not help, try the other direction and optimise coupling in the horizontal direction as well.
12. One pass of optimization in both vertical and horizontal direction may not be enough. So, if after one pass the contrast is not restored, more optimization passes can be made. Beware that fiber coupling optimization can take long depending on the number of steps made in one pass and number of passes needed. It is recommended to adjust the prism piezo between each pass of fiber coupling adjustment.

Cooldown helper program The above described algorithm can be readily automated. We wrote a cooldown helper program featuring a graphical user interface GUI which implements the above algorithm. The program connects to the oscilloscope to monitor the optical modes and the Attocube controller to control the piezo positioners. The program can also connect to a RF source which controls the applied phase modulation to the input light. The phase modulation would create sidebands with a known frequency separation. This is used as calibration to measure the mode quality factors during the cooldown. Moreover, the program can also connect to a variable optical attenuator to control the input optical power which is sent to the device in the dilution refrigerator.

The program GUI is shown in Fig. 4.2. The top left part displays the optical mode spectra from the oscilloscope. It can be requested via the 'Run once' or 'Run continuously' button. To save data transfer bandwidth, it is not turned on by default. Below the plot are the various parameters of the optics waveform as requested from the oscilloscope. They are continuously updated and monitored to detect any change. The accepted thresholds for these parameters can be changed in the mid left panel. If the value of the parameter falls below the accepted range some action will be triggered.

In the middle panel, various other parameters can also be adjusted such as maximum prism piezo DC voltage, step voltage magnitude and frequency and the keyboard shortcuts. The keyboard shortcuts help easily control the piezos in an intuitive manner. They can also be used to control the piezos remotely if needed. Added benefit of using the program to control the coupling is that the program records the steps taken and, hence, we can use this data to go back to approximately the previous coupling point, in case something goes wrong.

The program works by switching between various states. If the thresholds are not set, the program is uninitialized. After accepting the good coupling scenario by clicking button '*This is ideal*', the program starts. If all the measured parameters are within the threshold, the program displays the status '*Everything OK*' in the right corner. If any parameter drifts outside the accepted range, then program switches to the status '*Need optimization*'.

4. EXPERIMENTAL SETUP

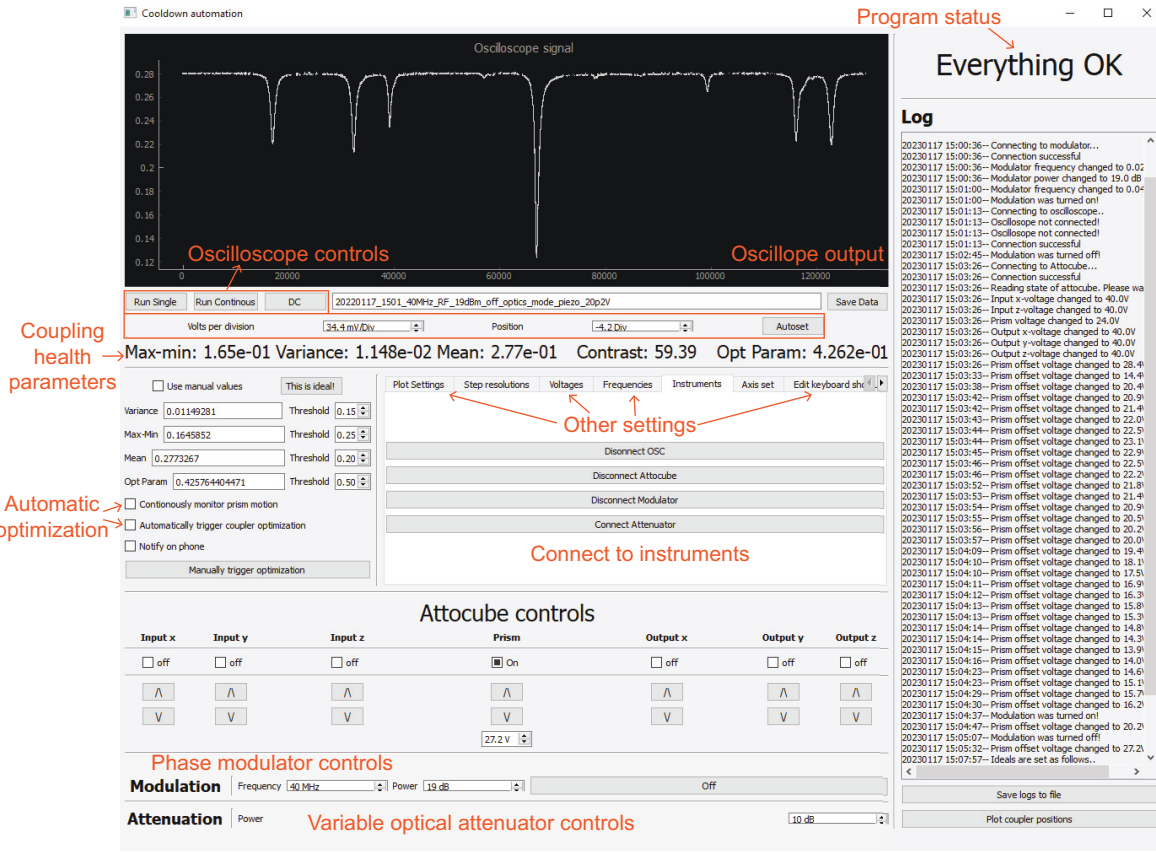


Figure 4.2: Cooldown helper program GUI.

At this point, we can choose to fix the problem manually or use one of the check boxes on the left side to automate the coupling process. If the required boxes are checked, the program can automatically correct for prism drifts and input-output fiber coupling. Different check boxes allow the program to modify prism and input-output fiber coupling. The optical coupling can also be manually triggered using the '*Manually trigger optimization*' button. A log of what has been changed is displayed on the right panel at all times. The log are automatically saved in a log folder and can be saved in a specific folder for further analysis via the '*Save logs to file*' button.

In the current version of program, the polarization drifts were not automatically corrected. However, automatic polarization drift correction in future can be implemented by using a motorized polarization paddle such as MPC320 from Thorlabs and adjusting the polarization before input-output coupling is modified.

4.4 Optical quality factor drop during the cooldown

One puzzling thing we observed during the cooldown was the steady drop in optical quality factors. At room temperature, we measured the intrinsic optical quality factor of $\sim 10^8$. After the cooldown at millikelvin temperature, we measured the quality factor again and found that it had dropped to $\sim 2 \times 10^7$. The mode quality factors did not change after that for as long as the resonator remained cold. However, about two and a half years later, we warmed up the system and without making any changes to the transducer, we cooled it down again. After the second cooldown, the quality factors dropped yet again by more than 3 times to $\sim 5 \times 10^6$.

Unfortunately, we did not take concrete data to verify the change in optical quality factor after the first warm-up.

This drop in the optical quality factor proved to be one of the biggest limiting factors of our device. To achieve the same cooperativity $C = 4n_p g_0^2 / (\kappa_o \kappa_e)$, the optical pump power required is proportional to the square of the optical linewidth κ_o . This is because not only the enhanced coupling rate $\sqrt{n_p} g_0$ needs to match to a bigger loss rate, but also more optical pump power is needed to achieve the same number of photons in the resonator n_p for a larger linewidth mode.

Unfortunately, the cause of this drop in the optical quality factor is still not known. We speculated that this might be due to adsorption of gases on the optical resonator surface at millikelvin temperatures. However, adsorption does not explain why the quality factors dropped even further on the subsequent cooldown.

Another speculation which might explain the drop in the quality factors is formation of micro-cracks in the optical resonator which can form in the process of closing the microwave cavity around the microwave resonator. The microwave cavity pushes even harder during the cooldown because aluminium contracts more than lithium niobate². As a result, there is a good possibility of damaging the pristine dielectric material exactly where the optical modes are expected. Upon cooldown, lithium niobate will shrink and the cracks will get larger deteriorating the optical quality factor. It is also not hard to imagine this shrinking not being fully reversible which will cause further loss in quality factor upon subsequent cooldowns.

This problem can be solved with a new design of transducer which includes a microwave cavity which does not push on the optical resonator exactly where the optical modes are present. We discuss this new design in chapter 10.

4.5 Room temperature measurement setup

The setup inside the dilution refrigerator needs to be complimented with an external signal preparation and measurement setup. The exact details of the measurement setup change with different experiments. For each following chapter, we used a slightly different setup as needed. The setups are explained in full detail in appendix C. Here we give a gist of the core components of the setup.

The measurement setup is divided in 4 parts - optics preparation and detection and microwave preparation and detection. The preparation of optics has usually two parts - preparation of the optical pump and the optical signal. We usually divide the 1550 nm laser into two parts to make the optical pump and signal. Continuous wave optical pump is just the laser itself, but when the optical pump is pulsed, we use an acousto-optic modulator to create optical pulses with sharp rise and fall times of ~ 10 ns.

The optical signal is produced with an optical single sideband (SSB) modulator. The optical single sideband works as shown in Fig. 4.3. The light is first divided into two parts with a phase modulator in between to control the phase in two arms (via an external bias voltage DC3). Each of the two arms are themselves an intensity modulator, which is made by a Mach-Zehnder interferometer modulated by an RF tone and biased with a DC voltage. The two arms are then combined where they interfere with each other before the light exits. Overall, the device

²Thermal expansion coefficient of aluminium is about $2.3 \times 10^{-5} \text{ K}^{-1}$ while that of lithium niobate is $4.1 \times 10^{-6} \text{ K}^{-1}$.

needs two RF tones and 3 DC voltage biases. The RF tones are made from one RF source which is split in two parts. One part is fed directly to the SSB modulator while the other part is attenuated and phase corrected to match the requirements. By controlling the phase between the RF tones and the DC biases, we can suppress any combination of the pump tone and the two produced sidebands. Usually, we keep only one sideband while suppressing both the pump and the other sideband to produce the optical signal at the desired offset from the optical pump.

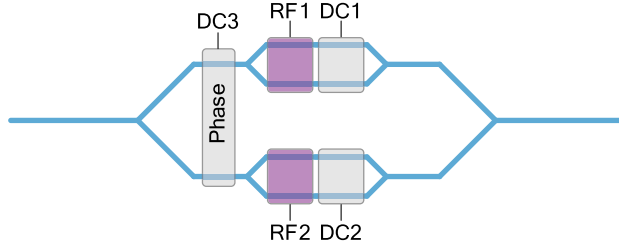


Figure 4.3: Optical dual parallel Mach-Zehnder interferometer used as single sideband modulator.

The optics is detected either via an optical spectrum analyzer (OSA) or, if more sensitivity is needed, via an optical balanced heterodyne setup. If heterodyne is used, we also need to prepare the local oscillator (LO) from the original laser. In this case, the laser is divided in three parts to produce the optical pump, signal and LO. The optical LO tone is produced by an electro-optic phase modulator. For phase modulation, we use the RF power which maximizes the power in first-order optical sideband which is used as LO frequency for heterodyne. In this regime, however, the phase modulator also produces other higher-order sidebands. If the optical LO is corrupted with extra frequency tones which do not beat with the optical signal at the measured frequency, these extra tones beat with the shot noise and produce extra noise. This reduces the efficiency of the optical heterodyne. As a result, to increase the heterodyne efficiency, we also used an optical Fabry-Pérot cavity filter to clean the optical LO tone when the heterodyne efficiency was of utmost importance.

The microwave preparation is done simply with RF sources. We use microwave switches to switch between vector network analyser (VNA) measurement or spectrum analyzer (SA) measurements. The SA has a maximum measurement bandwidth of 80 MHz. For higher bandwidth measurement, we use manual downconversion of microwave signal via IQ modulators using a microwave LO. The downconverted signal for both microwave and optics heterodyne detection is digitized at 1 Gigasamples per second. Theoretically, it allows us to measure a maximum of 500 MHz bandwidth according to Nyquist theorem [Sha49] but in our experiments we only went up to 200 MHz.

Note that, in our experiments, we use a lot of RF modulation. The RF modulation is produced via RF sources which are all synced to one 10 MHz Rubidium clock. The acousto-optic modulators which use 200 MHz modulation are also synced to the same clock to preserve phase coherence of the optical pump with the optical signal.

4.6 Conclusions

In this chapter, we have described the practical details of our experimental setup including the electrooptic device assembly, the cooldown process and a summary and a few key points about the room temperature setup outside the dilution refrigerator. We also discussed the

cooldown helper application which can be used as a short manual to use the software. In the next chapters, we will move on to the experimental results obtained with this electrooptic device.

CHAPTER 5

Transduction with a CW optical pump

5.1 Introduction

After cooling the electro-optics system down to millikelvin temperatures, the first experiment we do is transduction between the optics and microwave frequencies using the beam splitter interaction between the optical anti-Stokes sideband and the microwave mode. Here, we use a continuous wave (CW) pump and coherent signal drives to measure the transduction efficiency. Even though the experiment is purely classical, the motivation to cool the microwave system down to its ground state is to study the thermal noise properties of the transduction process. When working with quantum signals or interfacing with qubits, even a good transduction efficiency between the modes is useless if a transducer adds a lot of thermal noise on top of the transduced signal.

In this chapter, we describe how we measure the transduction efficiency of our system and the calibrations which are needed to accurately measure the efficiency. We also study in detail the thermal noise properties of our system as a function of applied pump power both in the frequency and time domains which let us conclude that our system is a good candidate for a pulsed-pump operation.

Acknowledgements This chapter is based on the work presented in Ref. [HRS⁺20]. Figure credits have been individually given in the figure captions.

5.2 Theory

Most of the needed theory is already covered in section 2.4 of chapter 2. We assume only the beam splitter like Hamiltonian between the optical anti-Stokes sideband and the microwave mode,

$$\hat{H}_{\text{int}} = \hbar g_0 \sqrt{n_p} (\hat{a}_t^\dagger \hat{a}_e + \hat{a}_t \hat{a}_e^\dagger). \quad (5.1)$$

Here, we have ignored the interaction of the microwave mode with the optical Stokes sideband. The assumption is fair because not only we suppress the interaction of optical Stokes sideband by hybridising the mode (as described in section 3.5) as shown in Fig. 5.1 but also because we only work with low cooperativities ($< 10^{-3}$) in this chapter. As we will see in chapter 7, the cross interaction between the microwave mode and different optical sidebands becomes

relevant only at high cooperativities ~ 1 . Solving the interaction Hamiltonian (Eq. 5.1) in steady state, the total transduction efficiency on resonance is obtained as,

$$\eta_{\text{tot}} = \Lambda^2 \eta_e \eta_o \frac{4C}{(1+C)^2} \quad (5.2)$$

where C is the cooperativity and η_i are the coupling efficiencies. The formula is exactly the same as described in chapter 2 except we have now added the optical mode mismatch factor Λ . The mode mismatch factor essentially only affects the external coupling rate for optics as $\kappa_{o,\text{ex}} \rightarrow \Lambda \kappa_{o,\text{ex}}$. This results in an additional Λ^2 factor in the formula for the total conversion efficiency corresponding to the two times light has to coupled in from a single mode fiber to optical WGM (for the optical pump) and vice versa on the output side (for the optical signal)¹.

We also define the internal conversion efficiency $\eta_{\text{int}} = \eta_{\text{tot}} / (\Lambda^2 \eta_e \eta_o)$ excluding the losses involved in coupling power from waveguides to cavities. In other words, η_{int} stands for the conversion efficiency for the exchange of photons inside the cavities. At $C = 1$, the internal conversion efficiency is 1. Beyond $C = 1$, it starts to drop due to energy oscillation between modes. In this case, the conversion rate is not matched with the out-coupling rates. This means that the total conversion efficiency is bounded by the coupling losses $\Lambda^2 \eta_e \eta_o$ at $C = 1$.

5.3 Experimental setup

The detailed experimental setup is described in appendix C. In summary, the electro-optic device is mounted on the mixing chamber plate in the dilution refrigerator. A series of attenuators attenuate the coherent microwave signal down to single photon levels (and corresponding room temperature thermal noise to $\ll 1$ quanta). After the signal reflects from the microwave cavity, it is deflected to another output line via a circulator. The output line amplifies the small microwave signal via a high-electron-mobility transistor (HEMT) amplifier. The microwave modes are characterized by a vector network analyzer (VNA). The output microwave power is measured by a spectrum analyzer (SA).

On the optics side, a 1550 nm laser is divided in two parts - optical pump and signal. The optical signal is produced from the optical pump frequency via a single sideband modulator (SSB). The sideband frequency can be adjusted by changing the input microwave frequency to the SSB. The optical pump and the signal are combined via a 99:1 coupler before sending the light to the dilution refrigerator. 10% of the reflected power is measured by an optical photodetector to measure the optical spectra or to lock the optical pump to the optical WGM resonator. 90% of the reflected light is detected by an optical SA either directly or after being amplified through an Erbium-doped fiber amplifier (EDFA) in case the optical signal is too small to measure.

Laser lock The only lock we used during the measurements with the CW optical pump was the locking of the laser light to the optical WGM resonator. The laser is locked to the reflected pump power from the optical cavity. The reflected power is the smallest at the resonance and increases if the laser is detuned to either side of the resonance. Since the only available information is the reflected power without any phase, the direction of the detuning of the laser cannot be predicted. The mode we are locking to is relatively broad (~ 10 MHz) compared to

¹For optical to microwave conversion, both the optical pump and the optical signal need to be coupled in resulting again in a Λ^2 factor.

the laser frequency drifts. As a result, we do not need a fast lock. A lock that works on the order ~ 100 ms would work.

We chose a digital implementation of the laser lock due to the ease of use and compatibility with the measurement script. The laser frequency can be controlled via a built-in piezo controller which is in turn controlled by sending commands to the laser via the telnet protocol. To lock the laser to the pump frequency, we measure the reflected pump power and digitize it to be read on a computer. Below, we describe a dynamic step algorithm to lock the laser frequency to the optical pump mode.

The basic idea of the algorithm 5.1 is to move the laser frequency in one direction and then another to find the point of minimum reflection. However, the algorithm depends heavily on the step size used to move the laser frequency. If the step size is too small, the noise can overwhelm the error signal and give wrong estimation of where the minimum is. Nevertheless, even with small step size, the algorithm will stochastically find the true minimum of the mode resonance but the process will be slow and uncertain. Choosing a bigger step size allows to avoid these problems but then the laser is never truly parked at resonance and the algorithm is constantly shifting the laser around trying to make sure that it is on resonance.

The best of both the worlds is achieved if we implement a dynamic step size approach. For this, we need the extra information about the reflected power on- and off-resonance. Using this information, we can predict how far away from resonance the laser is. We, then, interpolate the step size linearly between a chosen minimum and maximum step value according to the measured reflected power. With this approach, the algorithm takes larger steps when the laser is further away from resonance but the step sizes decrease as the laser approaches resonance and smallest steps are taken near resonance so as to not move the laser around too much once near resonance.

5.4 Setup characterization

The optical mode reflection spectra are shown in Fig. 5.1 featuring an $FSR = 8.818$ GHz and $\omega_p = 193.5$ THz. The full mode characterizations are done as described in chapter 3. The final obtained parameters are stated in table 5.1.

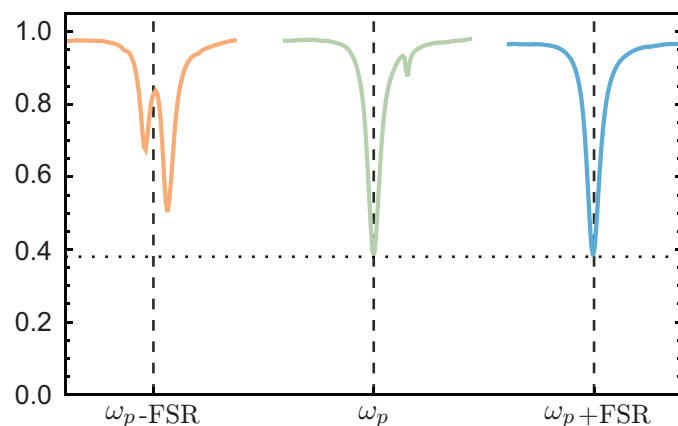


Figure 5.1: Reflected optical mode spectra for transduction results with a CW optical pump.

Optical heating of the microwave cavity We noticed that the microwave cavity properties change as a function of the applied optical pump power. This is attributed to the local thermal

Algorithm 5.1: Dynamic step size digital laser lock.

Data: $\max \leftarrow$ the max power reflected off-resonance,
 $\min \leftarrow$ the minimum power reflected on-resonance,
 $S_{\min} \leftarrow$ the smallest step size for laser piezo ($\sim \kappa_o/100$),
 $S_{\max} \leftarrow$ the biggest step size for laser piezo ($\sim \kappa_o/10$)

1 **Function** *interpolate(R)* : **is**

2 $x \leftarrow [-10, \min, \max, 10];$ /* Here, 10 and -10 are some
 absolute min and max possible value of R. */

3 $y \leftarrow [S_{\min}, S_{\min}, S_{\max}, S_{\max}];$

4 $x_{\text{new}} \leftarrow \text{interpolate1D}(R, x, y);$ /* Interpolate R on a 1D function
 described by x and y arrays. */

5 **return** $x_{\text{new}};$

6 **end**

7 $MD \leftarrow 1;$ /* Represents the movement direction */

8 $R \leftarrow \text{Measure reflected power of optical pump};$

9 $amp \leftarrow \text{Measure laser amplitude};$ /* The piezo voltage on laser */

10 **while** (*RunLock* is **True**) **do**

11 **while** **True** **do**

12 $R \leftarrow \text{Measure reflected power of optical pump};$

13 $step \leftarrow \text{interpolate}(R);$ /* Dynamic step size */

14 $\text{setLaserPiezo}(amp + step \times MD);$ /* Change laser piezo
 voltage */

15 $amp \leftarrow amp + step \times MD;$

16 $\text{sleepProgram}(0.05\text{s});$ /* For changes to take effect */

17 $R_{\text{new}} \leftarrow \text{Measure new reflected power of optical pump};$

18 **if** $R_{\text{new}} < R$ **then**

19 $R = R_{\text{new}};$

20 **continue** to Step 11;

21 **else**

22 **if** $MD = 1$ **then**

23 $MD \leftarrow -1;$ /* Change direction */

24 $R = R_{\text{new}};$

25 **continue** to Step 11;

26 **else**

27 $\text{setLaserPiezo}(amp - step \times MD);$ /* Go back to last best
 found position */

28 $amp \leftarrow amp - step \times MD;$

29 **break**; /* Break the inner while loop */

30 **end**

31 **end**

32 **end**

33 **end**

Parameter	Value	Unit	Description
$\kappa_o/2\pi$	18.9	MHz	Total optical linewidth
η_o	0.5	-	Optical coupling efficiency
Λ	0.62	-	Optical mode mismatch factor
$\kappa_e/2\pi$	10.4	MHz	Total microwave linewidth
η_e	0.35	-	Microwave coupling efficiency
FSR	8.818	GHz	Optical free spectral range

Table 5.1: Mode characterization for CW pump transduction.

heating caused by the high energy optical photons. We characterize the microwave cavity for the full range of optical pump powers we used in the experiment. The results are shown in the Fig. 5.2.

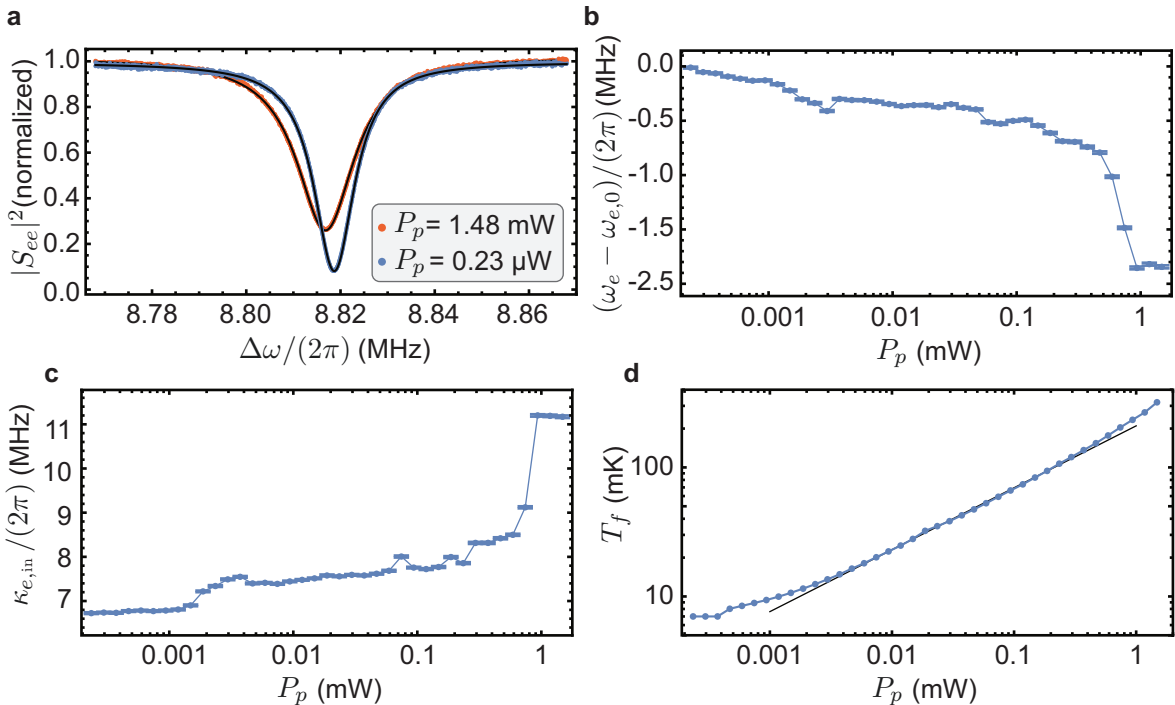


Figure 5.2: **Microwave cavity properties in the presence of laser light.** **a** Normalized reflected microwave spectra for the highest (lowest) applied pump power in red (blue). **b (c)** Change in microwave frequency resonance ω_e (intrinsic losses $\kappa_{e,\text{in}}$) as a function of applied optical pump power P_p on resonance. **d** Mixing chamber temperature T_f as a function of P_p with a power law fit $T_f \propto P_p^{0.48}$ (black line) of the intermediate power region. Figure adapted from Ref. [HRS⁺20].

The reflected microwave spectra in Fig. 5.2a shows that the microwave cavity broadens (due to increased internal losses $\kappa_{e,\text{in}}$) and red-shifts in response to optical power. The shift in microwave resonance frequency ω_e from its original (low power) position $\omega_{e,0}$ as a function of P_p is plotted in Fig. 5.2b and the increase in $\kappa_{e,\text{in}}$ is shown in Fig. 5.2c. The parameters change slowly with P_p until a phase transition happens around $P_p \sim 700 \text{ mW}$ when aluminium loses its superconductivity. Thereafter, the parameters seem to stop changing. We note that aluminium loses its superconductivity at a threshold temperature of 1.2 K and as shown in Fig. 5.2d, the mixing chamber temperature is still well below this threshold when the loss in

superconductivity happens. This is a proof that the microwave cavity suffers from local heating from the high power optics. Since aluminium is a bad conductor of heat in its superconducting state, it is difficult to dissipate this heat to the mixing chamber.

5.5 4-port calibration

The best way to calibrate the device's total transduction efficiency independent of the involved signal losses/gains of the setup is through a 4-port calibration. For this, we treat the device as a simple 4-port device - input optics, output optics, input microwave and output microwave (see Fig. 5.3). Thereafter, we define the various loss/gain from the 4 device ports to the 4 experimentally accessible ports via instruments such as VNA. β_1 and β_2 describe the attenuation/gain in the optical input and output path respectively. β_3 and β_4 describe the same for the microwave input and output port. η_{eo} and η_{oe} describe the total (*i.e.*, including the waveguide to resonator coupling losses) optics to microwave and microwave to optics conversion efficiency of the device.

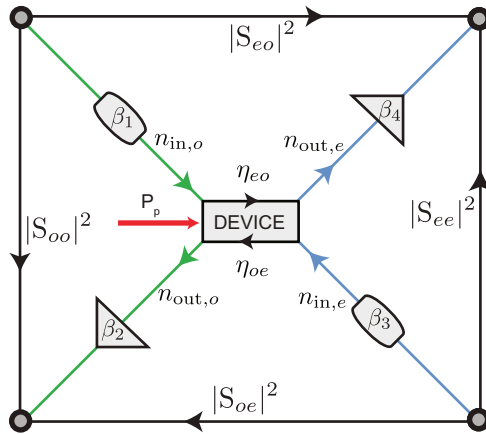


Figure 5.3: Four port calibration. Figure adapted from Ref. [HRS⁺20].

The 4 scattering parameters $|S_{ij}|^2 = |\frac{\hat{a}_{out,i}}{\hat{a}_{in,j}}|^2$, where \hat{a} represents a propagating mode, can be independently measured. $|S_{oo}|^2$ is the optical reflection spectrum and $|S_{oo}|^2(\Delta\omega) = \beta_1\beta_2$ when measured off-resonance, similarly $|S_{ee}|^2(\Delta\omega) = \beta_3\beta_4$ is the microwave reflection off-resonance and $|S_{eo}|^2(\omega_0) = \beta_1\beta_4\eta_{eo}$ and $|S_{oe}|^2(\omega_0) = \beta_2\beta_3\eta_{oe}$ is the measured conversion from optics to microwave and from microwave to optics on-resonance respectively. Assuming, $\eta_{oe} = \eta_{eo}$, the total conversion efficiency $\eta_{tot} = \sqrt{\eta_{oe}\eta_{eo}}$ is calculated as,

$$\eta_{tot} = \sqrt{\frac{|S_{oe}|^2(\omega_0) \cdot |S_{eo}|^2(\omega_0)}{|S_{oo}|^2(\Delta\omega) \cdot |S_{ee}|^2(\Delta\omega)}} \quad (5.3)$$

This calculation is independent of all the losses/gains of all the ports and thus provides a *in-situ* calibrated device conversion efficiency. Note that it is necessary to calculate the reflected power $|S_{oo}|^2$ and $|S_{ee}|^2$ off-resonance. This is because we need the total loss or gain of the whole input and detection chain combined for the case of no cavity interaction.

After calculating the η_{tot} and with the knowledge of one of the β_i parameter, all the other parameters are possible to calculate from the 4 measurements made. For this experiment, we independently measured the output microwave gain β_4 by measuring the output noise from a 50Ω load as a function of its temperature (see appendix B). Finally, we determined all the

β_i parameters - $\beta_1 = -4.81$ dB, $\beta_2 = -5.5$ dB (without EDFA), $\beta_2 = 30.8$ dB (with EDFA), $\beta_3 = -74.92$ dB and $\beta_4 = 67.05$ dB.

5.6 Transduction measurements

An optical pump is locked to ω_p with power P_p and applied to the optical cavity. The different scattering parameters $|S_{eo}|^2$ and $|S_{oe}|^2$ are then measured by sending the corresponding coherent signal and measuring the narrow-band, peak, coherent optical output power on the optical SA (OSA) and the same for microwave on SA. Example measurements of the converted power are shown in Fig. 5.4. The measured optical output shown in Fig. 5.4a shows that both optical sidebands are present around the pump. However, the Stokes sideband power is suppressed by a suppression ratio SR = 10.7 dB because of the hybridization of the optical Stokes mode as shown in Fig. 5.1. The microwave transduction measurement is shown in Fig. 5.4b. The optical to microwave conversion is shown with $P_p = 2.35$ μ W and optical signal power of only 161 nW referred to device ports. This corresponds to the generation of $n_e = 1.2$ intracavity microwave photons which is the center peak in the figure. The broadband Lorentzian output is the added thermal noise corresponding to the output photon flux of 0.4 photons $s^{-1}Hz^{-1}$. Thermal noise output is discussed in more details later in this chapter.

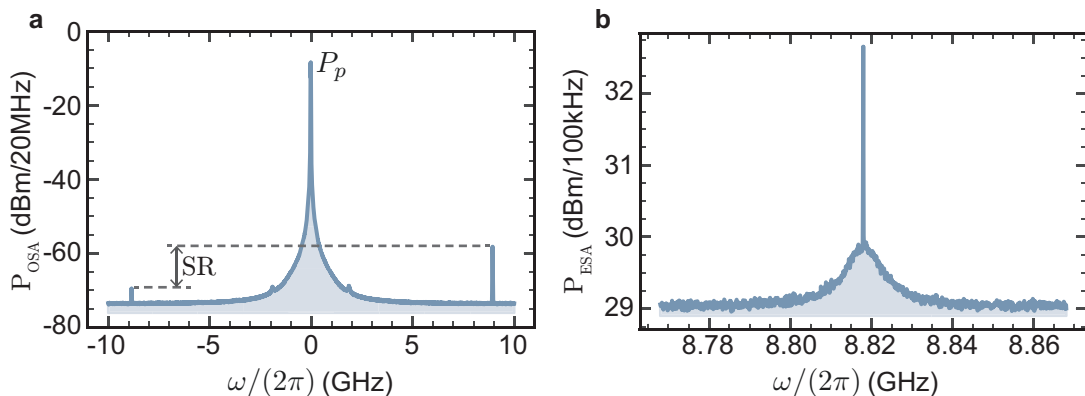


Figure 5.4: **a** (**b**) Microwave to optics (optics to microwave) transduction measurement in the frequency domain measured using the SAs. Figure adapted from Ref. [HRS⁺20].

Measuring the transduction parameters, the calibrated transduction efficiency is calculated as described in section 5.5. This calibrated transduction efficiency is shown in Fig. 5.5a as a function of the optical pump power P_p . The blue points show the measured total conversion efficiency η_{tot} and the orange points show $\eta_{int} = \eta_{tot}/(\eta_e\eta_o)$. The highest η_{tot} measured is 3.16×10^{-4} for $P_p = 1.48$ mW. A black arrow at around $P_p = 700$ μ W marks a sudden drop in η_{tot} . This drop happens because of sudden loss in superconductivity of aluminium due to excess optical heating as discussed in section 5.4. The loss of superconductivity results in a sudden increase of the microwave linewidth which reduces the cooperativity and thus the conversion efficiency for the same optical pump power P_p .

For the optical pump powers we applied, we expect $C \ll 1$ and thus η_{tot} to be linearly proportional to C . This is clearly observed in the Fig. 5.5a. We fit the curve with a linear function² (shown in grey dashed lines) and extract the cooperativities we measured in the range from $C = 3.24 \times 10^{-7}$ for the lowest pump power to $C = 1.68 \times 10^{-3}$ for the highest. The fit vacuum coupling constant $g_0/(2\pi) = 40$ Hz. From the Table 3.1 at low temperature

²Cooperatively C is linearly proportional to the pump power P_p .

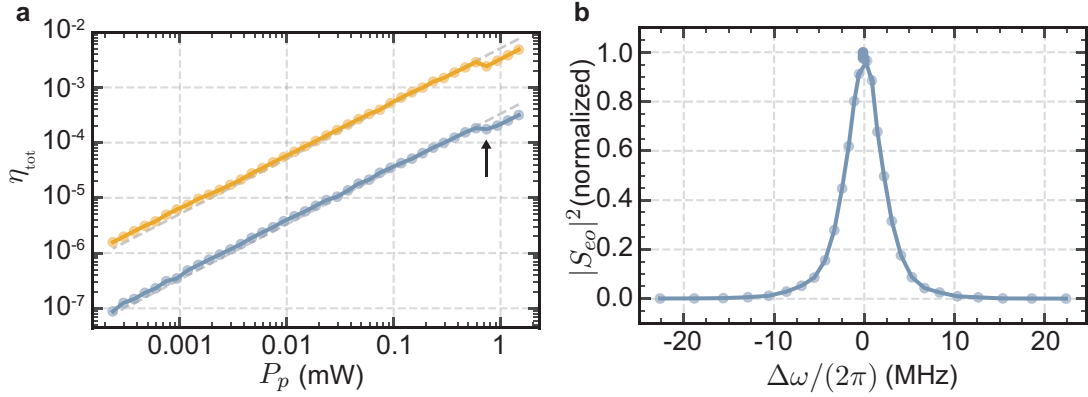


Figure 5.5: **a** Calibrated total (internal) conversion efficiency in blue (orange) as a function of optical pump power P_p . **b** Bandwidth of conversion measured by sweeping the optical signal frequency and measuring the converted microwave signal. Figure adapted from Ref. [HRS⁺20].

for a similar gap of about $1\mu\text{m}$ and around the frequency of optical FSR, we expect a $g_0/(2\pi) > 39\text{ Hz}$, which is in excellent agreement with the measured value of 40 Hz .

Until now, we have reported the transduction efficiency at the mode resonances. However, transduction happens also off-resonance albeit at a lower efficiency. To measure off-resonance transduction, we applied the coherent signal to be transduced slightly off-resonance from the signal mode resonance (the optical pump stays on resonance). The transduction efficiency is, then, plotted as a function of the off-resonance detuning $\Delta\omega$ as shown in Fig. 5.5b for optics to microwave conversion. The solid curve is the theoretical expectation $C \ll 1$ given by [Tsa11],

$$\frac{|S_{ij}(\Delta\omega)|^2}{|S_{ij}(\Delta\omega = 0)|^2} = \left(\left(1 - \frac{4(\Delta\omega)^2}{\kappa_o \kappa_e} \right)^2 + \frac{4(\Delta\omega)^2 (\kappa_o + \kappa_e)^2}{\kappa_o^2 \kappa_e^2} \right)^{-1} \quad (5.4)$$

We fit the FWHM of bandwidth $B/(2\pi) = 9.0\text{ MHz}$ for $P_p = 18.7\mu\text{W}$. The bandwidth of transduction depends on the linewidths of the microwave and optical cavities. In our case, the linewidth of the microwave cavity κ_e increases with the optical pump power due to increased internal microwave losses due to optical heating (as discussed in section 5.4). As a result, the bandwidth increases from 8.51 MHz (corresponding to $\kappa_e = 10.45\text{ MHz}$) for the lowest pump power to 10.68 MHz (corresponding to $\kappa_e = 14.85\text{ MHz}$) for the highest pump power.

5.7 Added noise

Transduction of a quantum state from one frequency to another is not useful when it is accompanied by a lot of noise. Thus, it is imperative to carefully study the noise characteristics of the transducer device. There are two major sources of noise. Firstly, the optical pump heats the dielectric due to absorption of photons, in turn, also thermally heating the microwave cavity walls which are in contact. This is the direct thermal heating. Additionally, there is stray light that can also break the cooper pairs in the superconducting microwave cavity producing quasi-particles. Both thermal heating and quasi-particles are responsible for increased surface resistance that increase the internal losses of the microwave cavity $\kappa_{e,\text{in}}$ as we already saw in section 5.4).

The microwave cavity is coupled to two thermal baths - the surrounding thermal bath at \bar{n}_b which couples via $\kappa_{e,\text{in}}$ and the thermal occupancy of waveguide \bar{n}_{wg} which couples via $\kappa_{e,\text{ex}}$.

The thermal occupancy of the microwave mode is, then, calculated as,

$$\bar{n}_e = \eta_e \bar{n}_{wg} + (1 - \eta_e) \bar{n}_b \quad (5.5)$$

The detected noise spectrum $N_{\text{det}}(\omega)$ is a Lorentzian noise spectrum and a function of \bar{n}_b and \bar{n}_{wg} ,

$$N_{\text{det}}(\omega) = \frac{4\kappa_{e,\text{in}}\kappa_{e,\text{ex}}}{\kappa_e^2 + 4\omega^2} (\bar{n}_b - \bar{n}_{wg}) + \bar{n}_{wg} + N_{\text{sys}} \quad (5.6)$$

where, $N_{\text{sys}} = 12.74 \pm 0.36$ is the broadband noise added by the detection chain amplifiers and losses (see appendix B). We calibrate the N_{sys} together with the microwave output gain β_4 by measuring the noise output from the microwave cavity when it is well thermalized to millikelvin temperature (see appendix B). At this point, when $\bar{n}_b = \bar{n}_{wg} = 0$, the detected noise $N_{\text{det}} = N_{\text{sys}}$ and thus, the detected power from the SA P_{ESA} as $N_{\text{det}} = P_{\text{ESA}}/(\hbar\omega_e\beta_4)$ can be calibrated using known value of N_{sys} . Finally, N_{out} is defined as $N_{\text{out}} = N_{\text{det}} - N_{\text{sys}}$.

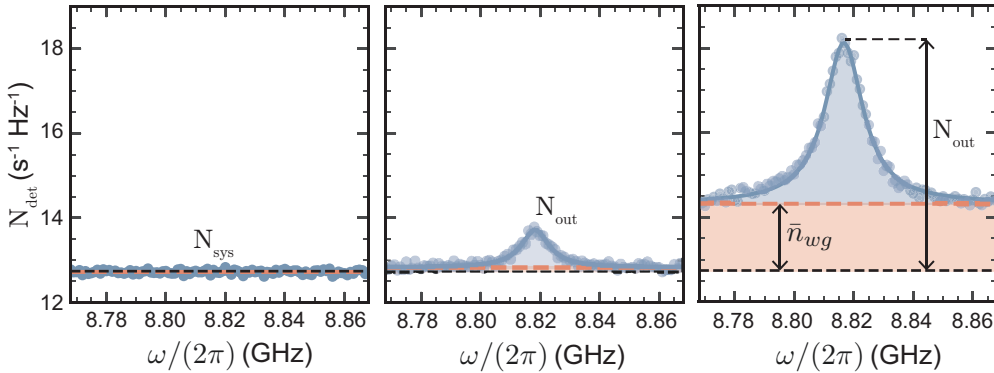


Figure 5.6: Measured output microwave noise spectra for $P_p = 0.23 \mu\text{W}$, $P_p = 14.82 \mu\text{W}$ and $P_p = 1.48 \text{mW}$ shown left to right. Figure adapted from Ref. [HRS⁺20].

Output microwave noise spectra, normalised with the baseline when there is no optical pump power $N_{\text{det}} = N_{\text{sys}}P_{\text{ESA}}/P_{\text{ESA},P_p=0}$, is shown in Fig. 5.6. The N_{sys} is plotted with black dashed lines and broad \bar{n}_{wg} with dashed red line. The solid blue line represents a fit to the Eqn. 5.6. The left most spectra is plotted for $P_p = 0.23 \mu\text{W}$ where extra noise from N_{sys} is barely discernible. The middle output spectra shows $N_{\text{out}} = 1.01 \pm 0.07$ for an intermediate $P_p = 14.82 \mu\text{W}$. Finally, in the right most panel, a clear distinction between $\bar{n}_{wg} = 0.13 \pm 0.04$ and $N_{\text{out}} = 5.51 \pm 0.20$ is seen. Note that for the right most panel, the mixing chamber temperature T_f corresponds to only $\bar{n}_f = 0.36$ photons at the microwave cavity frequency which is significantly cooler than the microwave cavity output showing the huge divide between local microwave cavity temperature compared to the mixing chamber temperature.

The full dependence of N_{out} (blue), \bar{n}_{wg} (red), \bar{n}_b (yellow) and \bar{n}_e (green) as a function of the optical pump power is shown in Fig. 5.7. Sub-photon microwave output noise as low as $N_{\text{out}} = 0.03^{+0.04}_{-0.03}$ and microwave mode occupancies as low as $\bar{n}_e = 0.025 \pm 0.005$ are achieved for a continuous wave pump power of $P_p = 0.59 \mu\text{W}$ where the total conversion efficiency is $\eta_{\text{tot}} = 2.3 \times 10^{-7}$.

All the noise metrics increase with the optical pump power. \bar{n}_b always stays more than \bar{n}_{wg} since the heating is local and the microwave cable is better thermalized with the dilution refrigerator. The noise metric increases smoothly and almost linearly in the beginning until the point marked by a black arrow. Around this point, the superconductivity of the aluminium breaks suddenly increasing the internal losses of the microwave cavity which reduces the N_{out} .

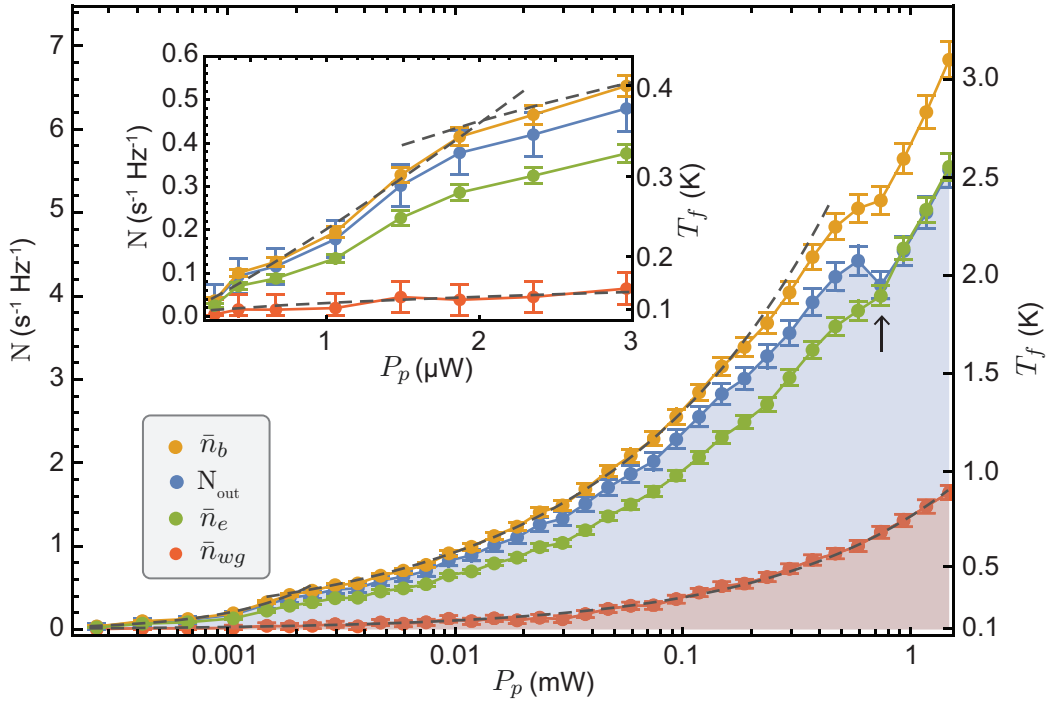


Figure 5.7: Frequency domain microwave noise characterization Microwave noise characteristics as a function of the optical pump power P_p . The black arrow marks the superconducting phase transition. The dashed gray lines indicate fitted power laws, specifically $\bar{n}_{wg} \propto P_p^{0.55}$ over the full range of powers, $\bar{n}_b \propto P_p^{1.14}$ up to $P_p \approx 2 \mu\text{W}$ (see inset), and $\bar{n}_b \propto P_p^{0.45}$ at higher powers. The error bars represent the 2σ fit error to Eqn. 5.6. Figure adapted from Ref. [HRS⁺20].

Also, at this point a slower temporary increase in \bar{n}_b is observed indicating that thermalization of the microwave cavity to the mixing chamber has improved further confirming that the aluminium microwave cavity has undergone a phase transition.

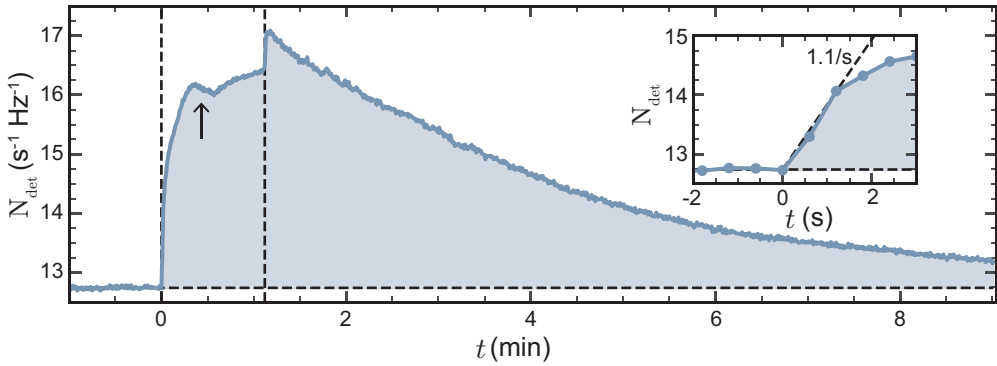


Figure 5.8: Time domain microwave noise characterization Microwave output noise measured at resonance with a 500 kHz resolution bandwidth where the optical pump tone with $P_p = 1.48 \text{ mW}$ is turned on at $t = 0$ for 1 minute. The inset shows the fastest heating rate of $1.1 \text{ photons s}^{-1}$. Figure adapted from Ref. [HRS⁺20].

Finally, we also study the time dynamics of the noise output. We measure the noise output from the microwave cavity at its resonance (500 kHz resolution bandwidth) as a function of time as shown in Fig. 5.8. At $t = 0$, we turn on the optical pump with $P_p = 1.48 \text{ mW}$ for 1 min (marked by vertical dashed lines). The output noise increases sharply as a result of

optical heating. In the inset, we see the fastest rate is only about $1.1 \text{ photons s}^{-1}$ which is seen in the very beginning. About 30 s in, we see the point where the superconductivity breaks (marked by black arrow) and noise output drops shortly before beginning to climb again. This process is promptly reversed when the light is turned off at the second vertical dashed line and the output noise increases sharply again (this is because as the superconductivity comes back, the internal losses decrease, increasing the coupling efficiency of the cavity quickly and, as a result, the output noise increases sharply as more thermal noise from the cavity couples out). Thereafter, we see the slow cooling via thermalization of the microwave cavity with the dilution refrigerator bath. Cooling back to ground state takes at least 1 hour.

5.8 Conclusions

With the experiments presented in this chapter, we prove that the electro-optic interaction between the modes can be observed. We successfully measure bidirectional conversion between the microwave and the anti-Stokes optical mode. We show this transduction process while the microwave mode is deep in its quantum ground state $\bar{n}_e = 0.025 \pm 0.005$ albeit with a small transduction efficiency of $\eta_{\text{tot}} \sim 10^{-7}$. This is the main gripe with the results presented in this chapter.

Conversion efficiencies can be increased by pumping the optical resonator with more optical power but we already saw that this solution quickly heats up the system to $\bar{n}_e \gg 1$. Also, to reach anywhere close $C = 1$, we need $\sim 100 \text{ mW}$ of optical pump power which is a rather unrealistic amount of power to be sent to the dilution refrigerator. It may seem that the only way out of this situation is to increase either coupling constant g_0 or drastically increase the mode quality factors of the microwave and optical cavities.

There is, however, a silver lining. Studying the output microwave noise as a function of time, we see that the microwave cavity heating rate is quite slow owing to its macroscopic size. The highest rate we saw was about $1.1 \text{ photons s}^{-1}$. This can seem quite high at first glance but given that our transducer has a bandwidth of $\sim 10 \text{ MHz}$, it can work with coherent signal pulses of length $\sim 100 \text{ ns}$. Given the rate at which the system heats up, we can expect almost negligible heating at such timescales and that any thermal heating would depend only on the average amount of optical pump power which would be directly related to the duty cycle of pulses being used. As a result, it seems by using an optical pump which is pulsed, we can get good conversion efficiencies while keeping the microwave cavity close to its ground state. These experiments with pulsed optics are discussed in the next chapters.

6 | CHAPTER

Low cooperativity pulsed transduction

6.1 Introduction

In the last chapter, it was concluded that using a pulsed optical pump approach could be useful to control the microwave heating due to optics while maintaining the same cooperativity. However, switching to a pulsed approach comes with a lot of associated challenges and new concepts that need to be understood.

In this chapter, we discuss the new changes that come along with using pulses instead of continuous wave sources. One of the most important of these changes is characterization of the single port cavities in time domain. We will also discuss the new experimental setup changes and related issues. Finally, we will study transduction with pulsed signals and ensure that we can still maintain phase faithfulness during transduction in this pulsed regime.

Acknowledgements This chapter is based on the work presented in Ref. [SHR⁺22]. Figure credits have been individually given in the figure captions.

6.2 Experimental setup

In this chapter, we do not yet pulse the optical pump rather we only pulse the coherent signals sent to the signal optical and microwave modes. The digital TTL pulse signal is produced by a digital delay generator (DDG). In this setup, we combine the optical pump with the optical signal to maintain phase stability between the optical pump and signal. The optical signal is still produced using the optical SSB which can be pulsed by pulsing the microwave source generating the sideband. But, in this case, we do not suppress the central carrier tone of the SSB which acts as the optical pump here. The local oscillator (LO) for optics is also produced via the optical SSB by combining the RF tone for the optical LO and signal before sending it to SSB. The final output from the optical SSB is amplified via the EDFA before sending to the dilution refrigerator. The microwave signal is pulsed via the microwave signal source.

The optics after the dilution refrigerator is detected with a fast photodetector (400 MHz bandwidth). The optical LO and signal are detuned by 200 MHz and the produced beating signal is detected with a fast photodetector. The beating signal is amplified one more time via an RF amplifier before digitization with a digitizer at 1 Giga-samples/s. The microwave LO is

also 200 MHz detuned from the microwave signal. Their beating signal is also digitized by the same digitizer. The final downconversion from 200 MHz to DC is done digitally.

Laser lock is same as in chapter 5 since the optical pump is still CW. The full setup is discussed in detail in appendix C.

6.3 Setup characterization

We start with characterizing the pulsing equipment. The TTL signal from the DDG rises from 10% of the max value to 90% of the max value in ~ 5 ns. The same rise time for the optical signal from the optical SSB is measured to be ~ 15 ns. The microwave pulsed signal is produced directly from the microwave source (SGMA100A) and has a rise time of ~ 5 ns.

Sending a pulsed signal to a single port cavity has a specific reflected shape which is completely characterized by the cavity parameters such as linewidth and coupling efficiency. Consequently, we can now independently characterize the optical and microwave modes both in the time and frequency domain. Characterization of the modes in frequency domain is already described in detail in chapter 3.

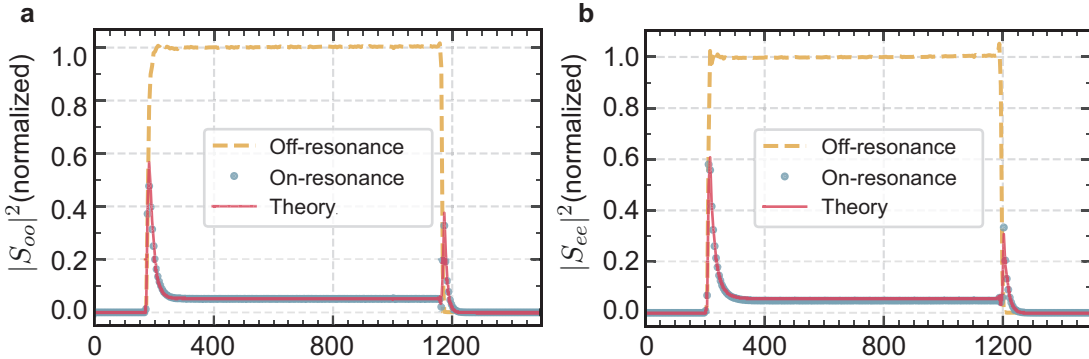


Figure 6.1: **Time domain system characterization for low cooperativity measurements.** **a (b)**, Normalized pulse reflection of a square pulse from the optical (microwave) cavity on and off resonance. The red curve is a theoretical fit obtained using time domain input-output theory. Figure adapted from Ref. [SHR⁺22].

Supplementary Fig. 6.1 shows the time domain characterization of the optics and microwave modes by sending a square pulse of a coherent tone to the cavity on and off resonance. The off resonant pulse reflects without any modifications and, thus, is used as a measurement of the input pulse shape (yellow dashed line). The shape of reflected pulse on resonance is calculated by solving the following equations for the time dynamics,

$$\dot{\bar{a}}_i = -\frac{\kappa_i}{2}\bar{a}_i - i\Delta_i\bar{a}_i + \sqrt{\kappa_{i,\text{ex}}}\bar{F}_i \quad (6.1a)$$

$$\bar{a}_{i,\text{out}} = \sqrt{\kappa_{i,\text{ex}}}\bar{a}_i - \bar{F}_i \quad (6.1b)$$

where $i \in \{o, e\}$ stands for both optics and microwave modes and Δ_i is the detuning between pump \bar{F}_i and mode resonance. In case of optics, one must take care of mode mismatch factor Λ by replacing $\sqrt{\kappa_{o,\text{ex}}} \rightarrow \Lambda\sqrt{\kappa_{o,\text{ex}}}$. The time dependence of the variables is suppressed in the equations. Nevertheless, the time dependent pump is inserted through $\bar{F}_i(t) = \sqrt{P_i(t)/(\hbar\omega_i)}$. The equations are solved numerically by using Euler's method. Reflected power on resonance is finally calculated as $|\bar{a}_{i,\text{out}}|^2$.

The reflected pulse on-resonance (from Fig. 6.1) is fit with the calculated reflected power where the off-resonance reflection is used as the pump shape. The fitted system parameters are shown in Supplementary Tab. 6.1. The parameters fully agree with those determined by frequency domain characterization except for the optical mode matching factor, Λ , which was determined to be 0.806 from the frequency domain characterization and 0.838 from the time domain characterization. We use the value obtained from time domain characterization which we believe is more accurate and directly applicable to the time domain conversion measurements.

Parameter	Description	Value
$\omega_o/2\pi$	Optical signal frequency	193 THz
$\kappa_o/2\pi$	Optical signal linewidth	15.55 MHz
η_o	Optical coupling efficiency	0.55
Λ	Optical mode mismatch factor	0.838
$\omega_e/2\pi$	Microwave mode frequency	8.803 GHz
$\kappa_e/2\pi$	Microwave signal linewidth	12.12 MHz
η_e	Microwave coupling efficiency	0.369
$g_0/2\pi$	Electro-optic coupling rate	37 Hz

Table 6.1: System parameters for low cooperativity measurements.

The shape of reflected pulse on resonance in Supplementary Fig. 6.1 is interesting to understand in more detail. The first peak occurs due to the rapid rise time of the input pulse which has much higher bandwidth than the cavity. Thus, most of it gets reflected before the cavity has the chance to accept any part of the input power. The initial peak is interrupted as the cavity gets the time to accept the input light (time taken is on the order of total linewidth of the cavity). It then starts re-emitting that light to cancel the input pulse reflection. This continues until a steady state is reached.

At the end of the input pulse, the input power drops much faster than the cavity bandwidth. As a result, the input power gets depleted while the cavity still full of intra-cavity photons. In this time, photon emission from the cavity does not get time to change much. As the input power drops, there is a moment when the cavity emission perfectly cancels out the input reflection leading to a point of zero reflection (more clearly seen for shorter pulses, see characterization in chapter 7). As the input power drops further, the emission from the cavity takes over and the reflected power rises again. Finally, only the emission from the cavity is left which slowly decays with a timescale corresponding to the cavity linewidth.

Note that this pulse shape, where the point of zero reflection happens towards the end, is only true for cavities that are undercoupled. This means that in the beginning of the pulse, the cavity emission was not able to overcome the input pulse reflection. This is the expectation from undercoupled cavities in steady state. For critically coupled cavities, the cavity emission matches the input power reflection, hence, the steady state would be the point of zero reflection. For overcoupled cavities, the cavity emission is more than the input power reflection in steady state and thus the point of zero reflection must already occur towards the beginning of the pulse. With this knowledge, we can verify the coupling efficiency (undercoupled or overcoupled) of the cavity with just power measurements. This remains ambiguous in frequency domain measurements until phase of reflected pulse is measured.

Intuitively, this advantage of time-domain measurements over the frequency-domain measurements can be understood as a pseudo-sweep of κ_{ex} by using a pulse to characterize the cavity rather than a continuous tone. For this pseudo-sweep to be most apparent, one must use an input pulse which has the rise time on the same order as the linewidth of the cavity being characterized and measure with a time resolution higher than these bandwidths.

In this chapter, we do not characterize the mode hybridization for the optics Stokes mode since, for low cooperativities, the full interaction is approximately reduced to just the simple 3-mode beam-splitter like interaction where only the TM coupling is irrelevant.

6.4 Low cooperativity conversion

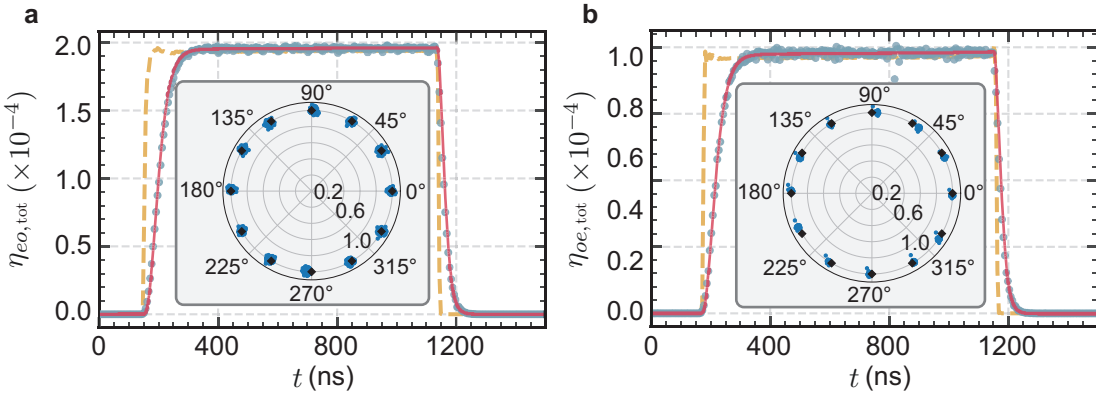


Figure 6.2: **Bidirectional conversion measurements for low cooperativity** **a** (**b**), Optics-to-microwave (microwave-to-optics) conversion for a continuous wave optical pump of $P_p = 134 \mu\text{W}$. The measured input signal pulses are shown with dashed yellow lines and the converted signals with blue dots (red line is theory). Phase coherence and stability of the signal phase is shown in the insets. Rhombuses represent the phase imprinted on the input signal and the blue points represent phase values extracted from subsequently measured converted pulses. Figure adapted from Ref. [SHR⁺22].

Figure 6.2(a) and (b) shows the calibrated time dependent measurement of a converted signal pulse in case of microwave-to-optics and optics-to-microwave conversion, respectively. These pulses are measured with a bandwidth of 200 MHz and shown together with a fit to the numerical model (red line) that takes the measured input pulses (yellow dashed lines) with a rise time of 15 ns and 5 ns respectively as input data along with system characteristics from Table 6.1. We find excellent agreement of all four time dependent scattering parameters using only one fit parameter, the input optical loss. The 10% to 90% rise time of the converted pulses in both directions of 85 ns is limited by the linewidths of the optical and microwave modes in this case of comparably low cooperativity $C = 3.4 \times 10^{-4}$. In chapter 7, we will see that this rise time will change in case of higher cooperativities when the conversion rate becomes comparable to the loss rates of the cavities.

Moreover, we also explicitly verify the faithful phase control and stability over subsequent pulses in both directions. For these measurements, we sweep the phase imprinted on the input signal pulses that need to be converted via the RF sources which produce the signal and measure the phase of the transduced signals. The measured phase along with the sent phase is shown in the insets of Fig. 6.2. The first measurement is set to zero phase and all the consequent measurements are then at 45° difference. We see that the measured phase is in excellent

agreement with the imprinted phase on input signal. This verifies that the transduction is phase-faithful.

Note that for the low cooperativity measurements, we choose to keep the optical pump, signal and LO in the same fiber from creation till detection. This ensures phase stability up to a minute. Taking advantage of the phase stability, we average the amplitudes of the extracted quadratures from digital downconversion rather than averaging the power. Averaging the amplitude provides better signal to noise ratio (SNR) with fewer averages than averaging the power (only while measuring coherent signals). Averaging the amplitudes is effectively equivalent to measuring longer. In other words, the bandwidth of measurement becomes smaller with the number of averages, equivalent to total time of amplitude averages (which scales linearly with number of averages). For coherent signals with small bandwidth, this improves the SNR as the bandwidth of the measurement gets smaller¹.

6.5 Conclusions

In this chapter, we introduce the pulsed measurements and confirm that conversion time scales are limited by loss rates of the cavities as expected. We also verify that the transduction is faithful in time domain. More importantly, we see time-domain characterization of single-port cavities which matches excellently with the frequency-domain characterizations. Equipped with this knowledge, we are now ready to look into measurements with a pulsed optical pump and higher cooperativities.

¹For broadband signal on broadband noise, it is best to match the measurement bandwidth to the signal bandwidth to get the best time resolution without losing a lot of SNR, as we will do in the noise measurements of chapter 7.

7 CHAPTER

High cooperativity pulsed transduction

7.1 Introduction

In this chapter, we use short ~ 100 ns optical pump pulses produced via acousto-optical modulators (AOMs) with high peak pulse power ~ 100 mW. The major experimental breakthrough which allowed us to achieve such high powers was using the EDFA with a pulsed input optical power. This is discussed in detail in this chapter. The achieved higher optical powers allow for cooperativities on the order of unity. In this regime, the conversion rate is on the order of the loss rates of the cavities making the time dynamics between the modes very interesting. We explore all the new effects and explain them in detail.

One of the more interesting parts of the chapter is, nevertheless, the noise output as a function of cooperativity. We see a myriad of new effects when exploring the noise output in frequency and time domain. On the microwave side, we observe the electro-optic cooling of the microwave mode and amplification of vacuum noise. On the optics side, we measure finite output noise which was transduced from the microwave domain.

With high cooperativity, the interaction of the microwave mode with the Stokes optical mode, even though suppressed, becomes important. We see the effects of amplification and divergence from the simple beam-splitter model. As a result, we use a more comprehensive five-mode model which includes the optical Stokes mode along with the optical TM mode which hybridises it.

Note that in this chapter, we refer to the optical anti-Stokes mode \hat{a}_t as the optical signal mode \hat{a}_o . Hence, in this chapter, \hat{a}_t and \hat{a}_o are equivalent.

Acknowledgements This chapter is based on the work presented in Ref. [SHR⁺22]. I would like to thank Liu Qiu for his contribution in writing the theory section which has been adapted in this chapter. Figure credits have been individually given in the figure captions.

7.2 The five mode model

In this chapter, we need to consider the interaction of the microwave mode \hat{a}_e with both the optical sidebands $\hat{a}_t \equiv \hat{a}_o$ and \hat{a}_s . The Stokes sideband is suppressed with the TM mode \hat{a}_{sm}

which is coupled to \hat{a}_s with a coupling rate J . Along with the optical pump mode \hat{a}_p , the full interaction Hamiltonian for our system is given by five total modes interacting with each other,

$$\hat{H}_{\text{int}} = \hbar g_0 (\hat{a}_e \hat{a}_p \hat{a}_o^\dagger + \hat{a}_e^\dagger \hat{a}_p \hat{a}_o) + iJ \hat{a}_s^\dagger \hat{a}_{sm} + \text{h.c.} \quad (7.1)$$

All the mode interactions are shown in Fig. 7.1.

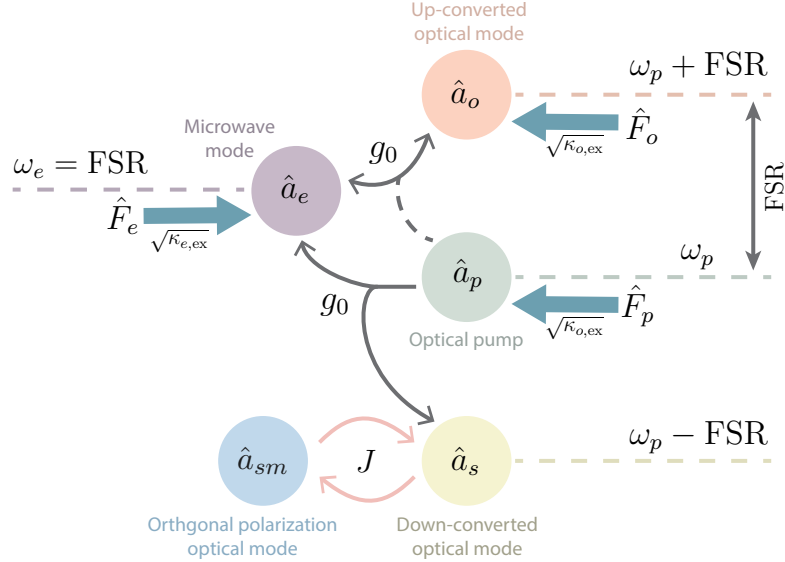


Figure 7.1: The 5 participating modes and their interactions. Figure adapted from Ref. [SHR²²].

7.2.1 Equations of motion

The time dynamics of these operators is derived using the Heisenberg equations of motion. The resulting system of equations is the following:

$$\dot{\hat{a}}_p = -i\Delta_p \hat{a}_p - \frac{\kappa_o}{2} \hat{a}_p - ig_0 (\hat{a}_s \hat{a}_e + \hat{a}_e^\dagger \hat{a}_o) + \Lambda \sqrt{\kappa_{o,\text{ex}}} \bar{F}_p + \sqrt{\kappa_{o,\text{in}}} \delta \hat{a}_{p,\text{in}} \quad (7.2a)$$

$$\dot{\hat{a}}_o = -i\Delta_o \hat{a}_o - \frac{\kappa_o}{2} \hat{a}_o - ig_0 \hat{a}_p \hat{a}_e + \Lambda \sqrt{\kappa_{o,\text{ex}}} \bar{F}_o + \sqrt{\kappa_{o,\text{ex}}} \delta \hat{a}_{o,\text{ex}} + \sqrt{\kappa_{o,\text{in}}} \delta \hat{a}_{o,\text{in}}, \quad (7.2b)$$

$$\dot{\hat{a}}_s = -i\Delta_s \hat{a}_s - \frac{\kappa_o}{2} \hat{a}_s - ig_0 \hat{a}_p \hat{a}_e^\dagger - iJ \hat{a}_{sm} + \sqrt{\kappa_{o,\text{ex}}} \delta \hat{a}_{s,\text{ex}} + \sqrt{\kappa_{o,\text{in}}} \delta \hat{a}_{s,\text{in}}, \quad (7.2c)$$

$$\dot{\hat{a}}_e = -i\Delta_e \hat{a}_e - \frac{\kappa_e}{2} \hat{a}_e - ig_0 \hat{a}_p \hat{a}_s^\dagger - ig_0 \hat{a}_p^\dagger \hat{a}_o + \sqrt{\kappa_{e,\text{ex}}} \bar{F}_e + \sqrt{\kappa_{e,\text{ex}}} \delta \hat{a}_{e,\text{ex}} + \sqrt{\kappa_{e,\text{in}}} \delta \hat{a}_{e,\text{in}}, \quad (7.2d)$$

$$\dot{\hat{a}}_{sm} = -i\Delta_{sm} \hat{a}_{sm} - \frac{\kappa_{sm}}{2} \hat{a}_{sm} - iJ \hat{a}_s + \sqrt{\kappa_{sm}} \delta \hat{a}_{sm,\text{in}}. \quad (7.2e)$$

Here, κ_j , $\kappa_{j,\text{ex}}$ and $\kappa_{j,\text{in}}$ are the total, extrinsic and intrinsic loss rates of respective modes, Δ_j are the detuning of the mode annihilation operators from their respective resonance frequencies, \bar{F}_j are the coherent drive terms given by $|\bar{F}_j| = \sqrt{P_j/\hbar\omega_j}$ and $\delta \hat{a}_{j,\text{in}}$ and $\delta \hat{a}_{j,\text{ex}}$ represent the Langevin noise operators for bath and waveguide respectively. The noise operators follow the following correlations

$$\langle \delta \hat{a}_{j,k}(t) \delta \hat{a}_{j,k}(t')^\dagger \rangle = (\bar{n}_k + 1) \delta(t - t'), \quad (7.3a)$$

$$\langle \delta \hat{a}_{j,k}(t)^\dagger \delta \hat{a}_{j,k}(t') \rangle = \bar{n}_k \delta(t - t'), \quad (7.3b)$$

where $k \in (\text{in}, \text{ex})$. For optics, both $\bar{n}_{\text{in}} = 0$ and $\bar{n}_{\text{ex}} = 0$, while for microwave, $\bar{n}_{\text{in}} = \bar{n}_b$ and $\bar{n}_{\text{ex}} = \bar{n}_{\text{wg}}$.

7.2.2 Coherent time-domain dynamics

We first focus on the coherent time domain dynamics. By linearizing the intra-cavity field for the modes $\hat{a}_j = \bar{a}_j + \delta\hat{a}_j$, with \bar{a}_j being the coherent field amplitude and $\delta\hat{a}_j$ the field fluctuations, we obtain the following coherent dynamics for the optical and microwave modes:

$$\dot{\bar{a}}_p = -i\Delta_p\bar{a}_p - \frac{\kappa_o}{2}\bar{a}_p - ig_0(\bar{a}_s\bar{a}_e + \bar{a}_e^*\bar{a}_o) + \Lambda\sqrt{\kappa_{o,\text{ex}}}\bar{F}_p, \quad (7.4a)$$

$$\dot{\bar{a}}_o = -i\Delta_o\bar{a}_o - \frac{\kappa_o}{2}\bar{a}_o - ig_0\bar{a}_p\bar{a}_e + \Lambda\sqrt{\kappa_{o,\text{ex}}}\bar{F}_o, \quad (7.4b)$$

$$\dot{\bar{a}}_s = -i\Delta_s\bar{a}_s - \frac{\kappa_o}{2}\bar{a}_s - ig_0\bar{a}_p\bar{a}_e^* - iJ\bar{a}_{sm}, \quad (7.4c)$$

$$\dot{\bar{a}}_e = -i\Delta_e\bar{a}_e - \frac{\kappa_e}{2}\bar{a}_e - ig_0\bar{a}_p\bar{a}_s^* - ig_0\bar{a}_p^*\bar{a}_o + \sqrt{\kappa_{e,\text{ex}}}\bar{F}_e, \quad (7.4d)$$

$$\dot{\bar{a}}_{sm} = -i\Delta_r\bar{a}_{sm} - \frac{\kappa_{sm}}{2}\bar{a}_{sm} - iJ\bar{a}_s. \quad (7.4e)$$

The output fields are then calculated as $\bar{a}_{e,\text{out}} = \sqrt{\kappa_{e,\text{ex}}}\bar{a}_e - \bar{F}_e$ for the microwave mode and $\bar{a}_{o,\text{out}} = \Lambda\sqrt{\kappa_{o,\text{ex}}}\bar{a}_o - \bar{F}_o$ for the upconverted optics mode. The above system of equations are numerically solved in the time domain using Euler's method. We use this method to model the classical time-dynamics of the system with arbitrary coherent pump pulses. The results of this numerical simulations will be used as theory in the next sections of this chapter.

7.2.3 Steady state model

The steady state for the time dynamics in eqns. 7.2 is solved similar to how it was done in chapter 2. After linearizing the eqns. 7.2, valid for a strong classical pump tone, we rewrite the noise part of the equation set in matrix form as

$$\dot{\mathbf{v}}(t) = \mathbf{M}\mathbf{v}(t) + \mathbf{K}\mathbf{A}(t), \quad (7.5)$$

where $\mathbf{v}(t)$ is $[\delta\hat{a}_o, \delta\hat{a}_o^\dagger, \delta\hat{a}_e, \delta\hat{a}_e^\dagger, \delta\hat{a}_s, \delta\hat{a}_s^\dagger, \delta\hat{a}_{sm}, \delta\hat{a}_{sm}^\dagger]^T$,

$$\mathbf{M} =$$

$$\begin{bmatrix} -i\Delta_o - \frac{\kappa_o}{2} & 0 & -ig & 0 & 0 & 0 & 0 & 0 \\ 0 & i\Delta_o - \frac{\kappa_o}{2} & 0 & ig^* & 0 & 0 & 0 & 0 \\ -ig^* & 0 & -i\Delta_e - \frac{\kappa_e}{2} & 0 & 0 & -ig & 0 & 0 \\ 0 & ig & 0 & i\Delta_e - \frac{\kappa_e}{2} & ig^* & 0 & 0 & 0 \\ 0 & 0 & 0 & -ig & -i\Delta_s - \frac{\kappa_s}{2} & 0 & -iJ & 0 \\ 0 & 0 & ig^* & 0 & 0 & i\Delta_s - \frac{\kappa_s}{2} & 0 & iJ \\ 0 & 0 & 0 & 0 & -iJ & 0 & -i\Delta_r - \frac{\kappa_r}{2} & 0 \\ 0 & 0 & 0 & 0 & 0 & iJ & 0 & i\Delta_r - \frac{\kappa_r}{2} \end{bmatrix}, \quad (7.6)$$

$$\mathbf{K} = \begin{bmatrix} \sqrt{\kappa_{o,\text{in}}} & \sqrt{\kappa_{o,\text{ex}}} & 0 & 0 & 0 & 0 & 0 \\ 0 & 0 & \sqrt{\kappa_{e,\text{in}}} & \sqrt{\kappa_{e,\text{ex}}} & 0 & 0 & 0 \\ 0 & 0 & 0 & 0 & \sqrt{\kappa_{s,\text{in}}} & \sqrt{\kappa_{s,\text{ex}}} & 0 \\ 0 & 0 & 0 & 0 & 0 & 0 & \sqrt{\kappa_{sm}} \end{bmatrix} \otimes \mathbf{1}_2, \quad (7.7)$$

and $\mathbf{A}(t) = [\delta\hat{a}_{o,\text{in}}, \delta\hat{a}_{o,\text{in}}^\dagger, \delta\hat{a}_{o,\text{ex}}, \delta\hat{a}_{o,\text{ex}}^\dagger, \delta\hat{a}_{e,\text{in}}, \delta\hat{a}_{e,\text{in}}^\dagger, \delta\hat{a}_{e,\text{ex}}, \delta\hat{a}_{e,\text{ex}}^\dagger, \delta\hat{a}_{s,\text{in}}, \delta\hat{a}_{s,\text{in}}^\dagger, \delta\hat{a}_{s,\text{ex}}, \delta\hat{a}_{s,\text{ex}}^\dagger, \delta\hat{a}_{sm}, \delta\hat{a}_{sm}^\dagger]$. Here, $g = g_0\sqrt{\bar{n}_p}$ is the parametrically enhanced electro-optic coupling strength and \bar{n}_p the intra-cavity optical pump photon number. Equation 7.5 is solved in the Fourier domain, yielding

$$\mathbf{v}(\omega) = \mathbf{S}(\omega)\mathbf{A}'(\omega), \quad (7.8)$$

where $S = [-M - i\omega \mathbb{1}]^{-1}$ and $A'(\omega) = KA(\omega)$. The output field can be obtained via the input-output theorem [GC85, Tsa11],

$$\delta\hat{a}_{j,\text{out}}(\omega) = -\delta\hat{a}_{j,\text{in}} + \sqrt{\kappa_{j,\text{ex}}}\delta\hat{a}_j, \quad (7.9)$$

with $j=o,s$. The total conversion efficiency on resonance is calculated from a single matrix element as

$$\eta_{\text{tot}} = |S_{oe}|^2 = |S_{eo}|^2 = \Lambda^2 \eta_e \eta_o \frac{4C \left(1 + C_J^{-1}\right)^2}{\left(1 + C + C_J^{-1}\right)^2}, \quad (7.10)$$

where $\eta_j = \kappa_{j,\text{ex}}/\kappa_j$ is the mode coupling efficiency, C is the multi-photon cooperativity defined as $C = 4\bar{n}_p g_0^2/(\kappa_o \kappa_e)$ and C_J , similarly, is the cooperativity related to the coupling J defined as $C_J = 4J^2/(\kappa_o \kappa_r)$. The factor Λ^2 is introduced by rewriting the external optical linewidth $\kappa_{o,\text{ex}} \rightarrow \Lambda^2 \kappa_{o,\text{ex}}$.

The conversion efficiency in the eqn. 7.10 is higher for the same C than that given by the simple two-mode beam splitter interaction $\eta_{2\text{-mode}} = 4\Lambda^2 \eta_e \eta_o C / (1 + C)^2$. This is due to the amplification provided by the interaction between the microwave and the optical Stokes mode. The gain due to amplification depends on the suppression ratio,

$$S = \Gamma_S / \Gamma_{AS} = (1 + C_J)^{-1} \quad (7.11)$$

where, Γ_S (Γ_{AS}) is the Stokes (anti-Stokes) scattering rate between the modes \hat{a}_e and \hat{a}_s (\hat{a}_o). Note that S is related to the amplitude rather than the power. In this chapter, we report the suppression as the ratio of the power scattered into the two sidebands which is S^2 .

For $J \rightarrow \infty$, i.e. perfect suppression $S^2 = 0$, Eq. 7.10 reduces to the simple two-mode model defining the (hypothetical) pure conversion efficiency without gain. This is because, for high J (or high C_J), the avoided crossing in the lower FSR optical mode is fully split, resulting in perfect suppression and no participation of the lower frequency sideband mode. Furthermore, for $C \ll 1$, we get back the linear dependence of conversion efficiency on C and no dependence on the value of C_J .

The opposite limit is $C_J = 0$ which means there is no avoided crossing in lower FSR optical mode and, thus, equal participation of both optical modes on either side of optical pump. In this limit, we get the maximum possible gain and the conversion efficiency formula reduces to $\eta_{J=0} = 4\Lambda^2 \eta_e \eta_o C$. In contrast to the case of just two modes, here the conversion efficiency does not saturate as C approaches 1.

7.2.4 Noise analysis

The noise spectrum of the output field can be obtained as,

$$S_{jj,\text{out}}(\Omega) = \int_{-\infty}^{+\infty} \langle \delta\hat{a}_{j,\text{out}}^\dagger(t) \delta\hat{a}_{j,\text{out}}(t') \rangle e^{i\Omega t} dt \quad (7.12)$$

via the Wiener-Khinchin theorem. The full expression of $S_{jj,\text{out}}(\Omega)$ is given below,

$$\begin{aligned} S_{oo,\text{out}}(\Omega) = & \Lambda \frac{\kappa_{o,\text{ex}}}{D} [g^4 \kappa_o |\chi_o \chi_s \chi_{sm}|^2 + g^4 J^2 \kappa_{sm} |\chi_o \chi_s \chi_{sm} \chi_e|^2 \\ & + g^2 \bar{n}_b \kappa_{e,\text{in}} |(1 + J^2 \chi_s \chi_{sm}) \chi_e \chi_o|^2 + \bar{n}_{\text{wg}} \kappa_{e,\text{ex}} |(1 + J^2 \chi_s \chi_{sm}) \chi_e \chi_o|^2] \end{aligned} \quad (7.13)$$

where $D = 1 + g^2\chi_o\chi_e + \chi_s[J^2\chi_{sm}(1 + g^2\chi_o\chi_e) - g^2\chi_e]$, and,

$$\begin{aligned} S_{ee,\text{out}}(\Omega) = & \frac{\kappa_{e,\text{ex}}}{D}[g^2\kappa_o|\chi_s\chi_{sm}|^2 + g^2J^2\kappa_{sm}|\chi_s\chi_{sm}\chi_e|^2 \\ & + \bar{n}_b\kappa_{e,\text{in}}|(1 + J^2\chi_s\chi_{sm})\chi_e|^2 + \bar{n}_{\text{wg}}\kappa_{e,\text{ex}}|(1 + J^2\chi_s\chi_{sm})\chi_e|^2] \end{aligned} \quad (7.14)$$

where we have suppressed the dependence of Ω mode susceptibilities χ_i . The mode susceptibilities are defined as, $\chi_i(\Omega) = [\kappa_i - i(\Omega - \Delta_i)]$.

The noise output is so complicated due to the complex mode coupling scheme and because the optical and microwave cavity linewidths being comparable in magnitude. The output photon flux is obtained by integrating the output noise spectrum over the specific measurement bandwidth

$$N_{j,\text{out}} = \int_{-\infty}^{+\infty} \mathcal{F}(\Omega)S_{jj,\text{out}}(\Omega)d\Omega, \quad (7.15)$$

where $\mathcal{F}(\Omega)$ is the measurement filter function. In the experiments discussed in later sections, we use a Gaussian filter with full width half max (FWHM) of 10 MHz.

The equivalent input noise is calculated accordingly¹

$$N_{j,\text{in}} = N_{j,\text{out}}/\eta_{\text{tot}}. \quad (7.16)$$

The predicted output noise takes gain into account and we use the total conversion efficiency η_{tot} that also includes finite gain and coupling losses in order to infer the equivalent added noise referenced to the input port where the (quantum) signal is fed into the transducer.

In the absence of the optical pump ($C=0$), the output microwave noise spectrum is simply given as a Lorentzian output (see chapter 5),

$$N_{e,\text{out},C=0}(\Omega) = \frac{4\kappa_{e,\text{in}}\kappa_{e,\text{ex}}}{\kappa_e^2 + 4\Omega^2}(\bar{n}_b - \bar{n}_{\text{wg}}) + \bar{n}_{\text{wg}}. \quad (7.17)$$

We use the output noise in absence of the optical pump to infer the bath temperature and subsequently calculate the equivalent mode occupancy of the microwave mode

$$\bar{n}_e = \frac{\bar{n}_b\kappa_{e,\text{in}} + \bar{n}_{\text{wg}}\kappa_{e,\text{ex}}}{\kappa_{e,\text{in}} + \kappa_{e,\text{ex}}}. \quad (7.18)$$

7.3 Experimental setup

Switching from the low cooperativity pulsed setup, many changes are made. The 1550 nm laser is divided into 3 parts - 50% of the power is used to produce the optical pump, a quarter of the other 50% is used to produce the optical signal at the optical anti-Stokes sideband frequency and, finally, the rest of the light is used to produce the optical LO for the heterodyne detection of the optical signal. The optical pump is pulsed by an AOM. The produced short pulse is significantly amplified by the EDFA. The amplified pulse has amplified spontaneous emission (ASE) noise from the EDFA which is filtered both in time by an AOM and in frequency by a Fabry-pérot (FP) cavity acting as a frequency filter. It is important to filter the noise in time as well because the continuous broadband ASE is significant (\sim mW) and, if sent to the dilution refrigerator, would heat up the microwave cavity thermally. Additionally, the pump is filtered in frequency domain because the broadband ASE added by the EDFA has a finite

¹Note that physical meaning of N_{in} is explained in detail in chapter 1.

contribution (few photons) at the optical signal frequency. Since we want the optical signal to have no more than vacuum noise, we also filter the pump in frequency domain. The optical signal is produced via the SSB modulator here as well. The optical LO is now produced via an optical phase modulator.

The output optical signal from the electro-optics device comes along with the strong optical pump pulse. The high power pulse can damage the detecting photo-diode. As a result, we separate the optical signal from the pump via another FP cavity. The transmission from the FP cavity is the optical signal which is sent directly to the balanced optical heterodyne setup for detection. The reflection from the FP cavity is the optical pump which is also detected by a fast (200 MHz) detector which is used to lock the laser to the optical WGM.

The microwave part of the setup remains unchanged from the previous experiments.

The full setup with all the details is explained in appendix [C.3](#).

Locks for measurements For the measurements presented in this chapter, we needed to run two locks simultaneously. The first is the laser locked to the optical pump mode similar to previous chapters but now adapted to a pulsed optical pump. The second is the pump cavity filter lock. The FP cavity which filters the optical pump pulse in frequency is tuned via temperature. The body of the cavity is made of aluminum with a good thermal expansion coefficient ($2.4 \times 10^{-5} \text{ m}/(\text{mK})$) and a good thermal conductivity (247 W/(mK)) making the cavity a good candidate for thermal frequency tuning. The temperature of the cavity is controlled by a Peltier element under the cavity. We lock the transmitted power from the FP cavity by tuning the current sent to the Peltier element.

The pulsed version of the laser lock is similar to the CW version. We still lock on resonance with the reflected power as even in the pulsed mode we have no way of knowing if the laser drifted to a specific direction of the resonance. We measure the pump pulse reflection which looks like reflection curve shown in Fig.[7.2a](#). We sample a point after the initial peak to measure the steady state reflected power. In this case, making a dynamic step is easier since we can predict the off-resonance reflected power (yellow dashed curve in Fig.[7.2a](#)) using the overshoot in the first peak. As a result, we sample the maximum of the reflection curve and use it as an anchor to decide the dynamic step size.

For the pump cavity filter lock, we measure the pump pulse by forking 1% of the pump power (see appendix [C.3](#)). We try to maximize this transmission by tuning the current sent to Peltier element. Since this is also a lock on the maximum with no linear error signal around the lock point, we use the same algorithm as the laser lock to keep the pump filter locked laser frequency.

The two locks are interdependent. If the pump filter drifts, it changes the transmitted power and, consequently, the reflected power which would perturb the laser lock. On the other hand, the laser lock changes the frequency which changes the FP filter cavity transmission. Although, in the laser lock we use the first overshoot as an indicator of input power, it is still not completely independent of input power fluctuations. A good way to deal with interdependent locks is to run them on different timescales running the more important locks on a faster time scale. In this case, we run the laser lock on a faster time scale ($\sim 5 \text{ Hz}$) and FP temperature lock on a slower timescale ($\sim 0.1 \text{ Hz}$).

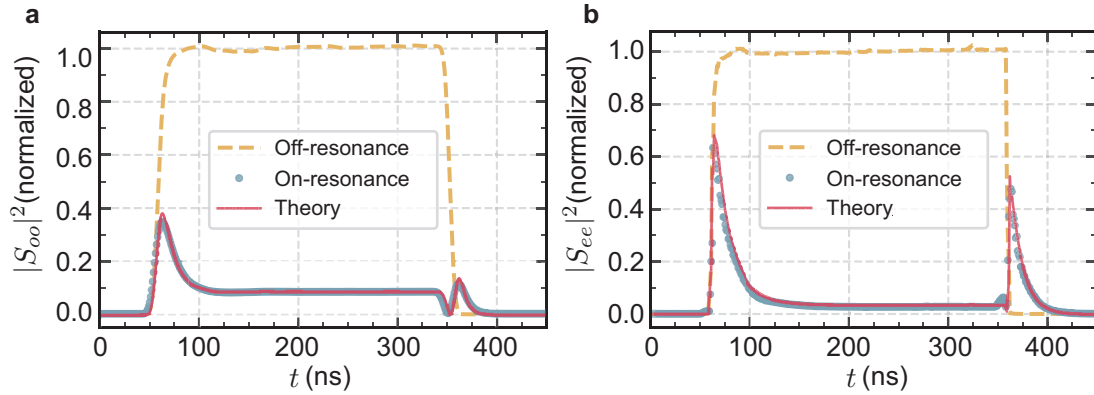


Figure 7.2: **Pulsed mode characterization** a (b) Pulsed characterization of optical (microwave) signal mode. Figure adapted from Ref. [SHR⁺22].

7.4 System characterization

For the high cooperativity measurements, we only characterized the optical and microwave mode in the time domain with the pulse reflection technique described in last chapter. Fig. 7.2 shows the pulsed characterization along with the fit theory curve. The fit parameters obtained from the characterization are shown in table 7.1.

As we saw already in the theory section, at higher cooperativities, the Stokes optical mode participates even though it is suppressed. As a result, the full characterization of the avoided crossing in the optical Stokes mode is needed. This is done in frequency domain as described already in chapter 3. The measured avoided crossing is shown in Fig. 7.3 and the fit parameters are reported in table 7.1. Note that the $\omega = 0$ point in Fig. 7.3 represents the effective FSR between the optical signal (anti-Stokes) mode and the optical pump.

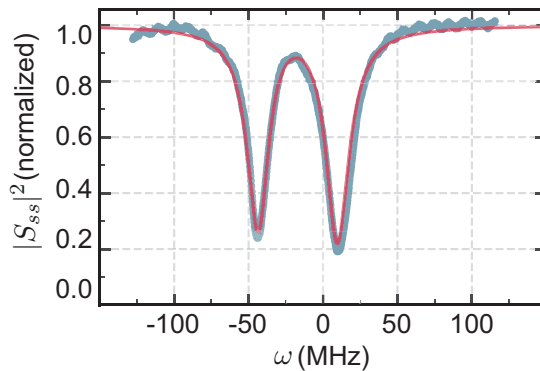


Figure 7.3: Characterization for Stokes mode avoided crossing for the high cooperativity pulsed measurements. Figure adapted from Ref. [SHR⁺22].

7.4.1 4-port calibration

We have already talked about 4-port calibration to independently calibrate the total conversion efficiency in the last chapters. We employ the same calibration again. However, now we use the microwave gain β_4 (between the device and the SA) as the known quantity, which was already measured independently in the chapter 5 and calculate the loss/gain in the remaining ports. We determine the following values: the optical input loss $\beta_1 = -6.33$ dB, the output

Parameter	Description	Value
$\omega_o/2\pi$	Optical signal frequency	193 THz
$\kappa_o/2\pi$	Optical signal linewidth	25.8 MHz
η_o	Optical coupling efficiency	0.58
Λ	Optical mode mismatch factor	0.78
$\omega_e/2\pi$	Microwave mode frequency	8.795 GHz
$\kappa_e/2\pi$	Microwave signal linewidth	13.706 MHz
η_e	Microwave coupling efficiency	0.408
$g_0/2\pi$	Electro-optic coupling rate	37 Hz
$J/2\pi$	TE-TM optical mode coupling rate	26.21 MHz
$\kappa_{sm}/2\pi$	Optical TM mode linewidth	9.96 MHz
$\Delta_s/2\pi$	Optical TE mode detuning	15.5 MHz
$\Delta_{sm}/2\pi$	Optical TM mode detuning	19.5 MHz

Table 7.1: System parameters for high cooperativity pulsed measurements.

optical gain $\beta_2 = 18.63$ dB, the microwave input loss $\beta_3 = -74.92$ dB and the microwave output gain $\beta_4 = 81.75$ dB (between the device and the digitizer).

7.4.2 Optical heterodyne detection

On the optical side, we detect the optical output signal using a balanced heterodyne setup, i.e. by beating the signal with a strong local oscillator with coherent optical field \bar{a}_{LO} at frequency of $\omega_o + \Omega_{\text{LO}}$. This results in a balanced photocurrent $\delta I(t) = i(-e^{i\Omega_{\text{LO}}t}\bar{a}_{\text{LO}}^*\delta\hat{a}_{o,\text{out}} + e^{-i\Omega_{\text{LO}}t}\bar{a}_{\text{LO}}\delta\hat{a}_{o,\text{out}}^\dagger)$. We thus obtain the symmetrized power spectral density,

$$S_I(\Omega) = \frac{1}{2} \int_{-\infty}^{\infty} \langle \overline{\{\delta I(t+t'), \delta I(t')\}} \rangle e^{i\Omega t} dt \quad (7.19)$$

The optical heterodyne efficiency or the equivalent noise floor level can be determined using the output gain β_2 and the absolute power measured in the baseline without any signal

$$P_{\text{baseline}} = \hbar\omega_o\beta_2 BW N_{o,\text{add}}, \quad (7.20)$$

where BW the measurement bandwidth and $N_{o,\text{add}}$ the equivalent noise in the heterodyne baseline.

Using the output optical gain β_2 , the equivalent noise floor in optics heterodyne $N_{o,\text{add}}$ is calculated to be 34.3 photons. The optical detection efficiency is low in our case for a number of reasons. There is a ≈ 3 dB loss while coupling the light from the device output, i.e. from the prism surface, to the optical fiber. An FP filter used to reject the strong optical pump for the balanced heterodyne detection introduces another 4 dB of loss. We only use the first order sideband generated from a phase modulator as the optical LO. Since the phase modulator produces many other optical tones which do not increase the signal but still increase the noise, it reduces the optical balanced heterodyne efficiency to about 17%. These are technical nonidealities of the setup, some of which we improve later to get better heterodyne efficiency.

7.5 High cooperativity pulsed conversion

We do high cooperativity pulsed conversion for two different possible cases - when the optical pump is pulsed and the signal is continuous wave and when the signal is pulsed while the

optical pump pulse is continuously on. In the first case, when the signal is continuous wave, the resonator cavity is pre-loaded with the signal photons and is in a steady state according to its internal and external losses. When the optical pump pulse arrives, the effective internal loss of the cavity changes because a new loss/conversion channel opens up and a new steady state has to be reached. Since the new loss channel is internal, it decreases the coupling efficiency and the new steady state intra-cavity photon numbers are lower than before the pump pulse. Meanwhile in the process of arriving to this steady state, temporarily, the conversion efficiency increases beyond the steady state owing to the extra intra-cavity photons (than allowed by the new steady state) as shown in Fig. 7.4(a). From another perspective, during this momentary overshoot, the coupling losses of the pre-loaded cavity are circumvented and the effective input signal coupling efficiency becomes 1 temporarily.

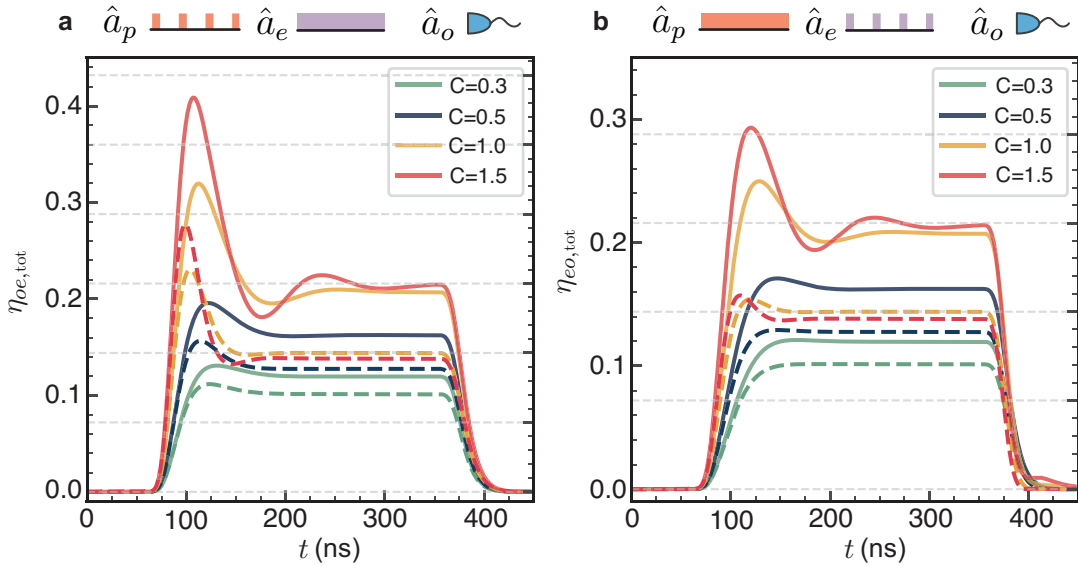


Figure 7.4: **Theory of pulsed conversion** **a** **(b)** Theoretical microwave to optics conversion with a pulsed optical pump and continuous signal (a pulsed optical signal and continuous pump). The solid (dashed) lines represent the case with $S^2 = 0.22$ ($S^2 = 0.0$). Figure adapted from Ref. [SHR⁺22].

For the case when the signal is pulsed while the optical pump is already on, the signal is never pre-loaded into the resonator. Nevertheless, we still see an overshoot in Fig. 7.4(b) where the signal is pulsed while the optical pump is continuous wave. The reason for this overshoot is the onset of coherent oscillation between microwave and optics due to a high conversion rate. The oscillations are clearly seen at higher cooperativities $C \gtrsim 1$ when the conversion rate clearly surpasses the loss rates of the cavities and the power can oscillate between the microwave and optical cavities before getting coupled out. Note that the first overshoot in case of Fig. 7.4(a) is always larger than in Fig. 7.4(b) for the same cooperativity because of the additional signal pre-loading effects because of the additional pre-loading of the cavity effect.

Lastly, we identify the differences between the case with finite gain $S^2 = 0.22$ (solid lines) and the case with no gain/perfect suppression of the Stokes sideband $S^2 = 0.0$ (dashed line). For no additional gain in the transduction, the pure steady state efficiency saturates to unity as expected at $C = 1$ and starts to drop after that. However, for a system with finite gain, this saturation doesn't happen and the internal steady state transduction coefficient keeps increasing beyond unity.

With this understanding, we move on to the experimental measurements. Fig. 7.5(a) and (c) shows the calibrated conversion efficiency for microwave-to-optics and optics-to-microwave conversion respectively for different cooperativities. The converted pulses are measured for two cases with a 200 MHz bandwidth, i.e. a CW signal (solid lines) and a pulsed signal while the pulsed optical pump pulse is on (dashed lines). The solid and dashed lines show the theoretical prediction from the numerical 5-mode model with the input optical loss as the only fit parameter. We generally find excellent agreement and assign the observed mismatch in Fig. 7.5(a) for the case of pulsed signals to a small amount of uncorrected output filter drift. We observe a similar behaviour as we predicted from theory. A larger overshoot in case the optical pump is pulsed and a smaller overshoot in case the signal is pulsed while the optical pump was already on.

For the measurement with $C = 0.49$, which corresponds to a parametrically enhanced coupling strength of $\sqrt{\bar{n}_p}g_0/(2\pi) = 6.58$ MHz with $\bar{n}_p = 3.16 \times 10^{10}$ pump photons for a pulse pump power of $P_p \approx 0.4$ W, we explicitly show real-time complex quadrature control in Fig. 7.5(b) and (d), as required for high-fidelity quantum communication protocols. A linear phase change is imprinted on the input signal pulses while keeping the amplitude constant resulting in cos and sin-like quadrature outputs. The measurements of the two converted quadratures match the input modulation closely. The only exception is during the beginning and the end of the optical pump pulse due to finite transducer bandwidth of 18 MHz for this C .

In Fig. 7.5(a) and (c), we do not go beyond $C = 0.49$. This is because beyond that cooperativity, we observed an unstable amplification peak at the end of the pulse. On further investigation, we realized that this amplification was a result of higher-order $\chi^{(3)}$ Kerr non-linearity. The full investigation and the related experiments are reported in section 7.7.

Nevertheless we realized we could go to higher cooperativities without entering this regime of instability if we used shorter, i.e. 100 ns optical pump pulses as shown in Fig. 7.6. With these higher cooperativities, we see now the highest microwave-to-optical conversion efficiency momentarily reaches up to 30% for a CW signal tone. The observed deviations from theory in Fig. 7.6(b) are caused by the slight broadening of the microwave mode linewidth due to the increased average bath temperature, in agreement with CW pump experiments (see section 5.4), an effect which the theory model does not take into account.

A summary of the measured transduction efficiencies as a function of the applied optical pulse power P_p and corresponding cooperativity C is presented in Fig. 7.7. The red and blue colors show measured peak and steady-state values respectively. Solid lines are predicted transduction efficiencies for our experimental parameters corresponding to $S^2 = 0.22$, while dashed lines represent the case of perfect suppression $S^2 = 0$. The blue shaded area thus represents the gain due to the not fully suppressed Stokes process. For $C \gtrsim 0.35$, the achieved internal transduction coefficient η_{in} , which we define operationally by dividing the measured η_{tot} by the measured coupling losses, can exceed 1. This is due to signal pre-loading into the cavity and coherent electro-optic oscillations in case of the extracted peak values (red symbols), as well as due to gain.

The blue circles indicate the corresponding pure conversion efficiencies (without gain) for itinerant photons up to $C = 0.92$, reaching $\eta_{in} = 0.995$ and $\eta_{tot} = 0.144$. Since pure conversion efficiency estimates are based on a simplified theory calculation, we decided to instead focus on the measured steady-state transduction values and take into account the finite gain when calculating the corresponding added conversion noise, as explained below. The measured higher peak efficiencies due to signal pre-loading on the other hand are relevant to

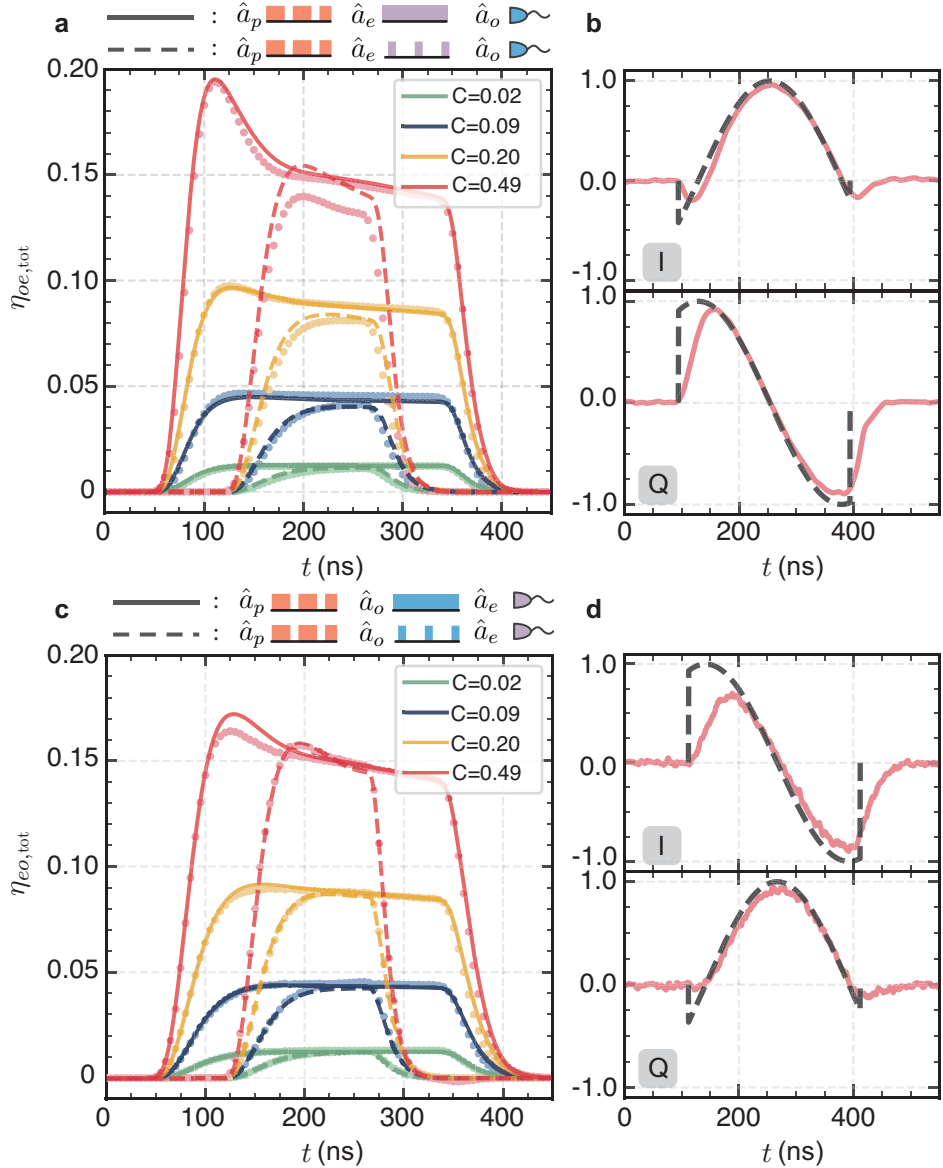


Figure 7.5: High cooperativity bidirectional conversion. Top (bottom) row panels show results for microwave-to-optics (optics-to-microwave) conversion. **a (c)**, Converted signal pulses (bright dots are calibrated measurements and lines are theory) for a 300 ns long optical pump pulse measured with a 500 Hz repetition rate for a CW signal (solid lines) and a pulsed signal (dashed lines). **b (d)**, Measured IQ quadrature modulation of the converted signal pulse (red lines) and the applied IQ quadrature modulation to the input signal (gray dashed lines) for $C = 0.49$. Figure adapted from Ref. [SHR⁺22].

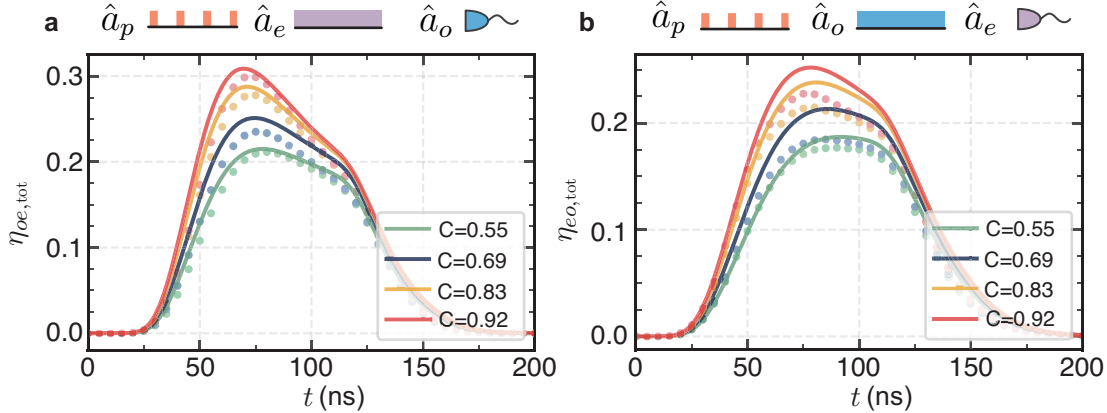


Figure 7.6: **High cooperativity bidirectional conversion with 100 ns long optical pump pulse.** **a (b)** Microwave to optics (optics to microwave) converted pulses (bright dots are calibrated measurements and lines are theory) for a 100 ns long optical pump pulse and a CW signal measured with a 500 Hz repetition rate. Figure adapted from Ref. [SHR⁺22].

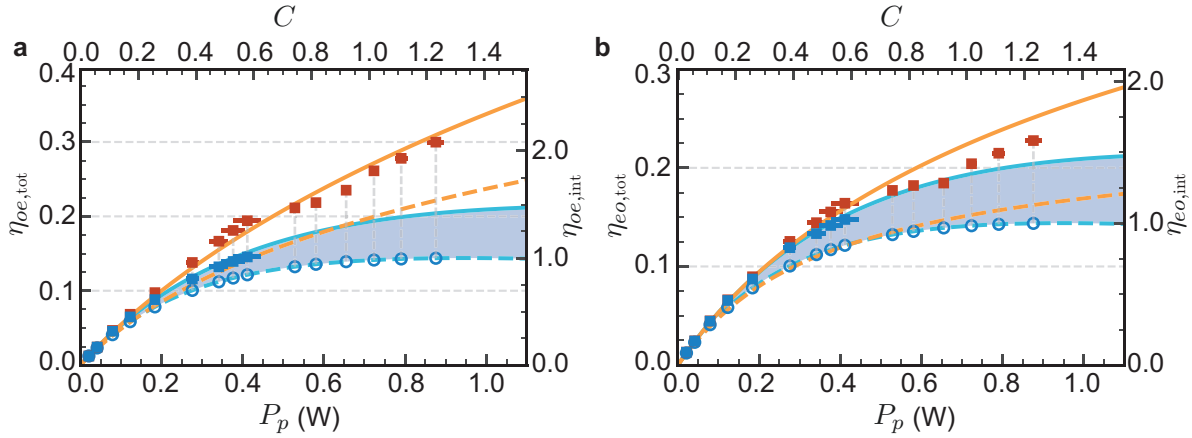


Figure 7.7: **Transduction efficiency summary.** **a (b)** Summary of measured steady state for microwave to optics (optics to microwave) conversion. Figure adapted from Ref. [SHR⁺22].

the future interfaces that can produce the signal photons inside the cavity and thus circumvent the microwave coupling losses.

7.6 Thermal and quantum noise

Noise measurements We measure the output microwave noise via phase-insensitive amplification of the weak microwave signal using a cryogenic HEMT amplifier [CDG⁺10]. The amplified microwave field is sent through subsequent amplifiers, and mixed with a microwave LO at room temperature. We calibrate the microwave output noise using the total detected system noise of 12.74 photons $s^{-1}Hz^{-1}$ which is the sum of the added noise due to microwave detection chain of 12.24 photons $s^{-1}Hz^{-1}$ and vacuum noise, as shown in the appendix B. Finally, $N_{e,out}$ is calculated after subtracting this background noise to report only the added noise due to the transducer. In all of the noise measurements in the main text we report the measured added noise due to the transducer, i.e. with the constant added noise due to loss and amplifiers subtracted.

Microwave noise measurements are made with two different bandwidths - 10 MHz for fast

noise detection (~ 100 ns time resolution) and 100 kHz for slower noise detection but with better SNR. The fast 10 MHz measurements are triggered to capture the output noise response during the pulse. On the other hand, the 100 kHz measurements are run continuously to measure the average thermal response of the triggered optical pump pulses. Due to their lower bandwidth and continuous measurement nature, they provide a superior SNR performance to 10 MHz measurements and, thus, are used to determine the thermal noise occupancy for much lower average optical pump powers. The main source of error for the slow, low occupancy measurements is the systematic absolute error due to long term drifts of the noise baseline that is subtracted. We measure and average the noise baseline over multiple hours (like the measurements) and multiple different days to determine the absolute standard error of ± 0.02 photons $s^{-1}Hz^{-1}$. This error along with the statistical error of the actual noise measurement is propagated to get the final error bars. In the case of fast measurements, which were averaged only over a few tens of minutes, we take into account a larger observed variation of the noise baseline on that timescale of ± 0.1 to ± 0.2 photons $s^{-1}Hz^{-1}$.

The slow 100 kHz measurements allow us to study noise dynamics of the system on a long time scale. Fig. 7.8 shows the average microwave noise output as the optical pump pulses corresponding to $C \sim 0.38$ with different repetition rates are turned on (marked region between vertical dashed lines). We observe that our system does not heat up immediately as soon as the pulses are turned on, rather it slowly reaches the steady state in a few minutes after the pulses are turned on. Moreover, the cooling time is even longer and it can take up to an hour to come back to the equilibrium occupancy depending on the average optical pump power applied. This matches the experiment already shown in section 5.7. The specific time scales are expected to depend critically of the thermal contact and conductivity of the localized heat source (the dielectric-superconducting sample) to the cold bath (the mixing chamber plate), as well as on the cooling power of the dilution refrigerator [MLR⁺21].

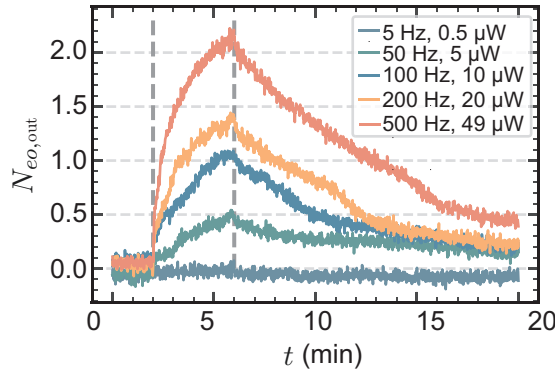


Figure 7.8: Microwave output noise as a function of average optical pump power. Output microwave noise dynamics measured on long time scales as a function of pulse repetition rate for optical pump pulses corresponding to $C \sim 0.38$. The region between vertical dashed lines marks the time interval during which the optical pump pulses are turned on. Figure adapted from Ref. [SHR⁺22].

For the highest repetition rates, the output microwave noise reaches close to 2 quanta. This corresponds to a local effective mode temperature on the order of 1 K. These temperatures are quite hot compared to a much colder mixing chamber temperature (~ 50 mK) of dilution refrigerator where the device is thermalized because of finite thermal conductivity of the dielectric resonator as well as the bulk superconducting aluminum cavity. We do, however, see a marginal increase in the mixing chamber temperatures as we increase the average optical

pump power sent to the device. For a fastest repetition rate of 500 Hz, the mixing chamber temperature increased to at most 60 mK from its base temperature of 7 mK.

Equivalence of noise for CW and pulsed optical pump Since this bulk electro-optic system has such long heating and cooling timescales, for short and fast repeating pulses, it is only the average optical power that determines the added thermal noise due to optical heating. Fig. 7.8 shows the equivalence between heating via optical pulses (red) and continuous optical power (blue) during the time interval marked by the two vertical dashed lines. We observe the same dynamics of the output microwave noise if the power level of average optical power is matched. This experiment shows that thermal noise can be tuned by changing the pulse repetition rates while keeping the same level of cooperativity. We use this feature of our device to do the next sweep.

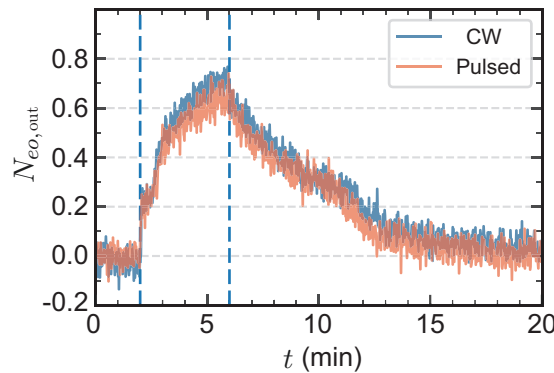


Figure 7.9: Equivalence of added thermal microwave noise CW optical power and optical pulses with same average optical power. Figure adapted from Ref. [SHR⁺22].

Noise dynamics Figure 7.10 captures the effect of the two relevant types of noise. The first is thermal noise due to optical pump absorption heating, which depends on the time-averaged optical power $P_{\text{avg}} = P_p t_p f_{\text{rep}}$ (as discussed earlier) with the pulse length t_p and the repetition rate f_{rep} . The second contribution is amplified vacuum noise due to finite transducer gain, which depends on \mathcal{S} and P_p . The shown output noise photon numbers are defined by integrating the noise emission spectrum $S_{ii,\text{out}}$ over the Gaussian measurement filter function as shown in eqn. 7.15.

Figure 7.10a shows the microwave noise output $N_{e,\text{out}}$ in the time domain, measured with a 10 MHz filter bandwidth (100 ns time resolution) centered at the microwave resonance, when 300 ns long optical pump pulses with $C = 0.38$ are applied (shaded region) with different repetition rates from 10 to 500 Hz. High repetition rates increase the measured average thermal output noise, which stays approximately constant during the measurement time of 3 μ s. During the pulse however, we observe either a classical or a quantum effect depending on the average thermal occupancy of the microwave mode. For higher mode temperature (red curve), parametric laser cooling of the microwave mode [Tsa10], due to up-conversion of noise to optics is dominant and in agreement with theory (gray arrow). But as the thermal noise is decreased for the same cooperativity, additional noise due to vacuum amplification overwhelms the parametric cooling effect. For the lowest occupancy curve with a 10 Hz repetition rate, the vacuum amplification is clearly observed during the pump pulse and in good agreement with theory (gray arrow). This last curve is measured with a lower suppression $\mathcal{S}^2 \approx 0.82$ (using a different set of optical modes with a different magnitude of avoided crossing) in order

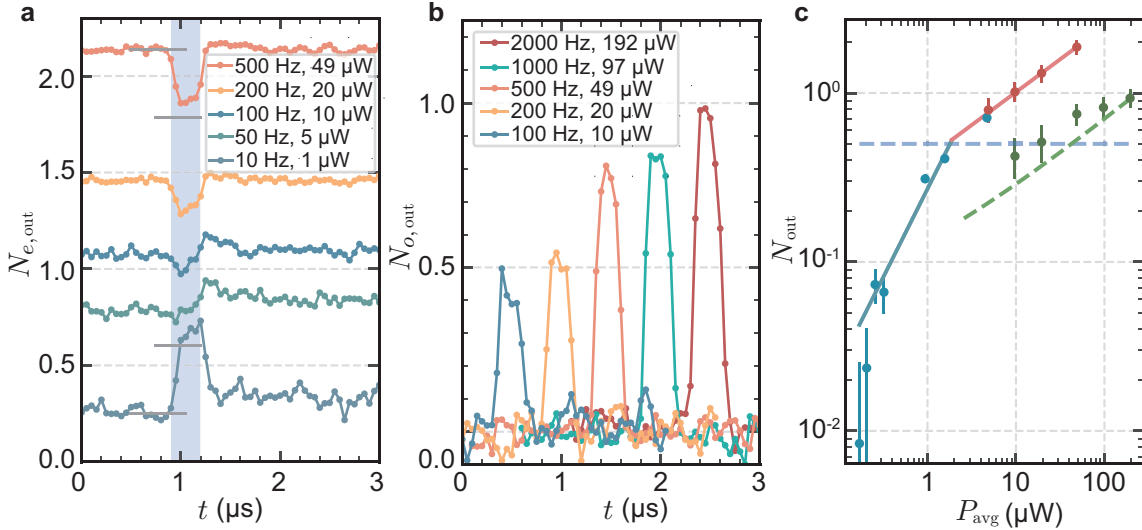


Figure 7.10: Output noise time dynamics and summary. **a**, $N_{e,\text{out}}$ for a 300 ns long optical pump pulse ($C = 0.38$) for different repetition rates f_{rep} (P_{avg}) measured with a 10 MHz bandwidth centered at the microwave resonance. The blue shaded region shows the times span when the optical pump is on. The gray arrows mark the noise change as predicted from theory. **b**, $N_{o,\text{out}}$ for the same optical pump pulses and various f_{rep} (P_{avg}) measured with a 10 MHz bandwidth centered at the optical signal frequency. The noise pulses are separated in time for better visibility. **c**, Compilation of all measured N_{out} for different time-averaged optical pump powers P_{avg} . Red and blue points represent measured $N_{e,\text{out}}$ with 10 MHz and 100 kHz bandwidths respectively. Green points represent $N_{o,\text{out}}$ measured with 10 MHz bandwidth. The solid lines represent power law fits. The green dashed line shows the predicted $N_{o,\text{out}}$ using the measured $N_{e,\text{out}}$. All the points are taken with $C = 0.38$ ($\eta_{\text{tot}} = 11.4\%$) except for the first three blue points which correspond to $C = 0.20$ ($\eta_{\text{tot}} = 8.0\%$), 0.24 ($\eta_{\text{tot}} = 9.1\%$), and 0.3 ($\eta_{\text{tot}} = 10.3\%$) respectively. (Figure adapted from Ref. [SHR²²].)

to enhance the effect for a better signal to noise ratio. We assign slight mismatches between the theoretical prediction and experiment to an expected small amount of thermal heating during the pulse.

The observation of parametric laser cooling implies the presence of noise at the output of the optical signal mode \hat{a}_o . $N_{o,\text{out}}$ is measured with a 10 MHz bandwidth around the optical signal frequency and shown in Fig. 7.10b. The optical pump pulses are the same as in Fig. 7.10a with varying repetition rates. With higher P_{avg} , the thermal microwave mode occupancy increases, thus, increasing the output optical noise.

We summarize these results in Fig. 7.10c as a function of P_{avg} . The $N_{i,\text{out}}$ during the pulse from Fig. 7.10a are shown as red points, and from Fig. 7.10b as green points, along with corresponding power law fits (solid lines). The dashed green line represents the predicted optical noise based on theory and the fitted microwave noise. In addition, we show the continuous microwave noise measurements conducted with a 100 kHz bandwidth for better signal to noise ratio at the lowest occupancies where the system is deep in its quantum ground state (blue points).

Noise output as a function of cooperativity and thermal occupancy In Fig. 7.11 we show the theoretical prediction of the $N_{e,\text{out}}$ and $N_{o,\text{out}}$ respectively as a function of the steady state microwave mode occupancy N_e and cooperativity C for the relevant experimental

case $S^2 = 0.22$. As a function of N_e , in Fig. 7.11a the contours change from left leaning to right leaning as the transition from quantum amplification to classical cooling occurs. The measurements from Fig. 7.11a are shown as circles where the inside color represents the experimentally measured value in excellent agreement with the theoretical prediction. Similarly, the predicted dependence of $N_{o,out}$ is shown in Fig. 7.11b where we included the measurements from Fig. 7.10b with good agreement with theory. Low bandwidth measurements (blue points in Fig. 7.10c) do not contain time-domain information and are therefore not included. These results provide strong evidence that P_{avg} fully determines the thermal noise limitations of this device.

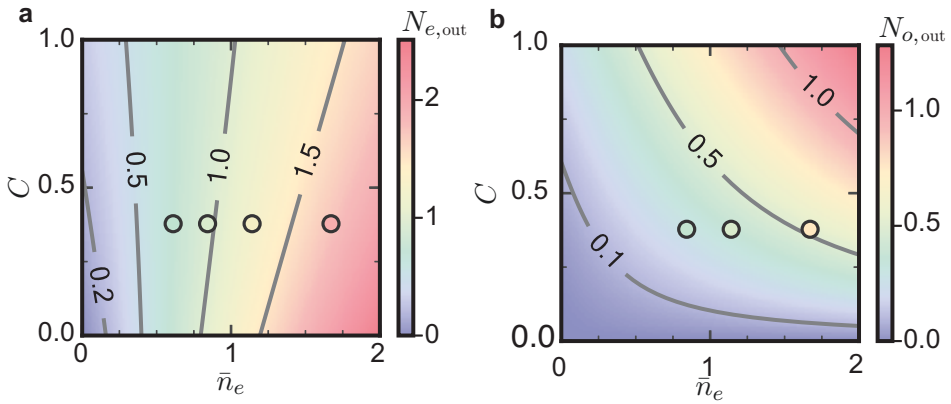


Figure 7.11: **a** (**b**) Density plot of the calculated $N_{e,out}$ ($N_{o,out}$) with 10 MHz bandwidth as a function of C and \bar{n}_e for $S^2 = 0.22$. The top 4 (first 3) measurements of $N_{e,out}$ ($N_{o,out}$) for the same S taken from Fig. 7.10a (b) are shown as circles with experimental values represented by the inside color. Figure adapted from Ref. [SHR⁺22].

Quantum cooperativity Low occupancies and high cooperativity are the preconditions for interesting cavity quantum electro-optics experiments in analogy to cavity optomechanics [Tsa10] as well as for quantum limited conversion. Figure 7.12 shows the calculated quantum cooperativity $C_q = C/\bar{n}_e$ - a measure of the electro-optic state transfer rate compared to the thermal decoherence rate of the microwave mode [AKM14] - for the measurements in Fig. 7.10c, where \bar{n}_e is inferred from the measured $N_{e,out}$. The achieved large $C_q \gg 1$ are a result of the low mode occupancies and encourage further investigations in the direction of two-mode squeezing of hybrid microwave and optical field states [RHBF19].

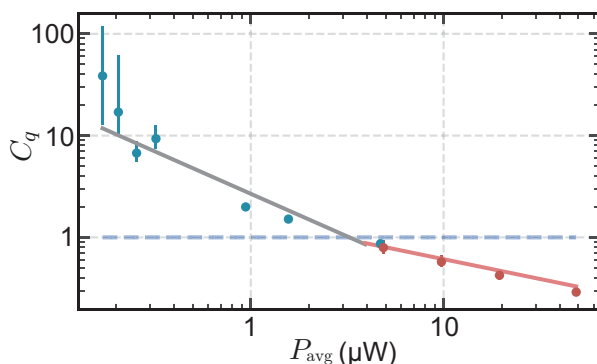


Figure 7.12: Inferred quantum cooperativity for the measured output noise values shown in Fig. 7.10(c). Figure adapted from Ref. [SHR⁺22].

Equivalent added noise referred to input The most relevant quantity that signifies quantum enabled conversion is the resulting equivalent added noise photon number referenced to the input of the converter where a non-classical input signal would be applied $S_{\text{out}}(\omega) = \eta_{\text{tot}}(S_{\text{in}}(\omega) + N_{\text{in}})$. The two measured $N_{i,\text{out}}$ include both thermal and quantum noise contributions and we calculate the resulting equivalent added input noise photon number with $N_{ij,\text{in}} = N_{i,\text{out}}/\eta_{\text{tot}}$. Low values of $N_{ij,\text{in}}$ therefore require simultaneously high efficiency and low output noise which are achieved.

Fig. 7.13a and b show $N_{ij,\text{in}}$ for optics-to-microwave ($N_{eo,\text{in}}$) and microwave-to-optics ($N_{oe,\text{in}}$) conversion respectively as a function of N_e and C for $\mathcal{S}^2 = 0.22$. The lowest 5 blue points from Fig. 7.10(c) are marked with crosses as the parameters we achieved experimentally. For $N_{eo,\text{in}}$, we reach $1.11^{+0.15}_{-0.07}$, and for $N_{oe,\text{in}}$, we reach as low as $0.16^{+0.02}_{-0.01}$ equivalent added noise photons. Here the confidence interval is taken from error propagation using the confidence interval of the measured $N_{i,\text{out}}$. As discussed in chapter 1, this puts our device in the regime (or close to) of quantum-enable transduction where probabilistic transduction schemes allow interesting experiments in the quantum domain.

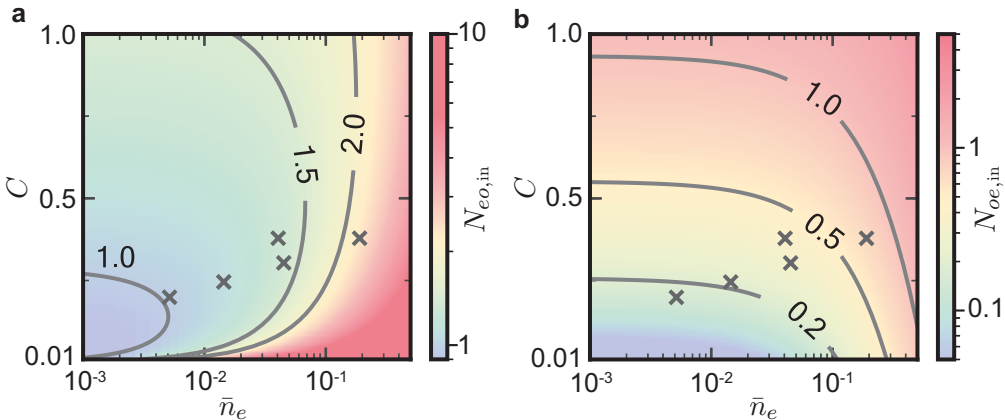


Figure 7.13: **a** (**b**) Inferred optics-to-microwave $N_{eo,\text{in}}$ (microwave-to-optics $N_{oe,\text{in}}$) equivalent added input noise as a function of C and \bar{n}_e for $\mathcal{S}^2 = 0.22$. Crosses mark the lowest 5 blue measurement points in Fig. 7.10(c). Figure adapted from Ref. [SHR²²].

7.7 Kerr effect

In Fig. 7.6 of the main text we show conversion up to a cooperativity of 0.92. This is because after a certain threshold input power, which also depends on the optical pump pulse length, we observe an extreme amplification at the end of the conversion pulse. Fig. 7.14 shows this effect for both microwave-to-optics and optics-to-microwave conversion cases. Since the amplification only happens at the end of the converted pulse, we are able to avoid it by applying a shorter optical pump pulse, at which point, the optical pump power could be further increased until the amplification appears again. The threshold power and hence the maximum achievable electro-optic cooperativity (without this amplification) therefore depends on the optical pump pulse length.

After a number of tests we came to the conclusion that this effect is most likely due to the third-order $\chi^{(3)}$ nonlinearity in lithium niobate, an effect that is commonly utilized in optical parametric amplifiers [KSV04]. We verified that amplification in the optical signal is present even when there is no coherent signal drive present and for cases when the microwave mode

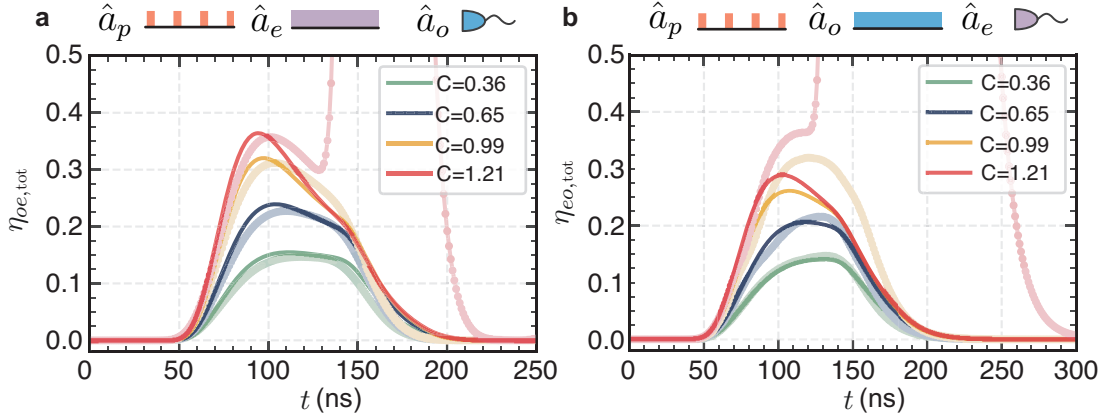


Figure 7.14: **Observation of amplification due to Kerr effect.** **a (b)** Time domain conversion in the microwave to optics (optics to microwave) direction for 100 ns optical pump pulses of different power and C . The points joined by light colored lines are measured experimentally. The thin bright lines are theoretical only taking into account the $\chi^{(2)}$ effect. After $C \approx 1$, we observe a delayed parametric amplification event. The measured transmission reaches as high as 11.4 in case of microwave to optics conversion and 13.1 in case of microwave to optics conversion (not visible). Figure adapted from Ref. [SHR⁺22].

is far detuned from the optical FSR. This proves that the effect is independent of the usual $\chi^{(2)}$ nonlinear interaction. However, when the microwave mode is matched with the optical FSR, we see amplification in the microwave signal as well due to strong optical sideband combined the $\chi^{(2)}$ mediated beam splitter interaction (conversion of the amplified optical signal). Note that the cooperativity threshold for amplification of $C \approx 1$, as shown in Fig. 7.14, is a coincidence and only valid for 100 ns optical pump pulses. For longer optical pump pulses, the cooperativity threshold for amplification becomes smaller and well below unity.

This parameter regime of seeing effects of both $\chi^{(2)}$ and $\chi^{(3)}$ nonlinearities together is, to best of our knowledge, novel. Producing coherent phase-locked microwave and optical drives together requires a systematic investigation and may prove useful in future.

7.8 Conclusions

High cooperativity electro-optics achieved in this chapter opens up a regime where many novel effects are seen. Finally, the rate of conversion is able to match the rate of loss of the cavities. This allows for a rich time dynamics which we have studied in detail. We measure high total conversion efficiencies - up to 15% in the steady state corresponding to almost unity conversion efficiency. Moreover, these high conversion efficiencies are not achieved at the cost of high added thermal noise. With the use of a pulsed optical pump, we keep the added thermal noise to a minimum. We even manage to achieve equivalent added noise referred to the input close to 1 for optics to microwave conversion direction and $\ll 1$ for microwave to optics conversion direction.

However, one of most exciting observed phenomena is observed in the measured output noise dynamics. We see that with high cooperativities, the output microwave noise can be reduced by applying an optical pump pulse - possibly the first instance of directly cooling a microwave cavity using optical light. Cooling of a mechanical cavity via optical light is now a routine in many optomechanics experiments [AKM14]. Following suite from these experiments, we

can measure direct electro-optical backaction between microwave and optical light similar to routinely measured backaction between mechanics and optics [KRC⁺05]. This is done in the next chapter.

We also observe amplification of vacuum noise for low thermal occupancy of microwave modes. In other words, this is the spontaneous downconversion between the microwave mode and the optical Stokes mode. Since the amplified signal originates from vacuum, it has correlations that go beyond the classical limit. This is termed as EPR correlations in the literature. In chapter 9, we measure these non-classical correlations between output microwave and optics noise and demonstrate entanglement between these for the first time.

CHAPTER 8

Electrooptic dynamical backaction

8.1 Introduction

In the last chapter, we experimentally achieve electrooptic cooperativities which are on the order of 1. In this regime, where the electrooptic coupling rate reaches the magnitude of loss rates of the involved cavities, the effects of microwave-optics coupling can alter the optical and microwave modes itself. This phenomenon is called backaction on a mode. It is routinely observed in opto-mechanical systems where the mechanical motion of the mirror can couple to the optical light in the optical cavity via the radiation pressure [KRC⁺05]. The discovery of this effect, owing to achieved high opto-mechanical cooperativities, led to a cascade of new experiments in the field of cavity opto-mechanics - such as laser cooling, squeezing, entanglement and quantum non-demolition measurements of microwave modes.

Similar results can also be observed between microwave and optical modes coupled via electrooptic interaction since the interaction Hamiltonian is the same as the one for opto-mechanical interaction. The main hurdle preventing similar electrooptic experiments, as mentioned above, was the difficulty in achieving high enough electrooptic cooperativity. The small vacuum coupling constant meant a large amount of optical pump power are required to achieve high cooperativities. However, higher optical powers in proximity to superconducting microwave cavities meant cooper pair breaking leading to quasi-particle generation and resulting shift and broadening of the microwave mode [FXL⁺21].

In our system, we use a bulk 3D microwave cavity which is cm-sized. The bulk of the microwave cavity gives space to the quasi-particles produced on the surface to run inside preventing the quasi-particle density at the superconductor surface from increasing sharply. As a result, we see negligible effects of quasi-particles even when pumping the optics cavity with ~ 100 mW optical power. We discuss this in detail in the chapter as excess delayed back action since it lingers even when the optical pump is long gone.

We also discuss the above mention back-action effects that we observe in our system such as effective narrowing and broadening of the modes, induced transparency and induced absorption. In the chapter, we discuss them under instantaneous back-action since they are observed instantaneously as the optical pump pulse is applied.

Acknowledgements This chapter is based on the work presented in Ref. [QSH⁺22]. I would like to thank Liu Qiu for doing the data analysis and producing the figures which have been

adapted in this chapter. Finally, Liu Qiu also wrote the text of Ref. [QSH⁺²²] which has been partially adapted in this chapter. Figure credits have been individually given in the figure captions.

8.2 Theory

We have already discussed the interaction Hamiltonian for our system with a 5-mode model in the previous chapter. For this chapter, we consider 6-modes interacting with each other in contrast to 5-mode model discussed in previous chapter, since here, we talk simultaneously about microwave mode's interaction with optical Stokes and anti-Stokes mode and suppressing one interaction or the other. Consequently, now we use two TM optical modes \hat{a}_{sm} and \hat{a}_{tm} which are degenerate with optical TE modes \hat{a}_s and \hat{a}_t respectively. The two TM optical modes are used to hybridize the TE modes as usual and to suppress the participation of optical TE modes in the interaction Hamiltonian.

The total interaction Hamiltonian of the multimode cavity electro-optical system is, thus, given by ,

$$\hat{H}_I/\hbar = g_0(\hat{a}_p^\dagger \hat{a}_s \hat{a}_e + \hat{a}_p^\dagger \hat{a}_t \hat{a}_e^\dagger + \text{h.c.}) + J_s(\hat{a}_s^\dagger \hat{a}_{sm} + \text{h.c.}) + J_t(\hat{a}_t^\dagger \hat{a}_{tm} + \text{h.c.}) \quad (8.1)$$

Here, J_s and J_t are the coupling rate between the TE and TM optical modes.

In an ideal case, the optical FSR matches the microwave frequency ω_e . However in practice, the Stokes and anti-Stokes mode can be detuned from the microwave frequency, due to FSR and ω_e mismatch or due to asymmetric FSR (see section 8.4). We take these mismatches into account by δ_s and δ_t which are detuning of the Stokes and the anti-Stokes mode with the effective FSR. In the case of symmetric FSR, we have $\delta_s = -\delta_t$. For simplicity, we assume the TM mode is of the same frequency of the corresponding Stokes or anti-Stokes mode.

We again write the quantum Langevin equation in matrix form and solve it in steady state as shown in Eqn. 7.5,

$$\mathbf{v}(\omega) = \mathbf{S} \cdot \mathbf{K} \cdot \mathbf{A}_{\text{in}}(\omega), \quad (8.2)$$

where, the noise operators are defined in the vector form, with the mode operator and input noise operator vectors being,

$$\begin{aligned} \mathbf{v}(\omega) &= [\hat{a}_s, \hat{a}_s^\dagger, \hat{a}_t, \hat{a}_t^\dagger, \hat{a}_{sm}, \hat{a}_{sm}^\dagger, \hat{a}_{tm}, \hat{a}_{tm}^\dagger, \hat{a}_e, \hat{a}_e^\dagger]^T, \\ \mathbf{A}_{\text{in}}(\omega) &= [\hat{a}_{s,\text{in}}, \hat{a}_{s,\text{in}}^\dagger, \hat{a}_{s,\text{ex}}, \hat{a}_{s,\text{ex}}^\dagger, \hat{a}_{t,\text{in}}, \hat{a}_{t,\text{in}}^\dagger, \hat{a}_{t,\text{ex}}, \hat{a}_{t,\text{ex}}^\dagger, \\ &\quad \hat{a}_{sm,\text{vac}}, \hat{a}_{sm,\text{vac}}^\dagger, \hat{a}_{tm,\text{vac}}, \hat{a}_{tm,\text{vac}}^\dagger, \hat{a}_{e,\text{in}}, \hat{a}_{e,\text{in}}^\dagger, \hat{a}_{e,\text{ex}}, \hat{a}_{e,\text{ex}}^\dagger]^T, \end{aligned} \quad (8.3)$$

with $\hat{a}_{j,\text{in}}$ ($\hat{a}_{j,\text{ex}}$) and $\hat{a}_{e,\text{in}}$ ($\hat{a}_{e,\text{ex}}$) the intrinsic (input) noise operator for optical and microwave

modes, and $\hat{a}_{j,\text{tm,vac}}$ the TM vacuum noise. $\mathbf{S} = [\mathbf{M} - i\omega \mathbb{1}]^{-1}$ with,

$$\mathbf{M} = \begin{pmatrix} -\delta_s - \frac{\kappa_o}{2} & 0 & 0 & 0 & -iJ_s & 0 & 0 & 0 & 0 & ig \\ 0 & \delta_s - \frac{\kappa_o}{2} & 0 & 0 & 0 & iJ_s & 0 & 0 & -ig & 0 \\ 0 & 0 & -\delta_t - \frac{\kappa_o}{2} & 0 & 0 & 0 & -iJ_t & 0 & ig & 0 \\ 0 & 0 & 0 & \delta_t - \frac{\kappa_o}{2} & 0 & 0 & 0 & iJ_t & 0 & -ig \\ -iJ_s & 0 & 0 & 0 & -\delta_s - \frac{\kappa_m}{2} & 0 & 0 & 0 & 0 & 0 \\ 0 & iJ_s & 0 & 0 & 0 & \delta_s - \frac{\kappa_m}{2} & 0 & 0 & 0 & 0 \\ 0 & 0 & -iJ_t & 0 & 0 & 0 & -\delta_t - \frac{\kappa_m}{2} & 0 & 0 & 0 \\ 0 & 0 & 0 & iJ_t & 0 & 0 & 0 & \delta_t - \frac{\kappa_m}{2} & 0 & 0 \\ 0 & ig & ig & 0 & 0 & 0 & 0 & 0 & -\frac{\kappa_e}{2} & 0 \\ -ig & 0 & 0 & -ig & 0 & 0 & 0 & 0 & 0 & -\frac{\kappa_e}{2} \end{pmatrix} \quad (8.4)$$

and,

$$\mathbf{K} = \begin{bmatrix} \sqrt{\kappa_{o,\text{ex}}} & \sqrt{\kappa_{o,\text{in}}} & 0 & 0 & 0 & 0 & 0 & 0 \\ 0 & 0 & \sqrt{\kappa_{o,\text{ex}}} & \sqrt{\kappa_{o,\text{in}}} & 0 & 0 & 0 & 0 \\ 0 & 0 & 0 & 0 & \sqrt{\kappa_m} & 0 & 0 & 0 \\ 0 & 0 & 0 & 0 & 0 & \sqrt{\kappa_m} & 0 & 0 \\ 0 & 0 & 0 & 0 & 0 & 0 & \sqrt{\kappa_{e,\text{in}}} & \sqrt{\kappa_{o,\text{ex}}} \end{bmatrix} \otimes \mathbb{1}_2, \quad (8.5)$$

where $\kappa_{j,\text{in}}$ and $\kappa_{j,\text{ex}}$ correspond to the intrinsic loss and external coupling rate of mode j . Here, we also assume the optical linewidth across the FSR is the same, $\kappa_o = \kappa_s = \kappa_t$ and $\kappa_m = \kappa_{sm} = \kappa_{tm}$.

We define the susceptibility of microwave or optical mode as,

$$\chi_j(\omega) = \frac{1}{\kappa_j/2 - i\omega}, \quad (8.6)$$

Here also, we define $\chi_o = \chi_s = \chi_t$ and $\chi_m = \chi_{sm} = \chi_{tm}$. We can obtain the effective susceptibility of microwave and optical mode $\chi_{j,\text{eff}}(\omega)$ from Eqn. 8.2. Note that it is easier to solve the equations if matrix \mathbf{S} is written in terms of susceptibilities $\chi_j(\omega)$. The output probing field can be obtained via input-output theorem, $\hat{a}_{j,\text{out}} = \hat{a}_{j,\text{in}} - \sqrt{\kappa_{j,\text{ex}}}\hat{a}_j$. From the output field, we can obtain the incoherent output noise spectral density via Wiener–Khinchin theorem in different detection schemes.

Here, we focus on the coherent response of the multimode cavity electrooptic system, where the amplitude reflection efficiency *in the lab frame* is given by,

$$S_{jj}(\omega + \omega_j) = 1 - \eta_j \kappa_j \chi_{j,\text{eff}}(\omega), \quad (8.7)$$

with $\eta_j = \kappa_{j,\text{ex}}/\kappa_j$ the external coupling efficient for mode j and ω_j being the absolute mode frequency of the mode j . In the experiment, it is easy to measure the relative change between the off-pulse and on-pulse response. With this relative measurement, and along with the measurement of the mode response with pulse off, we can calculate the mode response with the pulse-on. Consequently, it is good to define the spectral normalized reflection which is the ratio of the reflection efficiency between pulse on and off,

$$R_j(\omega) = |S_{jj}(\omega)/S_{jj,\text{off}}(\omega)|^2, \quad (8.8)$$

with $S_{jj,\text{off}}(\omega) = 1 - \kappa_{j,\text{ex}}\chi_j(\omega)$. Before the pulse is switched on, the absent back-action leads to $R_j(\omega) = 1$. During the pulse, the coherent and excess back-action leads to modification of $R_j(\omega)$. After the pulse, $R_j(\omega)$ restores to 1 if the measurement time is long enough.

Note that, in case of *on-resonant microwave probing*, the normalized reflection

$$R_e(\omega_e) = \left| \frac{1 - \kappa_{e,\text{ex}}/((\kappa_e + \delta\kappa_e)/2 + i\delta\omega_e)}{1 - 2\eta_e} \right|^2, \quad (8.9)$$

is more susceptible to the microwave frequency shift $\delta\omega_e$ compared to the linewidth change $\delta\kappa_e$.

8.2.1 Symmetric mode configuration

Symmetric mode configuration stands for $J_s = J_t = 0$ which means neither the Stokes nor the anti-Stokes interaction is suppressed. If we also assume ideal detunings ($\delta_s = \delta_{as} = 0$), microwave effective susceptibility remains the same,

$$\chi_{e,\text{eff}}(\omega) = \chi_e(\omega), \quad (8.10)$$

due to evaded electro-optical dynamical back-action. This means scattering to the optical Stokes mode balances with that to the optical anti-Stokes mode. In practice, however, there is some excess back-action causing $R_e(\omega)$ to deviate slightly from 1 because of other mechanisms - possibly quasi-particle production (see section 8.6.2).

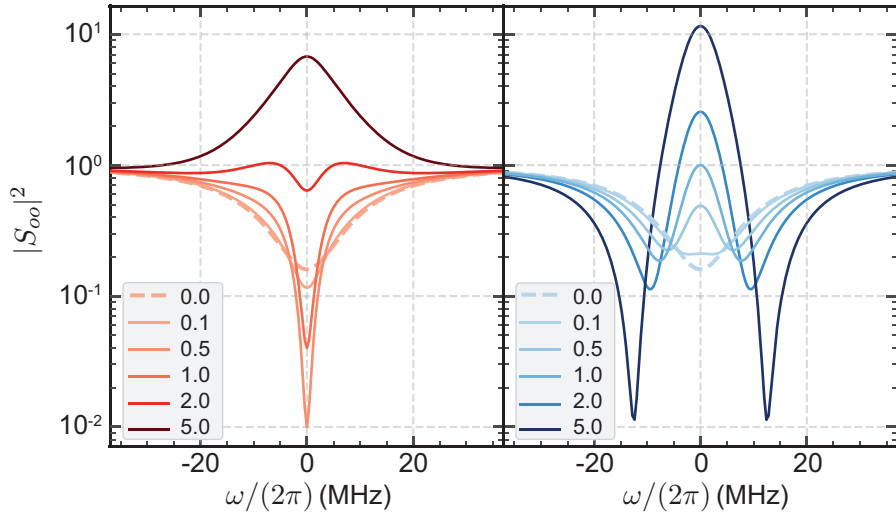


Figure 8.1: **Theoretical coherent optical response in the symmetric case at different C .** The left panel corresponds to the optical probing around the Stokes mode, while the right panel corresponds to optical probing around the anti-Stokes mode. (Parameters: $\kappa_o/2\pi = 30\text{MHz}$, $\eta_o = 0.3$, $\kappa_e/2\pi = 10\text{MHz}$) Figure adapted from Ref. [QSH⁺22].

Despite the absent dynamical back-action to the microwave mode, the optical susceptibility around the Stokes and anti-Stokes modes are changed,

$$\chi_{s/t,\text{eff}}(\omega) = \frac{1}{\chi_o(\omega)^{-1} \mp g^2/(\chi_e(\omega)^{-1} \pm g^2\chi_o(\omega))}. \quad (8.11)$$

In Fig. 8.1, we show the theoretical curves of the optical coherent response in the symmetric case ($J_{s/t} = 0$) at different C . For low C , $\chi_{s,\text{eff}}(\omega)$ and $\chi_{t,\text{eff}}(\omega)$ show similar behavior to

electro-optically induced absorption (EOIA) and transparency (EOIT), due to the constructive and destructive interference between the probe field and the electro-optical interaction induced field.

As C increases, both the Stokes and anti-Stokes mode probing response deviate from typical EOIA and EOIT behavior. For example, the optical reflection coefficient can even exceed unitary around resonance for anti-Stokes mode probing. Even in the symmetric case, the complex optical response of the multimode CEO system can be utilized for dispersion engineering of the probing field. At large C (e.g. $C \gg 2$), the symmetric multimode CEO system can function as a broadband electro-optical parametric amplifier for both Stokes and anti-Stokes signals.

8.2.2 Stokes mode configuration

In the Stokes case, i.e. $J_s = 0$, and the effective microwave susceptibility is given by,

$$\chi_{e,s}(\omega) = \frac{1}{\chi_e^{-1}(\omega) + g^2 \left(\frac{\chi_o(\omega + \delta_t)}{1 + J_t^2 \chi_o(\omega + \delta_t) \chi_m(\omega + \delta_t)} - \chi_o(\omega + \delta_s) \right)}. \quad (8.12)$$

The dynamical back-action results in microwave frequency shift (optical-spring effect) and linewidth decrease,

$$\begin{aligned} \delta\omega_e &= -\frac{4g^2\delta_s}{\kappa_o^2 + 4\delta_s^2} + \frac{4\delta_t g^2 (\kappa_m^2 - 4J_t^2 + 4\delta_t^2)}{8J_t^2 (\kappa_o \kappa_m - 4\delta_t^2) + (4\delta_t^2 + \kappa_o^2)(\kappa_m^2 + 4\delta_t^2) + 16J_t^4} \\ \delta\kappa_e &= -\frac{4g^2\kappa_o}{\kappa_o^2 + 4\delta_s^2} + \frac{4g^2 (\kappa_m (\kappa_o \kappa_m + 4J_t^2) + 4\delta_t^2 \kappa_o)}{8J_t^2 (\kappa_o \kappa_m - 4\delta_t^2) + (4\delta_t^2 + \kappa_o^2)(\kappa_m^2 + 4\delta_t^2) + 16J_t^4}, \end{aligned} \quad (8.13)$$

for the normal dissipation regime, i.e. $\kappa_o \gg \kappa_e$.

In the case of ideal detuning, i.e. $\delta_s = \delta_t = 0$,

$$\begin{aligned} \chi_{e,s}(\omega) &= \frac{1}{\chi_e^{-1}(\omega) - g^2 \chi_o(\omega) (1 - r_t(\omega))} \\ \chi_{s,\text{eff}}(\omega) &= \frac{1}{\chi_o^{-1}(\omega) - g^2 \chi_e(\omega) / (1 + g^2 \chi_e(\omega) \chi_o(\omega) r_t(\omega))} \end{aligned}, \quad (8.14)$$

where $r_t(\omega) = [1 + J_t^2 \chi_o(\omega) \chi_m(\omega)]^{-1} < 1$ is the ratio of anti-Stokes to Stokes scattering rate.

In the case of complete suppression of the anti-Stokes scattering $4J_t^2 \gg \kappa_o \kappa_m$, we obtain,

$$\begin{aligned} \chi_{e,s}(\omega) &= \frac{1}{\chi_e(\omega)^{-1} - g^2 \chi_o(\omega)} \\ \chi_{s,\text{eff}}(\omega) &= \frac{1}{\chi_o(\omega)^{-1} - g^2 \chi_e(\omega)} \end{aligned}, \quad (8.15)$$

which is *symmetric under interchange of microwave and the optical Stokes mode*.

As seen from the red curves in Fig. 8.2, the microwave response shows *effective narrowing in the normal dissipation regime (upper left)*, while *EOIA in the reversed dissipation regime (upper right)*. The optical response around the Stokes mode shows *EOIA in the normal dissipation regime (lower left)*, while *effective narrowing in the reversed dissipation regime (lower right)*. The asymmetric multimode CEO system can be adopted for "fast light" of optical (microwave) probing field in the normal (reversed) dissipation regime, with reduced group delay [Thé08, Boy09].

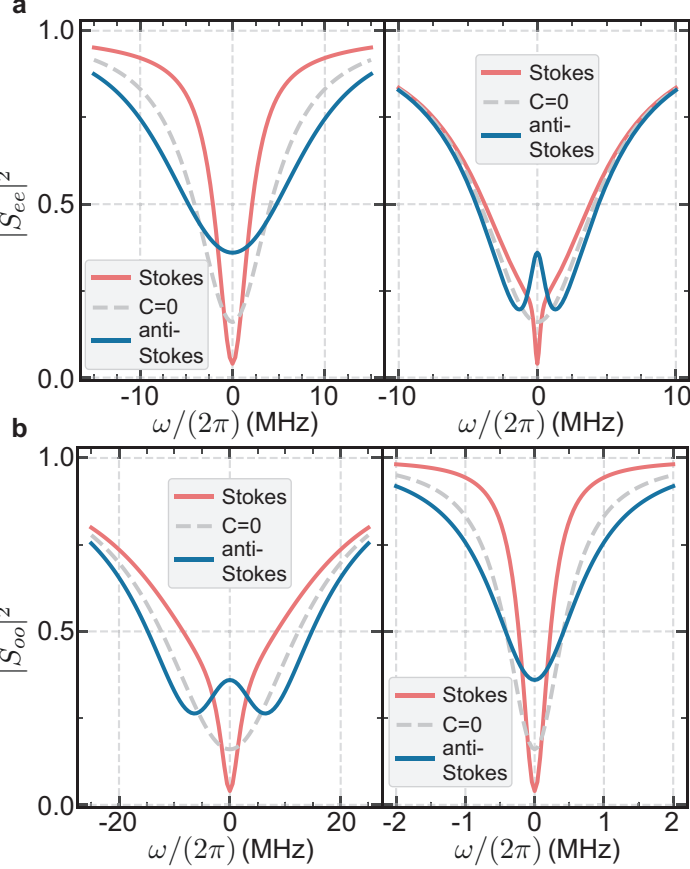


Figure 8.2: **Theoretical coherent multimode electro-optical dynamical back-action in normal and reversed dissipation regime.** The two left panels correspond to the normal dissipation regime with $\kappa_o \gg \kappa_e$. (Parameters: $\kappa_o/2\pi = 30\text{MHz}$, $\eta_o = 0.3$, $\kappa_e/2\pi = 10\text{MHz}$, $\eta_e = 0.3$, and $C = 0.5$) The red and blue solid curves correspond to the Stokes and anti-Stokes case with $C = 0.5$, while the dashed curves correspond to the original reflection coefficient with $C = 0$. The two right panels correspond to the reversed dissipation regime with $\kappa_o \ll \kappa_e$. (Parameters: $\kappa_o/2\pi = 1\text{MHz}$, $\eta_o = 0.3$, $\kappa_e/2\pi = 10\text{MHz}$, $\eta_e = 0.3$, and $C = 0.5$). Figure adapted from Ref. [QSH⁺22].

8.2.3 anti-Stokes mode configuration

In the anti-Stokes case, i.e. $J_t = 0$, the effective microwave susceptibility is given by,

$$\chi_{e,\text{as}}(\omega) = \frac{1}{\chi_e(\omega)^{-1} + g^2 \left(\chi_o(\omega + \delta_t) - \frac{\chi_o(\omega + \delta_s)}{1 + J_s^2 \chi_o(\omega + \delta_s) \chi_m(\omega + \delta_s)} \right)} \quad (8.16)$$

In this case, the dynamical back-action results in optical-spring effect and effective microwave linewidth increase,

$$\begin{aligned} \delta\omega_e &= \frac{4g^2\delta_t}{4\delta_t^2 + \kappa_o^2} - \frac{4g^2\delta_s(\kappa_m^2 - 4J_s^2 + 4\delta_s^2)}{8J_s^2(\kappa_o\kappa_m - 4\delta_s^2) + (\kappa_o^2 + 4\delta_s^2)(\kappa_m^2 + 4\delta_s^2) + 16J_s^4} \\ \delta\kappa_e &= \frac{4g^2\kappa_o}{4\delta_t^2 + \kappa_o^2} - \frac{4g^2(\kappa_m(\kappa_o\kappa_m + 4J_s^2) + 4\kappa_o\delta_s^2)}{8J_s^2(\kappa_o\kappa_m - 4\delta_s^2) + (\kappa_o^2 + 4\delta_s^2)(\kappa_m^2 + 4\delta_s^2) + 16J_s^4}, \end{aligned} \quad (8.17)$$

for the normal dissipation regime, i.e. $\kappa_o \gg \kappa_e$.

In the case of ideal detuning, i.e. $\delta_s = \delta_t = 0$,

$$\begin{aligned}\chi_{e,\text{eff}}(\omega) &= \frac{1}{\chi_e^{-1}(\omega) + g^2\chi_o(\omega)(1 - r_s(\omega))}, \\ \chi_{t,\text{eff}}(\omega) &= \frac{1}{\chi_o^{-1}(\omega) + g^2\chi_e(\omega)/(1 - g^2\chi_e(\omega)\chi_o(\omega)r_s(\omega))}\end{aligned}\quad (8.18)$$

where $r_s(\omega) = [1 + J_s^2\chi_o(\omega)\chi_m(\omega)]^{-1} < 1$ is the ratio of the Stokes to the anti-Stokes scattering rate. When the anti-Stokes scattering is fully suppressed ($4J_s^2 \gg \kappa_o\kappa_m$), we obtain,

$$\begin{aligned}\chi_{e,\text{as}}(\omega) &= \frac{1}{\chi_e(\omega)^{-1} + g^2\chi_o(\omega)} \\ \chi_{t,\text{eff}}(\omega) &= \frac{1}{\chi_o(\omega)^{-1} + g^2\chi_e(\omega)},\end{aligned}\quad (8.19)$$

which is *symmetric under interchange of microwave and the anti-Stokes mode*.

As seen from the blue curves in Fig. 8.2, the microwave response shows *effective broadening in the normal dissipation regime (upper left)*, while *EOIT in the reversed dissipation regime (upper right)*. The optical response around the anti-Stokes mode shows *EOIT in the normal dissipation regime (lower left)*, while *effective broadening in the reversed dissipation regime (lower right)*. The asymmetric multimode CEO system can be adopted for "slow light" of optical (microwave) probing field in the normal (reversed) dissipation regime, with increased group delay [Thé08, Boy09]. For simplicity, we assume the same cavity coupling coefficient 0.3 for both microwave and optical modes in the theoretical calculations in Fig. 8.2.

8.2.4 An intuitive picture

The mode interferences presented in Fig. 8.2 can also be understood more intuitively using loss rates involved with the optical and microwave modes and the electro-optic interaction acting as an effective extra loss rate. First, we consider the case of Fig. 8.2a, where $\kappa_e \ll \kappa_o$. For the optical Stokes mode suppression case, the electro-optic interaction deviates power from the microwave mode to the optical anti-Stokes mode. This effectively opens up an extra internal loss channel for the microwave mode (it is internal because the diverted power does not couple to the microwave waveguide). Since the electro-optic interaction effectively increase the internal losses of the microwave mode, we should expect it to get more undercoupled and broadened. This is exactly what we see in Fig. 8.2a. In case of anti-Stokes mode suppression, the electro-optic interaction with the optical Stokes mode, amplifies the power in the microwave mode coherently, effectively cancelling out the effect of the internal losses. As a result, in this case, the microwave mode internal losses are effectively reduced and we should thus expect it get more overcoupled and narrowed exactly as we see in Fig. 8.2a.

With the exact same reasoning, we can also understand the panel d of Fig. 8.2. In this panel, we assume the opposite $\kappa_o \ll \kappa_e$ and since electro-optic interaction is symmetric, the microwave and optical mode simply exchange roles keeping our initial intuitive reasoning intact.

For the remaining panels b and c of Fig. 8.2, the linewidth of the probed mode is larger than the mode it is interacting with. We can still view the mode interaction as change in effective internal loss rates of the probed modes but now since the interacting mode is narrower, the effect on the probed mode is more local and appears more as two separate Lorentzian functions.

8.3 Experimental setup

The measurements shown in this chapter were conducted with the measurements shown in the chapter 9. Please refer to section 9.3 of the next chapter for all the details regarding the experimental setup.

8.4 Mode characterization

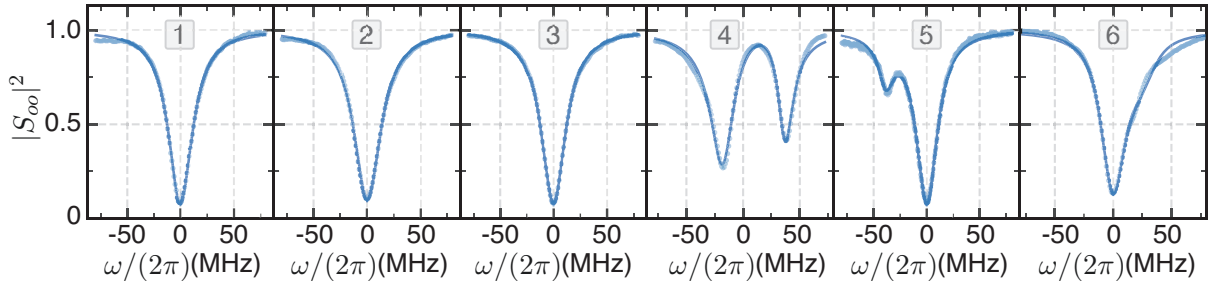


Figure 8.3: **Optical modes.** The optical TE mode family for dynamical backaction measurements. The separation between the more contrasted lobe between each mode is stated in table 8.1. We pump the mode 2 for symmetric scattering case, mode 3 for anti-Stokes mode suppression and mode 5 for Stokes mode suppression. Figure adapted from Ref. [QSH²²].

Optical modes

To experiment with different mode configurations (symmetric, Stokes and anti-Stokes), we use six optical TE modes of the same family (same p and q mode number) separated by one FSR. Fig 8.3 shows the normalized mode reflection $|S_{oo}|^2$ for each of the six modes. One of the mode is well hybridized by a degenerate TM mode (mode 4) and two are partially hybridised (mode 5 and 6). The separation between the modes is given in table 8.1 as the frequency gap between the main dips of each mode.

Modes	1 and 2	2 and 3	3 and 4	4 and 5	5 and 6
Separation	8.799GHz	8.799GHz	8.791GHz	8.817GHz	8.795GHz

Table 8.1: Calibrated frequency separation of the adjacent optical modes, shown as the distance between the main dip of each optical modes.

The mode characterization is done in frequency domain as stated in section 3.2.6. The optical TE mode 1, 2 and 3 shown in Fig 8.3 are fit with parameters - total linewidth $\kappa_o/2\pi \sim 26$ MHz, of which the external coupling rate is $\kappa_{o,\text{ex}}/2\pi \sim 10$ MHz with the mode mismatch factor $\Lambda = 0.83$. The split modes 4,5 and 6 are characterized as in section 3.5 and the fit parameters are reported in table 8.2.

Microwave modes

For the different optical mode configurations, we pumped on different optical modes and chose appropriate modes as the probe mode. The effective FSR in each case is given by the separation between the pump mode and the probe mode and the microwave frequency has to be matched to the effective FSR. For 3 out the 4 configurations we show, the effective FSR

Modes	$\kappa_o/2\pi$	$\kappa_{o,\text{ex}}/2\pi$	$\delta_o/2\pi$	$\kappa_{o,\text{tm}}/2\pi$	$\delta_{o,\text{tm}}/2\pi$	$J/2\pi$
4	34.6	8.9	-17.8	7.6	-18.5	26
5	24.7	9.8	5	17.4	28.3	13
6	24.3	9.2	-3.9	30	-18.7	10

Table 8.2: **Fit parameters for the split modes.** κ_o and κ_m correspond to the total loss rate of the TE and corresponding TM mode. δ_o and δ_m correspond to the cavity detuning of TE and corresponding TM mode to the main dip of the split mode, which is centered to zero in Fig. 8.3.

is 8.799 GHz and the Stokes mode suppressed configuration, the effective FSR is 8.795 GHz (see table 8.3).

As a result, we tune the microwave mode to the two required frequencies - 8.799 GHz and 8.795 GHz. The microwave mode is characterized with VNA reflection measurement (same as section 3.3.4). We fit the total linewidth $\kappa_e/2\pi = 11.6$ MHz with $\eta_e = 0.39$.

Pump Config.	Probing Mode	Pump Mode	Probe Mode	MW Frequency
Sym.	Stokes	2	1	8.799 GHz
Sym.	anti-Stokes	2	3	8.799 GHz
Stokes	Stokes	3	2	8.799 GHz
anti-Stokes	anti-Stokes	5	6	8.795 GHz

Table 8.3: **Measurement details for different mode and probing configurations.** The pump mode and probe mode indexes are given for each probing configurations. Microwave frequency is adjusted accordingly to match the pump and probing mode separation.

8.5 Measurement

To measure the coherent response experiments in the pulsed regime, we send a short optical pump pulse ($\tau \sim 500$ ns - 2 μ s) to the device, while keeping the weak microwave or optical probing field continuously on. The optical pump pulses are triggered at rate of 100Hz for all the experiments, except for the Stokes case (2Hz). We sweep the frequency of the probe signal around the probed mode to reconstruct the full microwave or optical response. For each frequency, the pulses are repeated 2500 times. In addition, we sweep the pump pulse power to investigate the power dependence of the dynamical back-action with peak power ~ 500 mW. The RF signal from the balanced heterodyne detection of the optical probing field and the frequency down-converted microwave signal are recorded by a digitizer. In our experiments, both optical and microwave LO are detuned by 40MHz from the probing signal frequency. All the dynamical back-action data are taken from the time domain traces at 1GS/s sampling rate for different mode and probing configurations, except for the delayed excess back-action data shown in Fig. 8.10, which is taken by the SA in the zero-span mode¹ at microwave resonance frequency with 200 MHz bandwidth.

¹Time domain measurement mode with no frequency sweep.

8.5.1 Mode susceptibility reconstruction

Here, we discuss how the mode susceptibility was reconstructed for different cooperativities and as a function of time. We have already defined the spectral normalized reflection for the probing field,

$$R_j(\omega) = |S_{jj}(\omega)/S_{jj,\text{off}}(\omega)|^2, \quad (8.20)$$

which we measure experimentally. We now argue that this measurement is enough to accurately reconstruct the effective mode susceptibility irrespective of other frequency dependent experimental parameters.

In the absence of the pump pulse, the output photon number of the probing field takes the form

$$\bar{n}_{\text{out,off}}(\omega) = \bar{n}_{\text{in}}(\omega)|S_{jj,\text{off}}(\omega)|^2\eta_d(\omega), \quad (8.21)$$

where $\bar{n}_{\text{in}}(\omega)$ and $\eta_d(\omega)$ are the frequency dependent input photon number and the detection efficiency. After the pump pulse arrives, the output photon number of the probing field is modified to,

$$\bar{n}_{\text{out}}(\omega) = \bar{n}_{\text{in}}(\omega)|S_{jj}(\omega)|^2\eta_d(\omega). \quad (8.22)$$

For long enough measurement time as in our experiments, the coherent response of the probing field restores to the state before the pulse starts. We thus approximate $S_{jj,\text{off}}(\omega)$ to $S_{jj}(\omega)|_{t=0}$. The ratio of $\bar{n}_{\text{out,off}}(\omega)$ and $\bar{n}_{\text{out}}(\omega)$ is the same as $R_j(\omega)$. Any frequency dependent imperfections simply cancel out and, thus, effective mode susceptibilities $S_{jj}(\omega)$ can be reconstructed accurately with just $R_j(\omega)$ and $S_{jj,\text{off}}(\omega)$.

In this chapter, we only focus on the output power in the detection. We perform digital down-conversion of the time-domain data at 40MHz for each probing frequency, where the averaged voltages over the pulses are adopted to obtain the mean power. We track the normalized reflection coefficient over time while scanning the probe field frequency,

$$R_j(\omega + \omega_{\text{LO},j}) = \frac{\bar{P}_{\text{out},j}(\omega)}{\bar{P}_{\text{out},j}(\omega)|_{t=0}}, \quad (8.23)$$

with $\omega_{\text{LO},j}$ the LO frequency and $\bar{P}_{\text{out},j}$ the averaged power of the RF field from digital down-conversion. Typical obtained on-resonant $R_j(\omega)$ in time domain are shown in Fig. 8.4. Since any input power fluctuation or change in detection as a function of time or frequency affects both on pulse and off pulse equally, by tracking them both in time and then taking the ratio, we avoid the complicated system calibration and frequency dependence on the input and detection sides, especially on the optical side due to the filter drifts (see section 9.3.1).

8.6 Results

8.6.1 Stationary Dynamical Back-action

We start with the temporal response on-resonance of the probed mode which is shown in Fig. 8.4. Before $t = 0$, there is no electro-optic interaction and the probed mode remains unchanged. When the optical pump pulse comes, the reflected power changes as dictated by the electro-optic interaction. The change in reflection before $t = 0$ and in the middle of the optical pump pulse ($t \sim 200$ ns) indicates how the mode response changed due to electro-optic interaction (at resonance in this case). We can similarly reconstruct the full coherent stationary spectral response by sweeping the probe tone frequency around the probed

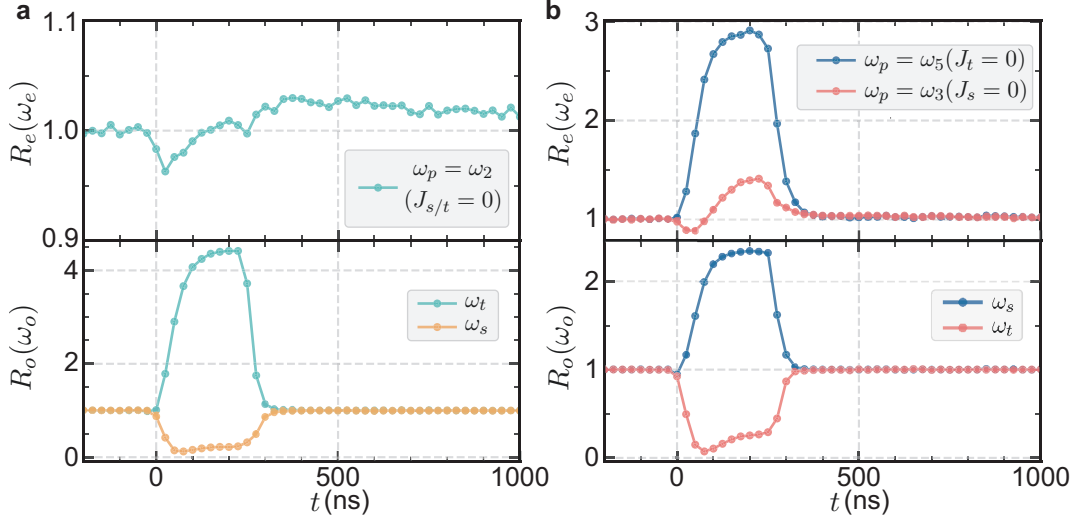


Figure 8.4: Dynamics of reflected probe tone. Temporal on-resonant response $R(\omega)$ [cf. Eq. 8.20] between pulse on and off (pump peak power ~ 500 mW). Left panel shows the symmetric case ($\omega_p = \omega_2$), with on-resonant microwave response (turquoise blue curve) in the upper panel and optical Stokes (orange curve) and anti-Stokes (turquoise blue curve) responses in the lower panel. Right panel shows the two asymmetric cases, i.e. the on-resonant microwave and optical Stokes responses (red curves) in the Stokes case ($\omega_p = \omega_3$), and the resonant microwave and optical anti-Stoke responses (blue curves) in the anti-Stokes case ($\omega_p = \omega_5$). Figure adapted from Ref. [QSH²²].

mode resonance. Repeating these frequency sweeps for different pump pulse powers in each configuration allows us to probe how the coherent stationary spectral response changes as a function of cooperativity.

We plot the $R_e(\omega)$ for the three different pump configurations in the upper panel of Fig. 8.5 using the same pump as in Fig. 8.4. Using the pulse-off response $|S_{ee,\text{off}}(\omega)|^2$ (which is plotted as dashed lines in the bottom panels of Fig. 8.5) and $R_e(\omega)$, we can reconstruct the full pulse-on mode response which are plotted as solid lines in bottom panels.

The solid lines in the upper panel of Fig. 8.5 and 8.7 come from a joint fit of the coherent microwave $R_e(\omega)$ and optical $R_o(\omega)$ response at the steady regime of the pulse for all the powers, with microwave linewidth, microwave external coupling rate, optical linewidth, optical external coupling rate as shared parameters.

For the symmetric case of balanced Stokes and anti-Stokes scattering, $R_e(\omega)$ remains unchanged as expected (center panel of Fig. 8.5). On the other hand, microwave mode response changes dramatically around the mode resonance for the two asymmetric cases due to strong dynamical back-action (left and right panels). The lower panels show the pulse-on (solid) and pulse-off (dashed) responses together. Compared to the pulse-off response, we observe microwave linewidth narrowing and a slight frequency increase in the Stokes case ($\omega_p = \omega_3$) and linewidth broadening in the anti-Stokes case ($\omega_p = \omega_5$) with an increased resonant reflection.

From the joint fit of the coherent microwave $R_e(\omega)$ and optical $R_o(\omega)$ response, we extract the microwave frequency shift ($\delta\omega_e$) and linewidth ($\delta\kappa_e$) change as a function of optical pump power for each pump configuration. This is shown in Fig. 8.6. For the symmetric case ($\omega_p = \omega_2$), no evident frequency or linewidth change is observed as expected due to the evaded back-action. For the anti-Stokes case ($\omega_p = \omega_5$) the microwave linewidth increases linearly

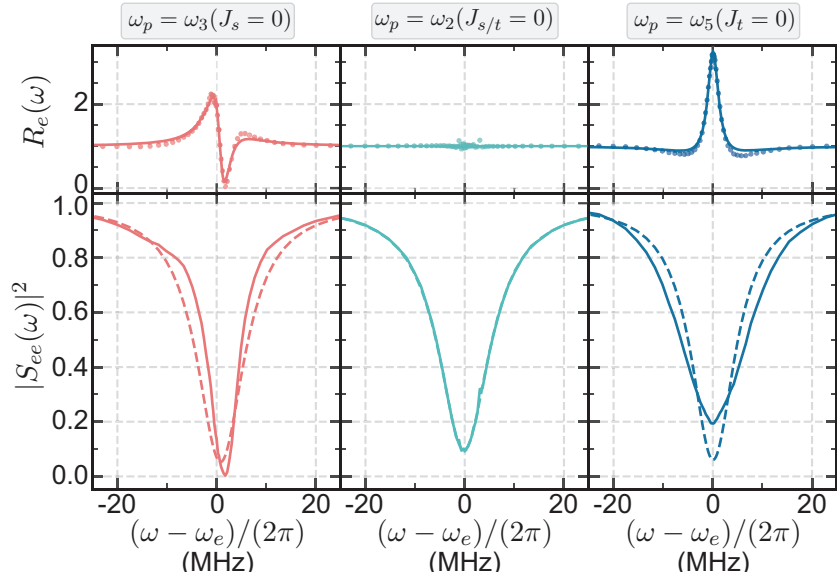


Figure 8.5: Stationary backaction in microwave mode. Microwave response measurements with the same pump power as in Fig. 8.4. The upper panel shows the stationary $R_e(\omega)$, with fitting curves as solid lines. The lower panel shows the reconstructed microwave reflection $|S_{ee}(\omega)|^2$ with the pump on (solid curve) and off (dashed curve) from the fitted parameters. Figure adapted from Ref. [QSH²²].

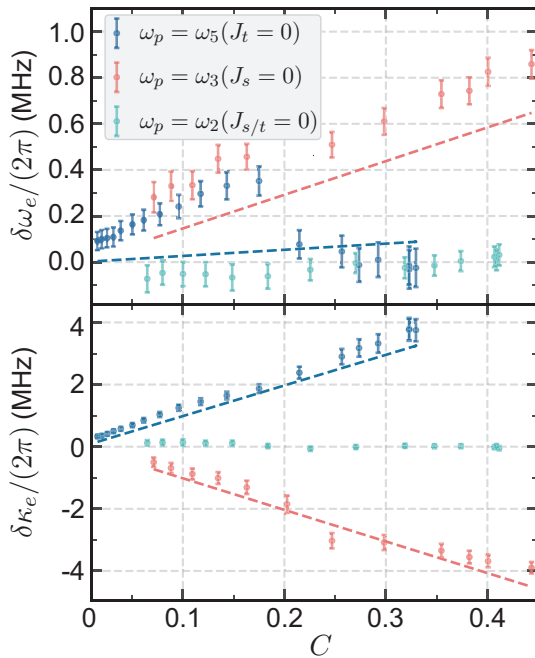


Figure 8.6: Microwave mode parameter change due to backaction. Fitted microwave frequency shift and linewidth change versus cooperativity C . Dashed lines are theoretical curves. Error bars represent the 95% confidence interval of the fit. Figure adapted from Ref. [QSH²²].

with C , while it decreases linearly for the Stokes case ($\omega_p = \omega_3$). We also make theoretical predictions (dashed lines), which are obtained from independent mode characterization and using a full dynamical back-action model incorporating optical response fitting parameters including imperfect frequency detunings [cf. Fig. 8.8]. The predictions match very well with experimental results for both asymmetric cases. The observed deviation of the microwave frequency change of $\sim 10^{-4}\omega_e$ in the anti-Stokes case can be attributed to small detuning uncertainties (sub-MHz) as discussed in the section 8.2.

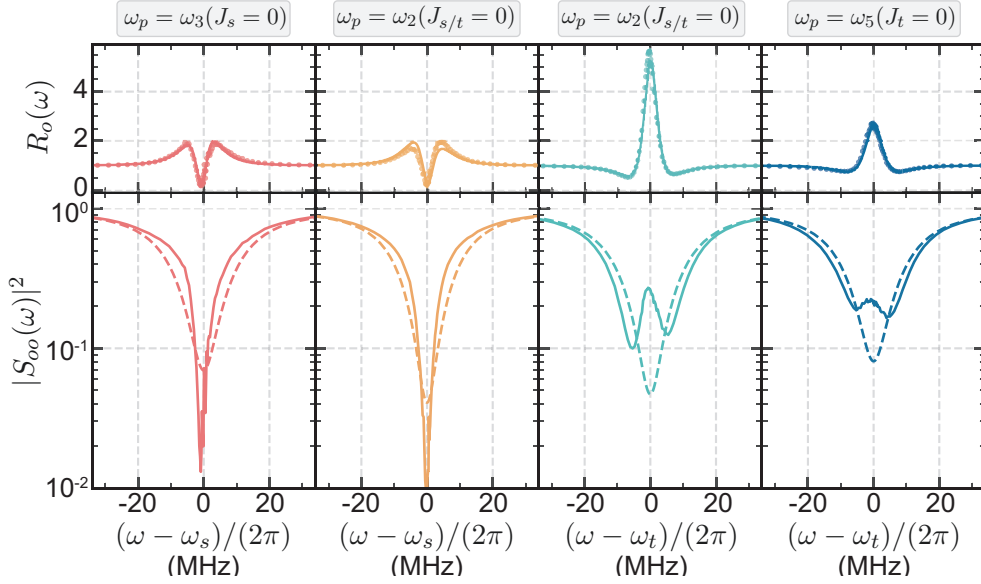


Figure 8.7: **Stationary backaction in optical modes.** Measurements with same pump power as in Fig. 8.4, with the two left panels for Stokes mode probing and the two right panels for anti-Stokes mode probing. The upper panel shows $R_o(\omega)$ with fitting curves (solid lines). The lower panel shows reconstructed optical reflection $|S_{oo}(\omega)|^2$ with pulse on (solid curve) and off (dashed curve) in logarithmic scale, which demonstrates EOIA in the Stokes case and EOIT in the anti-Stokes case. Figure adapted from Ref. [QSH⁺22].

The same measurements are repeated for the optics anti-Stokes and Stokes mode for the three pump configurations. For the balances case, we probe both the Stokes and anti-Stokes optical mode response but for the cases when one of the optical sideband was suppressed, we only probe the other unsuppressed optical signal mode. These measurements are shown in Fig. 8.7. Upper panels again show the normalized mode reflection $R_o(\omega)$ along with the joint fits (solid lines) for each mode configuration. The bottom panels show the pulse-off (dashed lines) and pulse-on (solid lines) mode responses for each case. The Stokes mode probing (left two panels) reveals similar electrooptic induced absorption (EOIA) for the Stokes and symmetric cases when the pump pulse is on, while the anti-Stokes mode probing (right two panels) indicates similar electrooptic induced transparency (EOIT) for the symmetric and anti-Stokes cases.

In Fig. 8.8, we show the on-resonant reflection efficiency versus C for different probing configurations with theoretical predictions shown in dotted lines. In the upper panel, $|S_{oo}(\omega_s)|^2$ at the Stokes mode resonance first approaches zero and then increases with C due to EOIA. For $C \gg 1$, the reflection efficiency eventually exceeds far above unity, which would enable parametric amplification of the Stokes signal. In the lower panel, $|S_{oo}(\omega_{as})|^2$ at the anti-Stokes resonance increases slowly as C increases due to EOIT. We note that, the different on-resonant $|S_{oo}|^2$ at low C is due to the slightly different external coupling efficiency of the optical modes.

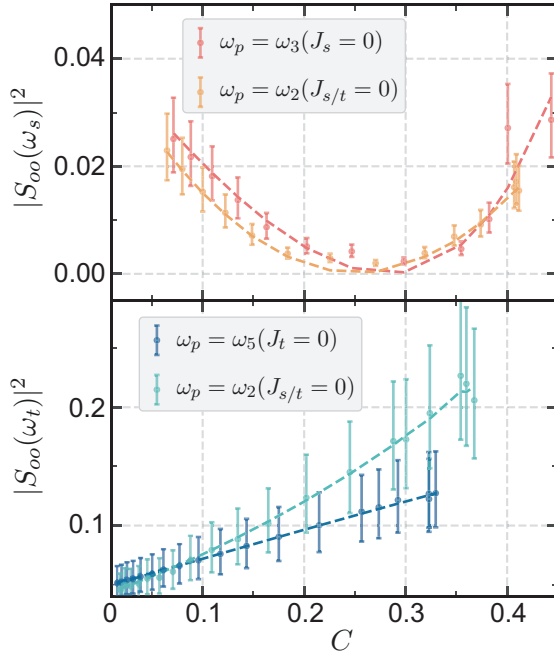


Figure 8.8: **Optical reflection change due to backaction.** The upper panel shows $|S_{oo}(\omega_s)|^2$ for the two Stokes mode probing cases, while the lower panel shows $|S_{oo}(\omega_{as})|^2$ for the two anti-Stokes mode probing cases. The corresponding theoretical curves are shown as dashed lines. Error bars indicate two standard deviations. Figure adapted from Ref. [QSH⁺22].

The highest cooperativity $C \sim 0.5$ in these measurements were limited due to parametric amplification kicking in due to Kerr nonlinearity, which is discussed in detail in section 7.7.

8.6.2 Transient back-action in microwave

In the previous section, we saw the spectral mode response of the signal modes. However, this spectral mode response is indicative of a steady-state which we assumed is established about 200 ns after the optical pump pulse arrives. But since the original data was taken in time-domain with a high enough bandwidth, we can also study the temporal back-action in the modes.

The transient back-action in microwave mode is especially interesting. Not only we observe an electro-optic dynamical backaction due to the $\chi^{(2)}$ nonlinearity, but we also witness evidence of some excess delayed backaction due to some other mechanism.

Dynamical back-action

Starting from the transient response from Fig. 8.4, we perform the joint fit of $R_o(\omega)$ and $R_e(\omega)$ incorporating the full DBA model and the cooperativity and detunings as the free parameters. The fit cooperativity is, then, plotted as a function of time in the upper panels of Fig. 8.9 for all different pump configurations. The fitted $C(t)$ increases smoothly in the beginning, as the optical pump pulse arrives, reaches stationary value in the middle (steady-state), and finally slowly decreases to zero after the optical pulse is gone. Similar to the Fig. 8.6, where the microwave resonance shift and linewidth change is plotted as a function of cooperativity, we now show the same parameters as a function of time in the bottom two panels of Fig. 8.9. The theoretical predictions are plotted as dashed line.

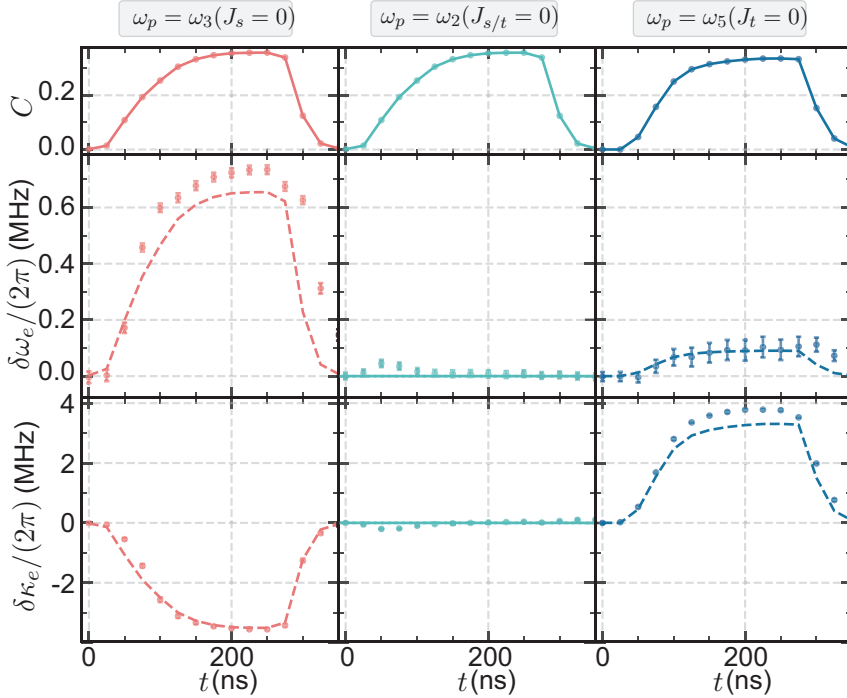


Figure 8.9: **Transient backaction in microwave mode.** Instantaneous coherent microwave responses during the pump pulse obtained for the same pump power as in Fig. 8.4. In each pump configuration, we perform a joint fit of $R_o(\omega)$ over the time of the pulse with the full dynamical back-action model, and extract the time dependent $C(t)$ (upper panel). Similarly, we perform a joint fit of $R_e(\omega)$ to obtain the frequency and linewidth changes (dots) over time, with corresponding theoretical curves (dashed lines) using the above fitted parameters from the optical coherent response. Error bars represent the 95% confidence interval of the fit. Figure adapted from Ref. [QSH⁺22].

The small blue shift of the microwave mode in the two asymmetric mode configurations is due to imperfect detunings (sub-MHz) as explained in SI 8.2. The linewidth change follows closely the predicted coherent electro-optical dynamical back-action, i.e. narrowing in the Stokes case and broadening in the anti-Stokes case. In the symmetric case, a very slight excess frequency drift ($\sim 10^{-5} \omega_e$) and linewidth change ($\sim 10^{-2} \kappa_e$) indicate a finite amount of *instantaneous excess back-action* to the microwave mode in the beginning and at the end of the pulse, due to the loading and unloading of the optical pump field.

Delayed excess back-action

After the pump pulse, we observe a small amount of excess back-action that remains in the microwave mode for a few μs , while it ceases immediately in the optical mode after the optical pump pulse is gone. We make measurement for both cases - when the microwave frequency matches the optical FSR (on-resonant case) and when it doesn't (off-resonant case). For both of these cases, we show the coherent microwave response $R_e(\omega_e)$ for the symmetric case ($J_{s/\text{as}} = 0$) over time using a similar pulse power as in Fig. 8.4 with different optical pump pulse lengths in Fig. 8.10. The behaviour is very similar for both the cases which rules out the electro-optical interaction as the main origin of the induced perturbation. The first bounce comes with the start of the optical pulse at $t = 0$ and it starts to decay after the pulse ends (marked with turquoise blue dot). However, after t_{ex} time, we observe a new maxima of reflection marked by purple dot. It seems that t_{ex} depends on the optical pump pulse length

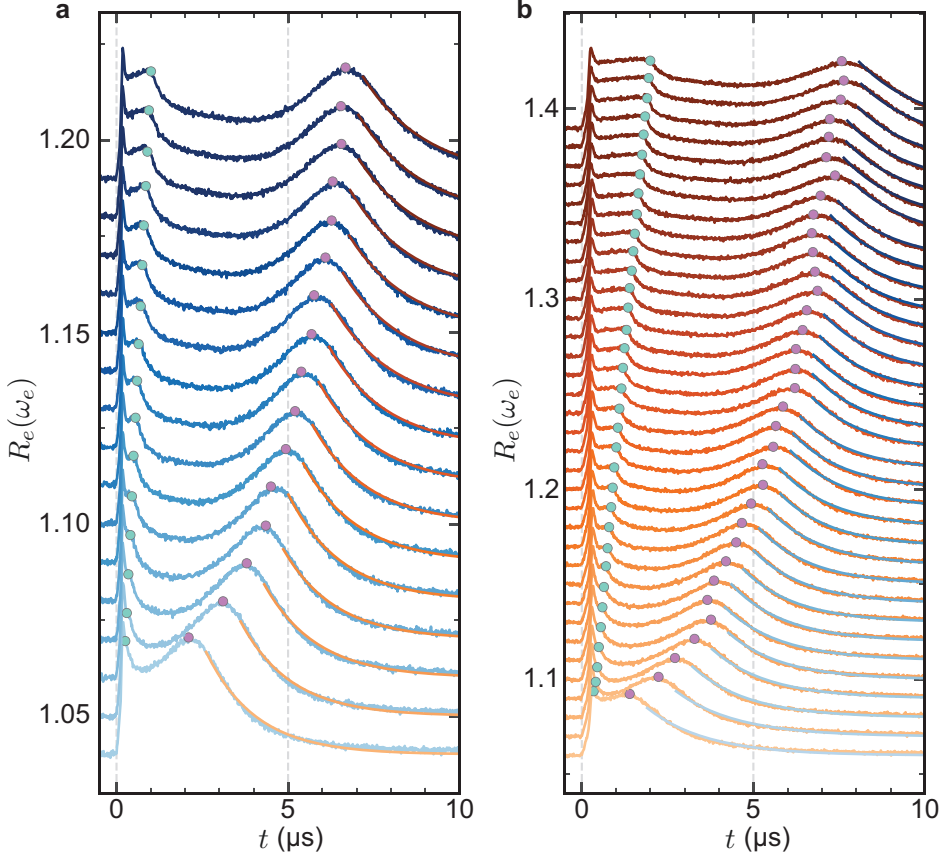


Figure 8.10: Excess delayed backaction in microwave. Instantaneous coherent microwave response in the symmetric case ($J_{s/\text{as}} = 0$) with different pulse lengths. **a** (**b**) show The on-resonant $\omega_e = FSR$ (off-resonant $\omega_e \neq FSR$) cases. The corresponding pulse end and the bounce of the delayed back-action are indicated with turquoise blue and purple dots, where the time difference is t_{ex} . The mean lifetime τ_{ex} is fitted from exponential decay of $R_e(\omega_e)$ after the bounce, shown as orange and blue curves in the left and right panels. Figure adapted from Ref. [QSH⁺22].

used which indicates an integrated optical pulse energy dependent excess mechanism that changes the microwave response. After the bounce, $R_e(\omega_e)$ continues to decrease exponentially to unity with a time constant τ_{ex} .

In Fig. 8.11, we show the extracted t_{ex} and τ_{ex} from the fitted time dependence for different pump pulse lengths from Fig. 8.10. In both the resonant and off-resonant cases, t_{ex} increases versus pulse length τ and saturates at $\sim 6 \mu\text{s}$ for long pulse lengths above $\sim 1 \mu\text{s}$, while the on-resonant excess back-action arrives later than the off-resonant one most likely related to electro-optical interaction. Interestingly, the fitted τ_{ex} ($\sim 1.6 \mu\text{s}$) is quite similar for both detuning cases, indicating a general underlying mechanism, e.g. light induced quasi-particles [MSKP20].

It is important to point out that the observed frequency shifts and linewidth changes are only on the order of 100kHz, i.e. 10^{-5} of the microwave resonant frequency as shown in Fig. 8.12. This is the stark difference we observe in our system compared to other systems where much larger frequency shift (larger than the cavity linewidth) are observed as a result of optical pump power [FXL⁺21]. This feature of our system lets us pump such huge amount of optical powers without any grave consequences.

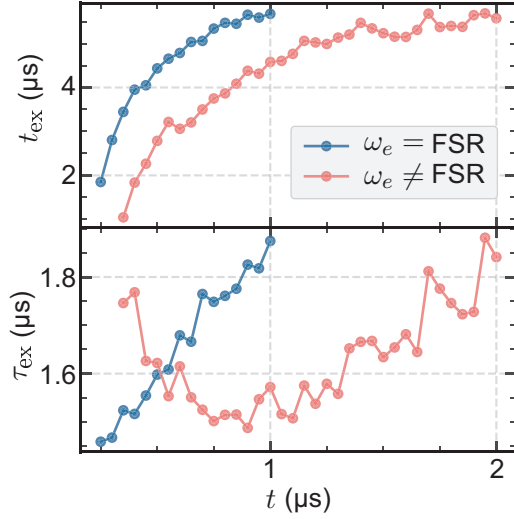


Figure 8.11: Extracted bounce time t_{ex} after the pulse is off and the mean decay time τ_{ex} as a function of pulse length. The blue and red curves correspond to the on-resonant and off-resonant cases. Figure adapted from Ref. [QSH⁺22].

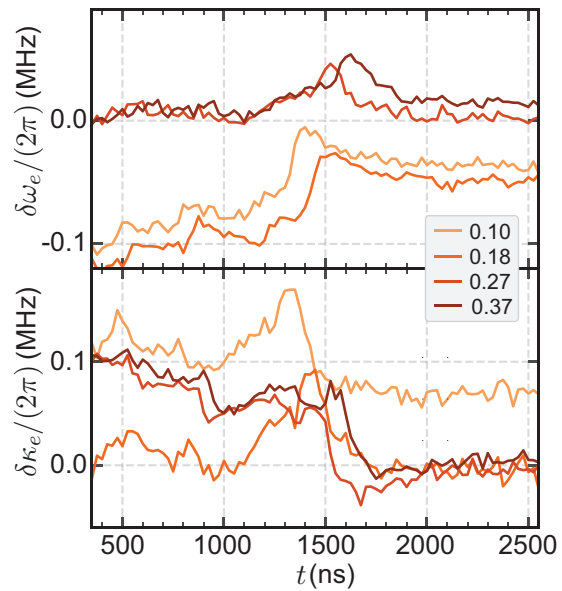


Figure 8.12: Fitted microwave frequency and linewidth change after the optical pulse. Different color corresponds to different C . Figure adapted from Ref. [QSH⁺22].

Another important point is that our device revives completely in only tens of μs after the optical pulse. Nevertheless, in all the presented experiments we adopt a trigger time of 10 ms for all pump configurations (500 ms in the Stokes case) to avoid thermal heating due - likely - to optical absorption.

8.7 Conclusions

In this chapter, we demonstrate electro-optical dynamical back-action with pulsed optical pump and near-unitary cooperativity. We show both stationary mode response in frequency domain and transient mode response when the optical pump arrives. All the presented results agree well with the 6-mode model presented in this chapter. We also take a deeper look into the excess delayed backaction to the microwave mode and find that it is surprisingly small for the high optical pump powers we use.

Now that we understand the electro-optical response of the signal modes and any adverse effects of pumping high optical powers into the system, we can measure the tiny changes in quantum noise due to electro-optic interaction. We already saw a signature of vacuum noise amplification in the chapter 7. In the next chapter, we measure this amplification in the microwave and Stoke mode more systematically and check whether the produced joint correlations can be pushed below the vacuum levels establishing entanglement between the modes.

CHAPTER 9

Entanglement between microwave and optics

9.1 Introduction

In the chapter 7, we find that an optical pump pulse with high-enough cooperativity would amplify (via the interaction with the Stokes optical mode) any noise present in microwave mode - including the vacuum noise. This amplified noise in the two modes (optical and microwave) is correlated owing to its origin from the same optical pump. If thermal or classical noise is amplified, the correlations thus generated are also classical, meaning such correlations can also be generated by classical means. However, if no classical signal or noise was present in the signal modes, the vacuum noise is amplified. The phenomenon is then called spontaneous parametric downconversion (SPDC). The amplified vacuum noise has correlations that go beyond the classical limit. In our particular case, the correlations exist when the noise from one mode is compared with the other. This is also known as two-mode squeezing because the noise in the one joint quadrature is squeezed while in the other is anti-squeezed. If the noise in the squeezed joint quadrature goes below the vacuum noise, for Gaussian bipartite states (as is the case here), the states are entangled.

In this chapter, we measure two-mode squeezing between the microwave \hat{a}_e and optical Stokes mode $\hat{a}_s \equiv \hat{a}_o$. Even though ideally we want no classical signal or noise in the signal modes, in practice, we always have some thermal noise in the microwave mode. The idea then is to lower the ratio of thermal noise to vacuum noise as much as possible. Consequently, here we work with a optical pump pulse rate of only 2 Hz to keep the average optical pump power extremely low. The other experimental challenges follow from this restriction. The optical pulses are only few 100 ns long allowing us to collect $< 1 \mu\text{s}$ worth of data per second. This meant that to collect enough data for proper statistics, we needed to measure for a really long time - on the order of days. Maintaining experimental stability for days was the biggest challenge. We discuss these challenges and solutions in detail. We also discuss the measurements which did not completely work but paved the way to the final entanglement measurement.

Acknowledgements This chapter is based on the work presented in Ref. [SQH⁺23]. I would like to thank Liu Qiu and Yuri Minoguchi for writing the theory section which has been adapted in this chapter and Liu Qiu and William Hease for his contribution in the data analysis and measurements. Figure credits have been individually given in the figure captions.

9.2 Theory

9.2.1 Covariance Matrix from Input-Output Theory

Quantum Langevin Equations

In this chapter, we focus on amplification interaction between the microwave mode \hat{a}_e and the optical Stokes mode $\hat{a}_s \equiv \hat{a}_o$. Now we suppress the interaction of the microwave mode with the optical anti-Stokes mode \hat{a}_t by hybridising it with the optical TM mode \hat{a}_{tm} which is degenerate with the \hat{a}_t mode. This results in a total interaction Hamiltonian,

$$\hat{H}_I/\hbar = g_0(\hat{a}_p^\dagger \hat{a}_e \hat{a}_o + \hat{a}_p^\dagger \hat{a}_e^\dagger \hat{a}_t) + J \hat{a}_t \hat{a}_{\text{tm}}^\dagger + h.c., \quad (9.1)$$

with g_0 as the vacuum electro-optical coupling rate.

Assuming a strong coherent optical pump, we can write an effective interaction Hamiltonian as,

$$\hat{H}_{I,\text{eff}}/\hbar = g(\hat{a}_e \hat{a}_o + \hat{a}_e \hat{a}_t^\dagger) + J \hat{a}_t \hat{a}_{\text{tm}}^\dagger + h.c., \quad (9.2)$$

with multiphoton coupling rate $g = \bar{a}_p g_0$. This includes both the two-mode-squeezing (TMS) interaction between the optical Stokes and microwave mode, and beam-splitter (BS) interaction between the optical anti-Stokes mode and microwave mode. Microwave-optics entanglement between the microwave and optical Stokes output field can be achieved via spontaneous parametric down-conversion (SPDC) process due to TMS interaction, which is further facilitated by the suppressed anti-Stokes scattering due to the strong coupling between anti-Stokes and TM modes. The full dynamics of the intracavity fluctuation field *in the rotating frame of the scattered sidebands and microwave resonance*, are now described by the quantum Langevin equations (QLE),

$$\dot{\hat{a}}_e = -\frac{\kappa_e}{2} \hat{a}_e - ig \hat{a}_o^\dagger - ig^* \hat{a}_t + \sqrt{\eta_e \kappa_e} \delta \hat{a}_{e,\text{in}} + \sqrt{(1-\eta_e) \kappa_e} \delta \hat{a}_{e,0}, \quad (9.3)$$

$$\dot{\hat{a}}_o = \left(i\delta_o - \frac{\kappa_o}{2} \right) \hat{a}_o - ig \hat{a}_e^\dagger + \sqrt{\eta_o \kappa_o} \delta \hat{a}_{o,\text{in}} + \sqrt{(1-\eta_o) \kappa_o} \delta \hat{a}_{o,0}, \quad (9.4)$$

$$\dot{\hat{a}}_t = \left(i\delta_t - \frac{\kappa_t}{2} \right) \hat{a}_t - ig^* \hat{a}_e - iJ \hat{a}_{\text{tm}} + \sqrt{\kappa_t} \delta \hat{a}_{t,\text{vac}}, \quad (9.5)$$

$$\dot{\hat{a}}_{\text{tm}} = \left(i\delta_{\text{tm}} - \frac{\kappa_{\text{tm}}}{2} \right) \hat{a}_{\text{tm}} - iJ \hat{a}_t + \sqrt{\kappa_{\text{tm}}} \delta \hat{a}_{\text{tm,vac}}, \quad (9.6)$$

with κ_j the total loss rate of the individual mode where $j \in (e, o, t, \text{tm})$, and η_k the external coupling efficiency of the input field where $k \in (e, o)$. δ_j corresponds to the frequency difference between mode j and scattered sidebands, with $\delta_o = \omega_{o,p} - \omega_e - \omega_o$ and $\delta_{t/\text{tm}} = \omega_{o,p} + \omega_e - \omega_{t/\text{tm}}$, which are mostly given by FSR and ω_e mismatch, with additional contributions from optical mode dispersion and residual optical mode coupling. We note that, for resonant pumping, we have $\delta_o = -\delta_t$ in the case of absent optical mode dispersion and residual mode coupling. In our experiments, we tune the microwave frequency to match the optical FSR, i.e. $\omega_e = \omega_{o,p} - \omega_o$.

We are interested in solving these equations in steady state since they can be analytically solved in steady state and, in the experiments, we will only work with the steady state. Again, we write the above equation in matrix form to solve it in steady state,

$$\dot{\mathbf{v}}(t) = \mathbf{M}(t) \mathbf{v}(t) + \mathbf{K} \mathbf{f}_{\text{in}}(t), \quad (9.7)$$

where,

$$\begin{aligned}\mathbf{v} &= (\hat{a}_e, \hat{a}_e^\dagger, \hat{a}_o, \hat{a}_o^\dagger, \hat{a}_t, \hat{a}_t^\dagger, \hat{a}_{\text{tm}}, \hat{a}_{\text{tm}}^\dagger)^\top, \\ \mathbf{f}_{\text{in}} &= (\delta\hat{a}_{e,0}, \delta\hat{a}_{e,0}^\dagger, \delta\hat{a}_{e,\text{in}}, \delta\hat{a}_{e,\text{in}}^\dagger, \delta\hat{a}_{o,0}, \delta\hat{a}_{o,0}^\dagger, \delta\hat{a}_{o,\text{in}}, \delta\hat{a}_{o,\text{in}}^\dagger, \delta\hat{a}_{t,\text{vac}}, \delta\hat{a}_{t,\text{vac}}^\dagger, \delta\hat{a}_{\text{tm},\text{vac}}, \delta\hat{a}_{\text{tm},\text{vac}}^\dagger)^\top,\end{aligned}\quad (9.8)$$

and,

$$\begin{aligned}\mathbf{M}(t) &= \\ &\left(\begin{array}{ccccccc} -\frac{\kappa_e}{2} & 0 & 0 & -ig(t) & -ig^*(t) & 0 & 0 \\ 0 & -\frac{\kappa_e}{2} + ig^*(t) & 0 & 0 & ig(t) & 0 & 0 \\ 0 & -ig(t)i\delta_o - \frac{\kappa_o}{2} & 0 & 0 & 0 & 0 & 0 \\ ig^*(t) & 0 & 0 & -i\delta_o - \frac{\kappa_o}{2} & 0 & 0 & 0 \\ -ig(t) & 0 & 0 & 0 & i\delta_t - \frac{\kappa_t}{2} & 0 & -iJ \\ 0 & ig^*(t) & 0 & 0 & 0 & -i\delta_t - \frac{\kappa_t}{2} & 0 \\ 0 & 0 & 0 & 0 & -iJ & 0 & iJ \\ 0 & 0 & 0 & 0 & 0 & i\delta_{\text{tm}} - \frac{\kappa_{\text{tm}}}{2} & 0 \\ 0 & 0 & 0 & 0 & iJ & 0 & -i\delta_{\text{tm}} - \frac{\kappa_{\text{tm}}}{2} \end{array} \right),\end{aligned}\quad (9.9)$$

$$\mathbf{K} = \left(\begin{array}{cccccc} \sqrt{(1-\eta_e)\kappa_e} & \sqrt{\eta_e\kappa_e} & 0 & 0 & 0 & 0 \\ 0 & 0 & \sqrt{(1-\eta_o)\kappa_o} & \sqrt{\eta_o\kappa_o} & 0 & 0 \\ 0 & 0 & 0 & 0 & \sqrt{\kappa_t} & 0 \\ 0 & 0 & 0 & 0 & 0 & \sqrt{\kappa_{\text{tm}}} \end{array} \right) \otimes \mathbb{1}_2 \quad (9.10)$$

Input-Output-Theory

The output fields of the CEO device are

$$\mathbf{f}_{\text{out}}(t) = (\hat{a}_{e,\text{out}}(t), \hat{a}_{e,\text{out}}^\dagger(t), \hat{a}_{o,\text{out}}(t), \hat{a}_{o,\text{out}}^\dagger(t))^\top, \quad (9.11)$$

which consist of a contribution which was entangled via the electro-optic interactions \mathbf{v} and a contribution which has not interacted with the device \mathbf{f}_{in} . The output field \mathbf{f}_{out} is written with the framework of input-output theory [GC85],

$$\mathbf{f}_{\text{out}}(t) = \mathbf{L}\mathbf{f}_{\text{in}}(t) - \mathbf{N}\mathbf{v}(t), \quad (9.12)$$

where we define the matrices

$$\mathbf{N} = (N_J, \mathbb{0}_4), \quad \text{with} \quad N_J = \text{Diag}(\sqrt{\eta_e\kappa_e}, \sqrt{\eta_e\kappa_e}, \sqrt{\eta_o\kappa_o}, \sqrt{\eta_o\kappa_o}), \quad (9.13)$$

and

$$\mathbf{L} = \begin{pmatrix} 0 & 1 & 0 & 0 & 0 & 0 \\ 0 & 0 & 0 & 1 & 0 & 0 \end{pmatrix} \otimes \mathbb{1}_2. \quad (9.14)$$

In the steady state, the correlations in the output field may be obtained by going to Fourier domain. Here we commit to following convention of the Fourier transformation

$$\hat{A}(\omega) = \frac{1}{\sqrt{2\pi}} \int_{-\infty}^{\infty} d\omega e^{i\omega t} \hat{A}(t), \quad (9.15)$$

with the hermitian conjugate

$$(\hat{A}(\omega))^\dagger = A^\dagger(-\omega). \quad (9.16)$$

Note that in this convention e.g. $[a_e(\omega), a_e^\dagger(\omega')] = \delta(\omega + \omega')$ are canonical pairs.

In our experiments, we concern ourselves with the correlations between the output propagating spectral modes of frequencies $\omega_e + \Delta\omega_e$ and $\omega_o - \Delta\omega_o$ respectively for microwave and optical fields [Bv05, ZGV15]. Due to energy conservation in the SPDC process, the focus is only on microwave and optical photon pairs around resonances with anti-correlated frequencies, i.e. $\Delta\omega_e = \Delta\omega_o = \Delta\omega$. For this reason, we choose the following vector of output fields in the rotating frame,

$$\mathbf{f}_{\text{out}}(\omega) = (\hat{a}_{e,\text{out}}(\omega), \hat{a}_{e,\text{out}}^\dagger(-\omega), \hat{a}_{o,\text{out}}(-\omega), \hat{a}_{o,\text{out}}^\dagger(\omega))^\top, \quad (9.17)$$

in the Fourier domain. From Eqn. (9.7) we obtain

$$\mathbf{v}(\omega) = \underbrace{[i\omega\mathbf{O} - \mathbf{M}]^{-1} \cdot \mathbf{K} \cdot \mathbf{f}_{\text{in}}(\omega)}_{=\mathcal{S}(\omega)}, \quad (9.18)$$

with

$$\mathbf{O} = \text{Diag}(1, -1, 1, 1) \otimes \sigma_z. \quad (9.19)$$

Here we defined the vector of modes

$$\mathbf{v}(\omega) = (\hat{a}_e(\omega), \hat{a}_e^\dagger(-\omega), \hat{a}_o(-\omega), \hat{a}_o^\dagger(\omega), \hat{a}_t(\omega), \hat{a}_t^\dagger(-\omega), \hat{a}_{\text{tm}}(\omega), \hat{a}_{\text{tm}}^\dagger(-\omega))^\top, \quad (9.20)$$

as well as the vector of input fields

$$\mathbf{f}_{\text{in}}(\omega) = (\delta\hat{a}_{e,0}(\omega), \delta\hat{a}_{e,0}^\dagger(-\omega), \delta\hat{a}_{e,\text{in}}(\omega), \delta\hat{a}_{e,\text{in}}^\dagger(-\omega), \delta\hat{a}_{o,0}(\omega), \delta\hat{a}_{o,0}^\dagger(-\omega), \delta\hat{a}_{o,\text{in}}(\omega), \delta\hat{a}_{o,\text{in}}^\dagger(-\omega), \delta\hat{a}_{t,\text{vac}}(\omega), \delta\hat{a}_{t,\text{vac}}^\dagger(-\omega), \delta\hat{a}_{\text{tm},\text{vac}}(\omega), \delta\hat{a}_{\text{tm},\text{vac}}^\dagger(-\omega))^\top \quad (9.21)$$

in the Fourier domain.

The output fields (see Eqn. (9.12)) of the CEO device are straight forwardly obtained since in the Fourier domain Eqn. (9.12) is algebraic,

$$\mathbf{f}_{\text{out}}(\omega) = \mathbf{L}\mathbf{f}_{\text{in}}(\omega) + \mathbf{N}\mathbf{v}(\omega) = (\mathbf{L} + \mathbf{N} \cdot [i\omega\mathbf{O} - \mathbf{M}]^{-1} \cdot \mathbf{K})\mathbf{f}_{\text{in}}(\omega). \quad (9.22)$$

The input noise operator correlations are given by,

$$\langle \mathbf{f}_{\text{in}}(\omega) \mathbf{f}_{\text{in}}^\dagger(\omega') \rangle = \mathbf{D}\delta(\omega + \omega'), \quad (9.23)$$

with

$$\mathbf{D} = \text{Diag}(\underbrace{\bar{n}_{e,\text{int}} + 1}_{\text{bath}:e}, \underbrace{\bar{n}_{e,\text{int}}}_{\text{waveguide}:e}, \underbrace{\bar{n}_{e,\text{wg}} + 1}_{\text{bath}:o}, \underbrace{\bar{n}_{e,\text{wg}}}_{\text{detector}:o}, \underbrace{1, 0}_{\text{bath}:t}, \underbrace{1, 0}_{\text{bath:tm}}). \quad (9.24)$$

The spectral correlations of different output fields can be simply obtained analytically from

$$\langle \mathbf{f}_{\text{out}}(\omega) \mathbf{f}_{\text{out}}^\dagger(\omega') \rangle = \underbrace{\mathcal{S}(\omega) \mathbf{D} \mathcal{S}^\dagger(-\omega)}_{\tilde{C}_{ff^\dagger}(\omega)} \delta(\omega + \omega'). \quad (9.25)$$

Here we implicitly define the 4×4 matrix of output mode correlations with a single entry reading

$$\langle \hat{a}_{\text{out}}(\omega) \hat{b}_{\text{out}}(\omega') \rangle = \tilde{C}_{ab}(\omega) \delta(\omega + \omega'), \quad (9.26)$$

where the operators $\hat{a}_{\text{out}}(\omega), \hat{b}_{\text{out}}(\omega)$ were chosen from components of $\mathbf{f}_{\text{out}}(\omega)$ in Eqn. (9.15).

Covariance Matrix of Filtered Output Fields

Practically, in the experiment, we can only measure the output signal for a finite time due to the pulsed nature of the optical pump. This means that the measured output fields, although in steady state, get inevitably filtered in time domain. We will now consider this situation analytically by defining output field modes from a windowed Fourier transformation. Next we will then show that these are indeed the experimentally observed signals.

We start by defining the (dimensionless) hermitian output field quadrature pair [ZGV15],

$$\hat{X}_\alpha(\omega_n) = \frac{1}{\sqrt{2T}} \int_{-T/2}^{T/2} d\tau e^{i\omega_n \tau} \hat{a}_{\alpha,\text{out}}(\tau) + \text{h.c.}, \quad (9.27)$$

$$\hat{P}_\alpha(\omega_n) = \frac{1}{\sqrt{2T}i} \int_{-T/2}^{T/2} d\tau e^{i\omega_n \tau} \hat{a}_{\alpha,\text{out}}(\tau) + \text{h.c.}, \quad (9.28)$$

which meets the canonical commutation relation $[\hat{X}_\alpha(\omega_n), \hat{P}_\beta(\omega_m)] = i\delta_{nm}\delta_{\alpha\beta}$ where $\alpha = e, o$. Due to the finite window of the Fourier transformation, the frequencies $\omega_n = \frac{2\pi}{T}n$ becomes discrete. The quadrature modes at discrete frequencies ω_n can now be rewritten in terms of the (dimensionful) output fields $\mathbf{f}_{\text{out}}(\omega)$ from Eqn. (9.22), which are defined in the continuous Fourier domain. Therefore the quadrature operators may be obtained by convolution with the a filter function $\mathcal{G}(\omega)$

$$\hat{X}_\alpha(\omega_n) = \frac{1}{\sqrt{2}} \int_{-\infty}^{\infty} d\omega \mathcal{G}(\omega_n - \omega) \hat{a}_{\alpha,\text{out}}(\omega) + \text{h.c.} \quad (9.29)$$

$$\hat{P}_\alpha(\omega_n) = \frac{1}{\sqrt{2}i} \int_{-\infty}^{\infty} d\omega \mathcal{G}(\omega_n - \omega) \hat{a}_{\alpha,\text{out}}(\omega) + \text{h.c.} \quad (9.30)$$

Here the filter is

$$\mathcal{G}(\omega) = \frac{1}{\sqrt{2\pi}} \int_{-\infty}^{\infty} d\tau e^{i\omega\tau} \frac{\mathbb{1}_{[0,T]}(\tau)}{\sqrt{T}} = \sqrt{\frac{2}{\pi T}} \frac{\sin(\omega T/2)}{\omega}, \quad (9.31)$$

which is obtained from a Fourier transformation of the unit function $\mathbb{1}_{[-T/2,T/2]}(t) = 1(0)$ for $|t| \leq T/2$ ($|t| > T/2$). A bipartite Gaussian state is characterized by the 4×4 covariance matrix (CM),

$$V_{AB}(\omega_n) = \frac{1}{2} \langle \{\delta\hat{A}(\omega_n), \delta\hat{B}(\omega_n)\} \rangle. \quad (9.32)$$

Here we defined $\delta\hat{A} = \hat{A} - \langle \hat{A} \rangle$ an operator with zero mean $\langle \delta\hat{A} \rangle = 0$ and the quadratures from

$$\hat{A}(\omega_n), \hat{B}(\omega_n) \in \{\hat{X}_e(\omega_n), \hat{P}_e(\omega_n), \hat{X}_o(-\omega_n), \hat{P}_o(-\omega_n)\} \quad (9.33)$$

and we also introduced the anti-commutator $\{\hat{A}, \hat{B}\} = \hat{A}\hat{B} + \hat{B}\hat{A}$. Note that the two-mode squeezing interaction results in correlation between frequency reversed pairs on the microwave ω_n and the optical side $-\omega_n$. Since in our setting all first moments $\langle \hat{A} \rangle = 0$, the evaluation of the covariance matrix in Eqn. (9.32) boils down to computing spectral correlations which are rewritten as

$$\begin{aligned} \langle \hat{A}(\omega_n) \hat{B}(\omega_n) \rangle &= \int_{-\infty}^{\infty} d\omega \int_{-\infty}^{\infty} d\omega' \mathcal{G}(\omega_n - \omega) \mathcal{G}(\omega_n - \omega') \langle \hat{A}(\omega) \hat{B}(\omega') \rangle \\ &= \int_{-\infty}^{\infty} d\omega \int_{-\infty}^{\infty} d\omega' \mathcal{G}(\omega_n - \omega) \mathcal{G}(-\omega_n - \omega') C_{AB}(\omega) \delta(\omega + \omega') \\ &= \int_{-\infty}^{\infty} d\omega \mathcal{F}(\omega_n - \omega) C_{AB}(\omega), \end{aligned} \quad (9.34)$$

where we used the property $\mathcal{G}(-\omega) = \mathcal{G}(\omega)$ and defined the effective filter $\mathcal{F}(\omega) = \mathcal{G}(\omega)^2$. Similar to Eqn. (9.25), we defined the quadrature correlations

$$C_{AB}(\omega) = (C(\omega))_{AB} = \frac{1}{2} \left(U \tilde{C}_{ff^\dagger}(\omega) U^\dagger + (U \tilde{C}_{ff^\dagger}(\omega) U^\dagger)^\top \right)_{AB}. \quad (9.35)$$

Here the unitary matrix $U = u \oplus u$, with

$$u = \frac{1}{\sqrt{2}} \begin{pmatrix} 1 & 1 \\ -i & i \end{pmatrix}, \quad (9.36)$$

corresponds to a rotation of the mode operators into quadrature operators $(\hat{X}_\alpha, \hat{P}_\alpha)^\top = u \cdot (\hat{a}_{\alpha,\text{out}}, \hat{a}_{\alpha,\text{out}}^\dagger)^\top$. The covariance matrix of the quadrature modes at the discrete frequencies ω_n is then obtained exactly by

$$V_{AB}(\omega_n) = \int_{-\infty}^{\infty} d\omega \mathcal{F}(\omega_n - \omega) C_{AB}(\omega), \quad (9.37)$$

where the quadrature correlations are convolved with an appropriate filter. This means convolution with the filter function is enough to take into account the finite measurement time in the experiment.

9.2.2 Heterodyne Detection, Added Noise and Filtering

Heterodyne Measurement

In this subsection, we discuss the quadrature extractions from the equivalent linear measurement, e.g. balanced heterodyne detection, with excess added noise [dBWB10]. In the heterodyne detection, the output field $\hat{a}_{\text{out}} e^{-i\omega_j t}$ ($j \in e, o$) is mixed with a strong coherent local oscillator field $\hat{a}_{\text{LO}}(t) = \alpha_{\text{LO}} e^{-i\omega_{\text{LO}} t}$ at a 50:50 beam-splitter, where the output field from the two ports are sent to a balanced photo-detector, which results in a photon current that is proportional to

$$\hat{I}_{\text{out}}(t) = e^{-i\Delta_{\text{LO}} t} \hat{a}_{\text{out}} + \hat{a}_{\text{out}}^\dagger e^{i\Delta_{\text{LO}} t}, \quad (9.38)$$

in the limit of strong LO ($\alpha_{\text{LO}} \gg 1$) with $\Delta_{\text{LO}} = \omega_{\text{LO}} - \omega_j$. Here also, we consider finite measurement interval of time T , on which we compute the windowed Fourier transformation of $\hat{I}_{\text{out}}(t)$,

$$\begin{aligned} \hat{I}_{\text{out}}(\omega_n) &= \frac{1}{\sqrt{T}} \int_0^T d\tau e^{i\omega_n \tau} \hat{I}_{\text{out}}(\tau) = \frac{1}{\sqrt{T}} \int_0^T d\tau e^{i\omega_n \tau} (e^{-i\Delta_{\text{LO}} \tau} \hat{a}_{\text{out}}(\tau) + e^{i\Delta_{\text{LO}} \tau} \hat{a}_{\text{out}}^\dagger(\tau)) \\ &= a_{\text{out}}(\omega_n - \Delta_{\text{LO}}) + a_{\text{out}}^\dagger(\omega_n + \Delta_{\text{LO}}), \end{aligned} \quad (9.39)$$

where in a slight abuse of notation we define the dimensionless output fields $a_{\text{out}}(\omega_n)$. In our experiments, we extract the quadratures of microwave and optical output field, by decomposing the heterodyne current spectra, in their real and imaginary parts which yields

$$\hat{I}_{\text{out}}(\omega_n) = \frac{1}{\sqrt{2}} \underbrace{(\hat{X}(\omega_n - \Delta_{\text{LO}}) + \hat{X}(-\omega_n - \Delta_{\text{LO}}))}_{\hat{I}_{X,\text{out}}(\omega_n)} + i \underbrace{[\hat{P}(\omega_n - \Delta_{\text{LO}}) - \hat{P}(-\omega_n - \Delta_{\text{LO}})]}_{\hat{I}_{P,\text{out}}(\omega_n)}, \quad (9.40)$$

where we define the quadrature output fields $\hat{a}_{\text{out}}(\omega_n) = (\hat{X}(\omega_n) + i\hat{P}(\omega_n))/\sqrt{2}$, in the same way as in Eqn. (9.27-9.28).

So far we have treated the photon current that results from a heterodyne measurement in terms of a time dependent hermitian operator $\hat{I}_{\text{out}}(t)$. In an actual experiment the heterodyne current is a real scalar $I(t)$ quantity which fluctuates in time and between different experimental runs. Taking the (fast) Fourier transform of this current and decomposing it in its real and imaginary parts then yields $I(\omega_n) = I_X(\omega_n) + iI_P(\omega_n)$. The theory of continuous measurements and quantum trajectories [WM08, WM09] tells us how to connect the measured scalar currents with the current operators from input-output theory [GC85]

$$\overline{I_A(\omega_n)I_B(\omega_m)} = \frac{1}{2}\langle\{\hat{I}_{A,\text{out}}(\omega_n), \hat{I}_{B,\text{out}}(\omega_m)\}\rangle, \quad (9.41)$$

where we define the statistical average $\overline{\dots}$ over many experimental runs.

Added Noise and Gain in Measurements

For the vacuum, the noise spectral density for both quadratures, are obtained by

$$S_{AA}(\omega_n) = \langle \hat{A}(\omega_n)\hat{A}(\omega_n) \rangle_{\text{vac}} = \frac{1}{2}, \quad (9.42)$$

for the hermitian operator $\hat{A} = \hat{X}, \hat{P}$. Note that due to the discreteness of the Fourier domain we do not have a Dirac delta as opposed to Eqn. (9.26). The noise spectrum of the heterodyne current is defined by $S_{II}(\omega) \equiv \overline{I(\omega_n)I(\omega_n)} = \langle \hat{I}_{\text{out}}(\omega_n)\hat{I}_{\text{out}}(\omega_n) \rangle$, where

$$S_{II}(\omega_n) = \frac{1}{2}(S_{XX}(\omega_n - \Delta_{\text{LO}}) + S_{PP}(\omega_n - \Delta_{\text{LO}}) + S_{XX}(\omega_n + \Delta_{\text{LO}}) + S_{PP}(\omega_n + \Delta_{\text{LO}})). \quad (9.43)$$

Focusing on the part of the spectrum located around Δ_{LO} ,

$$S_{II}(\omega_n + \Delta_{\text{LO}}) = \frac{1}{2}(S_{XX}(\omega_n) + S_{PP}(\omega_n) + 1), \quad (9.44)$$

assuming $\Delta_{\text{LO}} \gg \kappa_e, \kappa_o$. This indicates the simultaneous quadratures measurements and added shot noise in the heterodyne measurements, even without experimental imperfections.

So far we have focused on the ideal theory of the measurement and disregarded additional unknown sources of noise as well as the connection to the actually measured quantities. In practice, the *decomposed measured quadratures contain additional uncorrelated excess noise*, e.g. due to the added noise in the amplification or due to propagation losses [Cav82]. We model this by phenomenologically adding another uncorrelated noise process from an independent thermal reservoir and then multiplying by a gain factor which converts the number of measured photons to the actually monitored voltage. To illustrate this we consider a single output port with the added noise current $\hat{I}_{X/P,\text{add}}(\omega_n)$ and the frequency dependent calibration gain $G_{\text{det}}(\omega_n)$, where

$$\hat{I}_{X,\text{det}}(\omega_n) = \sqrt{G_{\text{det}}(\omega_n)}(\hat{I}_{X,\text{add}}(\omega_n) + \hat{I}_{X,\text{out}}(\omega_n)), \quad (9.45)$$

$$\hat{I}_{P,\text{det}}(\omega_n) = \sqrt{G_{\text{det}}(\omega_n)}(\hat{I}_{P,\text{add}}(\omega_n) + \hat{I}_{P,\text{out}}(\omega_n)). \quad (9.46)$$

We thus obtain the detected heterodyne noise spectral density,

$$\begin{aligned} S_{II,\text{det}}(\omega_n + \Delta_{\text{LO}}) &= G_{\text{det}}(\omega_n + \Delta_{\text{LO}})[S_{XX}(\omega_n) + S_{PP}(\omega_n) \\ &\quad + \underbrace{1 + S_{IX}I_{X,\text{add}}(\omega_n + \Delta_{\text{LO}}) + S_{IP}I_{P,\text{add}}(\omega_n + \Delta_{\text{LO}})}_{=2N_{\text{add}}}], \end{aligned} \quad (9.47)$$

where we define the spectra of the added noise $S_{I_O I_O, \text{add}}(\omega_n) = \langle \hat{I}_{O,\text{add}}(\omega_n) \hat{I}_{O,\text{add}}(\omega_n) \rangle$. The added noise N_{add} includes the excess vacuum noise from heterodyne measurement and the additional uncorrelated noise. Note that here the factor $\frac{1}{2}$ was absorbed in the detections gains. The gain $G_{\text{det}}(\omega_n)$ can be simply obtained on both microwave and optical side, from the cold measurements (optical pump off) with a known background. Eqn. (9.47) lays the foundation of microwave and optical calibrations in our CEO device.

In the experiments, we place the LO on opposite sites around the mode resonances, i.e.,

$$\Delta_{\text{LO},e} = -\Omega_{\text{IF}}, \quad \Delta_{\text{LO},o} = \Omega_{\text{IF}}, \quad (9.48)$$

where $\Omega_{\text{IF}} > 0$ is the intermediate frequency for down-mixing. The heterodyne output field can be obtained similar to Eqn. (9.39),

$$\begin{aligned} \hat{I}_{\text{out},e}(\omega_n + \Omega_{\text{IF}}) &= \frac{1}{\sqrt{2}} [(\hat{X}_e(-\omega_n) + \hat{X}_e(\omega_n + 2\Omega_{\text{IF}}) + i(-\hat{P}_e(-\omega_n) + \hat{P}_e(\omega_n + 2\Omega_{\text{IF}}))], \\ \hat{I}_{\text{out},o}(\omega_n + \Omega_{\text{IF}}) &= \frac{1}{\sqrt{2}} [\hat{X}_o(-\omega_n - 2\Omega_{\text{IF}}) + \hat{X}_o(\omega_n) + i(-\hat{P}_o(-\omega_n - 2\Omega_{\text{IF}}) + \hat{P}_o(\omega_n))], \end{aligned} \quad (9.49)$$

with noise spectrum given by,

$$\begin{aligned} S_{II,e}(\omega_n + \Omega_{\text{IF}}) &= \frac{1}{2}(S_{X_e X_e}(-\omega_n) + S_{P_e P_e}(-\omega_n)) + N_{e,\text{add}}, \\ S_{II,o}(\omega_n + \Omega_{\text{IF}}) &= \frac{1}{2}(S_{X_o X_o}(\omega_n) + S_{P_o P_o}(\omega_n)) + N_{o,\text{add}}. \end{aligned} \quad (9.50)$$

We note that, Eqn. (9.49) is adopted for *field quadrature extraction (including the added noise) from the heterodyne measurement*, which reveals correlations in the quadrature histogram [cf. Fig. 9.12]. Despite of the reversed sign in the expected field quadratures, microwave and optical output photons appear at the same frequency in the noise spectrum, i.e. $\omega_n + \Omega_{\text{IF}}$ [cf. Fig. 9.9].

Covariance Matrix from Realistic Heterodyne Measurements

Here we briefly explain the procedure of the covariance matrix reconstruction from the heterodyne measurements. The cross correlations of the detected heterodyne current spectra can be obtained via,

$$\mathcal{D}_{AB}(\omega_n) = \overline{\delta I_{A,\text{det}}(\omega_n + \Omega_{\text{IF}}) \delta I_{B,\text{det}}(\omega_n + \Omega_{\text{IF}})}, \quad (9.51)$$

where we define the centered current $\delta I_{O,\text{det}} = I_{O,\text{det}} - \overline{I_{O,\text{det}}}$, with

$$I_{O,\text{det}}(\omega_n) \in \{I_{X_e,\text{det}}(\omega_n), I_{P_e,\text{det}}(\omega_n), I_{X_o,\text{det}}(\omega_n), I_{P_o,\text{det}}(\omega_n)\}. \quad (9.52)$$

Similar to Eqn. (9.41)), we can obtain

$$\begin{aligned} \mathcal{D}_{AB}(\omega_n) &= \frac{1}{2} \langle \{\delta \hat{I}_{A,\text{det}}(\omega_n + \Omega_{\text{IF}}), \delta \hat{I}_{B,\text{det}}(\omega_n + \Omega_{\text{IF}})\} \rangle \\ &= \sqrt{G_{A,\text{det}}(\omega_n + \Omega_{\text{IF}}) G_{B,\text{det}}(\omega_n + \Omega_{\text{IF}})} \left[\underbrace{\frac{1}{2} \langle \{\delta \hat{A}(\omega_n), \delta \hat{B}(\omega_n)\} \rangle}_{=V_{AB}(\omega_n)} + N_{AB,\text{add}} \right], \end{aligned} \quad (9.53)$$

where we define the diagonal added noise matrix $N_{AB,\text{add}} = (N_{\text{add}})_{AB} = N_{A,\text{add}}\delta_{AB}$ with the calibrated added noise N_{add} and detection gain $G_{A,\text{det}}$.

This equation establishes how the covariance matrix of the quadrature operators [cf. Eqn. (9.37)] is reconstructed from heterodyne measurements, and how they can be compared with the results from idealized standard input-output theory Eqn. (9.32). For simplicity, in the later section 9.7, we define the *total measured covariance matrix including the added noise* as,

$$V_{AB,\text{meas}}(\omega_n) = \mathcal{D}_{AB}(\omega_n)/\sqrt{G_{A,\text{det}}(\omega_n + \Omega_{\text{IF}})G_{B,\text{det}}(\omega_n + \Omega_{\text{IF}})}, \quad (9.54)$$

with $V_{AB,\text{meas}}(\omega_n) = V_{AB}(\omega_n) + N_{AB,\text{add}}$.

We note that, in principle the location of both LOs can be arbitrary. As evident in Eqn. 9.53, our choice of the LO configuration, i.e. $\Delta_{\text{LO},e} = -\Delta_{\text{LO},o} = -\Omega_{\text{IF}}$, offers a simple solution to the quantification of the broadband quantum correlations, considering the limited detection bandwidth, frequency dependent gain, or microwave cavity frequency shift, which may result in the loss of quantum correlations during quadrature extractions in heterodyne measurements due to imperfect frequency matching.

9.2.3 Entanglement Detection

Duan Criterion

We will now discuss the criterion for inseparable or entangled states. Our starting point is the covariance matrix which we defined in Eqn. (9.32) and measured as outline in Eqn. (9.53). The experimentally measured covariance matrix is of the form

$$V = \begin{pmatrix} V_e & V_{eo} \\ V_{eo} & V_o \end{pmatrix} = \begin{pmatrix} V_{11} & 0 & \tilde{V}_{13} & \tilde{V}_{14} \\ 0 & V_{11} & \tilde{V}_{14} & -\tilde{V}_{13} \\ \tilde{V}_{13} & \tilde{V}_{14} & V_{33} & 0 \\ \tilde{V}_{14} & -\tilde{V}_{13} & 0 & V_{33} \end{pmatrix}. \quad (9.55)$$

Since there is no single mode squeezing, we have $V_{22} = V_{11}$ and $V_{44} = V_{33}$. For simplicity we have omitted the frequency argument ω_n of component. What we describe in the following will have to be repeated for every frequency component. The off-diagonal part in the covariance matrix which encodes the two-mode squeezing can be written as

$$V_{eo} \simeq V_{13}(\sin(\theta)\sigma_x + \cos(\theta)\sigma_z), \quad (9.56)$$

where we define $V_{13} = (\tilde{V}_{14}^2 + \tilde{V}_{13}^2)^{1/2}$ and the mixing angle $\tan(\theta) = \tilde{V}_{14}/\tilde{V}_{13}$. In our experimental setting \tilde{V}_{14} maybe non zero e.g. due to small finite detunings δ_o . For the detection of inseparability, we employ the criterion introduced by Duan, Gidke, Cirac and Zoller [DGCZ00]. This criterion states that if one can find local operations $U_{\text{Loc}} = U_e \otimes U_o$ such that the joint amplitude variance of $\hat{X}_+ = (\hat{X}_e + \hat{X}_o)/\sqrt{2}$ break the inequality,

$$\Delta X_+^2 = \langle U_{\text{Loc}}^\dagger \hat{X}_+^2 U_{\text{Loc}} \rangle < 1/2, \quad (9.57)$$

then the state is inseparable and, thus it must be concluded that it is entangled.

In this setting, it is enough to choose the local operations $U_{\text{Loc}} = U_e U_o$ to be a passive phase rotation on the optical mode only, with $U_e = \mathbb{1}$ and $U_o = e^{-i\varphi \hat{a}_o^\dagger \hat{a}_o}$, and phase rotation angle

φ . In the space of covariance matrices, this corresponds to the (symplectic) transformation $S_\varphi = \mathbb{1}_2 \oplus R_\varphi$, where we define the rotation matrix,

$$R_\varphi = \begin{pmatrix} \cos(\varphi) & \sin(\varphi) \\ -\sin(\varphi) & \cos(\varphi) \end{pmatrix}. \quad (9.58)$$

The local rotation of the phase $V(\varphi) = S_\varphi V S_\varphi^\top$ will act on the off diagonal part of the covariance matrix as,

$$V_{ea}(\varphi) = V_{13}(\cos(\theta - \varphi)\sigma_z + \sin(\theta - \varphi)\sigma_x). \quad (9.59)$$

With these local rotations the joint amplitude variance becomes

$$\Delta X_+^2(\varphi) = \langle (\hat{X}_e + \hat{X}_o \cos(\varphi) + \hat{P}_o \sin(\varphi))^2 \rangle / 2 = V_{11} + V_{33} + 2V_{13} \cos(\theta - \varphi). \quad (9.60)$$

We can similarly define the joint quadrature $\hat{P}_- = (\hat{P}_e - \hat{P}_o)/\sqrt{2}$, where $\Delta P_-^2(\varphi) = \Delta X_-^2(\varphi)$. The variance of the joint quadratures $\Delta X_+^2(\varphi)$ and $\Delta P_-^2(\varphi)$ is minimized at the angle $\varphi_- = \theta - \pi$

$$\Delta_{\text{EPR}}^- = \Delta X_+^2(\varphi_-) + \Delta P_-^2(\varphi_-) = 2(V_{11} + V_{33} - 2V_{13}), \quad (9.61)$$

which corresponds to the two-mode squeezing of microwave and optical output field, and the microwave-optics entanglement. In addition, the joint quadrature variance is maximized at the angle $\varphi_+ = \theta$ and we obtain

$$\Delta_{\text{EPR}}^+ = \Delta X_+^2(\varphi_+) + \Delta P_-^2(\varphi_+) = 2(V_{11} + V_{33} + 2V_{13}), \quad (9.62)$$

which corresponds to the anti-squeezing.

Logarithmic Negativity and Purity

A mixed entangled state can be quantified by the logarithmic negativity [Ple05],

$$E_N = \max [0, -\log(2\zeta_-)], \quad (9.63)$$

where ζ_- is the smaller symplectic eigenvalue of the partially time reverse covariance matrix and can be obtained analytically

$$\zeta_-^2 = \frac{S - \sqrt{S^2 - 4\det(V)}}{2} \quad (9.64)$$

where we defined the Seralian invariant $S = \det(V_e) + \det(V_o) + 2\det(V_{eo})$. Furthermore the purity of a bipartite Gaussian state is given by

$$\rho = \frac{1}{4\sqrt{\det(V)}}, \quad (9.65)$$

with $\rho = 1$ for a pure state i. e. the vacuum state.

9.3 Experimental setup

We made two main changes to the experimental setup from the high cooperativity setup from chapter 7. First, we switched the pump cavity filter lock to a analog PID lock. Second, we improved the optical LO efficiency by amplifying the phase modulator output with an EDFA and then filtering out only the relevant frequency component with a filter cavity. The measurement to collect enough amount of downconverted signal were slow and long. As a result, we made a lot of effort in stabilizing every aspect of the experiment. This resulted in us working with a number of locks for different variables and drifts in the experiment. All of the locks are described in the next subsection.

9.3.1 Measurement locks

Optical pump locks

The generation of clean and stable optical pulsed pump required three different locks running in parallel. Firstly, the pump filter cavity was locked to the laser tone. Secondly, the laser was locked to the optical pump whispering gallery mode. And finally, the polarization of the optical pump drifted slowly and needed to be stabilized on the longer time scales.

We have already talked about how any interdependent set of locks need to run on different time-scales so that they don't each other to instability in section 7.3. Since we were working with a pulsed optical pump which was repeated only at 2 Hz, the laser lock to optical pump mode which relied on the pump reflection could get reliable error signal only on the order of seconds. As a result, we chose to prioritize the pump filter cavity lock as the faster lock. The polarization lock was naturally the slowest since polarization drifts were slow - on the order of 10s of seconds.

Pump filter lock The pump filter lock which is tuned via the cavity temperature and is locked to cavity transmission. We take 1% of the cavity transmission and measure it with a photodetector. The output of the photodetector is pulsed (since the optical pump is pulsed). It is redirected to an extremely low pass filter which converts the pulsed output to basically an average DC voltage which is suitable as an error signal for a analog PID lock circuit (see appendix D). The lock circuit is designed in house and has only proportional and integration elements (no derivative). With this lock, we cannot lock at the maximum transmission anymore because now we need an asymmetric error signal around the lock point. Consequently, we lock at a flank near the maximum transmission. We were able to lock to 95% of the maximum of the cavity transmission with the right P and I settings. The lock chosen to be fast (< 1 s) using the P and I values.

Laser lock The laser lock to the pump mode is exactly the same as described in the 7.3. The only change is that now it is slow owing to slow availability rate of the optical pump reflection. It now works on the order of a second.

Polarization lock The polarization lock to the optical pump makes sure that the pump polarization is always as close to TE as possible. If the polarization drifts, the mode contrast will decrease as the TM component simply reflects without interacting with the cavity. If we only have the optical reflection information at a single frequency, it is hard to predict whether the increase in reflection is due to laser detuning from the resonance or due to polarization drift. In other words, the error signal for the laser lock to optical mode and the polarization lock look exactly the same.

With no way to differentiate, we rely on the fact that laser lock to make the polarization lock work. First, we design it to be much slower than the laser lock since they are essentially working with the exact same error signal. Secondly, we trigger the polarization lock only when the laser lock cannot bring the reflected error signal below a certain level. This is a hint that polarization may have drifted. Thereafter, the polarization is changed in gradual steps while the laser lock is running and statistics are collected on the error signal. If the error signal shows a downward trend, we continue moving in the same direction, otherwise we try a different direction. The polarization lock is stopped as soon as the error signal is again within the set threshold.

Optical detection locks

On the optical detection side, we need two more locks. One locks the output filter which rejects the optical pump to the optical output signal frequency. Second locks the optical LO filter to the required optical LO tone. The locks are slightly dependent on each other - the optical LO lock can reduce the efficiency of the LO which reduces the measurement efficiency of the optical signal detection. The same can also happen if the optical signal filter drifted leaving no way to differentiate between them. In this case, we run the optical LO faster since it has a faster and easier way of measuring the error signal.

Optical LO filter lock After the optical LO tone is filtered by a cavity, 1% of the power is forked to measure the transmission through the cavity using a power meter. The power is maximized at its peak using a digital lock (similar to one described in algorithm 5.1 albeit without the dynamical step). The cavity is stabilized to within 1 mK temperature using a analog PID lock. We can tune the cavity by changing the temperature set point digitally using the lock script.

Optical signal filter lock The optical signal filter cavity which rejects the optical pump is the same as the optical LO filter cavity. It is also stabilized to within 1 mK temperature using a analog PID lock. However, it can drift slowly on the order of hours. For the experiment, we need to send a coherent optical signal pulse to the detection along with a tiny downconverted signal. The error signal for this lock is the power in the detected coherent optical signal. The detected coherent signal power can reduce either because the signal filter has drifted reducing the signal power or the optical LO filter has drifted reducing the heterodyne efficiency. For this lock, we depend on the optical LO lock to work properly. We collect statistics of the measured coherent signal power over tens of minutes and make small adjustments to temperature set point of the PID which maintains the filter cavity temperature. The lock script tries to maximize the detected signal power by moving this set temperature point in small steps.

9.4 Measurement

9.4.1 Pulse scheme and phase stability

The premise of the measurement is to simply have a strong pulsed optical pump which amplifies the vacuum and produces the spontaneous downconversion between the microwave and optical signal mode. However, the measurement gets more complicated because of a few practical challenges posed by the experiment. One of the biggest challenge is the stability of phase in the detected signals. We attempt to measure two mode squeezing in continuous variable space. To successfully measure any squeezing, the phase of the detected needs to be aligned during the entire measurement. This is a big challenge especially if the measurements run for multiple days.

We use single mode fibers as optical waveguides to transport the light from optics generation to the electro-optic device and finally to the optical detection. The phase picked up by the optics inside the fiber is very sensitive to temperature of the fibers. Since the amount of fibers we used is on the order of tens of meters the phase stability from device to detection is only on the order of $\sim 100 \mu\text{s}$. Fiber stretchers can be employed to stabilize the phase but since the phase drift was rather fast in our system and the lock signal for the fiber stretcher would be

occasional (depending on the pulsing frequency 2 Hz in this experiment), we took a different direction to achieve phase stability.

We devise a two-pulse scheme as shown in Fig. 9.1. The first high power pulse 1 generates the entanglement signal. Then, after waiting for 1 μ s, we apply another weaker optical pump (about 10 times lower power to minimize microwave thermal heating) but this time followed by a coherent microwave signal tone. The coherent microwave signal tone stimulates the downconversion of the optical pump. This results in production of coherent amplified signal on the optics signal side. The sent microwave signal is reflected back too with a signature of this back-action event (see chapter 8).

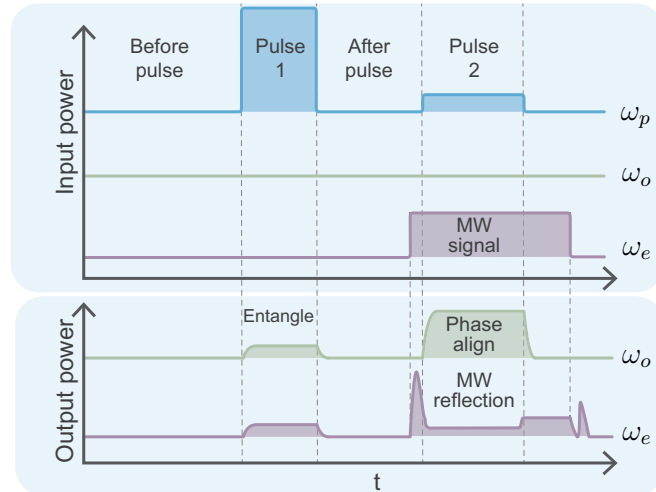


Figure 9.1: Schematic pulse sequence of a single measurement for two-mode squeezing measurements. Figure adapted from Ref. [SQH⁺23].

The produced optical signal is designed to have enough signal to noise such that the phase can be measured from a single produced pulse. Similarly, on the microwave side, single shot phase measurement can be made with the reflected microwave pulse. The idea behind the phase measurements is that by measuring the phase of produced optical signal and the reflected microwave signal, we can cancel out phase drifts originating anywhere in the experimental setup.

The fast short term drifts in optics are taken care of by the optical coherent pulse phase. Since the second optical pulse is also at the same frequency, we avoid any long term drifts that can happen between different frequencies travelling in the same fiber due to temperature dependent dispersion. The microwave phase remains stable for hours but can still drift slowly for a multiple day measurement. By measuring the phase of microwave reflected pulse, we can correct for slow drifts suffered in microwave signal generation and detection (production of microwave LO).

9.4.2 Measurement script

As described in the previous section, the measurement consists of multiple interdependent locks - most of which are digital. All the locks are managed by one measurement script which runs parallel interacting threads which control different locks in the experiment. The measurement script also launches a measurement thread which acquires the digitized data from the digitizer. The digitizer digitizes the measured voltages in 8-bit signed integers corresponding to a certain set voltage range. To save storage space, the script saves the digitized data as 8-bit integers

without converting them to voltages with double (16-bit) variables. Even though, we could have downconverted the data immediately after data acquisition and saved space by only saving the down-converted quadratures, we chose to store the full data because it allowed us to do a full frequency domain analysis as we will show in section 9.6.3.

9.5 System characterization

9.5.1 Optical modes

In this chapter, we show results from two different sets of optical modes shown in Fig. 9.2. The main difference between these mode sets is the amount of suppression of the anti-Stokes scattering rate compared to Stokes scattering rate given by scattering ratio $\mathcal{S} = \Gamma_{\text{AS}}/\Gamma_{\text{S}}$, which depends on the mode hybridisation of the anti-Stokes mode. The first set of optical mode (Fig. 9.2a) has $\mathcal{S} = -10.3 \text{ dB}$ on-resonance with an effective FSR = 8.799 GHz. The second set of optical modes with a lower $\mathcal{S} = -3.1 \text{ dB}$ have a different effective FSR = 8.791 GHz (Fig. 9.2b). Despite it being the same optical resonator, the FSR for the second set of optical modes is slightly different, because of partial hybridisation of the optical pump mode which alters the working FSR between the optical pump and signal mode, see section 3.5.

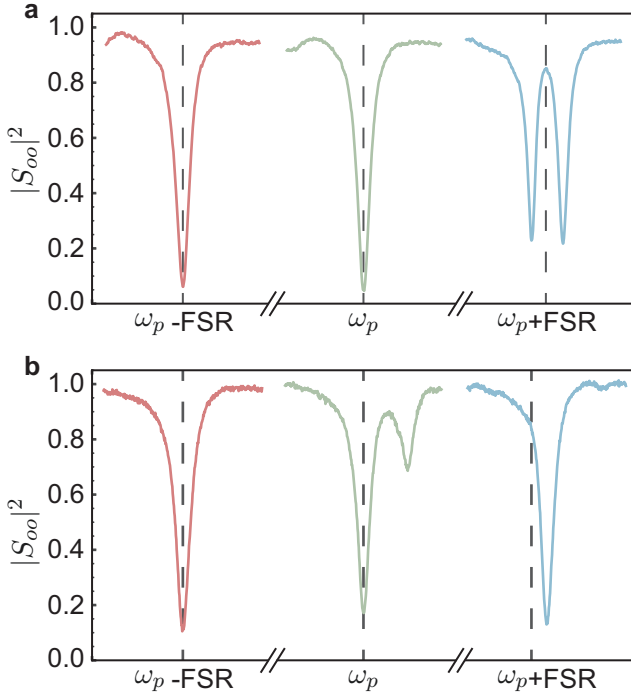


Figure 9.2: Normalized reflection intensity $|S_{oo}|^2$ spectra of optical modes \hat{a}_o , \hat{a}_p and \hat{a}_t in red, green and blue respectively. **a** (**b**) shows the optical mode spectra of the first (second) set of modes with the anti-Stokes and Stokes scattering ratio $\mathcal{S} = -10.3 \text{ dB}$ (-3.1 dB). The dashed line marks the effective FSR between the pump mode \hat{a}_p and the optical mode \hat{a}_o . Figure adapted from Ref. [SQH²³].

9.5.2 Added noise in detection

On the microwave side, added noise and corresponding gain due to a series of amplifiers and cable losses in the microwave detection chain is calibrated using a combination of a 50Ω

load. This has been discussed in detail in appendix B. For the two FSRs corresponding to two set of modes, the added noise has been calibrated carefully around a 11 MHz bandwidth (microwave linewidth). The added noise $N_{e,\text{add}}$ for 8.799 GHz and 8.791 GHz is found to be (13.09 ± 0.33) and (13.16 ± 0.34) respectively.

Optical added noise is calculated via 4-port calibration of the device. We use the calibrated transduction efficiency and $N_{e,\text{add}}$ in the microwave detection chain from to calculate the optical added noise. $N_{e,\text{add}}$ is firstly used to calculate the effective microwave detection gain. The microwave gain, along with the (off-resonant) microwave reflection measurement, is used to calculate the microwave input loss. Using this, we calculate the microwave signal power at the device, which, along with transduction efficiency, allows us to calculate the output optical power from the device. In conjunction with the measured output optical power at the end of the detection chain, the losses in the optical detection path and hence, the effective added noise with respect to the optical port of the device is calculated. The calculated optical added noise is $N_{o,\text{add}} = 5.54 \pm 0.21(7.42 \pm 0.22)$ for $\omega_e = 8.799$ GHz (8.791 GHz).

9.6 Data treatment

We conducted experiments with two different optical pump pulse length - 600 ns and 250 ns. Initially we started with longer pulses to get better measurement bandwidth (2 MHz for 500 ns of data per pulse). But after conducting multiple tests, we realized that the thermal heating resulting from longer pulses prevented us from clearly squeezing below vacuum. As a result, we later switched to shorter 250 ns optical pump pulses. This is explained in more details in the results section 9.7 later.

In this section, we describe all the steps for the data treatment in detail for 250 ns optical pump pulses (since they correspond to the final result), which includes the time domain analysis (Sec. 9.6.1), the pulse post-selection due to setup drift (Sec. 9.6.2), the frequency domain analysis (Sec. 9.6.3), and the quadrature correlations (Sec. 9.6.4).

9.6.1 Time-domain analysis

Both microwave and optical signals are detected via heterodyne detection by mixing with a strong local oscillator that is ~ 40 MHz detuned from respective mode resonance. The output heterodyne signals are digitized using a digitizer at 1 GigaSamples/second. First, we digitally downconvert the digitized data at $\omega_{\text{IF}} = 40$ MHz. This yields the two quadratures $I_{X_{e/o},\text{det}}(t)$ and $I_{P_{e/o},\text{det}}(t)$ of the microwave or optical output signal record with 40 MHz resolution bandwidth (using 25 ns time resolution). Fig. 9.3 shows the calibrated output power ($I_{X_{e/o},\text{out}}^2 + I_{P_{e/o},\text{out}}^2$) [cf. Eqn. 9.49] and the phase ($\arctan(I_{X_{e/o},\text{out}}/I_{P_{e/o},\text{out}})$) from a single pulse sequence. This includes the stochastic SPDC signals from a strong pump pulse, and the coherent stimulated downconverted signal from a weaker pump pulse together with a coherent microwave signal for calibration purposes. The SPDC signal produced by the first strong pulse is labeled by the shaded region for one single pulse, and the averaged output power over 1 million pulses is shown in Fig. 9.4. The coherent microwave reflection and stimulated parametric downconverted optical signal are adopted to obtain the phases during the pulse. We record this measured phase in both signal outputs during the second optical pump pulse for phase-drift correction in later post processing.

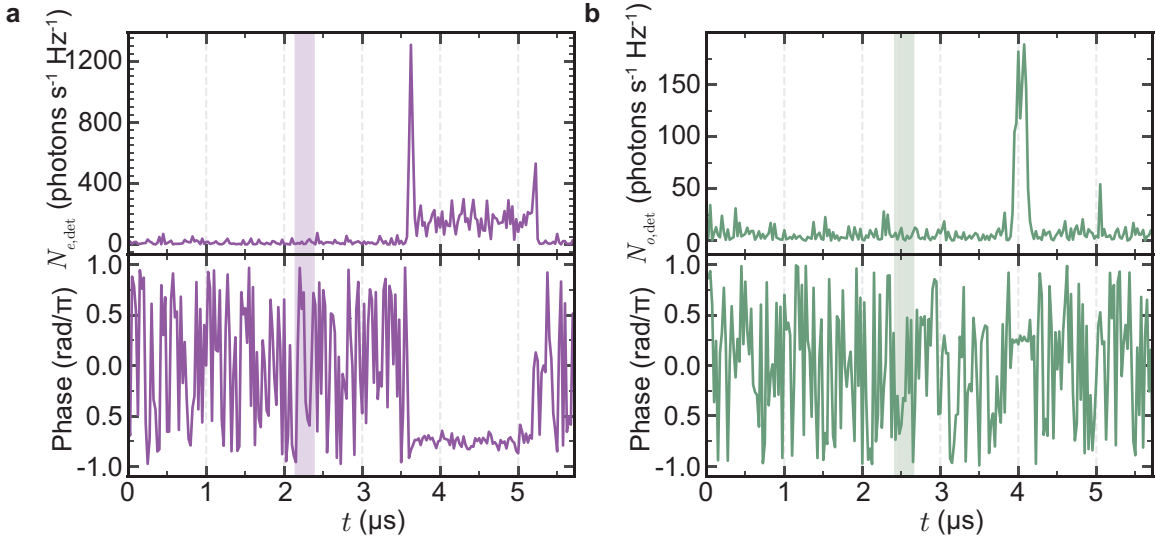


Figure 9.3: **Example single shot time-domain measurement.** **a** (**b**) show the measured microwave (optical) output signal downconverted at 40 MHz. The shaded part in each case shows the region of the SPDC signal (the first optical pump pulse). For a single pulse, the SNR of a SPDC signal is too small to be seen. However, during the second optical pump pulse, a coherent response is seen in both signal outputs where the phase can be measured with high SNR for each single shot. Figure adapted from Ref. [SQH⁺23].

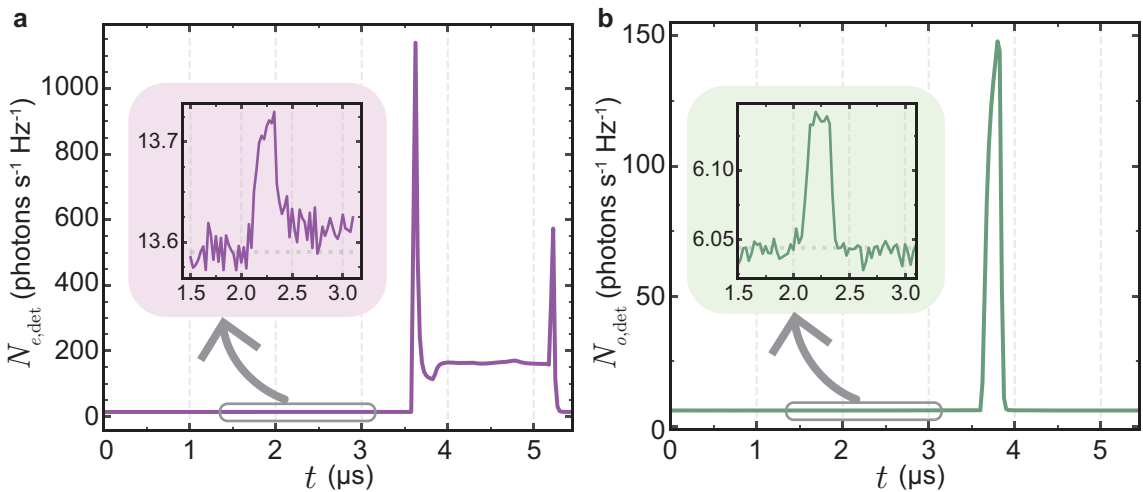


Figure 9.4: **Averaged time-domain measurement.** **a** (**b**) Measured output power in the \hat{a}_e (\hat{a}_o) mode in units of photons per second in a 1 Hz bandwidth and averaged over a million experiments. The SPDC signals are shown in the insets with the dashed gray lines indicating the calibrated detection noise floor $N_{j,\text{add}} + 0.5$. Figure adapted from Ref. [SQH⁺23].

Phase correction accuracy In order to determine the accuracy of a phase correction for the first pump pulse based on the phase measurement during the second pump pulse (see Fig. 9.1), we send a continuous microwave signal during both pump pulses and recorded the phase of the converted optical pulse during the first and the second optical pump pulse. Fig. 9.5 shows the phase difference between the first and second optical pump pulse for 2500 trials along with a normal distribution fit. Since we correct the phase in the first pump pulse based on the measured optical phase of the second optical pump pulse, the difference shows the limitations of this method. The fit variance for the distribution is 0.17 rad. On a similar set of model data, applying a random phase variation of 0.17 rad results in about 1.5-2.0% loss of correlations [cf. Sec. 9.6.4], whereas, we observe about 6-8% loss of correlations in the experiments. The imperfection in phase correction does not completely explain the decreased quantum correlations, which might be due to other experimental instabilities, especially the optical pump laser lock.

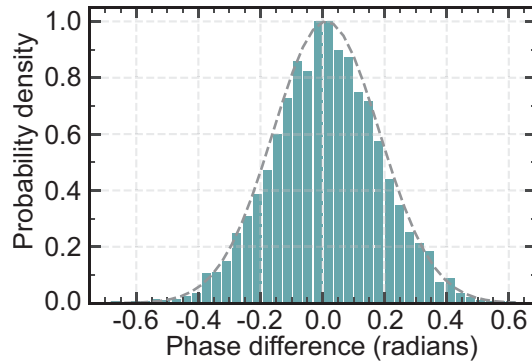


Figure 9.5: **Accuracy of phase correction scheme.** The histogram shows the difference in the measured phase between the first and second optical pump pulse. Figure adapted from Ref. [SQH⁺23].

9.6.2 Pulse post-selection

In our experiments, we use three temperature-stabilized optical filters, which may drift slowly in time. Two of them are used in the optical heterodyne detection (see section 9.3.1). The slow filter drifts can be identified from the amplitude of the coherent optical signal produced via stimulated parametric downconversion during the second optical pump pulse, which drops due to either the decreased transmission (if the signal filter, which rejects the optical pump, drifts) or the reduced LO power (if the optical LO filter drifts). This is evident in the histogram of the converted optical power during the second optical pump pulse as shown in Fig. 9.6a. The histogram is not symmetric and has a tail at the lower end.

To filter out the instances of drifted heterodyne detection, we select a threshold (in this case marked by a dashed line in Fig 9.6) and remove all pulses below the selected threshold along with 20 neighboring pulses (10 s in total time) before and after such instance. These threshold is chosen according to the filter drift and the filter temperature lock time-scales. After such filtering, usually about 10% of the data is removed and the histogram of the converted optical power during the second optical pump pulse becomes symmetric as shown in Fig. 9.6b.

9.6.3 Frequency domain analysis

After the time-domain analysis, we select three different time-snippets to analyze the data in the frequency domain - before-pulse, on-pulse and post-pulse defined with respect to the first

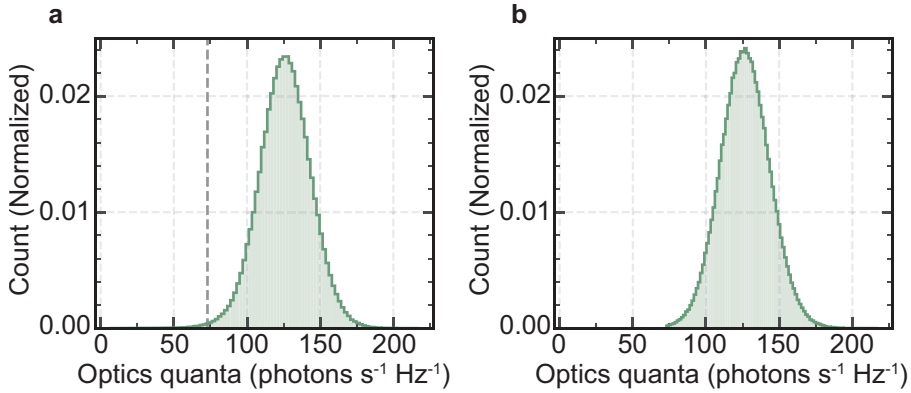


Figure 9.6: **Post-pulse selection.** The measured coherent optical power during the second optical pump pulse depends on the optical heterodyne gain and the received optical signal power. **a** shows the normalized histogram of this measured optical power over all the collected pulses. The same histogram after pulse post selection is shown in **b**. Figure adapted from Ref. [SQH⁺23].

optical pump pulse (see Fig. 9.1). The main challenge in processing the data in frequency domain is the proper normalization of the measured output spectrum [cf. Eqn. 9.47]. The microwave reflection baseline is not flat because of slight impedance mismatches between different components in the microwave detection chain. Similarly optical heterodyne shot noise floor is also not flat due to the frequency dependent balanced detector gain. In addition, we observe slight shift of a few millivolts each time in the digitizer measurements when a new measurement is launched and the digitizer is reinitialized. Combined with the fact that the amplifier gain in the microwave detection chain as well as the optical heterodyne gain (due to optical LO power drift) may drift over a long time, an in-situ calibration of vacuum noise level is needed.

In case of microwave, we need to first correct for the microwave reflection baseline distortion from impedance mismatch and then correct for the signal level shift caused by the digitizer. For the distorted baseline, we separately measure the microwave output spectrum when the microwave cavity is in its ground state (thermalized to 7 mK at mixing chamber). This measurement is shown in Fig 9.3a (gray) along with the measured before-pulse (cyan), on-pulse (purple) and after-pulse microwave noise spectrum (orange). Dividing the measured spectra with the cold cavity spectrum reveals a flat baseline Lorentzian noise spectra, however with an offset due to the digitizer drift. To correct for this offset, we perform an in-situ vacuum noise calibration using the off-resonance (waveguide) noise in the before-pulse microwave noise spectrum. An independent measurement of the microwave waveguide noise as a function of the average optical pump power (averaged over the full duty cycle) is shown in Fig. 9.8. The error bars (2σ deviation) result from the microwave detection chain gain and the measurement instrument drift. The power law fit reveals that the microwave waveguide noise grows almost linearly with average optical pump power, and only deviates significantly from 0 for optical pump power $> 3 \mu\text{W}$. By fitting additional power dependent measurements, shown in the Fig. 9.8, we verify that the observed noise floor corresponds to a waveguide bath occupancy of only $\bar{n}_{e,\text{wg}} = 0.001 \pm 0.0002 = 0.001 \pm 0.002$ at the very low average pump power of $\approx 0.12 \mu\text{W}$ used in this experiment with 250 ns long optical pump pulses. As a result, for the purpose of data analysis, we assume the microwave waveguide noise to be zero. In summary, we use the off-resonant waveguide noise for before-pulse microwave noise spectrum as an in-situ vacuum noise calibration.

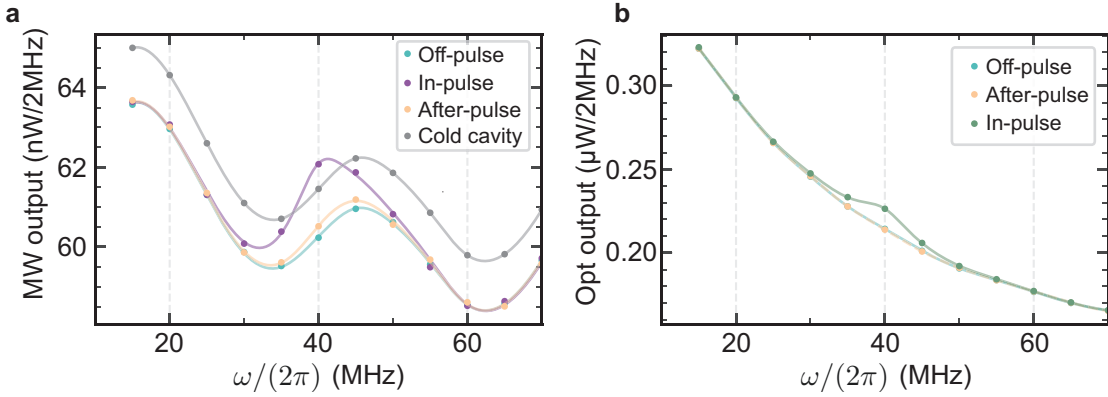


Figure 9.7: **Raw frequency domain measurements.** **a** shows the measured output spectra for time region before (during, after) the first optical pulse shown in cyan (purple, orange) as well as the cold cavity baseline in grey. Similarly, **b** shows the output spectra for the optical output before (during, after) the first optical pulse in cyan (green, orange). Figure adapted from Ref. [SQH⁺23].

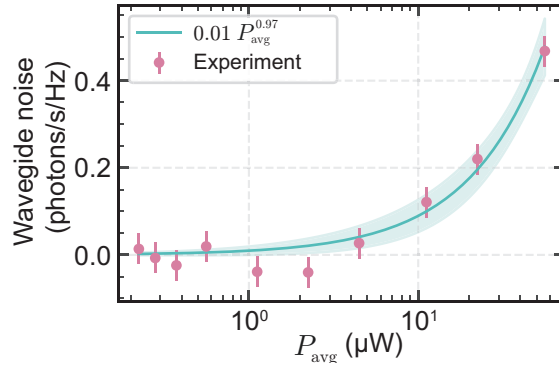


Figure 9.8: **Microwave waveguide noise as a function of the average optical pump power.** The error bars represent 2σ error. The solid line is a power law fit. We find the power law is actually quite close to a linear function. Figure adapted from Ref. [SQH⁺23].

In case of optics, the optical detection is shot-noise limited, and the excess LO noise at the optical signal frequency is suppressed by more than 40 dB using the pump filter cavity. We use the before-pulse optical noise spectrum as the vacuum noise level and normalize the optical on-pulse spectrum directly with the before-pulse in-situ calibration. Fig 9.3b shows noise spectrum (without normalization) of the optical off-pulse (cyan), on-pulse (green), and the after-pulse (yellow). The signal during the optical pump pulse is clearly visible, and the noise level is identical before and after the optical pulse.

The normalized noise spectra for both microwave and optics are shown in Fig. 9.9, where we can obtain the normalization gain [cf. Eqn. 9.47]. The figure shows the resulting average microwave noise spectra for all three time intervals with corresponding fit curves (dashed lines) and theory (solid line). Before and after the pump pulse, the on-resonant microwave output field takes on values above the vacuum level, with fitted intrinsic microwave bath occupancies $\bar{n}_{e,\text{int}} = 0.03 \pm 0.01$ and 0.09 ± 0.03 , respectively. The measured noise floor therefore corresponds to the shot noise equivalent level $N_{e,\text{add}} + 0.5$ (gray dashed lines). Fig. 9.9b shows the obtained average optical noise spectra during and after the pump, referenced to the measured shot noise level before the pulse. As expected, there is no visible increase of the optical noise level after the pulse.

During the pump pulse, an approximately Lorentzian shaped microwave and optical power spectrum are generated via the SPDC process (purple and green curve in Fig. 9.9). We perform a joint fit of the microwave and optical power spectral density during the pulse using a 5-mode theoretical model that includes the effects of measurement bandwidth. In this model, the in-pulse microwave bath occupancy $\bar{n}_{e,\text{int}} = 0.07 \pm 0.03$ and the cooperativity $C = 0.18 \pm 0.01$ are the only free fit parameters. Here the narrowed microwave linewidth $\kappa_{e,\text{eff}}/2\pi = 9.8 \pm 1.8$ MHz (taken from a Lorentzian fit) agrees with coherent electro-optical dynamical back-action (see section 8.2), where $\kappa_{e,\text{eff}} = (1 - C)\kappa_e$. This point to the fact that this cavity electro-optical device is deep in the quantum back-action dominated regime, a prerequisite for efficient microwave-optics entanglement generation.

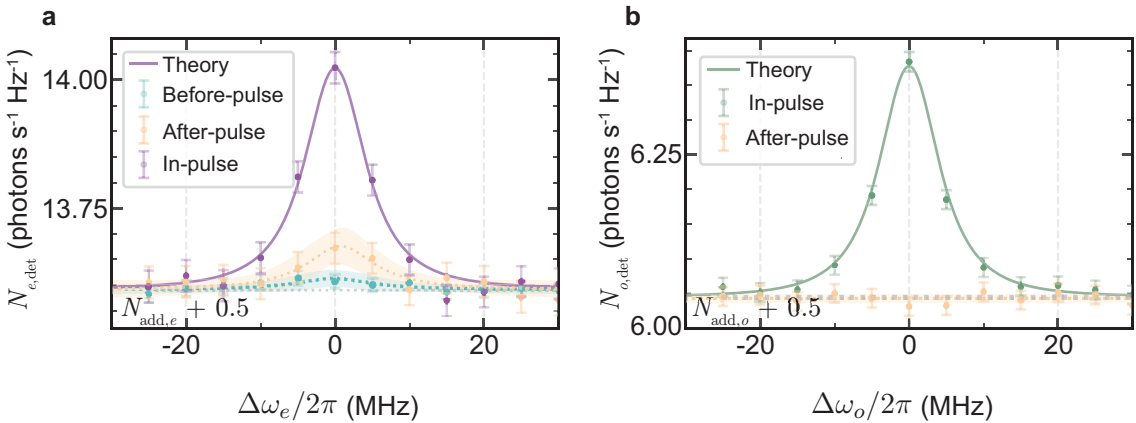


Figure 9.9: **Output noise in frequency-domain.** **a** Microwave output power spectral density vs. $\Delta\omega_e = \omega - \omega_e$ centered on resonance right during the three different time-snippets from Fig. 9.1. Yellow and green dashed lines are fits to a Lorentzian function, which yields the microwave bath occupancies before and after the entangling pulse. Error bars represent the 2σ statistical standard error and the shaded regions represent the 95% confidence interval of the fit. **b** Optical output power spectral density vs. $\Delta\omega_o = \omega_o - \omega$ during and after the first optical pump pulse. The in-pulse noise spectra are fit jointly with theory. Figure adapted from Ref. [SQH²³].

9.6.4 Joint-quadrature correlations

The detected output quadratures including excess added noise, i.e. $\hat{I}_{X_e,\text{out}}(\Delta\omega)$, $\hat{I}_{P_e,\text{out}}(\Delta\omega)$, $\hat{I}_{X_o,\text{out}}(\Delta\omega)$, $\hat{I}_{P_o,\text{out}}(\Delta\omega)$, can be obtained from the real and imaginary parts in the discrete Fourier transform of the photocurrent by normalizing to the detection gain [cf. Eqn. 9.49].

Similar to Sec. 9.2.3, we can define the joint detected quadratures, by applying phase rotation on the optical quadratures,

$$\begin{aligned} \hat{I}_{X,+}(\Delta\omega, \phi) &= \frac{\hat{I}_{X_e,\text{out}}(\Delta\omega) + [\hat{I}_{X_o,\text{out}}(\Delta\omega) \cos \phi - \hat{I}_{P_o,\text{out}}(\Delta\omega) \sin \phi]}{\sqrt{2}}, \\ \hat{I}_{P,-}(\Delta\omega, \phi) &= \frac{\hat{I}_{P_e,\text{out}}(\Delta\omega) - [\hat{I}_{X_o,\text{out}}(\Delta\omega) \sin \phi + \hat{I}_{P_o,\text{out}}(\Delta\omega) \cos \phi]}{\sqrt{2}}. \end{aligned} \quad (9.66)$$

To verify the non-classical correlation between the unitless quadrature variables for output microwave and optics field, i.e. $\hat{X}_e(\Delta\omega)$ & $\hat{X}_o(-\Delta\omega)$ and $\hat{P}_e(\Delta\omega)$ & $\hat{P}_o(-\Delta\omega)$, we can

calculate the phase dependent joint quadrature variance [cf. Eqn. 9.60],

$$\begin{aligned}\langle \hat{X}_+^2(\Delta\omega, \phi) \rangle &= \langle \hat{I}_{X,+}^2(\Delta\omega, \phi) \rangle - \frac{N_{e,\text{add}} + N_{o,\text{add}}}{2}, \\ \langle \hat{P}_-^2(\Delta\omega, \phi) \rangle &= \langle \hat{I}_{P,-}^2(\Delta\omega, \phi) \rangle - \frac{N_{e,\text{add}} + N_{o,\text{add}}}{2}.\end{aligned}\quad (9.67)$$

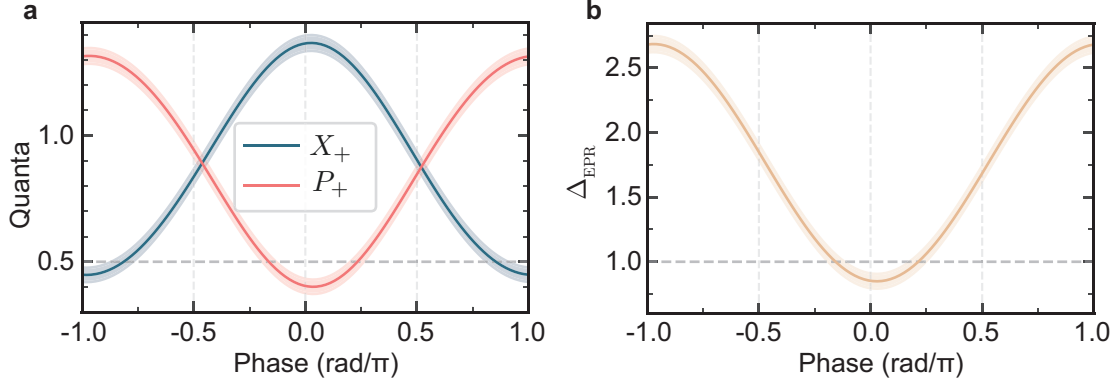


Figure 9.10: **Joint quadratures as a function of LO phase.** **a.** Joint quadratures at resonance $X_+(\Delta\omega = 0)$ and $P_+(\Delta\omega = 0)$ are plotted as a function of the local oscillator phase ϕ . **b.** Δ_{EPR} as a function of ϕ . The shaded region in both plots represents the 2σ statistical error. Figure adapted from Ref. [SQH⁺23].

For $\Delta\omega = 0$, we plot the joint quadrature variance as a function of local oscillator phase in Fig. 9.10 (a). The shaded region represent the 2σ statistical error in the calculated joint quadrature variances. The obtained resonant $\Delta_{\text{EPR}}(0, \phi)$ is shown in Fig. 9.10(b). The minimum and maximum of $\Delta_{\text{EPR}}(\phi)$ over the local oscillator phase are defined as $\min[\Delta_{\text{EPR}}] = \Delta_{\text{EPR}}^-$ and $\max[\Delta_{\text{EPR}}] = \Delta_{\text{EPR}}^+$. $\Delta_{\text{EPR}}^- < 1$ indicates non-classical joint correlations and squeezing below vacuum levels.

The broadband phase that minimizes $\Delta_{\text{EPR}}(\Delta\omega, \phi)$, i.e. $\phi_{\min}(\Delta\omega)$, reveals the difference in arrival times (group delay) between the microwave and optical signal output (Fig. 9.11a). After fixing the inferred time delay between the in-pulse arrival time of the microwave and optical signal, ϕ_{\min} becomes independent of frequency detuning from the mode resonances. Thus, by utilizing the broadband quantum correlations, we adjust for the differences in arrival times by ensuring that the slope of ϕ_{\min} with respect to detuning $\Delta\omega$ is minimized for all datasets we analyze.

9.6.5 Quadrature histogram raw data

As a sanity check, we can calculate the difference in two-variable quadrature histogram from the pulse-off (before-pulse) and pulse-on data. Structure in this difference histogram reveals presence of signal (extra noise) during the pulse-on part and any correlations present. Fig. 9.12 shows the normalized difference of the two-variable quadrature histograms obtained during and before the optical pump pulse based on the data shown in Figs. 9.9 and 9.15. These unprocessed histograms directly show the phase insensitive amplification in each channel as well as the correlations in (X_e, X_o) and (P_e, P_o) . Note however that - in contrast to the analysis in the main text - taking this difference does not lead to a valid phase space representation since also the vacuum noise of 0.5 together with the output noise of 0.026 ± 0.011 photons (due to the residual microwave bath occupancy right before the pulse) are subtracted, hence the negative values.

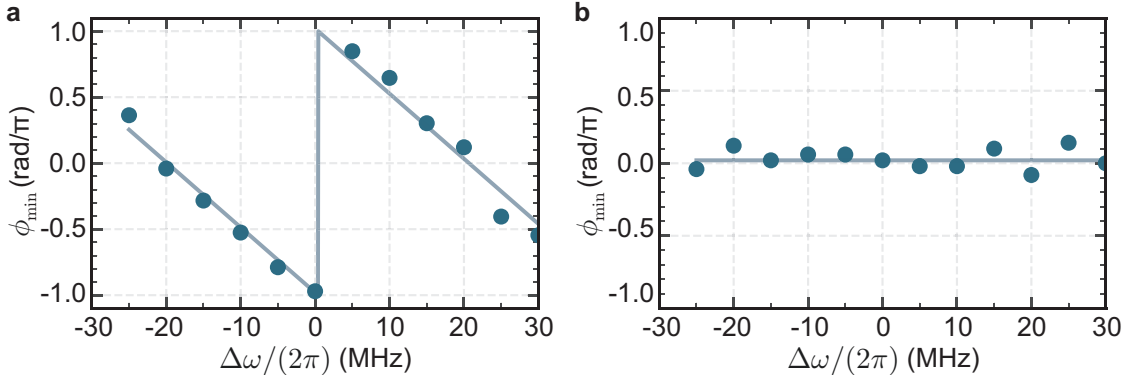


Figure 9.11: **Correcting the time delay between microwave and optical pulses.** The plots show the local oscillator phase ϕ_{\min} which minimizes $\Delta_{\text{EPR}}(\Delta\omega, \phi)$ as a function of detuning frequency $\Delta\omega$. **a** (**b**) shows the case when the time difference of arrival between the microwave and optics signals was 25 ns (≈ 0 ns). The solid lines are the linear fit to the experimental data. Figure adapted from Ref. [SQH⁺23].

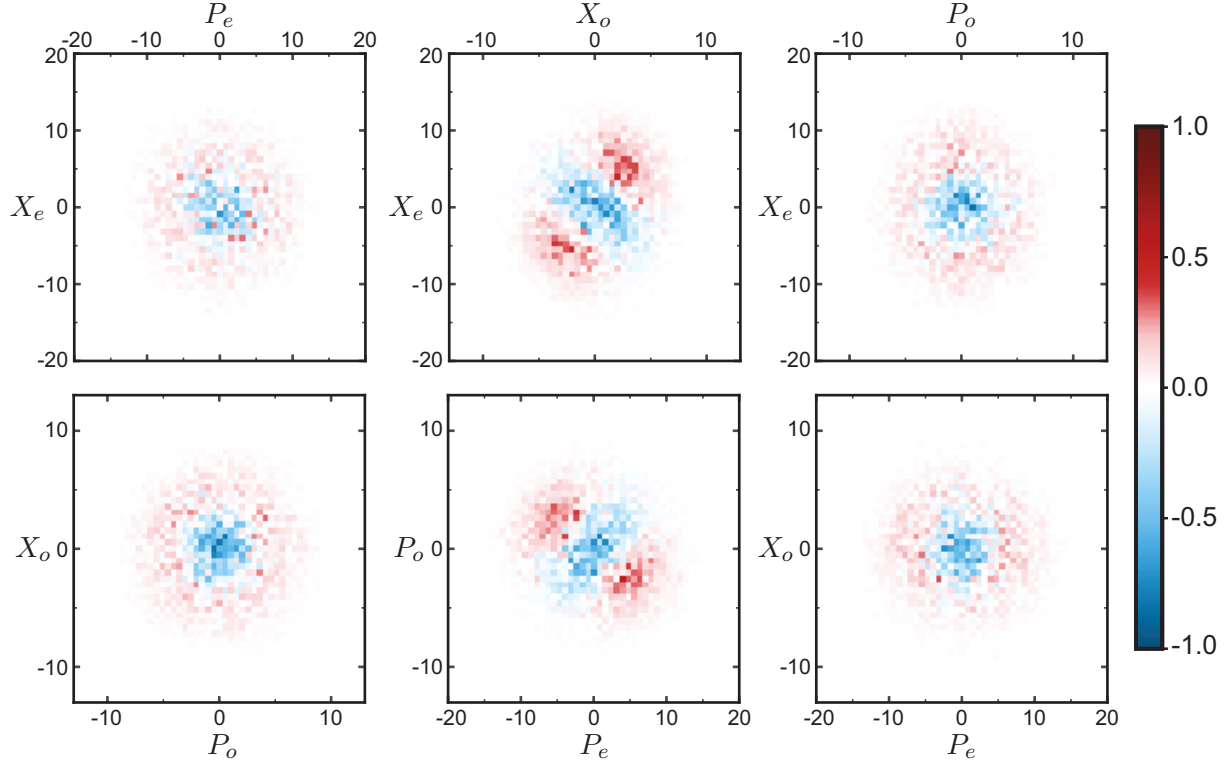


Figure 9.12: **Quadrature histogram raw data.** Normalized difference of the two-variable quadrature histograms obtained during and before the optical pump pulse based on the data shown in Figs. 9.9 and 9.15. Figure adapted from Ref. [SQH⁺23].

9.6.6 Error analysis

In the next section, we calculate the covariance matrix of the output field quadratures $V(\omega)$ from the extracted microwave and optical quadratures from frequency domain analysis [cf. Eqn. 9.53] The error in calculating the covariance matrix comes from two sources - the statistical error due to finite number of pulses, and the systematic error in the vacuum noise level calibration.

Statistical error

The error in the calculation of bivariate variances comes from the statistical uncertainties, arising from finite number of observations of a random sample. This error is the major component of our total error in diagonal covariance matrix elements. The error in calculating the variance of a sample distribution sampled from a Gaussian variable follows the Chi-squared distribution and is given as,

$$\text{Var}(\sigma^2) = \frac{2\sigma^2}{N-1}, \quad (9.68)$$

where, σ^2 is the variance of sample distribution and N is its size.

In addition, *the error in the covariance from a bivariate variable* is given by the Wishart distribution [Wis28]. For a general bivariate covariance matrix Σ given as,

$$\Sigma = \begin{pmatrix} \sigma_{11}^2 & \rho\sigma_{11}\sigma_{22} \\ \rho\sigma_{11}\sigma_{22} & \sigma_{22}^2 \end{pmatrix}, \quad (9.69)$$

the variance of the covariance matrix is given by,

$$\text{Var}(\Sigma) = \frac{1}{N-1} \begin{pmatrix} 2\sigma_{11}^4 & (1+\rho^2)\sigma_{11}^2\sigma_{22}^2 \\ (1+\rho^2)\sigma_{11}^2\sigma_{22}^2 & 2\sigma_{22}^4 \end{pmatrix}. \quad (9.70)$$

Systematic error

Although, the systematic error in our measurements are not as significant, they still are a noticeable source of error. Here the error in calculating the covariance matrix results form the error in the estimation of the vacuum noise levels. More specifically, the error in determining the added noise due to the microwave and optical detection chain, as discussed in Sec. 9.5.2. Propagating these systematic errors through the covariance matrix analysis is non-trivial, since calculating the error in variance of erroneous quantities is challenging. Therefore, we use a worst-case scenario approach to calculate the total error including the statistical error and the systematic error. We repeat the full analysis, including the statistical errors, for the lower and upper bound of the uncertainty range from the systematic errors for the microwave and optical added noise levels. Repeating the analysis expands the error bars in the calculated quantities. We take the extremum of all the error bars from all the repetitions of analysis to get the total error bar. In the following section, we report both statistical error and the total error.

9.7 Results

From the frequency analysis of the previous section, we have access to the normalized extracted quadrature variables for both microwave and optics output fields $X_i(\Delta\omega), P_i(\Delta\omega)$ as a function of frequency. For each frequency component the bipartite Gaussian state of

the propagating output fields can be fully characterized by the 4×4 covariance matrix (CM) $V_{ij} = \langle \delta u_i \delta u_j + \delta u_j \delta u_i \rangle / 2$, where $\delta u_i = u_i - \langle u_i \rangle$ and $u \in \{X_e, P_e, X_o, P_o\}$ (see section 9.2.3). The diagonal elements in V correspond to the individual output field quadrature variances in dimensionless units. These are obtained from the measured variances after subtracting the measured detection noise offsets shown in Fig. 9.9, i.e. $V_{ii}(\Delta\omega) = V_{ii,\text{meas}}(\Delta\omega_i) - N_{i,\text{add}}$. The obtained CM from the data in Fig. 9.9 at $\Delta\omega = 0$ is shown in Fig. 9.13 in its standard form. It corresponds to the quantum state of the propagating modes in the coaxial line and the coupling prism attached to the device output, i.e. before setup losses or amplification incur. The non-zero off-diagonal elements indicate strong correlations between microwave and optical quadratures.

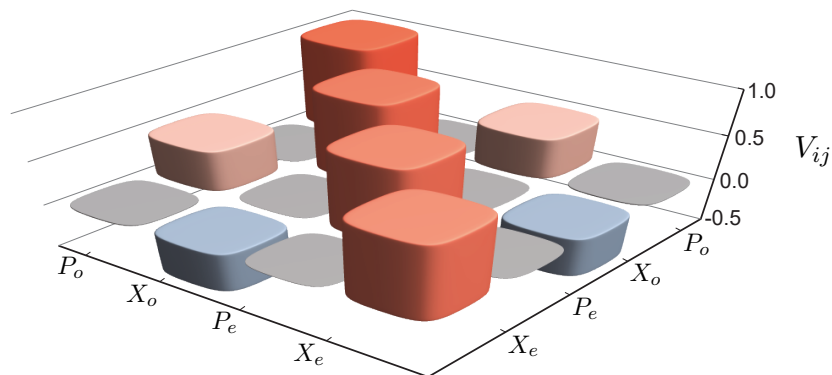


Figure 9.13: Measured covariance matrix V_{ij} in its standard form plotted for $\Delta\omega_j = 0$ from the data in Fig. 9.9. Figure adapted from Ref. [SQH⁺23].

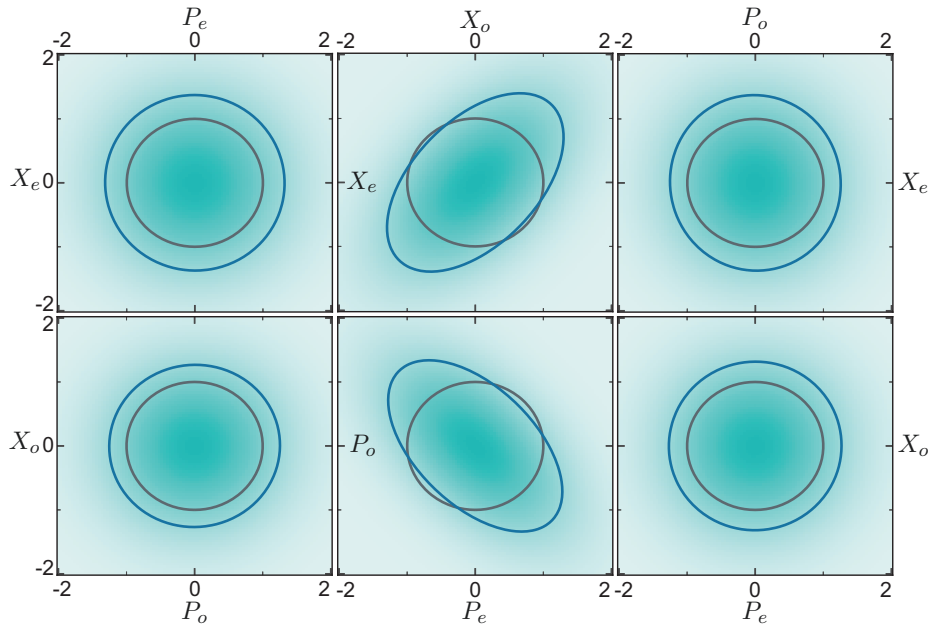


Figure 9.14: **Wigner function marginals at resonance** Wigner function marginals of different output quadrature pairs in comparison to vacuum for $\Delta\omega_j = 0$ from the data in Fig. 9.14. The contours in blue (grey) represent the $1/e$ fall-off from the maximum for the measured state (vacuum). Figure adapted from Ref. [SQH⁺23].

The two-mode squeezed quadratures are more intuitively visualized in terms of the quasi-

probability Wigner function,

$$W(\mathbf{u}) = \frac{\exp[-\frac{1}{2}\mathbf{u}V^{-1}\mathbf{u}^T]}{\pi^2\sqrt{\det(V)}}, \quad (9.71)$$

where $\mathbf{u} = (X_e, P_e, X_o, P_o)$. Different marginals of this Wigner function are shown in Fig. 9.14, where the (X_e, X_o) and (P_e, P_o) marginals show two-mode squeezing in the diagonal and off-diagonal directions. Middle two cross-quadrature marginals show two-mode squeezing below the vacuum level in the diagonal and off-diagonal directions. The two show a slightly different amount of squeezing, which is due to the statistical uncertainty in the measured CM.

Figure 9.15 shows the amount of two-mode squeezing between microwave and optical photon pairs. Correlations are observed at $\Delta\omega_j = \pm(\omega - \omega_j)$ around the resonances due to energy conservation in the SPDC process. The averaged microwave quadrature variance (purple dots) $\bar{V}_{11} = (V_{11} + V_{22})/2$ and the averaged optics quadrature variance (green dots) $\bar{V}_{33} = (V_{33} + V_{44})/2$ are shown in the top panel along with the prediction from our five-mode theory (solid line) and a simple fit to a Lorentzian function (dashed line), showing perfect agreement. Measured microwave-optical correlations (yellow dots) $\bar{V}_{13} = (V_{13} - V_{24})/2$ and the Lorentzian fit (dashed line) lie slightly below the theoretical prediction (solid line), which we assign to remaining imperfections in the phase stability (see section 9.6.1).

The bottom two panels of Fig. 9.15 show the squeezed and anti-squeezed joint quadrature variances $\Delta_{\text{EPR}}^{\mp} = \bar{V}_{11} + \bar{V}_{33} \mp 2\bar{V}_{13}$ (red and blue color respectively). We observe two-mode squeezing below the vacuum level, i.e. $\Delta_{\text{EPR}}^- < 1$, with a bandwidth close to the effective microwave linewidth. The maximal on-resonant two-mode squeezing is $\Delta_{\text{EPR}}^- = 0.85^{+0.05}_{-0.06}$ (2σ , 95% confidence) for ~ 1 million pulses with $\bar{V}_{11} = 0.93$, $\bar{V}_{33} = 0.84$ and $\bar{V}_{13} = 0.46$. Hence, this deterministically generated microwave-optical state violates the Duan-Simon separability criterion by $> 5\sigma$. Note that this error also takes into account systematical error in the added noise calibration used for scaling the raw data. These values correspond to a state purity of $\rho = 1/(4\sqrt{\det[V]}) = 0.44$ [cf. Eqn. 9.65] and demonstrate microwave-optical entanglement between output photons with a logarithmic negativity of $E_N = 0.17$ [cf. Eqn. 9.63].

9.7.1 Earlier attempts at measuring two-mode squeezing

It is important to note the experimental steps and failures that led to the measurement shown in Fig. 9.15. Before experimenting with 250 ns long optical pump pulses, we were using 600 ns long optical pump pulses and a different set of optical modes with a worse suppression ratio of $S = -3.1$ dB (see section 9.5.1). A sample measurement with a 600 ns is shown in Fig. 9.16 similar to Fig. 9.15. It can be observed that compared to Fig. 9.15, in this case, the Δ_{EPR}^- is not clearly below 1. Although a general trend of lower Δ_{EPR}^- values is observed around the resonance $\Delta\omega_j = 0$, the trend is not clear enough to have confidence in the generated two-mode squeezing beyond any doubt. It seemed that Δ_{EPR}^- just hovers around the value of 1 and dips sometimes below 1.

Power sweep We made an optical pump power sweep with these optical modes to check any dependence of two-mode squeezing with the optical pump power. The power sweep is shown in Fig. 9.17 with each data point based on 170000-412500 individual measurements each with a 2 Hz repetition rate. We show the in-pulse microwave thermal occupancy $\bar{n}_{e,\text{int}}$ for before-pulse, after-pulse and in-pulse regimes as a function of the peak optical pump power. The in-pulse occupancy is obtained by the joint theory fit and approximated with a constant

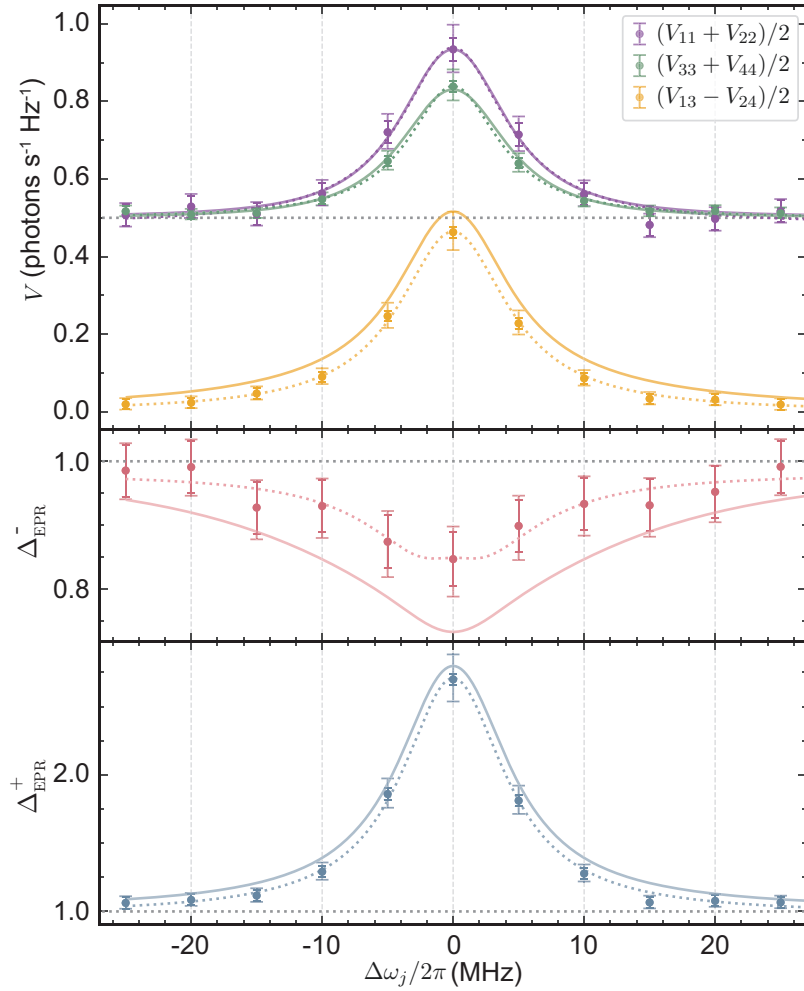


Figure 9.15: **Squeezing with 250 ns optical pump pulse** Data from Fig. 9.14. Top panel, the measured average microwave output noise $\bar{V}_{11} = (V_{11} + V_{22})/2$ (purple), the average optical output noise $\bar{V}_{33} = (V_{33} + V_{44})/2$ (green) and the average correlations $\bar{V}_{13} = (V_{11} - V_{24})/2$ (yellow) as a function of the measurement detunings. The solid lines represent the joint theory fit and the dashed lines are individual Lorentzian fits to serve as a guide to eye. The middle (bottom) panel shows two-mode squeezing Δ_{EPR}^- in red (anti-squeezing Δ_{EPR}^+ in blue) calculated from the top panels. The darker color error bars represent the 2σ statistical error and the outer (faint) 2σ error bars also include the systematic error in calibrating the added noise of the measurement setup. Figure adapted from Ref. [SQH⁺23].

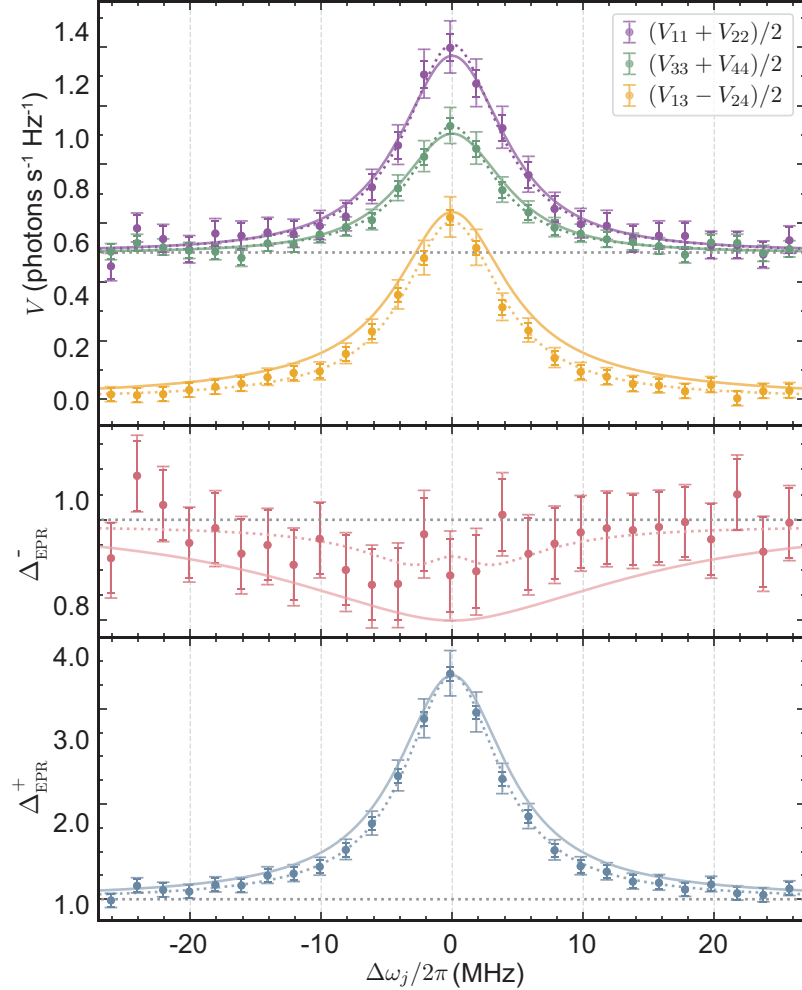


Figure 9.16: **Squeezing with 600 ns optical pump pulse** Refer to figure caption of Fig. 9.15.

function (solid line). The microwave mode thermal bath occupancy $\bar{n}_{e,int}$ changes little as a function of the peak optical pump power at the device and is approximated with a constant function (solid maroon line in the top panel). The middle panel shows the on-resonance mean CM elements. They scale with cooperativity and are in excellent agreement with theory (solid lines) based on the $\bar{n}_{e,int}$. The bottom two panels show the *on-resonance* squeezing Δ_{EPR}^- and anti-squeezing Δ_{EPR}^+ along with theory (solid lines). The theoretically predicted values always falls behind the predicted squeezing and anti-squeezing due to imperfections of phase corrections as we have already discussed. We see that all but one of the measured mean Δ_{EPR}^- are below the vacuum level and for three power settings we even see $> 2\sigma$ significance for entanglement. However, since all the CM elements increase at a similar rate with optical pump power, Δ_{EPR}^- changes little in the shown cooperativity range. The anti-squeezing Δ_{EPR}^+ scales up with cooperativity as expected. With this power sweep, we concluded that changing the optical pump power is not the way to finally getting a proper Δ_{EPR}^- values which is well below 1.

After the power sweep, we looked for better set of optical modes and found a different set with better suppression ratio of $S = -10.3$ dB (see section 9.5.1). We repeated the measurement with 600 ns long optical pump pulses. One of the interesting attempt is shown in Fig. 9.18. Compared to Fig. 9.16, the main difference lies in the fact that Δ_{EPR}^- in the middle panel exhibits a clear double-dip shape. This is because the correlations \bar{V}_{13} have a wider bandwidth

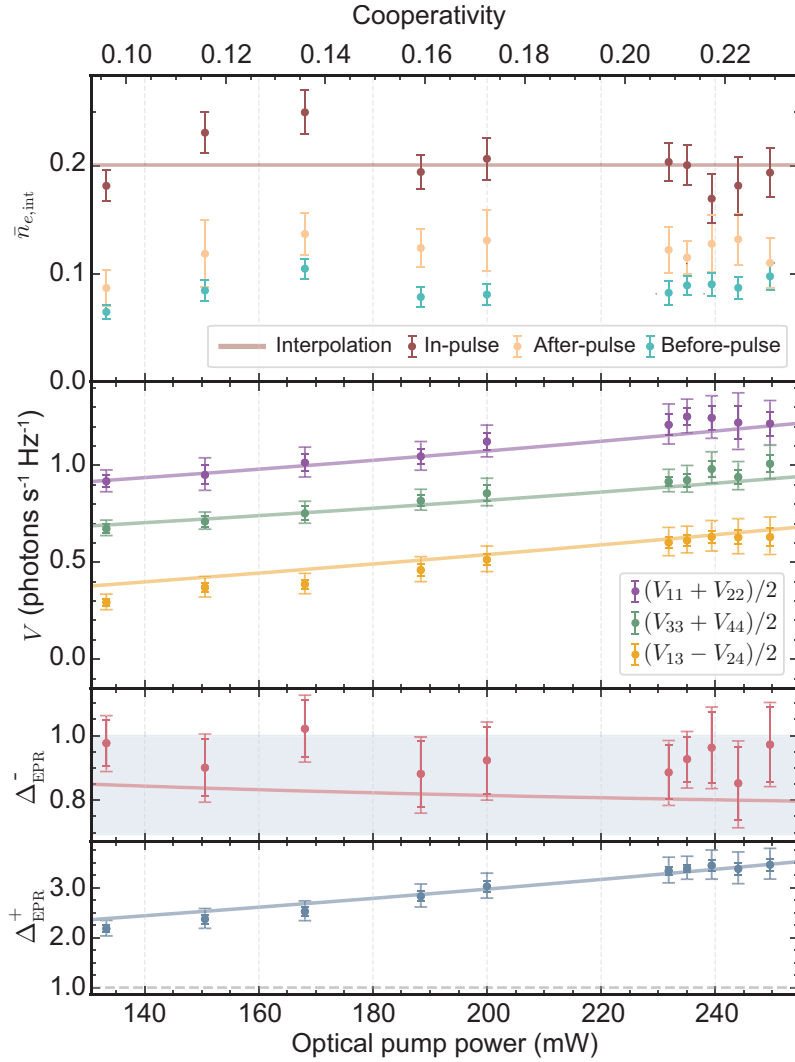


Figure 9.17: Power dependence of CM elements. The top panel shows the microwave mode thermal bath occupancy $\bar{n}_{e,\text{int}}$ for before-pulse, after-pulse and in-pulse regimes as a function of the peak optical pump power at the device and the corresponding cooperativity. The bottom two panels show the *on-resonance* squeezing Δ_{EPR}^- and anti-squeezing Δ_{EPR}^+ calculated from the middle panel along with theory (solid lines). The darker color error bars represent the 2σ statistical error and the outer (faint) error bars also include systematic errors. Figure adapted from Ref. [SQH⁺23].

than the emitted noise spectra (\bar{V}_{11} and \bar{V}_{33}), which get narrowed due to dynamical back-action (see previous chapter 8). If these wider bandwidth correlations don't clearly overwhelm the emitted noise, interference between two Lorentzian functions of different widths (dashed line) leads to the specific shape of Δ_{EPR}^- . We can also confirm this using the 5-mode model theory if we increase the internal thermal bath occupancy for microwave. The theory plot (solid red line) in Fig. 9.18 does not exhibit the double-dip line-shape due to higher expected correlations compared to the experimentally observed values.

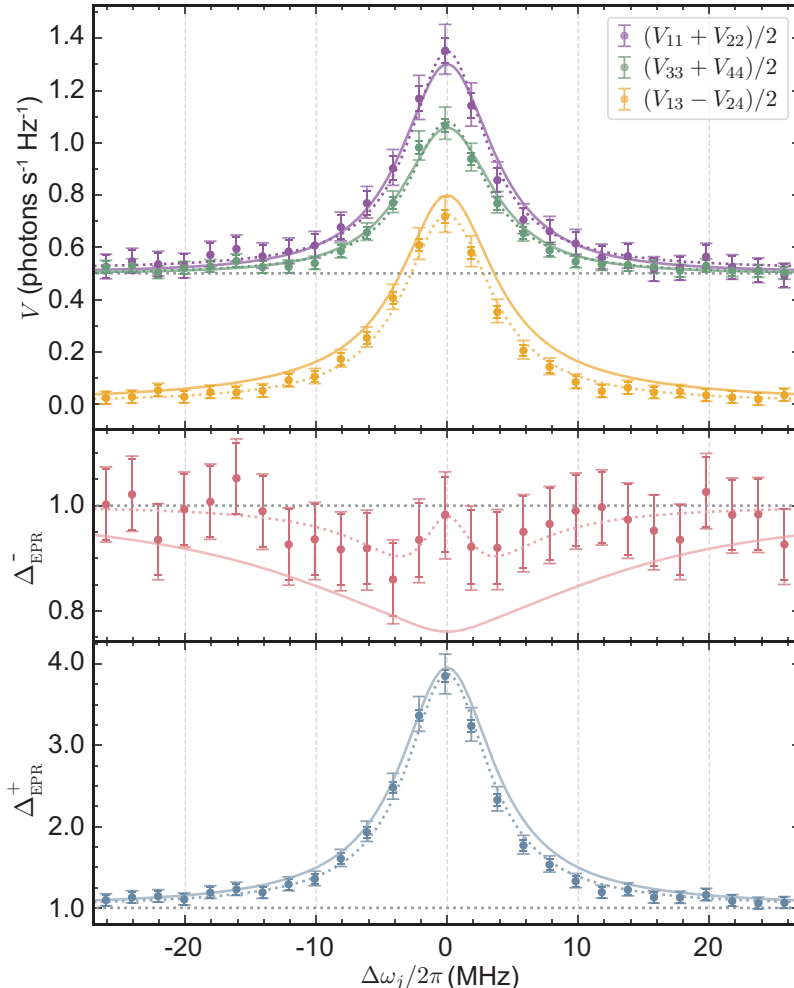


Figure 9.18: **Squeezing with 600 ns optical pump pulse** Refer to figure caption of Fig. 9.15.
Figure adapted from Ref. [SQH⁺23].

These results indicated that a 600 ns optical pump pulse heat the microwave mode to a degree which is large enough to prevent a clear observation of squeezing over the full bandwidth below the vacuum level ($\Delta_{\text{EPR}}^- < 1$). This gave us an hint to switch to shorter 250 ns optical pump pulses to prevent heating of microwave mode. However, the smaller pulses meant smaller measurement time and larger bandwidth. Since the emission bandwidth of the SPDC signal is ~ 10 MHz, only a 5 MHz measurement bandwidth possible with 250 ns (200 ns taken after steady state) optical pump pulses meant a worse signal to noise ratio. To combat this, we increase the number of statistics collected to 1 million which took about 6 days.

9.8 Conclusions

In conclusion, we have clearly demonstrated deterministic quantum entanglement between propagating microwave and optical photons, thus establishing a non-classical communication channel between circuit quantum electrodynamics and quantum photonics. We find that reducing the microwave thermal noise is the most crucial aspect to finally achieving this result. We suspect that the phase stability in the experiment is still not adequate and can be made better. It is hard to say if the phase stability on the shorter time scales need to be improved or if there are some long term phase drifts crippling the system.

Currently, our device can readily be used for probabilistic heralding assisted protocols [[DLCZ01](#), [ZWZ⁺20](#), [KRH⁺21](#)] to mitigate optical setup losses and extend the entanglement to room temperature fiber optics. In the future, we would want to increase the pulse repetition rate by orders of magnitude with improved thermalization, higher microwave and optical quality factors, and electro-optic coupling enhancements which will reduce the required pump power and the associated thermal load. Coupling efficiency improvements to the signal modes will allow for higher levels of two-mode squeezing and facilitate also deterministic entanglement distribution schemes [[AMFR22](#)], teleportation-based state transfer [[RHBF19](#), [WCFZ21](#)] and quantum-enhanced remote detection [[BGW⁺15](#)].

Since we show entanglement between itinerant photons, our device can readily be integrated in any system. Being fully compatible with superconducting qubits in a millikelvin environment such a device will facilitate the integration of remote superconducting quantum processors into a single coherent optical quantum network. This is not only relevant for modularization and scaling [[BDG⁺22](#), [ACC⁺22](#)], but also for efficient cross-platform verification of classically intractable quantum processor results [[KMC22](#)].

CHAPTER 10

Outlook

10.1 Introduction

We started this thesis with a vision. The vision of a multinode quantum network with hybrid systems all connected with optical photons as the quantum information carriers. With the intention to fill a hole in this vision, we tried to bridge the gap between microwave and optical frequencies via electrooptics in the quantum limit. With the use of a pulsed optical pump, we were able to show a total device transduction efficiency of $\sim 10\%$ between these frequencies with added noise referred to the input either close to 1 or comfortably below 1 for the two transduction directions. Since we could also achieve high electrooptic cooperativities, we were able to show direct dynamical backaction effects between the optical and microwave modes similar to those observed in optomechanics and atomic physics several years ago. A combination of having high electrooptic cooperativity at the same time as having the microwave mode close to its ground state allowed us to measure two-mode squeezing between microwave and optical modes for the first time.

Although these are remarkable achievements, the prospect of connecting microwave-based quantum computers via optical photons still remains challenging. Current transduction efficiencies allow only for heralded quantum communication protocols while deterministic communication protocols remain well beyond reach. Even though we showed entanglement between itinerant microwave and optical photons, it was quite weak owing to coupling losses to cavities and added thermal noise in the microwave mode. The entanglement is lost by the time we detect the optical photon due to more transmission losses associated with filtering out the optical pump photon and inefficient heterodyne detection.

Due to additional losses and added noise either due to amplification or thermal heating, we have been limited by what we can do with our electrooptic device, even though we have already achieved close to unity cooperativities. As a result, one of the next steps is to fix these problems - reduce the need for high optical pump power by increasing the quality factor of the cavities and reduce coupling losses by using overcoupled cavities. We propose to fix these issues with a new transducer design. We discuss this new design in detail in this chapter.

However, the limitations of current transducer devices should not prevent us from attempting some preliminary experiments. The obvious direction is to integrate the imperfect transducer with superconducting circuit qubits - the most mature microwave qubit technology, as some experiments have already done [DUM⁺22]. Currently, these experiments focus on reading out the classical microwave signal which encodes the state of qubit after transducing it in the

optical domain. The next step can be to read out the qubit with just the optical light and the transducer, which is first used to produce the microwave signal that measures the qubit and then subsequently transduces it back to optical domain for final detection.

Highly non-classical quantum states that are easy to generate using qubits [HSG⁺07, MSKP20] can be transduced to the optical domain for further characterization and verification. After ensuring we can convert quantum states from the microwave to the optical domain, we can move on to the task of producing and verifying quantum entanglement between a superconducting qubit and an optical photon. And finally, using such entanglement between two pairs of qubits and optical photons, we can use entanglement swapping [PBWZ98] to entangle two qubits via optical photons [RKK⁺22]. We also discuss these experiments briefly in this chapter.

10.2 New transducer design

In section 4.4, we discussed one of the biggest unexpected problems which limited the performance of our device in a major way. The problem was a drop in optical quality factors by about 10 times as the device was cooled down to millikelvin temperatures. We speculated that this might be due to micro-cracks that form on the rim of optical WGM resonator when the microwave cavity is closed around it. On the other hand, in Section 3.3.4, we discussed how the microwave mode quality factors were also not as high as expected due to possible piezoelectric coupling losses with the lithium niobate resonator.

Both of these problems can be solved, by making a few design changes to the transducer. A new design as proposed by Rueda *et al.* [RHBF19] is shown in Fig. 10.1. The main idea behind this re-design is to avoid clamping the fragile lithium niobate (LN) disk at the rims exactly where the optical modes exist. Not only should this prevent any damage to rims when closing the cavity, it can also reduce the piezoelectric losses of the microwave field and avoid air gaps that reduce g_0 and change ω_e unpredictably. The theory is that by not clamping the LN disk at the rims, we will remove the mechanical loss channel imporing the microwave quality factors. Another big advantage of this design is that now the microwave capacitor can come much closer to the optical mode (d in Fig. 10.1 which can now be independent of optical resonator's thickness) eliminating the need to make the optical resonator thinner to increase the coupling between the microwave and optical mode.

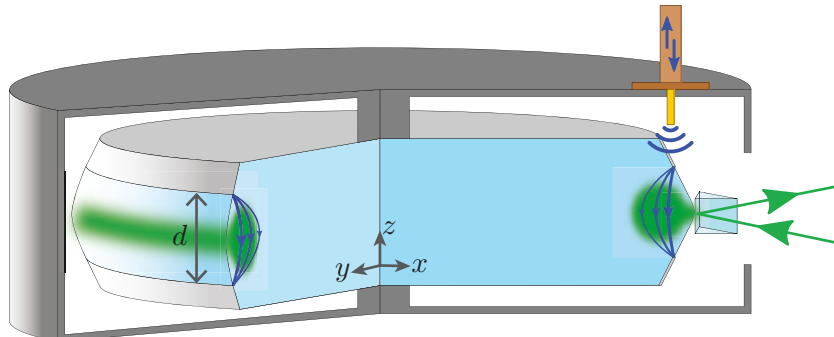


Figure 10.1: **Proposed new design of transducer.** The new design was proposed by Rueda *et al.* [RHBF19]. The main difference from the design in this thesis is that now the optical resonator is clamped at the center and an evaporated film of superconducting material extends up to the optical mode forming the capacitor rings. Optical fields are represented in green and those for microwave in blue. Figure adapted from Ref. [RHBF19].

However, the new design also poses some challenges. The fabrication is considerably harder since now the polished surface of the optical resonator needs to be finished first and then protected during the further metal deposition steps. Depositing metal as shown in the new design is also not easy since a clean gap has to be left where the optical modes exist. Moreover, the thin film of metal would not stick strongly to the LN crystal making the metal surface easy to scratch and damage. These damages will increase the internal losses of the microwave mode down the line.

We have already done some preliminary tests with a transducer sample with a design similar to what is shown in Fig 10.1. The sample was fabricated with a 500 μm LN disk albeit with metal deposition only on top and bottom and not on sides. Upon cooling down this center clamped design, we found no measurable drop in optical quality factors. This is a good sign and solves one of the biggest problem with our current transducer. The microwave quality factor, on the other hand, remained the same. However, this can be due to damage to metal deposition layer or imperfect contact of the bulk cavity to the deposition layer. We expect that this can be fixed in future with better fabrication techniques as independent tests of this cavity design without optics coupling (but still a dielectric in the microwave cavity) have showed $\sim 3\text{-}5$ times improvement in the internal quality factor.

10.3 Possible experiments with current imperfect transducer

Even though deterministic quantum state conversion or high fidelity entanglement generation is still out of reach with the current device (mostly due to coupling losses), there are several novel experiments we can do with lower total conversion efficiencies and finite amount of added noise. In this section, we list a few future experiments which are possible.

10.3.1 Masing

Masing comes from MASER which stands for microwave amplification through stimulated emission of radiation - in other words, laser but for microwaves. Generation of low noise coherent microwave signals is not just useful for applications in radar and internet communication but lately it has also been useful in controlling microwave-based qubits for quantum computing and communication.

Apart from using electronics, one of best ways to generate low noise microwave signals is to use soliton combs [LLR⁺20]. The idea is to use the optical Kerr effect to produce a resonant comb in a high quality resonator with an FSR that matches the microwave frequency. The produced optical comb can be detected by a high speed photodiode which will in turn produce the required RF signal. High quality resonators lower the threshold required to start the amplification of the comb sidebands. The FSR of the resonator determines the RF frequency produced.

Although the experiment in Ref. [LLR⁺20] is ground-breaking, it still suffers from a few problems. The method needs a photodiode for its operation. The noise is still limited by the thermo-refractive effect which jitters the FSR and thus introduces noise in produced RF signal.

In section 7.7, we talk about the same phenomenon where the $\chi^{(3)}$ Kerr effect produces an amplification after a certain amount of energy is circulating in the optical resonator. However, in our system, the microwave mode is also supported by its own resonant cavity. With the

additional $\chi^{(2)}$ property of lithium niobate, the microwave frequency is immediately generated in the device and readily extracted with the microwave cavity. This eliminates the need of a photodiode. Therefore, our setup can be used in a dilution refrigerator as a low-noise microwave source producing a noise-free RF tone *in situ* without the need of attenuation to suppress the thermal noise from room temperature.

Thermo-refractive noise results from temperature fluctuation of refractive index of the optical resonator. These fluctuations are proportional to the square of the temperature of the optical resonator [KG18]. When working at millikelvin temperatures, these temperature fluctuations would be highly suppressed eliminating the main source of noise in the generated RF frequency.

Since we have already seen the evidence of Kerr effect masing in our system and the generated microwave signal, only systematic studies which characterize the produced RF tone and measure its phase noise need to be conducted.

10.3.2 All-optical qubit readout

With the current transduction efficiencies, we cannot do deterministic one-way conversion of quantum states. However, certain tasks such as measuring the state of a superconducting qubit which is coupled to a resonator can be done using classical signals [BHW⁰⁴]. Delaney *et. al.* [DUM²²] have already demonstrated this measurement of a qubit in the optical domain. Nevertheless, in both of these experiments, the input classical microwave tone which initially probes the microwave resonator for the qubit state is generated from an RF source and only the reflected microwave signal containing the phase information about the qubit state is transduced to the optical domain for detection. Hence, these experiments only eliminate the detection side of the microwave readout chain.

The optical detection of a superconducting qubit can be taken one-step further. Both preparation and detection of microwave signals can be done optically. The biggest challenge for this measurement is, now, the transducer is used two times - first to generate the microwave signal using the optical signal and the optical pump and then after probing the microwave signal with this newly generated signal, converting it back to the optical domain using the transducer. Since now transduction is needed two times, the transduction efficiency will come into the equation with a squared and lower transduction efficiencies will be even more penalised. As a result, using a transducer with low transduction efficiency for an all-optical readout experiment is quite difficult.

There is one other challenge involved if only one transducer is used for this task as shown in Fig. 10.2. Since, the optical signal which generates the microwave signal would be at the same frequency as the transduced optical signal originating from the reflected microwave signal that carries the information about the qubit state, and since usually the optical path length between the transducer and the qubit will only be a few nanoseconds, we can assume that the transduced and initial optical signal will interfere with each other. And the information about the state of the qubit will be hidden in this interference (either in amplitude or phase or a combination of both). The visibility of this interference will depend on the square of the transduction efficiency. The greater the transduction efficiency, the more power is reflected back to optics and more contrasted is the interference. This is different from the usual microwave readout scheme since, in case of microwaves, the input signal to the resonator and the reflected signal from the resonator are separated from each other via a circulator. A microwave circulator can still be used in case of all-optical readout but, in that case, two

separate transducers will be needed - one to generate the microwave signal and another to transduce it back to optical domain.

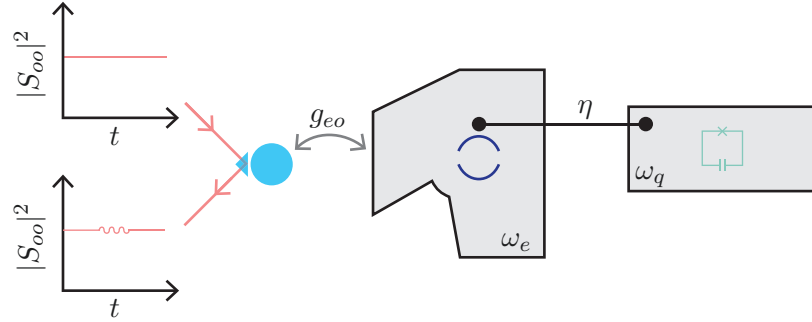


Figure 10.2: **All-optical qubit readout.** A continuous probe tone at optical resonance is sent to the optical resonator. The optical resonator couples to the microwave cavity at ω_e with the parametrically enhanced coupling constant g_{eo} . The microwave cavity is connected to the qubit cavity (at ω_q) with a transmission line with transmission constant η . Depending on the state of the qubit, $\omega_e = \omega_q$ or $|\omega_e - \omega_q| \gtrsim \kappa_q$, the linewidth of qubit cavity. The change in the reflected optical signal which indicates the state of the qubit depends on g_{eo} and η .

If the interference due to backaction from qubit is too small, we can use a clever way to detect it. The strong initial optical signal which is mostly reflected due to low transduction efficiency can act as a natural local oscillator for the transduced optical signal carrying the information about the state of the qubit. After eliminating the optical pump through an optical filter, we can simply separate the optical signal via a 50-50 beam splitter and do homodyne detection.

There is another way to artificially conjure a circulator even with one transducer. Since the signals we work with are in any case classical, we do not need single sideband transduction. We can work with a symmetric optical FSR and allow both beam-splitter interaction and amplification interaction at the same time. With this as the starting point, we can use the optical anti-Stokes sideband and the optical pump to initially generate the microwave signal. Then, after probing the qubit, the reflected microwave signal will get transduced again to optical anti-Stokes frequency and amplify the optical Stokes frequency. However, since the optical Stokes frequency was initially empty, only the re-transduced microwave signal exists at that frequency with no additional signals. Hence, with this trick, we can separate the initial optical signal with the transduced optical signal without the need of a real circulator or two transducers.

10.3.3 Single optical photons from superconducting qubits

Superconducting qubits [DWM04] are highly nonlinear systems which allow production and shaping of the wavepacket of high-fidelity single photon states using superconducting qubits on demand in frequency-tunable systems [HSG⁺07] or in non-tunable systems [LFM⁺09]. Using a microwave-optic transducer, these photons can be upconverted to the optical domain to produce single optical photons which are usually produced using optically-active quantum dots [SSW17].

Generating and characterizing the fidelity of produced single optical photons would not only be the proof that the transducer can be used in quantum application but also an interesting way to verify the non-classicality of the states produced by superconducting qubits using well-established methods from quantum optics.

For example, we can verify the non-classicality of single photons using the intensity correlation function $g^{(2)}$ [Gla63]. It is measured by correlating the output of two intensity or photon number detectors measuring at the output ports of a 50-50 beam splitter as function of difference in time of arrival or the distance between the two detectors and splitter. As a function of difference in time of arrive τ , it is defined as ratio of intensity correlations,

$$g^{(2)}(\tau) = \frac{\langle a^\dagger(t)a^\dagger(t+\tau)a(t+\tau)a(t) \rangle}{\langle a^\dagger(t)a(t) \rangle^2}. \quad (10.1)$$

For $\tau = 0$, the $g^{(2)}(0)$ is simply the coincidence detection of photons at the two photo-detectors normalised to the individual number of photons detected on each detector.

The $g^{(2)}(0)$ correlation is different for coherent light/vacuum ($g^{(2)}(0) = 1$), thermal noise ($g^{(2)}(0) = 2$) or uncorrelated light and single photon fock states ($g^{(2)}(0) = 0$). A value of $g^{(2)}(0) < 1$ would prove some amount of non-classicality in the measured state. An idea for an interesting experiment with the transducer can be to upconvert single microwave photons generated via a superconducting qubit and then characterize the $g^{(2)}$ correlations in the upconverted optical signal. If $g^{(2)}(0) < 1$ can be measured, it will be an important benchmark experiment proving some quantum properties can be preserved after transduction of quantum states.

10.3.4 Qubit-photon entanglement

The first entanglement between a superconducting qubit and an itinerant microwave photon was shown by Eichler *et. al.* in 2012 [ELF¹²]. In their experiment, they demonstrated preparation of the state $|\psi\rangle = (|0e\rangle + |1g\rangle)/\sqrt{2}$. The first index of the joint state represents the number of microwave photons in the microwave resonator and the second index of the state represents the qubit state. The full state $|\psi\rangle$ represents a maximally entangled state between the presence of microwave photon and the state of the qubit.

After preparing this state, the entangled microwave photon can simply be up-converted to the optics domain. This will successfully produce entanglement between a superconducting qubit and an optical photon. We can verify this entanglement in the Fock basis. However, detection of above mentioned entangled state is extremely sensitive to the optical photon loss. The reason is one can easily correlate the presence of a photon, measured with a click from a single optical photon detector [MVS¹³], with the qubit state verified to be in the ground state. But correlating the presence of no photon with the excited qubit state is non-trivial. To be sure about a state measurement with 'no photon', we must have a really high detection efficiency of the up-converted photon (any loss with detection efficiency will add to error in state measurement). This is rather challenging since there are always unavoidable optical losses between the transducer and the single photon detector - most of which come from the optical filters which need to suppress a high power pump very close to the optical signal frequency that need to be detected. Even in the case of single photon detection and qubit in ground state, the measured can be corrupted from the dark counts of the detector. This makes the practical verification of this entanglement rather difficult.

A solution to the above problem can be to produce the entanglement in a different basis between the qubit and the microwave photon. In this case, both the states of the qubit are entangled with the presence of a single photon, but the two states correspond to the microwave photons arriving at different times, $|\psi\rangle = (|Le\rangle + |Eg\rangle)/\sqrt{2}$, where the first index now stands for an early or late photon [THH¹⁹]. Upconverting this time-bin encoded microwave photon

to the optical domain, we can again verify entanglement between the qubit and the optical photon. However, in this case, verification of the entanglement is less sensitive to losses since we can always herald the measurement of the qubit to the detection of the optical photon on the detector. All the cases when the photons were lost would simply be ignored. The penalty for more optical losses will be paid in terms of longer measurement times instead of loss of entanglement fidelity.

10.3.5 Remote qubit entanglement

After achieving the qubit-optical photon entanglement, we can consider the problem of remote qubit entanglement connected via an optical channel. To achieve remote entanglement, we need to start with two systems in two dilution refrigerators both of which will feature a pair of entangled optical photon and qubit. Once these two entangled pairs are generated, we can simply swap the entanglement [PBWZ98] from the pairs of optical photon and qubit to the two qubits by performing a joint detection (Bell state measurement) of the two optical photons. The final remaining entanglement between the qubits can be easily verified by measuring them individually and then correlating the measurements.

Although, in principle, the steps leading up to remote qubit entanglement are not complicated, there are still a few caveats that one must keep in mind. Currently, the bandwidths of the transducers are not very high ~ 10 MHz and it is rather difficult to control the optical FSR (due to how the resonators are fabricated). As a result, we can expect the frequency of the optical photons from different devices to not match perfectly. For Bell state measurement, we want to erase the 'which photon' information before they are detected. Hence, keeping them as similar as possible is advantageous.

Some amount of frequency mismatch is allowed due to Heisenberg's uncertainty principle, $\Delta\omega\Delta t > 2\pi$. Accordingly, if the two photons are completely detected within a time Δt , we can afford a frequency mismatch of $\Delta\omega$ given by the uncertainty principle. The smaller the Δt , the larger frequency mismatch can be afforded. The time of arrival between photons can be easily matched within a nanosecond by adding more optical fiber for the early photon. As a result, Δt will be mostly limited by the spread of the optical photon which in turn would be related to the bandwidth of the original microwave photon which was entangled with the qubit. Of course, we can always chose to detect in a smaller time-bin as is easily allowed by current single photon detectors [MVS⁺13], but artificially reducing the Δt below the photon pulse length would reduce the probability of detection making the measurements slower.

With the results presented in chapter 9, we can use the same method to entangle two microwave photons in two different dilution refrigerators. All the same caveats will also apply in this case except after the entanglement swap, we will end up with microwave photons which are entangled in two different dilution refrigerators instead of direct qubit entanglement. Once the entanglement between remote microwave photons is achieved, we can use them to drive two separate remote qubits to entangle them.

10.4 Final conclusions

In this thesis, we have shown several experiments under the general domain of quantum electrooptics experiments from quantum transduction between microwave and optics to quantum entanglement between the same frequencies. The current status of the experiments suffer from a few problems ranging from small (for deterministic transduction) transduction

10. OUTLOOK

efficiencies to weak entanglement fidelities. However, with modest improvements in the system such as improved design and better quality cavities, many of these problems can be solved opening the door to many practical experiments such as the ones mentioned in the previous section.

There is still a long road ahead before we can finally make microwave quantum technologies compatible with optics and get one more step closer to a fully working quantum internet that includes microwave technologies. In this thesis, we made a few steps towards this goal and laid the foundation for many more benchmark experiments that are still remaining.

Bibliography

- [AAA⁺23] Rajeev Acharya, Igor Aleiner, Richard Allen, Trond I. Andersen, Markus Ansmann, Frank Arute, Kunal Arya, Abraham Asfaw, Juan Atalaya, Ryan Babbush, Dave Bacon, Joseph C. Bardin, Joao Basso, Andreas Bengtsson, Sergio Boixo, Gina Bortoli, Alexandre Bourassa, Jenna Bovaird, Leon Brill, Michael Broughton, Bob B. Buckley, David A. Buell, Tim Burger, Brian Burkett, Nicholas Bushnell, Yu Chen, Zijun Chen, Ben Chiaro, Josh Cogan, Roberto Collins, Paul Conner, William Courtney, Alexander L. Crook, Ben Curtin, Dripto M. Debroy, Alexander Del Toro Barba, Sean Demura, Andrew Dunsworth, Daniel Eppens, Catherine Erickson, Lara Faoro, Edward Farhi, Reza Fatemi, Leslie Flores Burgos, Ebrahim Forati, Austin G. Fowler, Brooks Foxen, William Giang, Craig Gidney, Dar Gilboa, Marissa Giustina, Alejandro Grajales Dau, Jonathan A. Gross, Steve Habegger, Michael C. Hamilton, Matthew P. Harrigan, Sean D. Harrington, Oscar Higgott, Jeremy Hilton, Markus Hoffmann, Sabrina Hong, Trent Huang, Ashley Huff, William J. Huggins, Lev B. Ioffe, Sergei V. Isakov, Justin Iveland, Evan Jeffrey, Zhang Jiang, Cody Jones, Pavol Juhas, Dvir Kafri, Kostyantyn Kechedzhi, Julian Kelly, Tanuj Khattar, Mostafa Khezri, Mária Kieferová, Seon Kim, Alexei Kitaev, Paul V. Klimov, Andrey R. Klots, Alexander N. Korotkov, Fedor Kostritsa, John Mark Kreikebaum, David Landhuis, Pavel Laptev, Kim-Ming Lau, Lily Laws, Joonho Lee, Kenny Lee, Brian J. Lester, Alexander Lill, Wayne Liu, Aditya Locharla, Erik Lucero, Fionn D. Malone, Jeffrey Marshall, Orion Martin, Jarrod R. McClean, Trevor McCourt, Matt McEwen, Anthony Megrant, Bernardo Meurer Costa, Xiao Mi, Kevin C. Miao, Masoud Mohseni, Shirin Montazeri, Alexis Morvan, Emily Mount, Wojciech Mruczkiewicz, Ofer Naaman, Matthew Neeley, Charles Neill, Ani Nersisyan, Hartmut Neven, Michael Newman, Jiun How Ng, Anthony Nguyen, Murray Nguyen, Murphy Yuezhen Niu, Thomas E. O'Brien, Alex Opremcak, John Platt, Andre Petukhov, Rebecca Potter, Leonid P. Pryadko, Chris Quintana, Pedram Roushan, Nicholas C. Rubin, Negar Saei, Daniel Sank, Kannan Sankaragomathi, Kevin J. Satzinger, Henry F. Schurkus, Christopher Schuster, Michael J. Shearn, Aaron Shorter, Vladimir Shvarts, Jindra Skruzny, Vadim Smelyanskiy, W. Clarke Smith, George Sterling, Doug Strain, Marco Szalay, Alfredo Torres, Guifre Vidal, Benjamin Villalonga, Catherine Vollgraff Heidweiller, Theodore White, Cheng Xing, Z. Jamie Yao, Ping Yeh, Juhwan Yoo, Grayson Young, Adam Zalcman, Yaxing Zhang, Ningfeng Zhu, and Google Quantum AI. Suppressing quantum errors by scaling a surface code logical qubit. *Nature*, 614(7949):676–681, February 2023.
- [AAB⁺19] Frank Arute, Kunal Arya, Ryan Babbush, Dave Bacon, Joseph C Bardin, Rami Barends, Rupak Biswas, Sergio Boixo, Fernando G S L Brandao, David A Buell, Brian Burkett, Yu Chen, Zijun Chen, Ben Chiaro, Roberto Collins, William

Courtney, Andrew Dunsworth, Edward Farhi, Brooks Foxen, Austin Fowler, Craig Gidney, Marissa Giustina, Rob Graff, Keith Guerin, Steve Habegger, Matthew P Harrigan, Michael J Hartmann, Alan Ho, Markus Hoffmann, Trent Huang, Travis S Humble, Sergei V Isakov, Evan Jeffrey, Zhang Jiang, Dvir Kafri, Kostyantyn Kechedzhi, Julian Kelly, Paul V Klimov, Sergey Knysh, Alexander Korotkov, Fedor Kostritsa, David Landhuis, Mike Lindmark, Erik Lucero, Dmitry Lyakh, Salvatore Mandrà, Jarrod R McClean, Matthew McEwen, Anthony Megrant, Xiao Mi, Kristel Michelsen, Masoud Mohseni, Josh Mutus, Ofer Naaman, Matthew Neeley, Charles Neill, Murphy Yuezhen Niu, Eric Ostby, Andre Petukhov, John C Platt, Chris Quintana, Eleanor G Rieffel, Pedram Roushan, Nicholas C Rubin, Daniel Sank, Kevin J Satzinger, Vadim Smelyanskiy, Kevin J Sung, Matthew D Trevithick, Amit Vainsencher, Benjamin Villalonga, Theodore White, Z Jamie Yao, Ping Yeh, Adam Zalcman, Hartmut Neven, and John M Martinis. Quantum supremacy using a programmable superconducting processor. *Nature*, 574(7779):505–510, October 2019.

- [ABDP62] J. A. Armstrong, N. Bloembergen, J. Ducuing, and P. S. Pershan. Interactions between Light Waves in a Nonlinear Dielectric. *Physical Review*, 127(6):1918–1939, September 1962.
- [ACC⁺22] James Ang, Gabriella Carini, Yanzhu Chen, Isaac Chuang, Michael Austin DeMarco, Sophia E. Economou, Alec Eickbusch, Andrei Faraon, Kai-Mei Fu, Steven M. Girvin, Michael Hatridge, Andrew Houck, Paul Hilaire, Kevin Kruslich, Ang Li, Chenxu Liu, Yuan Liu, Margaret Martonosi, David C. McKay, James Misewich, Mark Ritter, Robert J. Schoelkopf, Samuel A. Stein, Sara Sussman, Hong X. Tang, Wei Tang, Teague Tomesh, Norm M. Tubman, Chen Wang, Nathan Wiebe, Yong-Xin Yao, Dillon C. Yost, and Yiyu Zhou. Architectures for Multinode Superconducting Quantum Computers, December 2022.
- [AEE⁺22] Koji Azuma, Sophia E. Economou, David Elkouss, Paul Hilaire, Liang Jiang, Hoi-Kwong Lo, and Ilan Tzitrin. Quantum repeaters: From quantum networks to the quantum internet, December 2022.
- [AKM14] Markus Aspelmeyer, Tobias J. Kippenberg, and Florian Marquardt. Cavity optomechanics. *Reviews of Modern Physics*, 86(4):1391–1452, December 2014.
- [AMFR22] J. Agustí, Y. Minoguchi, J. M. Fink, and P. Rabl. Long-distance distribution of qubit-qubit entanglement using Gaussian-correlated photonic beams. *Physical Review A*, 105(6):062454, June 2022.
- [APP⁺14] R. W. Andrews, R. W. Peterson, T. P. Purdy, K. Cicak, R. W. Simmonds, C. A. Regal, and K. W. Lehnert. Bidirectional and efficient conversion between microwave and optical light. *Nature Physics*, 10(4):321–326, April 2014.
- [ARC⁺15] R. W. Andrews, A. P. Reed, K. Cicak, J. D. Teufel, and K. W. Lehnert. Quantum-enabled temporal and spectral mode conversion of microwave signals. *Nature Communications*, 6(1):10021, November 2015.
- [AWB⁺20] G. Arnold, M. Wulf, S. Barzanjeh, E. S. Redchenko, A. Rueda, W. J. Hease, F. Hassani, and J. M. Fink. Converting microwave and telecom photons with a silicon photonic nanomechanical interface. *Nature Communications*, 11(1):4460, September 2020.

- [BCMS19] Colin D. Bruzewicz, John Chiaverini, Robert McConnell, and Jeremy M. Sage. Trapped-ion quantum computing: Progress and challenges. *Applied Physics Reviews*, 6(2):021314, June 2019.
- [BDG⁺22] Sergey Bravyi, Oliver Dial, Jay M. Gambetta, Darío Gil, and Zaira Nazario. The future of quantum computing with superconducting qubits. *Journal of Applied Physics*, 132(16):160902, October 2022.
- [BGW⁺15] Shabir Barzanjeh, Saikat Guha, Christian Weedbrook, David Vitali, Jeffrey H. Shapiro, and Stefano Pirandola. Microwave Quantum Illumination. *Physical Review Letters*, 114(8):080503, February 2015.
- [BHJ⁺22] Francesco Borsoi, Nico W. Hendrickx, Valentin John, Sayr Motz, Floor van Riggelen, Amir Sammak, Sander L. de Snoo, Giordano Scappucci, and Menno Veldhorst. Shared control of a 16 semiconductor quantum dot crossbar array, September 2022.
- [BHP⁺13] H. Bernien, B. Hensen, W. Pfaff, G. Koolstra, M. S. Blok, L. Robledo, T. H. Taminiau, M. Markham, D. J. Twitchen, L. Childress, and R. Hanson. Heralded entanglement between solid-state qubits separated by three metres. *Nature*, 497(7447):86–90, May 2013.
- [BHW⁺04] Alexandre Blais, Ren-Shou Huang, Andreas Wallraff, S. M. Girvin, and R. J. Schoelkopf. Cavity quantum electrodynamics for superconducting electrical circuits: An architecture for quantum computation. *Physical Review A*, 69(6):062320, June 2004.
- [BKU⁺22] B. M. Brubaker, J. M. Kindem, M. D. Urmey, S. Mittal, R. D. Delaney, P. S. Burns, M. R. Vissers, K. W. Lehnert, and C. A. Regal. Optomechanical Ground-State Cooling in a Continuous and Efficient Electro-Optic Transducer. *Physical Review X*, 12(2):021062, June 2022.
- [BL20] Antoine Browaeys and Thierry Lahaye. Many-body physics with individually controlled Rydberg atoms. *Nature Physics*, 16(2):132–142, February 2020.
- [Boh35] N. Bohr. Can Quantum-Mechanical Description of Physical Reality be Considered Complete? *Physical Review*, 48(8):696–702, October 1935.
- [Boy08] Robert W. Boyd. *Nonlinear Optics*. Elsevier, Academic Press, Amsterdam Heidelberg, 3. ed edition, 2008.
- [Boy09] Robert W. Boyd. Slow and fast light: Fundamentals and applications. *Journal of Modern Optics*, 56(18-19):1908–1915, October 2009.
- [BRM⁺20] M. K. Bhaskar, R. Riedinger, B. Machielse, D. S. Levonian, C. T. Nguyen, E. N. Knall, H. Park, D. Englund, M. Lončar, D. D. Sukachev, and M. D. Lukin. Experimental demonstration of memory-enhanced quantum communication. *Nature*, 580(7801):60–64, April 2020.
- [BRX⁺20] John G. Bartholomew, Jake Rochman, Tian Xie, Jonathan M. Kindem, Andrei Ruskuc, Ioana Craiciu, Mi Lei, and Andrei Faraon. On-chip coherent microwave-to-optical transduction mediated by ytterbium in YVO₄. *Nature Communications*, 11(1):3266, June 2020.

- [BSS⁺13] I. Breunig, B. Sturman, F. Sedlmeir, H. G. L. Schwefel, and K. Buse. Whispering gallery modes at the rim of an axisymmetric optical resonator: Analytical versus numerical description and comparison with experiment. *Optics Express*, 21(25):30683–30692, December 2013.
- [BSS⁺14] T. Bagci, A. Simonsen, S. Schmid, L. G. Villanueva, E. Zeuthen, J. Appel, J. M. Taylor, A. Sørensen, K. Usami, A. Schliesser, and E. S. Polzik. Optical detection of radio waves through a nanomechanical transducer. *Nature*, 507(7490):81–85, March 2014.
- [Bv05] Samuel L. Braunstein and Peter van Loock. Quantum information with continuous variables. *Reviews of Modern Physics*, 77(2):513–577, June 2005.
- [BVAC13] Joerg Bochmann, Amit Vainsencher, David D. Awschalom, and Andrew N. Cleland. Nanomechanical coupling between microwave and optical photons. *Nature Physics*, 9(11):712–716, November 2013.
- [Cav82] Carlton M. Caves. Quantum limits on noise in linear amplifiers. *Physical Review D*, 26(8):1817–1839, October 1982.
- [CCC20] Daniele Cuomo, Marcello Caleffi, and Angela Sara Cacciapuoti. Towards a distributed quantum computing ecosystem. *IET Quantum Communication*, 1(1):3–8, 2020.
- [CdF⁺05] C. W. Chou, H. de Riedmatten, D. Felinto, S. V. Polyakov, S. J. van Enk, and H. J. Kimble. Measurement-induced entanglement for excitation stored in remote atomic ensembles. *Nature*, 438(7069):828–832, December 2005.
- [CDG⁺10] A. A. Clerk, M. H. Devoret, S. M. Girvin, Florian Marquardt, and R. J. Schoelkopf. Introduction to quantum noise, measurement, and amplification. *Reviews of Modern Physics*, 82(2):1155–1208, April 2010.
- [CHL01] D. A. Cohen, M. Hosseini-Zadeh, and A. F. J. Levi. High-Q microphotonic electro-optic modulator. *Solid-State Electronics*, 45(9):1577–1589, September 2001.
- [CVM⁺23] Lorcán O. Conlon, Tobias Vogl, Christian D. Marciak, Ivan Pogorelov, Simon K. Yung, Falk Eilenberger, Dominic W. Berry, Fabiana S. Santana, Rainer Blatt, Thomas Monz, Ping Koy Lam, and Syed M. Assad. Approaching optimal entangling collective measurements on quantum computing platforms. *Nature Physics*, pages 1–7, January 2023.
- [DBJK⁺21] Conner Dailey, Colin Bradley, Derek F. Jackson Kimball, Ibrahim A. Sulai, Szymon Pustelný, Arne Wickenbrock, and Andrei Derevianko. Quantum sensor networks as exotic field telescopes for multi-messenger astronomy. *Nature Astronomy*, 5(2):150–158, February 2021.
- [dBWB10] Marcus P. da Silva, Deniz Bozyigit, Andreas Wallraff, and Alexandre Blais. Schemes for the observation of photon correlation functions in circuit QED with linear detectors. *Physical Review A*, 82(4):043804, October 2010.
- [DGCZ00] Lu-Ming Duan, G. Giedke, J. I. Cirac, and P. Zoller. Inseparability Criterion for Continuous Variable Systems. *Physical Review Letters*, 84(12):2722–2725, March 2000.

- [DLCZ01] L.-M. Duan, M. D. Lukin, J. I. Cirac, and P. Zoller. Long-distance quantum communication with atomic ensembles and linear optics. *Nature*, 414(6862):413–418, November 2001.
- [DRC17] C. L. Degen, F. Reinhard, and P. Cappellaro. Quantum sensing. *Reviews of Modern Physics*, 89(3):035002, July 2017.
- [DSG⁺16] Aymeric Delteil, Zhe Sun, Wei-bo Gao, Emre Togan, Stefan Faelt, and Ataç Imamoğlu. Generation of heralded entanglement between distant hole spins. *Nature Physics*, 12(3):218–223, March 2016.
- [DUM⁺22] R. D. Delaney, M. D. Urmey, S. Mittal, B. M. Brubaker, J. M. Kindem, P. S. Burns, C. A. Regal, and K. W. Lehnert. Superconducting-qubit readout via low-backaction electro-optic transduction. *Nature*, 606(7914):489–493, June 2022.
- [DWM04] M. H. Devoret, A. Wallraff, and J. M. Martinis. Superconducting Qubits: A Short Review, November 2004.
- [ELF⁺12] C. Eichler, C. Lang, J. M. Fink, J. Govenius, S. Filipp, and A. Wallraff. Observation of Entanglement between Itinerant Microwave Photons and a Superconducting Qubit. *Physical Review Letters*, 109(24):240501, December 2012.
- [EPR35] A. Einstein, B. Podolsky, and N. Rosen. Can Quantum-Mechanical Description of Physical Reality Be Considered Complete? *Physical Review*, 47(10):777–780, May 1935.
- [FC72] Stuart J. Freedman and John F. Clauser. Experimental Test of Local Hidden-Variable Theories. *Physical Review Letters*, 28(14):938–941, April 1972.
- [FSSL16] Matthew R. Foreman, Florian Sedlmeir, Harald G. L. Schwefel, and Gerd Leuchs. Dielectric tuning and coupling of whispering gallery modes using an anisotropic prism. *JOSA B*, 33(11):2177–2195, November 2016.
- [FSW⁺20] Moritz Forsch, Robert Stockill, Andreas Wallucks, Igor Marinković, Claus Gärtner, Richard A. Norte, Frank van Otten, Andrea Fiore, Kartik Srinivasan, and Simon Gröblacher. Microwave-to-optics conversion using a mechanical oscillator in its quantum ground state. *Nature Physics*, 16(1):69–74, January 2020.
- [FXL⁺21] Wei Fu, Mingrui Xu, Xianwen Liu, Chang-Ling Zou, Changchun Zhong, Xu Han, Mohan Shen, Yuntao Xu, Risheng Cheng, Siha Wang, Liang Jiang, and Hong X. Tang. Cavity electro-optic circuit for microwave-to-optical conversion in the quantum ground state. *Physical Review A*, 103(5):053504, May 2021.
- [FZC⁺18] Linran Fan, Chang-Ling Zou, Risheng Cheng, Xiang Guo, Xu Han, Zheng Gong, Siha Wang, and Hong X. Tang. Superconducting cavity electro-optics: A platform for coherent photon conversion between superconducting and photonic circuits. *Science Advances*, 4(8):eaar4994, August 2018.
- [GBB⁺20] Xueshi Guo, Casper R. Breum, Johannes Borregaard, Shuro Izumi, Mikkel V. Larsen, Tobias Gehring, Matthias Christandl, Jonas S. Neergaard-Nielsen, and Ulrik L. Andersen. Distributed quantum sensing in a continuous-variable entangled network. *Nature Physics*, 16(3):281–284, March 2020.

- [GC85] C. W. Gardiner and M. J. Collett. Input and output in damped quantum systems: Quantum stochastic differential equations and the master equation. *Physical Review A*, 31(6):3761–3774, June 1985.
- [GHV⁺09] Simon Gröblacher, Jared B. Hertzberg, Michael R. Vanner, Garrett D. Cole, Sylvain Gigan, K. C. Schwab, and Markus Aspelmeyer. Demonstration of an ultracold micro-optomechanical oscillator in a cryogenic cavity. *Nature Physics*, 5(7):485–488, July 2009.
- [GI19] Laszlo Gyongyosi and Sandor Imre. A Survey on quantum computing technology. *Computer Science Review*, 31:51–71, February 2019.
- [GJC12] Daniel Gottesman, Thomas Jennewein, and Sarah Croke. Longer-Baseline Telescopes Using Quantum Repeaters. *Physical Review Letters*, 109(7):070503, August 2012.
- [Gla63] Roy J. Glauber. The Quantum Theory of Optical Coherence. *Physical Review*, 130(6):2529–2539, June 1963.
- [GLLG19] Yu Guo, Bi-Heng Liu, Chuan-Feng Li, and Guang-Can Guo. Advances in Quantum Dense Coding. *Advanced Quantum Technologies*, 2(5-6):1900011, 2019.
- [GLM11] Vittorio Giovannetti, Seth Lloyd, and Lorenzo Maccone. Advances in quantum metrology. *Nature Photonics*, 5(4):222–229, April 2011.
- [GZ00] C. W. (Crispin W.) Gardiner and P. (Peter) Zoller. *Quantum Noise : A Handbook of Markovian and Non-Markovian Quantum Stochastic Methods with Applications to Quantum Optics*. Berlin ; New York : Springer, 2000.
- [HBU⁺18] A. P. Higginbotham, P. S. Burns, M. D. Urmey, R. W. Peterson, N. S. Kampel, B. M. Brubaker, G. Smith, K. W. Lehnert, and C. A. Regal. Harnessing electro-optic correlations in an efficient mechanical converter. *Nature Physics*, 14(10):1038–1042, October 2018.
- [HFZ⁺20] Xu Han, Wei Fu, Changchun Zhong, Chang-Ling Zou, Yuntao Xu, Ayed Al Sayem, Mingrui Xu, Siha Wang, Risheng Cheng, Liang Jiang, and Hong X. Tang. Cavity piezo-mechanics for superconducting-nanophotonic quantum interface. *Nature Communications*, 11(1):3237, June 2020.
- [HHHH09] Ryszard Horodecki, Paweł Horodecki, Michał Horodecki, and Karol Horodecki. Quantum entanglement. *Reviews of Modern Physics*, 81(2):865–942, June 2009.
- [HKR⁺12] M. Hafezi, Z. Kim, S. L. Rolston, L. A. Orozco, B. L. Lev, and J. M. Taylor. Atomic interface between microwave and optical photons. *Physical Review A*, 85(2):020302, February 2012.
- [HOT⁺16] R. Hisatomi, A. Osada, Y. Tabuchi, T. Ishikawa, A. Noguchi, R. Yamazaki, K. Usami, and Y. Nakamura. Bidirectional conversion between microwave and light via ferromagnetic magnons. *Physical Review B*, 93(17):174427, May 2016.
- [HPC⁺22] Simon Hönl, Youri Popoff, Daniele Caimi, Alberto Beccari, Tobias J. Kippenberg, and Paul Seidler. Microwave-to-optical conversion with a gallium phosphide photonic crystal cavity. *Nature Communications*, 13(1):2065, April 2022.

- [HRS⁺20] William Hease, Alfredo Rueda, Rishabh Sahu, Matthias Wulf, Georg Arnold, Harald G.L. Schwefel, and Johannes M. Fink. Bidirectional Electro-Optic Wavelength Conversion in the Quantum Ground State. *PRX Quantum*, 1(2):020315, November 2020.
- [HSG⁺07] A. A. Houck, D. I. Schuster, J. M. Gambetta, J. A. Schreier, B. R. Johnson, J. M. Chow, L. Frunzio, J. Majer, M. H. Devoret, S. M. Girvin, and R. J. Schoelkopf. Generating single microwave photons in a circuit. *Nature*, 449(7160):328–331, September 2007.
- [HSZ⁺20] Jeffrey Holzgrafe, Neil Sinclair, Di Zhu, Amirhassan Shams-Ansari, Marco Colangelo, Yaowen Hu, Mian Zhang, Karl K. Berggren, and Marko Lončar. Cavity electro-optics in thin-film lithium niobate for efficient microwave-to-optical transduction. *Optica*, 7(12):1714–1720, December 2020.
- [HVG⁺18] Jingshan Han, Thibault Vogt, Christian Gross, Dieter Jaksch, Martin Kiffner, and Wenhui Li. Coherent Microwave-to-Optical Conversion via Six-Wave Mixing in Rydberg Atoms. *Physical Review Letters*, 120(9):093201, March 2018.
- [HWFZ20] He-Liang Huang, Dachao Wu, Daojin Fan, and Xiaobo Zhu. Superconducting quantum computing: A review. *Science China Information Sciences*, 63(8):180501, July 2020.
- [HZM⁺17] He-Liang Huang, Qi Zhao, Xiongfeng Ma, Chang Liu, Zu-En Su, Xi-Lin Wang, Li Li, Nai-Le Liu, Barry C. Sanders, Chao-Yang Lu, and Jian-Wei Pan. Experimental Blind Quantum Computing for a Classical Client. *Physical Review Letters*, 119(5):050503, August 2017.
- [ISMM03] Vladimir S. Ilchenko, Anatoliy A. Savchenkov, Andrey B. Matsko, and Lute Maleki. Whispering-gallery-mode electro-optic modulator and photonic microwave receiver. *JOSA B*, 20(2):333–342, February 2003.
- [JLL⁺17] Haowei Jiang, Rui Luo, Hanxiao Liang, Xianfeng Chen, Yuping Chen, and Qiang Lin. Fast response of photorefraction in lithium niobate microresonators. *Optics Letters*, 42(17):3267–3270, September 2017.
- [JPB⁺16] C. Javerzac-Galy, K. Plekhanov, N. R. Bernier, L. D. Toth, A. K. Feofanov, and T. J. Kippenberg. On-chip microwave-to-optical quantum coherent converter based on a superconducting resonator coupled to an electro-optic microresonator. *Physical Review A*, 94(5):053815, November 2016.
- [JPM⁺19] Wentao Jiang, Rishi N. Patel, Felix M. Mayor, Timothy P. McKenna, Patricio Arrangoiz-Arriola, Christopher J. Sarabalis, Jeremy D. Witmer, Raphaël Van Laer, and Amir H. Safavi-Naeini. Lithium niobate piezo-optomechanical crystals. *Optica*, 6(7):845–853, July 2019.
- [JSD⁺20] Wentao Jiang, Christopher J. Sarabalis, Yanni D. Dahmani, Rishi N. Patel, Felix M. Mayor, Timothy P. McKenna, Raphaël Van Laer, and Amir H. Safavi-Naeini. Efficient bidirectional piezo-optomechanical transduction between microwave and optical frequency. *Nature Communications*, 11(1):1166, March 2020.
- [JZ02] M. Jazbinšek and M. Zgonik. Material tensor parameters of LiNbO₃ relevant for electro- and elasto-optics. *Applied Physics B*, 74(4):407–414, April 2002.

- [KBDGL19] E. T. Khabiboulline, J. Borregaard, K. De Greve, and M. D. Lukin. Quantum-assisted telescope arrays. *Physical Review A*, 100(2):022316, August 2019.
- [KBK⁺15] Gershon Kurizki, Patrice Bertet, Yuimaru Kubo, Klaus Mølmer, David Petrosyan, Peter Rabl, and Jörg Schmiedmayer. Quantum technologies with hybrid systems. *Proceedings of the National Academy of Sciences*, 112(13):3866–3873, March 2015.
- [KG18] N. M. Kondratiev and M. L. Gorodetsky. Thermorefractive noise in whispering gallery mode microresonators: Analytical results and numerical simulation. *Physics Letters A*, 382(33):2265–2268, August 2018.
- [KGK⁺23] V. Krutyanskiy, M. Galli, V. Krcmarsky, S. Baier, D. A. Fioretto, Y. Pu, A. Mazloom, P. Sekatski, M. Canteri, M. Teller, J. Schupp, J. Bate, M. Meraner, N. Sangouard, B. P. Lanyon, and T. E. Northup. Entanglement of Trapped-Ion Qubits Separated by 230 Meters. *Physical Review Letters*, 130(5):050803, February 2023.
- [Kim08] H. J. Kimble. The quantum internet. *Nature*, 453(7198):1023–1030, June 2008.
- [KKB⁺14] P. Kómár, E. M. Kessler, M. Bishof, L. Jiang, A. S. Sørensen, J. Ye, and M. D. Lukin. A quantum network of clocks. *Nature Physics*, 10(8):582–587, August 2014.
- [KLH⁺15] Boris Korzh, Charles Ci Wen Lim, Raphael Houlmann, Nicolas Gisin, Ming Jun Li, Daniel Nolan, Bruno Sanguinetti, Rob Thew, and Hugo Zbinden. Provably secure and practical quantum key distribution over 307 km of optical fibre. *Nature Photonics*, 9(3):163–168, March 2015.
- [KMC⁺96] A. Kling, J. G. Marques, J. G. Correia, M. F. da Silva, E. Diéguez, F. Agulló-López, and J. C. Soares. Study of structural differences between stoichiometric and congruent lithium niobate. *Nuclear Instruments and Methods in Physics Research Section B: Beam Interactions with Materials and Atoms*, 113(1):293–295, June 1996.
- [KMC22] Johannes Knörzer, Daniel Malz, and J. Ignacio Cirac. Cross-Platform Verification in Quantum Networks, December 2022.
- [KRC⁺05] T. J. Kippenberg, H. Rokhsari, T. Carmon, A. Scherer, and K. J. Vahala. Analysis of Radiation-Pressure Induced Mechanical Oscillation of an Optical Microcavity. *Physical Review Letters*, 95(3):033901, July 2005.
- [KRH⁺21] Stefan Krastanov, Hamza Raniwala, Jeffrey Holzgrafe, Kurt Jacobs, Marko Lončar, Matthew J. Reagor, and Dirk R. Englund. Optically Heralded Entanglement of Superconducting Systems in Quantum Networks. *Physical Review Letters*, 127(4):040503, July 2021.
- [KSS⁺23] Aishwarya Kumar, Aziza Suleymanzade, Mark Stone, Lavanya Taneja, Alexander Anferov, David I. Schuster, and Jonathan Simon. Quantum-enabled millimetre wave to optical transduction using neutral atoms. *Nature*, 615(7953):614–619, March 2023.

- [KSV04] T. J. Kippenberg, S. M. Spillane, and K. J. Vahala. Kerr-Nonlinearity Optical Parametric Oscillation in an Ultrahigh-Q Toroid Microcavity. *Physical Review Letters*, 93(8):083904, August 2004.
- [LCC17] Guoping Lin, Aurélien Coillet, and Yanne K. Chembo. Nonlinear photonics with high-Q whispering-gallery-mode resonators. *Advances in Optics and Photonics*, 9(4):828–890, December 2017.
- [LFM⁺09] P. J. Leek, S. Filipp, P. Maurer, M. Baur, R. Bianchetti, J. M. Fink, M. Göppl, L. Steffen, and A. Wallraff. Using sideband transitions for two-qubit operations in superconducting circuits. *Physical Review B*, 79(18):180511, May 2009.
- [LLR⁺20] Junqiu Liu, Erwan Lucas, Arslan S. Raja, Jijun He, Johann Riemensberger, Rui Ning Wang, Maxim Karpov, Hairun Guo, Romain Bouchand, and Tobias J. Kippenberg. Photonic microwave generation in the X- and K-band using integrated soliton microcombs. *Nature Photonics*, 14(8):486–491, August 2020.
- [LTN⁺22] K. S. Lee, Y. P. Tan, L. H. Nguyen, R. P. Budoyo, K. H. Park, C. Hufnagel, Y. S. Yap, N. Møbjerg, V. Vedral, T. Paterek, and R. Dumke. Entanglement in a qubit-qubit-tardigrade system. *New Journal of Physics*, 24(12):123024, December 2022.
- [LZL⁺21] Li-Zheng Liu, Yu-Zhe Zhang, Zheng-Da Li, Rui Zhang, Xu-Fei Yin, Yue-Yang Fei, Li Li, Nai-Le Liu, Feihu Xu, Yu-Ao Chen, and Jian-Wei Pan. Distributed quantum phase estimation with entangled photons. *Nature Photonics*, 15(2):137–142, February 2021.
- [Mat78] Bernard S. Matisoff. *Handbook of Electronics Manufacturing Engineering*. Van Nostrand Reinhold, New York, 1978.
- [MBPT20] S. M. Masloboeva, I. V. Biryukova, M. N. Palatnikov, and N. A. Teplyakova. Magnesium-and-Zinc-Doped Lithium Niobate Crystals: Preparation and Characterization. *Russian Journal of Inorganic Chemistry*, 65(6):924–931, June 2020.
- [MCD⁺21] C. Monroe, W. C. Campbell, L.-M. Duan, Z.-X. Gong, A. V. Gorshkov, P. W. Hess, R. Islam, K. Kim, N. M. Linke, G. Pagano, P. Richerme, C. Senko, and N. Y. Yao. Programmable quantum simulations of spin systems with trapped ions. *Reviews of Modern Physics*, 93(2):025001, April 2021.
- [MD85] A. Mansingh and A. Dhar. The AC conductivity and dielectric constant of lithium niobate single crystals. *Journal of Physics D: Applied Physics*, 18(10):2059, October 1985.
- [MHS⁺11] Konstantinos Moutzouris, George Hloupis, Ilias Stavrakas, Dimos Triantis, and Ming-Hsien Chou. Temperature-dependent visible to near-infrared optical properties of 8 mol% Mg-doped lithium tantalate. *Optical Materials Express*, 1(3):458–465, July 2011.
- [MLR⁺21] Sonia Mobassem, Nicholas J. Lambert, Alfredo Rueda, Johannes M. Fink, Gerd Leuchs, and Harald G. L. Schwefel. Thermal noise in electro-optic devices at cryogenic temperatures. *Quantum Science and Technology*, 6(4):045005, July 2021.

- [MS99] Pierre Meystre and Murray Sargent. *Elements of quantum optics: with 218 problems*. Springer, Berlin, 3. ed edition, 1999.
- [MSI⁺07] Andrey B. Matsko, Anatoliy A. Savchenkov, Vladimir S. Ilchenko, David Seidel, and Lute Maleki. On fundamental quantum noises of whispering gallery mode electro-optic modulators. *Optics Express*, 15(25):17401–17409, December 2007.
- [MSKP20] Mohammad Mirhosseini, Alp Sipahigil, Mahmoud Kalaei, and Oskar Painter. Superconducting qubit to optical photon transduction. *Nature*, 588(7839):599–603, December 2020.
- [MVS⁺13] F. Marsili, V. B. Verma, J. A. Stern, S. Harrington, A. E. Lita, T. Gerrits, I. Vayshenker, B. Baek, M. D. Shaw, R. P. Mirin, and S. W. Nam. Detecting single infrared photons with 93% system efficiency. *Nature Photonics*, 7(3):210–214, March 2013.
- [MW95] Leonard Mandel and Emil Wolf. *Optical Coherence and Quantum Optics*. Cambridge University Press, Cambridge, 1995.
- [MWP⁺20] Timothy P. McKenna, Jeremy D. Witmer, Rishi N. Patel, Wentao Jiang, Raphaël Van Laer, Patricio Arrangoiz-Arriola, E. Alex Wollack, Jason F. Herrmann, and Amir H. Safavi-Naeini. Cryogenic microwave-to-optical conversion using a triply resonant lithium-niobate-on-sapphire transducer. *Optica*, 7(12):1737–1745, December 2020.
- [MWT⁺10] D. Marcos, M. Wubs, J. M. Taylor, R. Aguado, M. D. Lukin, and A. S. Sørensen. Coupling Nitrogen-Vacancy Centers in Diamond to Superconducting Flux Qubits. *Physical Review Letters*, 105(21):210501, November 2010.
- [MZF⁺18] W. F. McGrew, X. Zhang, R. J. Fasano, S. A. Schäffer, K. Beloy, D. Nicolodi, R. C. Brown, N. Hinkley, G. Milani, M. Schioppo, T. H. Yoon, and A. D. Ludlow. Atomic clock performance enabling geodesy below the centimetre level. *Nature*, 564(7734):87–90, December 2018.
- [NSS⁺08] Chetan Nayak, Steven H. Simon, Ady Stern, Michael Freedman, and Sankar Das Sarma. Non-Abelian anyons and topological quantum computation. *Reviews of Modern Physics*, 80(3):1083–1159, September 2008.
- [OLB⁺14] Christopher O'Brien, Nikolai Lauk, Susanne Blum, Giovanna Morigi, and Michael Fleischhauer. Interfacing Superconducting Qubits and Telecom Photons via a Rare-Earth-Doped Crystal. *Physical Review Letters*, 113(6):063603, August 2014.
- [Ora02] Anatolii N. Oraevsky. Whispering-gallery waves. *Quantum Electronics*, 32(5):377, May 2002.
- [PBWZ98] Jian-Wei Pan, Dik Bouwmeester, Harald Weinfurter, and Anton Zeilinger. Experimental Entanglement Swapping: Entangling Photons That Never Interacted. *Physical Review Letters*, 80(18):3891–3894, May 1998.
- [PG08] Steven Prawer and Andrew D. Greentree. Diamond for Quantum Computing. *Science*, 320(5883):1601–1602, June 2008.

- [PHB⁺21] M. Pompili, S. L. N. Hermans, S. Baier, H. K. C. Beukers, P. C. Humphreys, R. N. Schouten, R. F. L. Vermeulen, M. J. Tiggelman, L. dos Santos Martins, B. Dirkse, S. Wehner, and R. Hanson. Realization of a multinode quantum network of remote solid-state qubits. *Science*, 372(6539):259–264, April 2021.
- [PKD18] Timothy J. Proctor, Paul A. Knott, and Jacob A. Dunningham. Multiparameter Estimation in Networked Quantum Sensors. *Physical Review Letters*, 120(8):080501, February 2018.
- [Ple05] M. B. Plenio. Logarithmic Negativity: A Full Entanglement Monotone That is not Convex. *Physical Review Letters*, 95(9):090503, August 2005.
- [PMFS19] David Petrosyan, Klaus Mølmer, József Fortágh, and Mark Saffman. Microwave to optical conversion with atoms on a superconducting chip. *New Journal of Physics*, 21(7):073033, July 2019.
- [PPH⁺22] Amélie Piveteau, Jef Pauwels, Emil Håkansson, Sadiq Muhammad, Mohamed Bourennane, and Armin Tavakoli. Entanglement-assisted quantum communication with simple measurements. *Nature Communications*, 13(1):7878, December 2022.
- [PTD⁺12] Jarryd J. Pla, Kuan Y. Tan, Juan P. Dehollain, Wee H. Lim, John J. L. Morton, David N. Jamieson, Andrew S. Dzurak, and Andrea Morello. A single-atom electron spin qubit in silicon. *Nature*, 489(7417):541–545, September 2012.
- [PTD⁺13] Jarryd J. Pla, Kuan Y. Tan, Juan P. Dehollain, Wee H. Lim, John J. L. Morton, Floris A. Zwanenburg, David N. Jamieson, Andrew S. Dzurak, and Andrea Morello. High-fidelity readout and control of a nuclear spin qubit in silicon. *Nature*, 496(7445):334–338, April 2013.
- [PW09] Young-Shin Park and Hailin Wang. Resolved-sideband and cryogenic cooling of an optomechanical resonator. *Nature Physics*, 5(7):489–493, July 2009.
- [QSH⁺22] Liu Qiu, Rishabh Sahu, William Hease, Georg Arnold, and Johannes M. Fink. Coherent optical control of a superconducting microwave cavity via electro-optical dynamical back-action, October 2022.
- [RHBF19] Alfredo Rueda, William Hease, Shabir Barzanjeh, and Johannes M. Fink. Electro-optic entanglement source for microwave to telecom quantum state transfer. *npj Quantum Information*, 5(1):1–11, November 2019.
- [RKK⁺22] Curtis L. Rau, Akira Kyle, Alex Kwiatkowski, Ezad Shojaee, John D. Teufel, Konrad W. Lehnert, and Tasshi Dennis. Entanglement Thresholds of Doubly Parametric Quantum Transducers. *Physical Review Applied*, 17(4):044057, April 2022.
- [RKRR14] Andreas Reiserer, Norbert Kalb, Gerhard Rempe, and Stephan Ritter. A quantum gate between a flying optical photon and a single trapped atom. *Nature*, 508(7495):237–240, April 2014.
- [RL11] C. A. Regal and K. W. Lehnert. From cavity electromechanics to cavity optomechanics. *Journal of Physics: Conference Series*, 264(1):012025, January 2011.

- [RNH⁺12] Stephan Ritter, Christian Nölleke, Carolin Hahn, Andreas Reiserer, Andreas Neuzner, Manuel Uphoff, Martin Mücke, Eden Figueroa, Joerg Bochmann, and Gerhard Rempe. An elementary quantum network of single atoms in optical cavities. *Nature*, 484(7393):195–200, April 2012.
- [RNM⁺10] T. Rocheleau, T. Ndukum, C. Macklin, J. B. Hertzberg, A. A. Clerk, and K. C. Schwab. Preparation and detection of a mechanical resonator near the ground state of motion. *Nature*, 463(7277):72–75, January 2010.
- [RS18] Alfredo Rolando Rueda Sanchez. Resonant Electrooptics, 2018.
- [RSC⁺16] Alfredo Rueda, Florian Sedlmeir, Michele C. Collodo, Ulrich Vogl, Birgit Stiller, Gerhard Schunk, Dmitry V. Strekalov, Christoph Marquardt, Johannes M. Fink, Oskar Painter, Gerd Leuchs, and Harald G. L. Schwefel. Efficient microwave to optical photon conversion: An electro-optical realization. *Optica*, 3(6):597–604, June 2016.
- [RSK⁺19] Alfredo Rueda, Florian Sedlmeir, Madhuri Kumari, Gerd Leuchs, and Harald G. L. Schwefel. Resonant electro-optic frequency comb. *Nature*, 568(7752):378–381, April 2019.
- [RWM⁺18] Ralf Riedinger, Andreas Wallucks, Igor Marinković, Clemens Löschauer, Markus Aspelmeyer, Sungkun Hong, and Simon Gröblacher. Remote quantum entanglement between two micromechanical oscillators. *Nature*, 556(7702):473–477, April 2018.
- [SAR⁺09] A. Schliesser, O. Arcizet, R. Rivière, G. Anetsberger, and T. J. Kippenberg. Resolved-sideband cooling and position measurement of a micromechanical oscillator close to the Heisenberg uncertainty limit. *Nature Physics*, 5(7):509–514, July 2009.
- [Sch35] E. Schrödinger. Discussion of Probability Relations between Separated Systems. *Mathematical Proceedings of the Cambridge Philosophical Society*, 31(4):555–563, October 1935.
- [SFF⁺14] Gerhard Schunk, Josef U. Fürst, Michael Förtsch, Dmitry V. Strekalov, Ulrich Vogl, Florian Sedlmeir, Harald G. L. Schwefel, Gerd Leuchs, and Christoph Marquardt. Identifying modes of large whispering-gallery mode resonators from the spectrum and emission pattern. *Optics Express*, 22(25):30795–30806, December 2014.
- [SFV⁺17] Florian Sedlmeir, Matthew R. Foreman, Ulrich Vogl, Richard Zeltner, Gerhard Schunk, Dmitry V. Strekalov, Christoph Marquardt, Gerd Leuchs, and Harald G. L. Schwefel. Polarization-Selective Out-Coupling of Whispering-Gallery Modes. *Physical Review Applied*, 7(2):024029, February 2017.
- [Sha49] C.E. Shannon. Communication in the Presence of Noise. *Proceedings of the IRE*, 37(1):10–21, January 1949.
- [SHR⁺22] Rishabh Sahu, William Hease, Alfredo Rueda, Georg Arnold, Liu Qiu, and Johannes M. Fink. Quantum-enabled operation of a microwave-optical interface. *Nature Communications*, 13(1):1276, March 2022.

- [SMM⁺16] Dmitry V. Strekalov, Christoph Marquardt, Andrey B. Matsko, Harald G. L. Schwefel, and Gerd Leuchs. Nonlinear and quantum optics with whispering gallery resonators. *Journal of Optics*, 18(12):123002, November 2016.
- [SP11] Amir H. Safavi-Naeini and Oskar Painter. Proposal for an optomechanical traveling wave phonon–photon translator. *New Journal of Physics*, 13(1):013017, January 2011.
- [SP19] Sergei Slussarenko and Geoff J. Pryde. Photonic quantum information processing: A concise review. *Applied Physics Reviews*, 6(4):041303, December 2019.
- [SQH⁺23] Rishabh Sahu, Liu Qiu, William Hease, Georg Arnold, Yuri Minoguchi, Peter Rabl, and Johannes M. Fink. Entangling microwaves with optical light, January 2023.
- [SSMY09] D. V. Strekalov, A. A. Savchenkov, A. B. Matsko, and N. Yu. Efficient upconversion of subterahertz radiation in a high-Q whispering gallery resonator. *Optics Letters*, 34(6):713–715, March 2009.
- [SSW17] Pascale Senellart, Glenn Solomon, and Andrew White. High-performance semiconductor quantum-dot single-photon sources. *Nature Nanotechnology*, 12(11):1026–1039, November 2017.
- [SZ97] Marlan O. Scully and M. Suhail Zubairy. *Quantum Optics*. Cambridge University Press, Cambridge, 1997.
- [SZR⁺17] Mohammad Soltani, Mian Zhang, Colm Ryan, Guilhem J. Ribeill, Cheng Wang, and Marko Loncar. Efficient quantum microwave-to-optical conversion using electro-optic nanophotonic coupled resonators. *Physical Review A*, 96(4):043808, October 2017.
- [Thé08] Luc Thévenaz. Slow and fast light in optical fibres. *Nature Photonics*, 2(8):474–481, August 2008.
- [THH⁺19] Anna Tchebotareva, Sophie L. N. Hermans, Peter C. Humphreys, Dirk Voigt, Peter J. Harmsma, Lun K. Cheng, Ad L. Verlaan, Niels Dijkhuizen, Wim de Jong, Anaïs Dréau, and Ronald Hanson. Entanglement between a Diamond Spin Qubit and a Photonic Time-Bin Qubit at Telecom Wavelength. *Physical Review Letters*, 123(6):063601, August 2019.
- [THRL08] J. D. Teufel, J. W. Harlow, C. A. Regal, and K. W. Lehnert. Dynamical Backaction of Microwave Fields on a Nanomechanical Oscillator. *Physical Review Letters*, 101(19):197203, November 2008.
- [Tsa10] Mankei Tsang. Cavity quantum electro-optics. *Physical Review A*, 81(6):063837, June 2010.
- [Tsa11] Mankei Tsang. Cavity quantum electro-optics. II. Input-output relations between traveling optical and microwave fields. *Physical Review A*, 84(4):043845, October 2011.
- [UCB⁺12] Imam Usmani, Christoph Clausen, Félix Bussières, Nicolas Sangouard, Mikael Afzelius, and Nicolas Gisin. Heralded quantum entanglement between two crystals. *Nature Photonics*, 6(4):234–237, April 2012.

- [VGH⁺19] Thibault Vogt, Christian Gross, Jingshan Han, Sambit B. Pal, Mark Lam, Martin Kiffner, and Wenhui Li. Efficient microwave-to-optical conversion using Rydberg atoms. *Physical Review A*, 99(2):023832, February 2019.
- [VSPC16] Amit Vainsencher, K. J. Satzinger, G. A. Peairs, and A. N. Cleland. Bi-directional conversion between microwave and optical frequencies in a piezoelectric optomechanical device. *Applied Physics Letters*, 109(3):033107, July 2016.
- [WCFZ21] Jing Wu, Chaohan Cui, Linran Fan, and Quntao Zhuang. Deterministic Microwave-Optical Transduction Based on Quantum Teleportation. *Physical Review Applied*, 16(6):064044, December 2021.
- [WCL14] Lewis A. Williamson, Yu-Hui Chen, and Jevon J. Longdell. Magneto-Optic Modulator with Unit Quantum Efficiency. *Physical Review Letters*, 113(20):203601, November 2014.
- [WDB⁺22] Matthew J. Weaver, Pim Duivestein, Alexandra C. Bernasconi, Selim Scharmer, Mathilde Lemang, Thierry C. van Thiel, Frederick Hijazi, Bas Hensen, Simon Gröblacher, and Robert Stockill. An integrated microwave-to-optics interface for scalable quantum computing, October 2022.
- [Wis28] John Wishart. The Generalised Product Moment Distribution in Samples from a Normal Multivariate Population. *Biometrika*, 20A(1/2):32–52, 1928.
- [WM08] D.F. Walls and Gerard J. Milburn, editors. *Quantum Optics*. Springer, Berlin, Heidelberg, 2008.
- [WM09] Howard M. Wiseman and Gerard J. Milburn. *Quantum Measurement and Control*. Cambridge University Press, Cambridge, 2009.
- [WMA⁺20] Jeremy D. Witmer, Timothy P. McKenna, Patricio Arrangoiz-Arriola, Raphaël Van Laer, E. Alex Wollack, Francis Lin, Alex K.-Y. Jen, Jingdong Luo, and Amir H. Safavi-Naeini. A silicon-organic hybrid platform for quantum microwave-to-optical transduction. *Quantum Science and Technology*, 5(3):034004, April 2020.
- [XMZ⁺20] Feihu Xu, Xiongfeng Ma, Qiang Zhang, Hoi-Kwong Lo, and Jian-Wei Pan. Secure quantum key distribution with realistic devices. *Reviews of Modern Physics*, 92(2):025002, May 2020.
- [XPv⁺21] Xiao Xue, Bishnu Patra, Jeroen P. G. van Dijk, Nodar Samkharadze, Sushil Subramanian, Andrea Corna, Brian Paquelet Wuetz, Charles Jeon, Farhana Sheikh, Esdras Juarez-Hernandez, Brando Perez Esparza, Huzaifa Rampurawala, Brent Carlton, Surej Ravikumar, Carlos Nieva, Sungwon Kim, Hyung-Jin Lee, Amir Sammak, Giordano Scappucci, Menno Veldhorst, Fabio Sebastian, Masoud Babaie, Stefano Pellerano, Edoardo Charbon, and Lieven M. K. Vandersypen. CMOS-based cryogenic control of silicon quantum circuits. *Nature*, 593(7858):205–210, May 2021.
- [XSF⁺21] Yuntao Xu, Ayed Al Sayem, Linran Fan, Chang-Ling Zou, Sihao Wang, Risheng Cheng, Wei Fu, Likai Yang, Mingrui Xu, and Hong X. Tang. Bidirectional interconversion of microwave and light with thin-film lithium niobate. *Nature Communications*, 12(1):4453, July 2021.

- [YML⁺20] Yong Yu, Fei Ma, Xi-Yu Luo, Bo Jing, Peng-Fei Sun, Ren-Zhou Fang, Chao-Wei Yang, Hui Liu, Ming-Yang Zheng, Xiu-Ping Xie, Wei-Jun Zhang, Li-Xing You, Zhen Wang, Teng-Yun Chen, Qiang Zhang, Xiao-Hui Bao, and Jian-Wei Pan. Entanglement of two quantum memories via fibres over dozens of kilometres. *Nature*, 578(7794):240–245, February 2020.
- [ZGV15] Stefano Zippilli, Giovanni Di Giuseppe, and David Vitali. Entanglement and squeezing of continuous-wave stationary light. *New Journal of Physics*, 17(4):043025, April 2015.
- [ZHA⁺15] Manjin Zhong, Morgan P. Hedges, Rose L. Ahlefeldt, John G. Bartholomew, Sarah E. Beavan, Sven M. Wittig, Jevon J. Longdell, and Matthew J. Sellars. Optically addressable nuclear spins in a solid with a six-hour coherence time. *Nature*, 517(7533):177–180, January 2015.
- [ZKW⁺22] A. M. J. Zwerver, T. Krähenmann, T. F. Watson, L. Lampert, H. C. George, R. Pillarisetty, S. A. Bojarski, P. Amin, S. V. Amitonov, J. M. Boter, R. Caudillo, D. Correas-Serrano, J. P. Dehollain, G. Droulers, E. M. Henry, R. Kotlyar, M. Lodari, F. Lüthi, D. J. Michalak, B. K. Mueller, S. Neyens, J. Roberts, N. Samkharadze, G. Zheng, O. K. Zietz, G. Scappucci, M. Veldhorst, L. M. K. Vandersypen, and J. S. Clarke. Qubits made by advanced semiconductor manufacturing. *Nature Electronics*, 5(3):184–190, March 2022.
- [ZSST20] Emil Zeuthen, Albert Schliesser, Anders S. Sørensen, and Jacob M. Taylor. Figures of merit for quantum transducers. *Quantum Science and Technology*, 5(3):034009, May 2020.
- [ZWD⁺20] Han-Sen Zhong, Hui Wang, Yu-Hao Deng, Ming-Cheng Chen, Li-Chao Peng, Yi-Han Luo, Jian Qin, Dian Wu, Xing Ding, Yi Hu, Peng Hu, Xiao-Yan Yang, Wei-Jun Zhang, Hao Li, Yuxuan Li, Xiao Jiang, Lin Gan, Guangwen Yang, Lixing You, Zhen Wang, Li Li, Nai-Le Liu, Chao-Yang Lu, and Jian-Wei Pan. Quantum computational advantage using photons. *Science*, 370(6523):1460–1463, December 2020.
- [ZWG⁺23] Silvia Zorzetti, Changqing Wang, Ivan Gonin, Sergey Kazakov, Timergali Khabiboulline, Alexander Romanenko, Vyacheslav P. Yakovlev, and Anna Grassellino. Milli-Kelvin measurements of permittivity and loss tangent of lithium niobate, February 2023.
- [ZWZ⁺20] Changchun Zhong, Zhixin Wang, Changling Zou, Mengzhen Zhang, Xu Han, Wei Fu, Mingrui Xu, S. Shankar, Michel H. Devoret, Hong X. Tang, and Liang Jiang. Proposal for Heralded Generation and Detection of Entangled Microwave–Optical-Photon Pairs. *Physical Review Letters*, 124(1):010511, January 2020.
- [ZZ21] Zheshen Zhang and Quntao Zhuang. Distributed quantum sensing. *Quantum Science and Technology*, 6(4):043001, July 2021.
- [ZZH⁺20] Na Zhu, Xufeng Zhang, Xu Han, Chang-Ling Zou, Changchun Zhong, Chiao-Hsuan Wang, Liang Jiang, and Hong X. Tang. Waveguide cavity optomagnonics for microwave-to-optics conversion. *Optica*, 7(10):1291–1297, October 2020.

[ZZL⁺21] Si-Ran Zhao, Yu-Zhe Zhang, Wen-Zhao Liu, Jian-Yu Guan, Weijun Zhang, Cheng-Long Li, Bing Bai, Ming-Han Li, Yang Liu, Lixing You, Jun Zhang, Jingyun Fan, Feihu Xu, Qiang Zhang, and Jian-Wei Pan. Field Demonstration of Distributed Quantum Sensing without Post-Selection. *Physical Review X*, 11(3):031009, July 2021.

APPENDIX A

Single photon electric field for a travelling wave

For the purpose this thesis, here, we will derive the single photon electric field for a whispering gallery mode traveling wave in a hollow-cylindrical volume with the radius a and thickness R . The volume of the hollow-cylinder is given as $V = 4\pi har$, where h is the height of the cylinder. We assume the electric field of form,

$$E(r, z, \phi, t) = E_0 \Theta(|r - R| < a) \cos(k\phi - \omega t) \quad (\text{A.1})$$

where, Θ is the heaviside function, k is the wave-vector amplitude and other symbols have their usual meaning.

The energy in the wave in a dielectric medium with electrical and magnetic permittivity as ϵ and μ is given as,

$$W = \frac{1}{\tau} \int \int \left(\frac{1}{2} \epsilon |E_0 \Theta(|r - R| < a) \cos(k\phi - \omega t)|^2 + \frac{1}{2\mu} |B(r, z, \phi, t)|^2 \right) dt dV \quad (\text{A.2})$$

where, τ is the time-period of the electro-magnetic(EM) wave. Since, the dt integral is over one time time-period, and thus $\int \cos^2(k\phi - \omega t) dt = \tau/2$. Next, we use the fact that the average energy between electric and magnetic fields is equal in an EM wave. Solving then, $W = \hbar\omega$ for a single photon energy, we get,

$$\hbar\omega = \frac{\epsilon E_o^2}{2} \int |\Theta(|r - R| < a)|^2 r dr dz d\phi \quad (\text{A.3})$$

The integral left is just the volume of the hollow cylinder. So, we can derive the single photon electric field E_0 as,

$$E_0 = \sqrt{\frac{2\hbar\omega}{\epsilon V}} \quad (\text{A.4})$$

Substituting this in eq. A.1, we derive the electric-field for a single photon for a travelling wave.

APPENDIX B

Microwave transmission line calibration

The microwave output line needs to be carefully calibrated since it forms the basis of the 4-port measurements and directly affects the output noise photon calibration. The output transmission line is comprised of a chain of amplifiers which are not quantum-limited, *i.e.* have a finite noise temperature. The total added noise temperature T_a of the full chain of amplifiers is given by Friis law,

$$T_a = T_1 + \frac{T_2}{G_1} + \frac{T_3}{G_1 G_2} + \dots \quad (\text{B.1})$$

where T_i (G_i) are the added noise temperature and gain of amplifiers from source to detection. Since the gain values are usually quite high, the final noise temperature of the detection chain depends mostly on T_1 and all the subsequent terms adding to only diminishing values.

The noise temperature T_a is related to the added noise photon number n_a via Plank's law as,

$$n_a = 1 / [\exp(\hbar\omega/k_B T_a) - 1] \quad (\text{B.2})$$

For a high-electron-mobility-transistor (HEMT) amplifier, the noise temperature specified for about 9 GHz is 4 K which corresponds to ~ 5 added noise photons. The gain of HEMT amplifiers around this frequency is about 44 dB. The full microwave output chain has more amplifiers and there are also be losses before the HEMT, so expected added noise photons for the full detection chain is ~ 12 photons with a gain of about 66 dB.

This added noise and corresponding gain due to the amplifiers and including any cable losses in the microwave detection chain is calibrated using a combination of a 50Ω load, a thermometer and a resistive heater that are thermally connected. The microwave detection chain is identical for the signals from the 50Ω load and the microwave cavity reflection, except for a small difference in cable length which we adjust for.

To calibrate the detection chain, we heat the 50Ω load with the resistive heater and record the amplified noise spectrum $P_{50\Omega}(\omega)$ as a function of temperature of 50Ω load $T_{50\Omega}$. The output noise detected over a bandwidth B , $P_{50\Omega}$, as a function of $T_{50\Omega}$ is given as,

$$P_{50\Omega} = \hbar\omega_e GB \left[\frac{1}{2} \coth \left(\frac{\hbar\omega_e}{2k_B T_{50\Omega}} \right) + N_{e,\text{add}} \right], \quad (\text{B.3})$$

with ω_e the center microwave frequency, $N_{e,\text{add}}$ (G) the added noise (gain) of the microwave detection chain, and k_B the Boltzmann constant.

We record the noise output spectra $P_{50\Omega}(\omega)$ over ~ 1 GHz range for a range of load temperatures $T_{50\Omega}$ from base temperature of the mixing chamber ~ 7 mK up to ~ 2 K. Selecting a bandwidth of $B = 11$ MHz (about the linewidth of the microwave cavity) around a specific frequency, in this case $\omega_e = 8.799$ GHz, we can fit the detected microwave power $P_{50\Omega}$ as a function of $T_{50\Omega}$ with eqn. B.3. In Fig. B.1, we show the detected noise $N_{e,\text{det}} = P_{50\Omega}/(\hbar\omega_e GB)$ as a function of $T_{50\Omega}$ along with a fit using eqn. B.3, with two fitting parameters G and $N_{e,\text{add}}$.

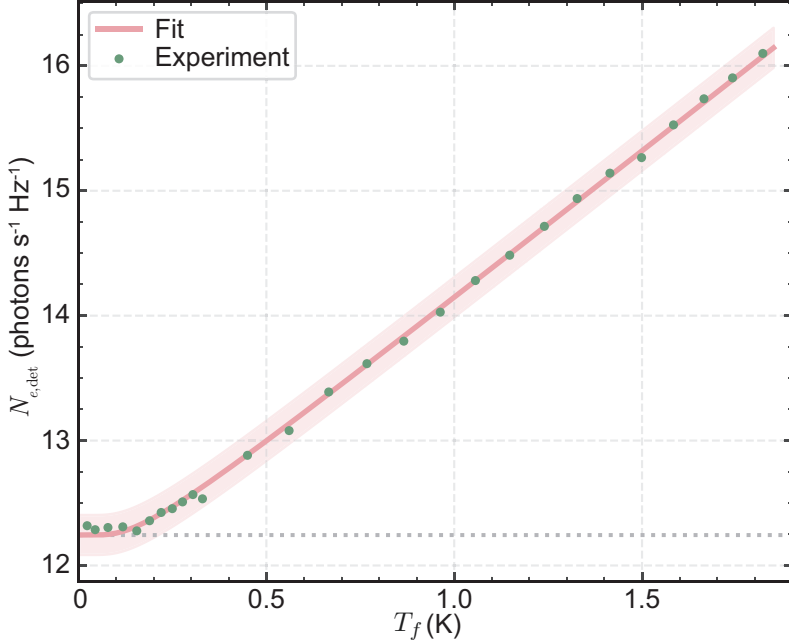


Figure B.1: Characterization of the added noise in the microwave detection chain. Measured output noise from a 50Ω calibration load as a function of its temperature T_f . The measured noise is plotted in units of photons as $N_{\text{det}}^{50\Omega} = P_{50\Omega}/(\hbar\omega_e GB)$. The dashed line at the bottom represents the fitted vacuum noise level in addition to the added noise. The red line and shaded region represents the fit and the 95% confidence interval around it. (Figure adapted from Ref. [SQH⁺23].)

By fitting the same parameters for the full range of recorded frequencies, we show the dependence of $N_{e,\text{det}}$ and the gain G as a function of microwave frequency (along with 2σ error as fill area) in Fig. B.2. The variation in the detected noise and gain is due to the impedance mismatch and reflections between components in the microwave detection chain. Since the optical FSR in our experiments is ~ 8.8 GHz, the added noise for microwave chain around these frequencies fall from $10.5 - 11.5$. Although, the variation around the frequencies we work with is not huge, it is good to calibrate the microwave transmission line for the relevant frequency.

As shown in the experimental setups (appendix C), the 50Ω calibration load is on a different port of the microwave switch. The microwave cable length between the switch and the 50Ω is 30.5 cm whereas that between the switch and the microwave cavity is 73 cm. This extra cable length and its loss needs to be added to the $T_{50\Omega}$ calibration to get the equivalent calibration for the microwave cavity.

The cable loss between the microwave cavity and the switch is easily measured by reflecting the microwave signal either directly from the switch (reset port) or from the microwave cavity (off-resonance to prevent cavity losses). The difference in measured power gives the two-way loss for the cable length (73 cm). The square root for this loss is the one way cable loss which

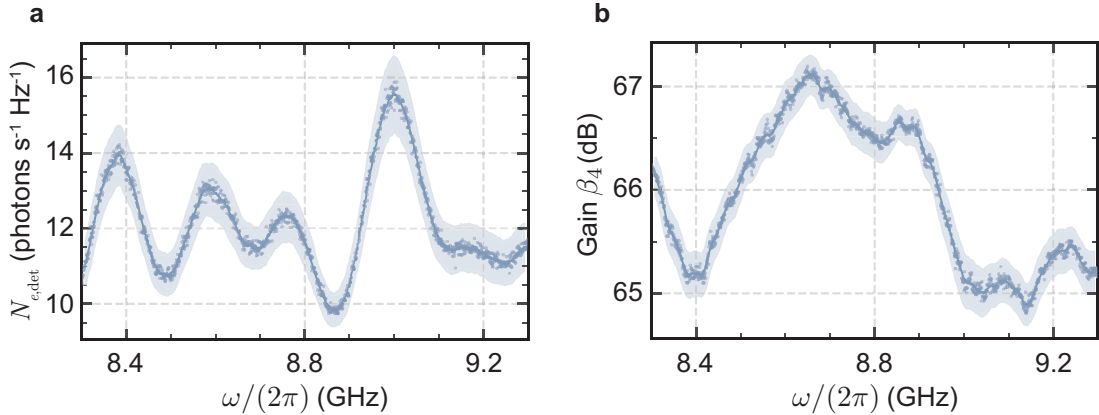


Figure B.2: **Microwave added noise and gain spectra.** **a (b)** The measured added noise in units of photons as $N_{det}^{50\Omega} = P_{50\Omega}/(\hbar\omega_e GB)$ (gain) as a function of microwave frequency. The shaded area represents the 2σ error in fit from eqn. B.3. (Figure adapted from Ref. [SQH⁺23].)

is about -0.88 dB. Assuming that the loss is linearly proportional to the cable length, we calculate the loss due to the extra cable length between the 50Ω load and the microwave cavity, 73–30.5 cm. Including the cable losses L (in absolute unit), the effective added noise increases ($N_{e,\text{add}} \rightarrow N_{e,\text{add}}/L$) while the gain decreases ($G \rightarrow G \times L$).

Finally, we also need to consider an additional error due to the temperature sensor inaccuracy of 2.5%. Although this does not change the final $N_{e,\text{add}}$ and G , it increases the uncertainty realized in these numbers.

For the CW optical pump measurements in chapter 5, the optical FSR was 8.8 GHz. For this microwave frequency, we determined the added noise for the 50Ω load to be 10.66 ± 0.15 and gain $\beta_4 = (67.65 \pm 0.05)$ dB. Adjusting for the cable loss and the temperature sensor uncertainty, the final adjusted added noise was (12.74 ± 0.36) and the adjusted gain $\beta_4 = (67.05 \pm 0.16)$ dB. All the stated errors are 2σ . The same numbers were used for the pulsed optical pump experiments in chapter 7.

However, for the two mode squeezing measurements in chapter 9, these numbers and the associated errors were of utmost importance, and therefore, careful calibration even for the closest of the relevant frequencies was done individually. All the numbers are reported in table B.1.

Table B.1: The added noise and gain in microwave detection chain (1σ errors shown)

Detection Chain	8.799 GHz		8.791 GHz	
	$N_{e,\text{add}}$	G (dB)	$N_{e,\text{add}}$	G (dB)
50Ω load (with fitting error)	11.74 ± 0.08	66.67 ± 0.02	11.76 ± 0.09	66.72 ± 0.03
MW cavity (including cable loss)	13.09 ± 0.09	66.20 ± 0.02	13.16 ± 0.10	66.23 ± 0.03
MW cavity (including temperature sensor uncertainty)	13.09 ± 0.33	66.20 ± 0.12	13.16 ± 0.34	66.23 ± 0.12

APPENDIX C

Experimental setups

C.1 Continuous wave optical pump setup

See Fig. C.1. A tunable laser is equally split (50/50) into two paths at the optical coupler OC1. The upper path is used as the optical pump and it goes through a variable optical attenuator VOA1 that allows to vary the optical pump power. The optical pump can then be either sent directly to the cryostat fiber, or it can go first through an electro-optic modulator (EOM) in order to create sidebands for spectroscopy calibration. The second path (horizontal) is used to generate the optical signal. It goes also through a variable optical attenuator and it is then frequency up-shifted by ω_e (\sim FSR) using a single sideband EO-modulator with suppressed carrier (SSB-SC) driven by a microwave source with local oscillator frequency ω_e (S1). A small fraction (1%) of this signal is picked up and sent directly to an optical spectrum analyzer (OSA) for sideband and carrier suppression ratio monitoring. The rest (99%) is recombined with the pump at OC2, sent to the fridge input fiber and the total power is monitored with a power meter (PM). The optical tones are focused on the prism with a GRIN-lens which then feeds the WGM resonator via evanescent coupling. Polarization controllers PC2 and PC3 are set to achieve maximum coupling to a TE polarized cavity mode. The reflected (or created) optical sideband signal and the reflected pump are collected with the second GRIN-lens and coupled to the cryostat output fiber. The optical signal is then split: 90% of the power goes to the OSA and 10% is sent to a photodiode (PD), which is used for mode spectroscopy and to lock on the optical mode resonance during the conversion measurement. The 90% arm is either sent directly to the OSA, or goes through an EDFA for amplification, depending on the microwave to optics converted signal power. On the microwave side, the signal is sent from the microwave source S2 (or from the VNA for microwave mode spectroscopy) to the fridge input line via the microwave combiner (MC1). The input line is attenuated with attenuators distributed between 4 K and 10 mK with a total of 60 dB in order to suppress room temperature microwave noise. Circulator C1 redirects the reflected tone from the cavity to the amplified output line, while C2 redirects noise coming in from the output line to a matched 50Ω termination. The output line is amplified at 4 K by a HEMT-amplifier and then at room temperature again with a low noise amplifier (LNA). The output line is connected to switch MS1, to select between an ESA or a VNA measurement. Lastly, microwave switch MS2 allows to swap the device under test (DUT) for a temperature $T_{50\Omega}$ controllable load, which serves as a broad band noise source in order to calibrate the output line's total gain and added noise (see Appendix B).

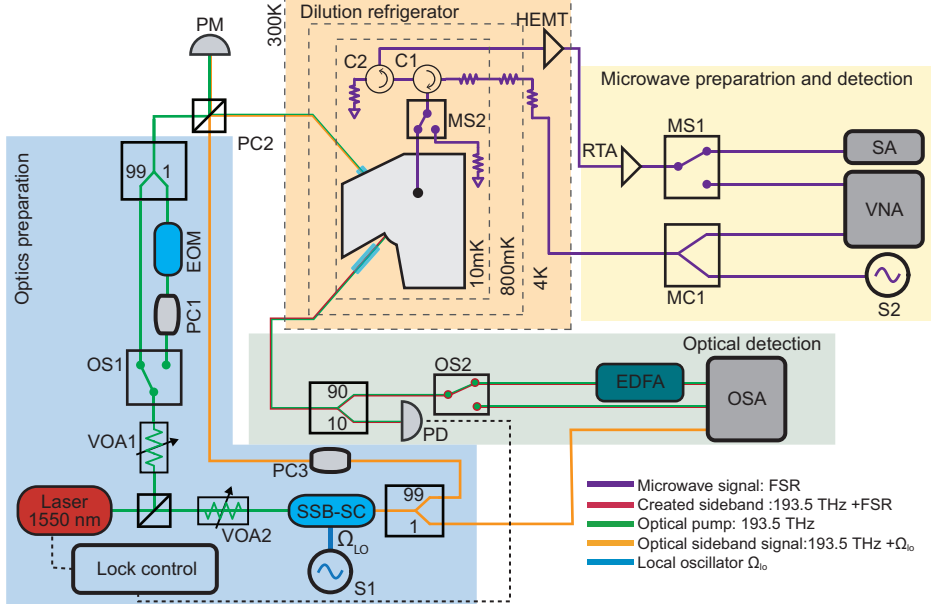


Figure C.1: Continuous wave optical pump experimental setup. (Figure taken from Ref. [HRS⁺20].)

C.2 Low cooperativity CW optical pump setup

See Fig. C.2. A tunable laser at frequency ω_p is sent through a variable optical attenuator (VOA1) to control the power output. Thereafter, the laser is sent to a single sideband (SSB) modulator. The modulator operates in a mode where the central pump frequency is allowed to pass through and only the lower sideband is suppressed. The SSB is connected to two microwave sources. The arrangement allows us to independently control the optical signal tone and the optical local oscillator (LO) tone, 200 MHz detuned, independently. The optical signal source S2 is also connected to a digital delay generator (DDG) to make pulses at the right time. The modulated output from the SSB is divided in two parts - 1% is used to monitor the suppression ratio of the sidebands using an optical spectrum analyzer (OSA), 99% is sent to an Erbium-doped fiber amplifier (EDFA) and amplified before being sent to the dilution refrigerator (DR). In the DR, the setup remains the same as in Fig. C.1. Outside the DR, the output light is separated in two parts - 1% is detected directly on a photo-diode (PD) to lock the laser to the optical pump mode and 99% is sent to a high speed photo-diode HSPD (400 MHz). The presence of the optical LO and signal in the same fiber means that the optical signal can be easily detected at the set frequency via downconversion. The output signal from HSPD is sent to an amplifier RTA3 before sent for digitization. On the microwave side, the setup is essentially the same as in Fig. C.1. The only difference is that, now, the output line is connected to switch MS1 and MS2, to select between an ESA, a VNA or a digitizer measurement via manual downconversion using MW LO S4 (200 MHz detuned).

C.3 High cooperativity pulsed optical pump setup

See Fig. C.3. A tunable laser at frequency ω_p is divided into two equal parts - one to serve as the optical pump and the other to produce the optical signal and the optical local oscillator (LO). The optical pump side (left) first passes through a variable optical attenuator (VOA1) to control the power sent in this arm and is then sent to an acousto-optic modulator (AOM1).

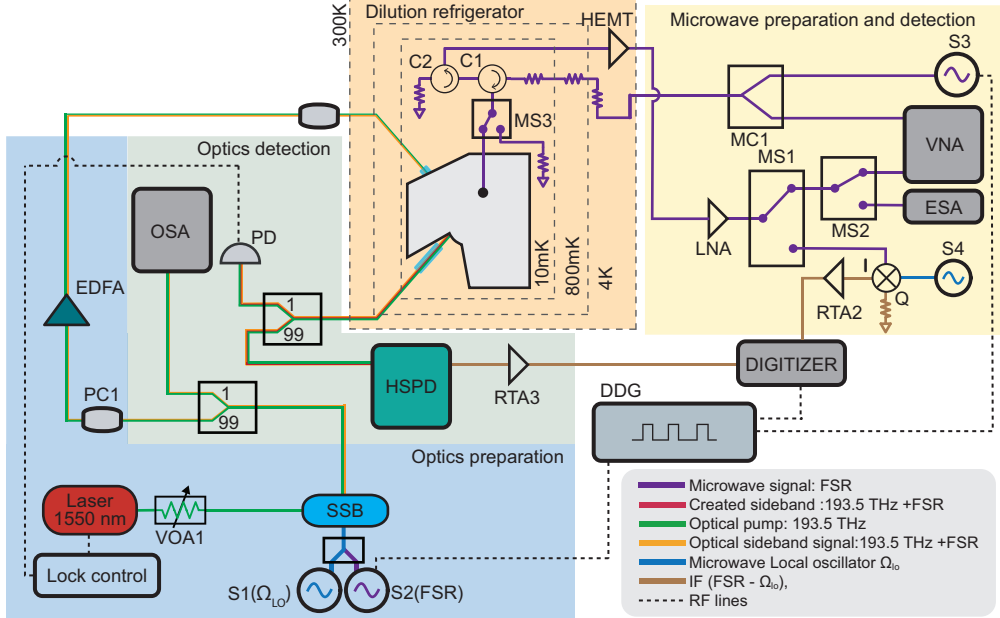


Figure C.2: Low cooperativity CW optical pump experimental setup. (Figure taken from Ref. [SHR²²].)

The AOM is accurately pulsed using a digital delay generator (DDG). The produced optical pulses are sent to an Erbium-doped fiber amplifier (EDFA) where they are amplified. The output of the EDFA is sent to another AOM2. The second AOM is also connected to DDG and acts as a window filter in time to suppress the broad band spontaneous emission noise from the EDFA. The optical pump pulse is further cleaned with a filter cavity F1 (50 MHz linewidth with ~ 15 GHz FSR), which is locked to the laser frequency (circulator C3 ensures that reflected noise from cavity F1 is dissipated) before being combined with the signal arm and sent to the dilution refrigerator (DR). The signal arm (right of the laser) is first divided in two parts - the optical LO and the optical signal. 25% of the light in signal arm is used to produce the optical signal. After passing through attenuator VOA2, the optical signal is produced using a single sideband modulator (SSB). This time we suppress both the central pump frequency and the lower sideband frequency keeping only the upper sideband as the optical signal. The SSB is driven by a microwave source S1 which is also connected to the DDG to accurately pulse the optical signal. The optical signal is divided in two parts - 1% is reserved to monitor the sideband suppression ratio via an optical spectrum analyzer (OSA), 99% is sent to DR after combining with the optical pump. The 75% light on the right side of the laser is used to produce the optical LO via a phase modulator (PM). The PM is operated via a microwave source S2 with a power such that the central tone is suppressed. Finally, the optical LO is sent directly to the optical heterodyne setup. The optics inside the DR has been explained in Fig. C.1. The output light from the DR is sent to filter F2 (50 MHz linewidth with ~ 40 dB suppression) to reject the strong optical pump. The reflected optical pump from cavity F2 is captured by photodiode PD1 via the circulator C4. The reflected optical pump measurement is used to lock the laser to the optical pump mode. The cleaned optical signal is sent to the heterodyne setup and measured with a balanced photo-detector (BPD). The output signal is amplified via a room temperature amplifier RTA1 before being sent to a digitizer. The microwave side of the setup is explained in Fig. C.2.

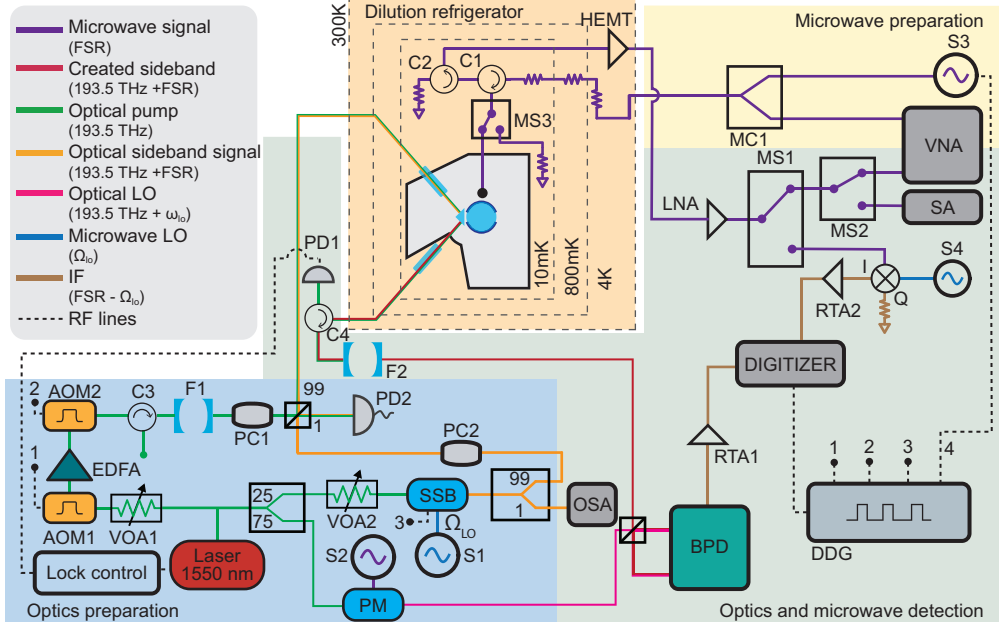


Figure C.3: High cooperativity pulsed optical pump experimental setup. (Figure taken from Ref. [SHR²²].)

C.4 Pulsed optical pump setup for two-mode squeezing

See Fig. C.4. The whole setup for this measurement was essentially the same as described in section C.3. The only difference is that the optical LO, which is produced via a phase modulator PM, is now detuned by $\omega_{\text{IF}}/2\pi = 40$ MHz. Since the PM produces many sidebands, we improve the optical heterodyne efficiency by suppressing the undesired sidebands via filter F3 (~ 50 MHz linewidth with 15 GHz FSR), reflection is rejected by circulator C5. F3 is temperature-stabilized and locked to the transmitted power similar to F1. The optical LO is also amplified via EDFA2 before the optical balanced heterodyne.

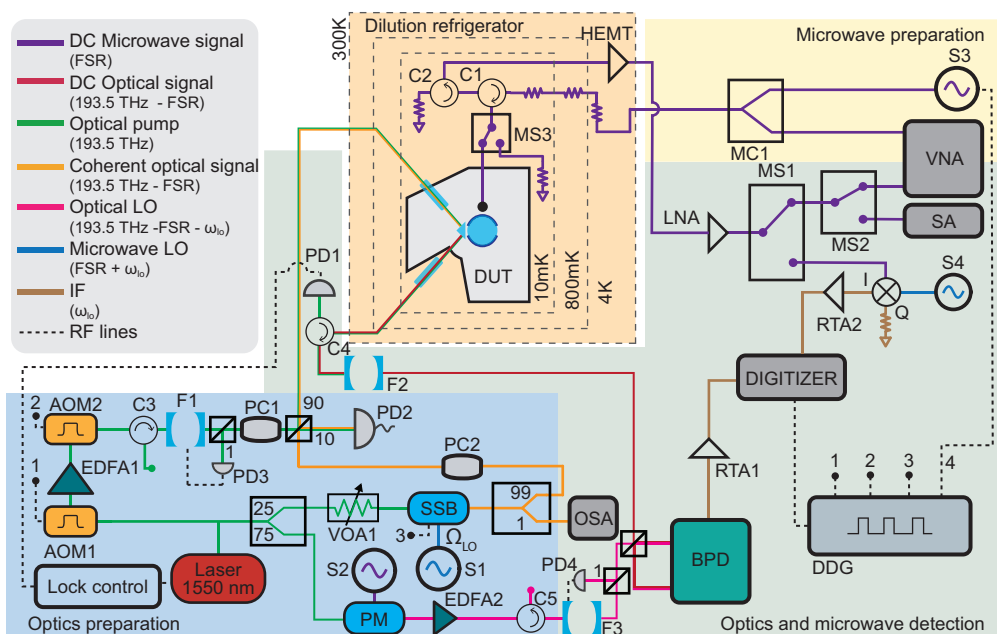


Figure C.4: Pulsed optical pump experimental setup for two-mode squeezing. (Figure taken from Ref. [SQH⁺23].)

D

APPENDIX

Optical pump PID lock

The optical pump is produced from the laser by amplification through EDFA (Erbium-doped fiber amplifier). EDFA amplifies the optical power by pumping and creating population inversion in a material to make it an optically active gain medium. Usually, the inverted population will be relaxed through stimulation of an input optical signal which will, in turn, amplify the optical signal. However, in absence of any signal, vacuum energy can also relax the inverted population spontaneously resulting in something called broadband amplified spontaneous emissions (ASE) noise.

The ASE noise is spread over multiple FSRs of the optical resonator and, therefore, is also naturally present at the optical signal frequency (one FSR away from the optical pump). Since we do not want any noise present at the optical signal frequency, we clean the optical pump in frequency domain using an optical Fabry-Pérot filter. The filter has an FSR of ~ 15 GHz such that near the optical WGM FSR, the filter has maximum suppression. The filter also has a linewidth of ~ 50 MHz so that sharp pulses with ~ 10 ns rise times can pass through the filter.

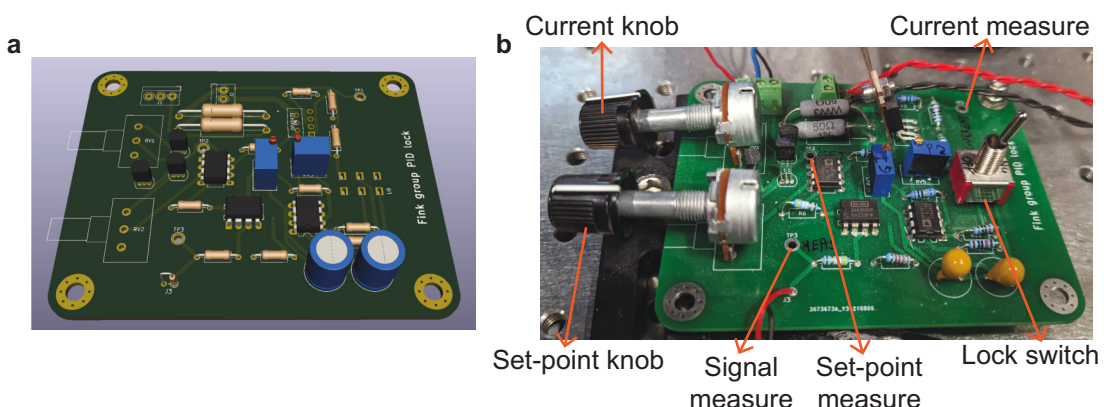


Figure D.1: **The PID circuit used in optical pump lock.** a 3D rendering of the designed PID circuit. b Final completed circuit. Various measurement ports and used knobs and switches are labelled.

The Fabry-Pérot filter is custom made by gluing plano-concave mirrors on an aluminium cavity structure. Since aluminium has high thermal expansion coefficient, we can control the length of the optical cavity and thus its resonance frequency by tuning the temperature. Consequently,

we place the optical filter on a Peltier element. By controlling the current through the Peltier element, we can control the resonance frequency of the optical cavity.

For chapter 7, we controlled the current through the Peltier element through a digital algorithm. But for chapter 8 and 9, we switched to a using a PID (Propotional Integral Derivative) lock shown in Fig. D.1. We took 1% of the light transmitting through the filter and measured it with a photodiode. After passing through an extremely low pass filter (to convert the pulsed output from photodiode to basically DC signal), we feed it to the PID as an error signal.

The PID lock tries to keep the error signal close to a set-point which can be set via a knob shown in Fig. D.1b. The error signal is changed by changing the current through the Peltier element which is controlled by the PID as well. By increasing or decreasing the current through the Peltier element, the optical cavity resonance is changed and thus the transmitted power. We can choose a set-point which is close to maximum (about 90%) but not maximum such that by moving the cavity resonance forward or backward, the transmitted power also behaves linearly. This means error signal is proportional to the Peltier drive. In this state, the lock can be started by flicking the switch shown in Fig. D.1b. Note that sometimes, the error signal measured from photodiode is not fully linear over the full cavity resonance tuning. This can happen for example if photodiode is saturating. In this case, adjusting the optical attenuation before the photodiode may solve the issue.

The PID circuit shown in Fig. D.1 was home-designed and only has proportional and integral elements. When the lock-switch is set to off, the current through the Peltier element can be controlled by the 'Current knob' and measured as the voltage between 'Current measure' port and ground. Similarly, the set-point can be changed and measured through its ports and knobs. Finally, the input error signal can be measured as voltage between the 'Signal measure' and ground. It is usually around 200 mV. Full optical FSR of the optical filter cavity can be explored by applying current corresponding between -2.5 V to 2.5 V. The full schematic of the PID circuit is shown in Fig. D.2.

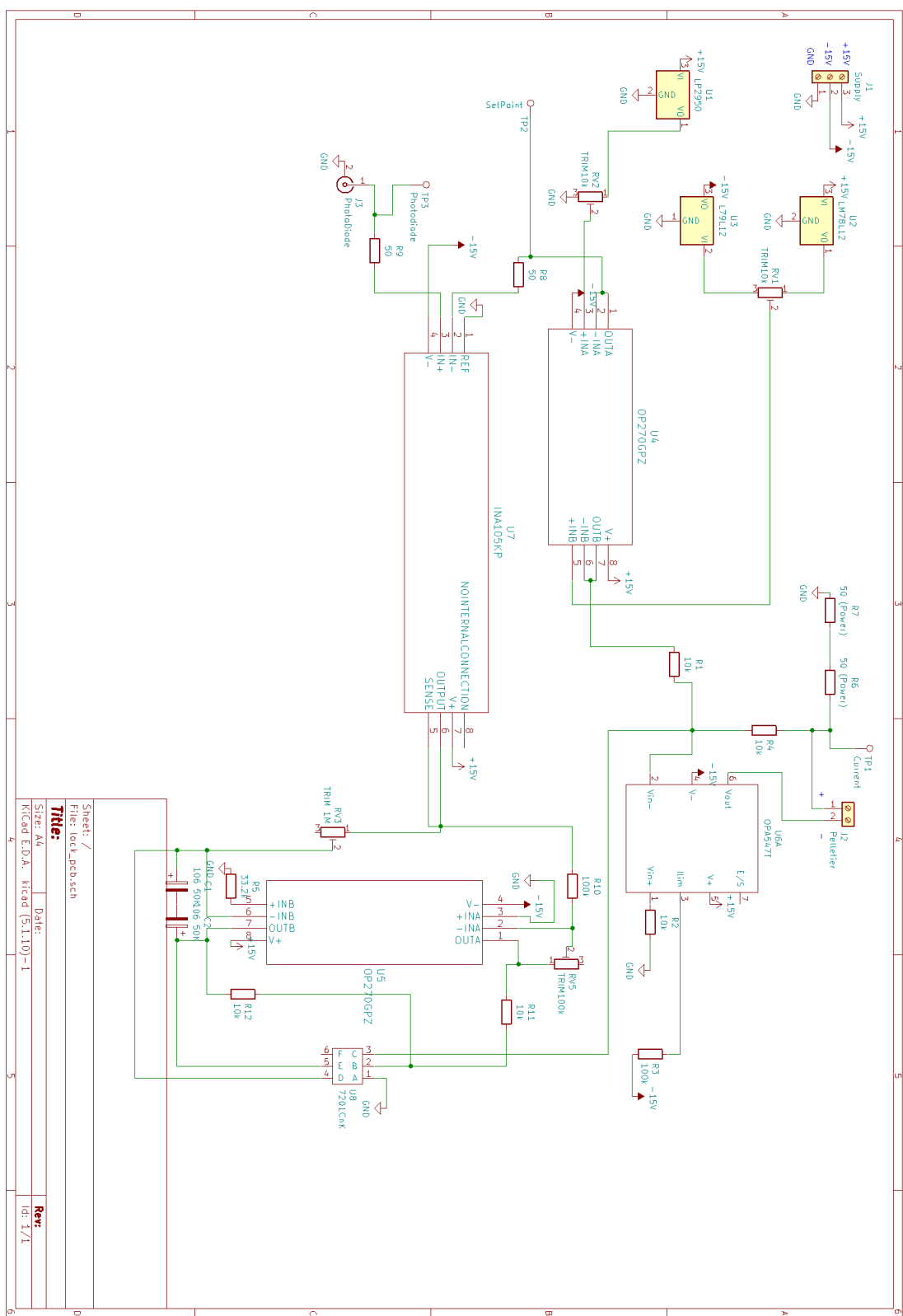


Figure D.2: Circuit schematic for the PID lock used for optical pump lock. The PID controls the current to a Peltier element which changes the temperature of an optical cavity, in turn changing its frequency.

